A Common Thread in
Unconventional Superconductivity:
The Functional Renormalization Group
in Multi-Band Systems

vorgelegt von

Christian Platt

aus Wetzlar

Würzburg, 2012

Eingereicht am: _____

bei der Fakultät für Physik und Astrophysik

1. Gutachter: Prof. Dr. Werner Hanke

2. Gutachter: _____

3. Gutachter: _____

der Dissertation

Vorsitzende(r): _____

1. Prüfer: Prof. Dr. Werner Hanke

2. Prüfer: _____

3. Prüfer: _____

im Promotionskolloquium

Tag des Promotionskolloquiums: _____

Doktorurkunde ausgehändigt am: _____

Abstract

The superconducting properties of complex materials like the recently discovered iron-pnictides or strontium-ruthenate are often governed by multi-orbital effects. In order to unravel the superconductivity of those materials, we develop a multi-orbital implementation of the functional renormalization group and study the pairing states of several characteristic material systems.

Starting with the iron-pnictides, we find competing spin-fluctuation channels that become attractive if the superconducting gap changes sign between the nested portions of the Fermi surface. Depending on material details like doping or pnictogen height, these spin fluctuations then give rise to $s_\pm$-wave pairing with or without gap nodes and, in some cases, also change the symmetry to d-wave. Near the transition from nodal $s_\pm$-wave to d-wave pairing, we predict the occurrence of a time-reversal symmetry-broken $(s+id)$-pairing state which avoids gap nodes and is therefore energetically favored.

We further study the electronic instabilities of doped graphene, another fascinating material which has recently become accessible and which can effectively be regarded as multi-orbital system. Here, the hexagonal lattice structure assures the degeneracy of two d-wave pairing channels, and the system then realizes a chiral $(d + id)$-pairing state in a wide doping range around van-Hove filling. In addition, we also find spin-triplet pairing as well as an exotic spin-density wave phase which both become leading if the long-ranged hopping or interaction parameters are slightly modified, for example, by choosing different substrate materials.

Finally, we consider the superconducting state of strontium-ruthenate, a possible candidate for chiral spin-triplet pairing with fascinating properties like the existence of half-quantum vortices obeying non-Abelian statistics. Using a microscopic three orbital description including spin-orbit coupling, we demonstrate that ferromagnetic fluctuations are still sufficient to induce this $\hat{z}(p_x \pm ip_y)$-pairing state. The resulting superconducting gap reveals strong anisotropies on the d_{xy}-dominated Fermi-surface pocket and nearly vanishes on the other remaining two pockets.

Kurzfassung

Die supraleitenden Eigenschaften von komplexen Materialsystemen, wie den erst kürzlich entdeckten Eisen-Pniktiden oder den Strontium-Ruthenaten, sind oftmals durch das Zusammenspiel vieler elektronischer Orbitale bestimmt. Um die Supraleitung in derartigen Systemen besser zu verstehen, entwickeln wir in dieser Arbeit eine Multi-Orbital-Implementierung der funktionalen Renormierungsgruppe und untersuchen die Elektronenpaarung in verschiedenen charakteristischen Materialverbindungen.

In den Eisen-Pniktiden finden wir hierbei mehrere Spinfluktuationskanäle, die eine Elektronenpaarung hervorrufen, sofern die Paarwellenfunktion einen Vorzeichenwechsel zwischen den verschiedenen genesteten Bereichen der Fermifläche aufweist. Abhängig von den spezifischen Materialeigenschaften, wie der Dotierung oder der Position des Pniktogenatoms, führen diese Spinfluktuationen dann zu $s_\pm$-wellenartiger Paarung mit durchgängiger Energielücke oder mit Knoten auf der Fermifläche. In manchen Fällen wird zudem auch d-wellenartige Paarung induziert, die in der Nähe des Übergangs zur $s_\pm$-Symmetrie einen gemischten $(s + id)$-Zustand mit gebrochener Zeitinversionssymmetrie aufweist. Diese neuartige Phase zeigt faszinierende Eigenschaften, wie zum Beispiel das spontane Entstehen von Suprastömen am Probenrand und um nichtmagnetische Störstellen. Auf Grund der durchgängigen Energielücke ist dieser $(s + id)$-Zustand energetisch begünstigt.

Im Folgenden untersuchen wir zudem auch die elektronischen Instabilitäten eines weiteren außergewöhnlichen Materials – dotiertes Graphen. Diese rein zweidimensionale Kohlenstoffverbindung ist schon seit mehreren Jahren im Fokus der Festkörperforschung und wurde mittlerweile auch durch neuartige experimentelle Verfahren dotiert, ohne die zugrundeliegende hexagonale Gittersturktur merklich zu stören. Eine theoretische Beschreibung dieses Systems erfordert die Berücksichtigung zweier nicht-equivalenter Gitterplätze, was wiederum effektiv als Zwei-Orbital-System aufgefasst werden kann. Durch die besondere Symmetrie der hexagonalen Gitterstruktur sind beide d-wellenartigen Paarungskanäle entartet und ähnlich der $(s+id)$-Paarung in den Pniktiden finden wir hier eine chirale $(d + id)$-Paarung in einem weiten Dotierungsbereich um van-Hove Füllung. Des Weiteren identifizieren wir Spin-Triplet-Paarung und eine exotische Form der Spindichtewelle, welche beide durch leichte Veränderung der langreichweitigen Hüpfam-

plituden und Wechselwirkungensparameter realisiert werden können.

Als drittes Beispiel betrachten wir die Supraleitung in dem Strontium-Ruthenat Sr_2RuO_4. Die Besonderheit dieser Materialverbindung liegt in der möglichen Realisierung einer chiralen Spin-Triplet Paarung, die wiederum faszinierende Eigenschaften wie die Existenz von halbganzzahligen Fluss-vortizes mit nicht-Abelscher Vertauschungsstatistik aufweisen würde. Mittels eines mikroskopischen Drei-Orbital-Modells und der Berücksichtigung von Spin-Bahn-Kopplung finden wir hierbei, dass moderate ferromagnetische Spinfluktuationen immer noch ausreichen, um diesen speziellen Paarungszustand anzutreiben. Die berechnete Energielücke zeigt im Weiteren sehr starke Anisotropien auf dem d_{xy}-Orbital-dominierten Bereich der Fermifläche und verschwindet nahezu vollständig auf den anderen beiden Fermiflächen.

Contents

Chapter 1

Introduction

The phenomenon of superconductivity is still one of the most fascinating manifestations of quantum physics on a macroscopic scale. Upon cooling below a characteristic transition temperature T_c, superconductivity occurs in certain materials and implies the complete vanishing of electrical resistance as well as an expulsion of internal magnetic fields. The potential applications of this phenomenon are truly amazing, ranging from electric power generation and distribution to levitated transport systems and superconducting electronics. Unfortunately, a widespread and commercial usage of these technologies is obstructed by the extremely low transition temperatures. For this reason, the discovery of the cuprate materials [1] in the late eighties with an unprecedented T_c above the nitrogen boiling point caused great interest and rekindled the dream of room-temperature superconductivity. However, after more than two decades of intense research, the highest available T_c is still far from room temperature, and a comprehensive understanding of the cuprates has not yet been accomplished. Another breakthrough then followed in 2008 when high-T_c superconductivity was found in the material class of iron-pnictides [2]. Although the transition temperatures there were not as high as in the cuprates, the huge variety of compounds as well as the complex interplay of magnetism, crystal structure and superconductivity triggered an enormous interest within the condensed matter community. In particular, the diversity of different compounds opened new possibilities to study high-T_c superconductivity and also promised new compounds with tailored properties for technical applications.

Today, our basic understanding of superconductivity still relies on the celebrated work of Bardeen, Cooper and Schrieffer (BCS) [3]. According to their BCS theory, pairs of electrons with zero total momentum condense into a collective quantum state that appears insensitive to any kind of disruptions which usually cause electrical resistance. However, whereas the condensation of electron pairs is at the heart of each superconductor, the mechanism responsible for pairing as well as the form of the pair wave func-

tion depend on the particular material compound. For example, in the first superconductors, considered by BCS, a weak attractive interaction based on quantized lattice deformations (phonons) induces the condensation of electron pairs with zero total angular momentum and spin-singlet structure. Beside this conventional pairing, other mechanisms with more exotic pair wave functions of spin-triplet or higher angular momentum structure were proposed in certain other superconductors. Analogous to the orbitals in a hydrogen atom, the pairing states are often termed as s-wave, p-wave and so on, although rotational symmetry in a crystal is broken, and the form of the associated pair wave functions attains the above orbital structure only near the gamma-point of the Brillouin zone (continuum limit). In order to determine the pairing symmetry of a superconductor, various experimental methods have been developed throughout the years and identified a d-wave pairing state in the cuprates. Nevertheless, although the pairing symmetry in the cuprates narrowed down the possible mechanisms, the precise origin of high-T_c superconductivity in the cuprates remains unsolved.

In this thesis, we start with an investigation of superconductivity in the iron-pnictides. At the first glance, the cuprates and the iron-pnictides appear quite similar: both reveal a magnetically ordered ground state in their undoped parent compounds and both become superconducting upon doping. In addition, cuprates and iron-pnictides are both layered systems and display an electronic structure that is mainly determined by unfilled d-orbitals. However, there are also crucial differences. For example, in the undoped cuprates, the effective one-band description actually implies a metallic state, but the system instead shows a Mott-insulating behavior due to strong local Coulomb interactions. At the same time, the iron-pnictides with only weak to moderate interactions require a multi-orbital description and feature semi-metallic behavior. It is currently believed that much of the anomalous properties of the cuprates, for example the poorly understood pseudogap phase, originate from the stronger Coulomb interaction and are probably not apparent in the iron-pnictides. For this reason, the complexity of the iron-pnictides arises primarily from the involved multi-orbital physics and not so much from strong interaction effects. In this thesis, we therefore apply the method of functional renormalization group (RG) which, on the one hand, enables an unbiased investigation of weakly to moderately correlated materials and also allows to capture the full complexity of a multi-orbital problem.

In Chapter 2, we introduce the functional RG as a theoretical tool for analyzing the electronic instabilities of multi-orbital systems. In particular, we discuss the derivation of the underlying flow equations, the necessary approximations, as well as the use of symmetries to reduce the numerical effort.

In Chapter 3, we review some basic properties of superconductivity in general and discuss certain experimental methods to determine the pair

wave function in a given superconductor. In addition, we also derive a self-contained symmetry classification of superconducting order on different lattices with and without spin-orbit coupling. This scheme is then extended to general crystal structures and also to general particle-particle and particle-hole condensates.

In Chapter 4, we start with a brief summary on the most relevant structural, magnetic and superconducting properties of iron-pnictides. In the following, we then study the pairing symmetries as well as the underlying pairing mechanisms of various iron-pnictide compounds. Here, we demonstrate how the multi-pocket Fermi surface and the multi-orbital interactions drive different competing spin-fluctuation channels. These competing fluctuations then give rise to $s_{\pm}$-wave pairing with or without gap nodes and even lead to d-wave superconductivity. Based on this understanding, we propose different possibilities to influence the competing pairing channels and also to realize a new time-reversal symmetry broken $(s + id)$-pairing state. Besides the pairing state of the iron-pnictides, we also explore the magnetically ordered state as well as other subleading ordering tendencies.

The developed multi-orbital version of the functional RG likewise applies to material systems with non-equivalent lattice sites. In Chapter 5, we therefore consider the electronic instabilities of graphene, the two-dimensional analog of graphite. Using certain dopants or electrolytic gating, graphene can nowadays be doped up to van-Hove filling without causing too much disorder in the underlying lattice structure. During that chapter, we describe a variety of fascinating phases that could possibly be realized in doped graphene. The prevailing one is the chiral $(d + id)$ superconducting phase with quantized values in certain response functions reflecting the topological nature of this pairing state. In addition, we also demonstrate how longer-ranged Coulomb interactions can lead to spin-triplet pairing or to an exotic spin-density wave phase. This is of particular interest, as the longer-ranged interactions can be tuned by different substrate materials.

In Chapter 6, we address another multi-orbital problem, the superconducting state of strontium-ruthenate Sr_2RuO_4 (SRO). Although being isostructural to the cuprates, SRO turned out to be quite different and possibly realizes a chiral $(p + ip)$-pairing state. However, despite a large number of theoretical studies in this field, the pairing mechanism in SRO as well as the detailed gap symmetry are still under debate. For this reason, we start with a microscopic three-orbital description and explore the competing orders by means of functional RG. We illustrate how moderate ferromagnetic fluctuations are still sufficient to drive p-wave pairing, and we demonstrate that the $(p + ip)$-pairing is energetically favored due to the effect of spin-orbit coupling. In addition, we also compare the calculated superconducting gap with recent experiments and investigate the effect of doping, for example by replacing strontium with lanthanum. Finally, in Chapter 7, we summarize the key findings and methodical progress developed in this thesis.

Chapter 2

Functional Renormalization Group

Interacting electron systems commonly display a huge variety of fascinating phenomena such as superconductivity, magnetic ordering or the formation of exotic quantum liquids. These phenomena usually emerge at scales far below the bare energy scale of the microscopic Hamiltonian (see Fig. 2.1a). In order to interpolate between those scales, it appears natural to treat degrees of freedom with different energy scales successively, descending from high to low energies. Using a functional-integral formulation of the partition function, this idea can be implemented by integrating out high-energy modes step by step and by adjusting the action accordingly. This procedure then generates a one-parameter family of actions which interpolates between the microscopic theory at high energies and an effective low-energy description (see Fig. 2.1b). At the same time, infrared singularities which signal an instability of the normal state are approached in a controlled way. In fact, the required partial integration of modes can almost never be performed in an exact way, and one has to resort to approximate treatments. Yet, for an infinitesimal mode elimination, the resulting change of the action can be expressed in a formally exact flow equation. In a similar way, the functional renormalization group rephrases the process of mode elimination in terms of an exact flow equation for certain generating functionals. The benefit of this flow equation lies, on the one hand, in its transparent approximation schemes and also in its flexibility concerning the choice of flow parameters or the choice of alternative generating functionals.

Starting with a general derivation of the functional flow equations at the beginning of this chapter, we discuss the effect of various flow parameters as well as the implications of symmetry and the necessity of approximations.

(a)   (b)
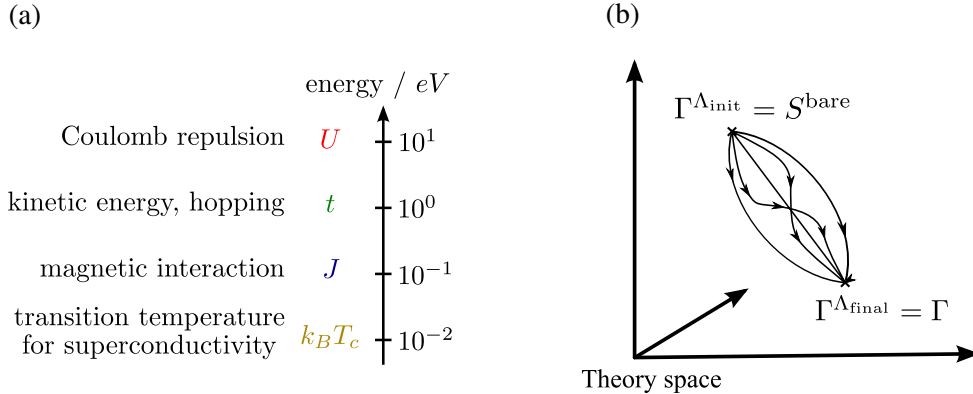
Figure 2.1: (a) Important energy scales in high-T_c cuprate superconductors. (b) Flow of the effective action, starting at $\Gamma^{\Lambda_{init}} = S^{\text{bare}}$ for large values of Λ and approaching the full effective action at $\Lambda = 0$. Different trajectories correspond to distinct choices of the flow parameter.

2.1 Functional Flow Equations

In the following section, we introduce the concept of generating functionals and the notion of functional flow equations. In particular, we define the so-called effective action as a generating functional of the one-particle irreducible (1PI) vertex functions and derive its corresponding flow equation. Using certain approximation schemes for an efficient numerical treatment, the 1PI flow equation then serves as the main computational tool throughout the following work.

As a starting point, we consider an interacting fermion system described by the action

$$S(\overline{\psi}, \psi) = -\int_{k,k'} Q_{k,k'} \overline{\psi}_k \psi_{k'} + \int_{k_1,k_2,k_1',k_2'} U_{k_1,k_2,k_1',k_2'} \overline{\psi}_{k_1} \overline{\psi}_{k_2} \psi_{k_1'} \psi_{k_2'} \quad (2.1)$$

with Grassmann fields $\overline{\psi}, \psi$, the inverse bare propagator

$$Q_{k,k'} = \delta_{kk'} \cdot \left(G_k^0\right)^{-1} = \delta_{kk'} \cdot (ik_0 - \xi_b(\boldsymbol{k})), \quad (2.2)$$

and some two-particle interaction U. We further employed the notation of $k = (k_0, \boldsymbol{k}, \sigma, b)$ including fermionic Matsubara frequencies k_0, momenta $\boldsymbol{k}$ as well as internal degrees of freedom like spin projections σ or band indices b. The dispersion $\xi_b(\boldsymbol{k})$ in (2.2) then characterizes the one-particle energy as a function of momentum $\boldsymbol{k}$ and band index b. In addition, the integral $\int_k$ contains integration and summation over each entry in k and also includes prefactors like temperature and volume.

Based on the action $S(\overline{\psi}, \psi)$ in (2.1), we can infer thermodynamic quan-

tities like the grand-canonical partition function

$$Z = \int D(\overline{\psi}, \psi) e^{-S(\overline{\psi}, \psi)} \tag{2.3}$$

or the imaginary-time ordered Green functions

$$G_{k_1, \dots, k_n; k_1', \dots, k_n'} = \frac{1}{Z} \int D(\overline{\psi}, \psi) e^{-S(\overline{\psi}, \psi)} \psi_{k_1} \dots \psi_{k_n} \overline{\psi}_{k_n'} \dots \overline{\psi}_{k_1'}, \tag{2.4}$$

just by choosing the appropriate functional averages. It is further convenient to define the generating functional

$$W[\eta, \overline{\eta}] = \int D(\overline{\psi}, \psi) e^{-S(\overline{\psi}, \psi) + (\overline{\eta}, \psi) + (\overline{\psi}, \eta)} \tag{2.5}$$

with source terms

$$(\overline{\eta}, \psi) := \int_k \overline{\eta}_k \psi_k, \quad (\overline{\psi}, \eta) := \int_k \overline{\psi}_k \eta_k$$

such that (2.4) can be rephrased by derivatives of $W[\eta, \overline{\eta}]$ with respect to the fields η and $\overline{\eta}$. Taking the logarithm of (2.5), one obtains another generating functional

$$\mathcal{G}[\eta, \overline{\eta}] = -\ln(W[\eta, \overline{\eta}]) \tag{2.6}$$

which, again by functional differentiation, provides the connected n-particle Green functions

$$G_{k_1, \dots, k_n; k_1', \dots, k_n'}^{c(2n)} = -\left\langle \psi_{k_1} \dots \psi_{k_n} \overline{\psi}_{k_n'} \dots \overline{\psi}_{k_1'} \right\rangle_c \tag{2.7}$$

$$= (-1)^n \left. \frac{\partial^{2n} \mathcal{G}[\eta, \overline{\eta}]}{\partial \overline{\eta}_{k_1} \dots \partial \overline{\eta}_{k_n} \partial \eta_{k_n'} \dots \partial \eta_{k_1'}} \right|_{\eta = \overline{\eta} = 0}.$$

Note that the $(-1)^n$ factor here results from the commutation of $\partial/\partial\eta$ with the field $\overline{\psi}$ in the source term of (2.5).

During the next paragraph, we want to derive an exact flow equation for the generating functional in (2.6). The essential idea here is to circumvent the direct integration in $\mathcal{G}$ by constructing a one-parameter family of generating functionals $\mathcal{G}^\Lambda$ that interpolates between a solvable starting point at large values of Λ and the full functional at $\Lambda = 0$. One possibility to construct this one-parameter dependence is by replacing $Q \to Q^\Lambda$ in the bare action (2.1) such that

$$Q_{k,k'}^\Lambda \sim \begin{cases} Q_{k,k'}, & \text{for } \Lambda \to 0 \\ \infty, & \text{for } \Lambda \to \infty \end{cases}. \tag{2.8}$$

As a consequence, the generating functional $\mathcal{G}^\Lambda$ fulfills the required boundary conditions of

$$\mathcal{G}^\Lambda \sim \begin{cases} \mathcal{G}, & \text{for } \Lambda \to 0 \\ 0, & \text{for } \Lambda \to \infty \end{cases}, \tag{2.9}$$

where the trivial case $\mathcal{G}^{\Lambda \to \infty} = 0$ results from the infinite mass term in (2.8), which freezes out all particle propagation. In order to approach possible singularities in a controlled way, we further require that the parameter dependence of Q^Λ regularizes infrared divergences, which in turn may arise from the unbound propagator at zero frequencies and at Fermi-surface momenta. The extrapolation of $\mathcal{G}^\Lambda$ from large values of Λ down to $\Lambda = 0$ can then be considered as an initial value problem, which is nothing but the searched for flow equation. We can thus rephrase the functional integration of Eq. (2.6) into a formally exact differential equation:

$$\begin{aligned} \partial_\Lambda \mathcal{G}^\Lambda[\eta, \overline{\eta}] &= -e^{\mathcal{G}^\Lambda[\eta, \overline{\eta}]} \partial_\Lambda e^{-\mathcal{G}^\Lambda[\eta, \overline{\eta}]} \\ &= -e^{\mathcal{G}^\Lambda[\eta, \overline{\eta}]} \int D(\overline{\psi}, \psi) \left(\overline{\psi}, \dot{Q}^\Lambda \psi \right) e^{-S(\overline{\psi}, \psi) + (\overline{\eta}, \psi) + (\overline{\psi}, \eta)} \\ &= e^{\mathcal{G}^\Lambda[\eta, \overline{\eta}]} \left(\partial_\eta, \dot{Q}^\Lambda \partial_{\overline{\eta}} \right) e^{-\mathcal{G}^\Lambda[\eta, \overline{\eta}]} \tag{2.10} \\ &= e^{\mathcal{G}^\Lambda[\eta, \overline{\eta}]} \left(\int_{k, k'} \partial_{\eta_k} \dot{Q}^\Lambda_{kk'} \partial_{\overline{\eta}_{k'}} e^{-\mathcal{G}^\Lambda[\eta, \overline{\eta}]} \right) \\ &= \int_{k, k'} \left\{ \left(-\partial_{\eta_k} \mathcal{G}^\Lambda[\eta, \overline{\eta}] \right) \dot{Q}^\Lambda_{kk'} \left(-\partial_{\overline{\eta}_{k'}} \mathcal{G}[\eta, \overline{\eta}] \right) + \dot{Q}^\Lambda_{kk'} \left(-\partial_{\eta_k} \partial_{\overline{\eta}_{k'}} \mathcal{G}[\eta, \overline{\eta}] \right) \right\} \\ &= \left(\left(\partial_\eta \mathcal{G}^\Lambda[\eta, \overline{\eta}] \right), \dot{Q}^\Lambda \left(\partial_{\overline{\eta}} \mathcal{G}[\eta, \overline{\eta}] \right) \right) + \mathrm{tr} \left(\dot{Q}^\Lambda \left(\partial_{\overline{\eta}} \partial_\eta \mathcal{G}[\eta, \overline{\eta}] \right) \right). \tag{2.11} \end{aligned}$$

Using the Taylor expanded functional $\mathcal{G}^\Lambda$ in the above flow equation, this provides an infinite hierarchy of differential equations for the respective Taylor coefficients, the connected Green functions $G^{c(2n)}$. Yet, the connected Green functions $G^{c(2n)}$ contain tree-like diagrams of 1PI vertex functions, and the corresponding isolated propagators can lead to technical problems within the flow equations [4]. In addition, the trivial initial condition of $\mathcal{G}^{\Lambda \to \infty} = 0$ also appears to be unfavorable as it absorbs any informations about the original system.

It is therefore more convenient to derive a flow equation for the 1PI vertex generating functional or effective action Γ^Λ, which is determined by the Legendre transformation of $\mathcal{G}^\Lambda$:

$$\Gamma^\Lambda[\zeta, \overline{\zeta}] = \mathcal{G}^\Lambda[\eta, \overline{\eta}] + (\overline{\eta}^\Lambda, \zeta) + (\overline{\zeta}, \eta^\Lambda). \tag{2.12}$$

Here, the conjugate fields $\overline{\zeta}, \zeta$ are defined as

$$\zeta = -\frac{\partial \mathcal{G}^\Lambda}{\partial \overline{\eta}}, \quad \overline{\zeta} = \frac{\partial \mathcal{G}^\Lambda}{\partial \eta}, \tag{2.13}$$

and it is also important to note that $\overline{\eta}^\Lambda$, η^Λ are actually Λ-dependent functions of $\overline{\zeta}$ and ζ due to (2.13). The 1PI vertex functions can then be obtained by computing derivatives with respect to the conjugate fields

$$\gamma_{k_1,\ldots,k_n;k_1',\ldots,k_n'}^{\Lambda(2n)} = \left. \frac{\partial^{2n}\Gamma^\Lambda[\zeta,\overline{\zeta}]}{\partial\overline{\zeta}_{k_1}\ldots\partial\overline{\zeta}_{k_n}\partial\zeta_{k_n'}\ldots\partial\zeta_{k_1'}}\right|_{\zeta=\overline{\zeta}=0}. \tag{2.14}$$

In order to derive the corresponding flow equation for the effective action Γ^Λ, we first note that (2.12) implies the following reciprocity relation for the second derivatives Γ^Λ and $\mathcal{G}^\Lambda$:

$$\boldsymbol{\partial}^2\Gamma^\Lambda[\overline{\zeta},\zeta] = \left(\partial^2 G^\Lambda[\overline{\eta},\eta]\right)^{-1} \tag{2.15}$$

with

$$\boldsymbol{\partial}^2\Gamma^\Lambda[\overline{\zeta},\zeta] = \begin{pmatrix} \frac{\partial^2\Gamma^\Lambda}{\partial\overline{\zeta}_{k_1}\partial\zeta_{k_1'}} & \frac{\partial^2\Gamma^\Lambda}{\partial\overline{\zeta}_{k_1}\partial\overline{\zeta}_{k_1'}} \\ \frac{\partial^2\Gamma^\Lambda}{\partial\zeta_{k_1}\partial\zeta_{k_1'}} & \frac{\partial^2\Gamma^\Lambda}{\partial\zeta_{k_1}\partial\overline{\zeta}_{k_1'}} \end{pmatrix} \tag{2.16}$$

$$\partial^2 G^\Lambda[\overline{\eta},\eta] = \begin{pmatrix} -\frac{\partial^2\mathcal{G}^\Lambda}{\partial\overline{\eta}_{k_1'}\partial\eta_{k_1}} & \frac{\partial^2\mathcal{G}^\Lambda}{\partial\overline{\eta}_{k_1'}\partial\overline{\eta}_{k_1}} \\ \frac{\partial^2\mathcal{G}^\Lambda}{\partial\eta_{k_1'}\partial\eta_{k_1}} & -\frac{\partial^2\mathcal{G}^\Lambda}{\partial\eta_{k_1'}\partial\overline{\eta}_{k_1}} \end{pmatrix}.$$

For the lowest order Taylor expansion, this then yields

$$\gamma_{k;k'}^{\Lambda(2)} = \left(G_{k;k'}^{\Lambda(2)}\right)^{-1} = Q_{k,k'}^\Lambda - \Sigma_{k,k'}^\Lambda, \tag{2.17}$$

and, for higher order terms, all connected Green functions are obtained by summing tree-like diagrams of 1PI vertex functions with equal or lower order [5]. Using the reciprocity relation (2.15) as well as (2.11), we can now determine the flow equation for the effective action Γ^Λ:

$$\begin{aligned} \partial_\Lambda\Gamma^\Lambda[\zeta,\overline{\zeta}] &= \partial_\Lambda\mathcal{G}[\eta^\Lambda,\overline{\eta}^\Lambda] + (\partial_\Lambda\overline{\eta}^\Lambda,\zeta) + (\overline{\zeta},\partial_\Lambda\eta^\Lambda) \\ &= \partial_\Lambda\mathcal{G}[\eta^\Lambda,\overline{\eta}^\Lambda]\big|_{\eta^\Lambda,\overline{\eta}^\Lambda \text{ fixed}} \\ &\overset{(2.11)}{=} \left(\left(\partial_\eta\mathcal{G}^\Lambda\right),\dot{Q}^\Lambda\left(\partial_{\overline{\eta}}\mathcal{G}\right)\right) + \text{tr}\left(\dot{Q}^\Lambda\left(\partial_{\overline{\eta}}\partial_\eta\mathcal{G}\right)\right) \\ &\overset{(2.15)}{=} -\left(\overline{\zeta},\dot{Q}^\Lambda\zeta\right) - \text{tr}\left(\dot{Q}^\Lambda\left(\left(\boldsymbol{\partial}^2\Gamma^\Lambda[\zeta,\overline{\zeta}]\right)^{-1}\right)_{11}\right) \\ &= -\left(\overline{\zeta},\dot{Q}^\Lambda\zeta\right) - \frac{1}{2}\text{tr}\left(\dot{\boldsymbol{Q}}^\Lambda\left(\boldsymbol{\partial}^2\Gamma^\Lambda[\zeta,\overline{\zeta}]\right)^{-1}\right). \end{aligned} \tag{2.18, 2.19}$$

Here, the notation $(\cdots)_{11}$ relates to the $(1,1)$-element of the matrix $\boldsymbol{\partial}^2\Gamma^\Lambda$ given in Eq. (2.16), and the bold quantity $\dot{\boldsymbol{Q}}^\Lambda$ in (2.19) denotes

$$\dot{\boldsymbol{Q}}^\Lambda = \text{diag}(\dot{Q}^\Lambda, -\dot{Q}^{\Lambda T}).$$

Unlike the flow equation for the generating functional $\mathcal{G}^\Lambda$, the one in (2.19) reveals a nontrivial initial condition of $\Gamma^{\Lambda\to\infty} = S$, with S denoting the bare action in (2.1). The complete solution of (2.19) would then describe the evolution from the bare action towards the full effective action and would hence provide all 1PI vertex functions as well as the connected Green functions in a tree like series.

Unfortunately, the direct solution of the functional flow equation (2.19) is only possible for a very small number of systems. However, as one is primarily interested in a few number of 1PI vertex functions, it is therefore convenient to expand both sides in powers of the fields and to calculate the flow only for certain 1PI vertex functions. For this purpose, we first rewrite the effective action in a series of fields

$$\Gamma^\Lambda[\zeta,\overline{\zeta}] = \sum_{m=0}^{\infty} \mathcal{A}^{(2m)\Lambda}[\overline{\zeta},\zeta] \tag{2.20}$$

with

$$\mathcal{A}^{(2m)\Lambda}[\overline{\zeta},\zeta] = \frac{(-1)^m}{(m!)^2} \int_{\substack{k_1,\dots,k_m \\ k_1',\dots,k_m'}} \gamma^{(2m)\Lambda}_{k_1',\dots,k_m';k_1,\dots,k_m} \overline{\zeta}_{k_1'}\cdots\overline{\zeta}_{k_m'}\zeta_{k_m}\cdots\zeta_{k_1}.$$

In order to obtain a similar series expansion for the inverse $\left(\boldsymbol{\partial}^2\Gamma^\Lambda[\zeta,\overline{\zeta}]\right)^{-1}$ on the right-hand side of (2.19), we first introduce the matrix

$$\boldsymbol{U}^\Lambda[\overline{\zeta},\zeta] = \boldsymbol{\partial}^2\Gamma^\Lambda[\zeta,\overline{\zeta}]\big|_{\zeta=\overline{\zeta}=0} - \boldsymbol{\partial}^2\Gamma^\Lambda[\zeta,\overline{\zeta}]$$

together with its series expansion

$$\boldsymbol{U}^\Lambda[\overline{\zeta},\zeta] = -\sum_{m=2}^{\infty} \boldsymbol{\partial}^2\mathcal{A}^{(2m)\Lambda}[\overline{\zeta},\zeta]. \tag{2.21}$$

Now, by making use of $\boldsymbol{\partial}^2\Gamma^\Lambda\big|_{\zeta=\overline{\zeta}=0} = \left(\boldsymbol{G}^\Lambda\right)^{-1}$ from (2.17), the inverse $\left(\boldsymbol{\partial}^2\Gamma^\Lambda\right)^{-1}$ is given by the following geometric series

$$\begin{aligned}
\left(\boldsymbol{\partial}^2\Gamma^\Lambda[\zeta,\overline{\zeta}]\right)^{-1} &= \left(\left(\boldsymbol{G}^\Lambda\right)^{-1} - \boldsymbol{U}^\Lambda[\overline{\zeta},\zeta]\right)^{-1} \\
&= \left(\boldsymbol{1} - \boldsymbol{G}^\Lambda\boldsymbol{U}^\Lambda[\overline{\zeta},\zeta]\right)^{-1}\boldsymbol{G}^\Lambda \\
&= \left(\boldsymbol{1} + \boldsymbol{G}^\Lambda\boldsymbol{U}^\Lambda[\overline{\zeta},\zeta] + \boldsymbol{G}^\Lambda\boldsymbol{U}^\Lambda[\overline{\zeta},\zeta]\boldsymbol{G}^\Lambda\boldsymbol{U}^\Lambda[\overline{\zeta},\zeta] + \dots\right)\boldsymbol{G}^\Lambda.
\end{aligned} \tag{2.22}$$

We then insert (2.22) into the right-hand side of the flow equation (2.19) which gives rise to

$$\begin{aligned}
\partial_\Lambda\Gamma^\Lambda[\zeta,\overline{\zeta}] &= -\left(\overline{\zeta},\dot{\boldsymbol{Q}}^\Lambda\zeta\right) - \frac{1}{2}\mathrm{tr}\left(\dot{\boldsymbol{Q}}^\Lambda\left(\boldsymbol{1} + \boldsymbol{G}^\Lambda\boldsymbol{U}^\Lambda + \boldsymbol{G}^\Lambda\boldsymbol{U}^\Lambda\boldsymbol{G}^\Lambda\boldsymbol{U}^\Lambda + \dots\right)\boldsymbol{G}^\Lambda\right) \\
&= -\left(\overline{\zeta},\dot{\boldsymbol{Q}}^\Lambda\zeta\right) - \mathrm{tr}\left(\dot{\boldsymbol{Q}}^\Lambda\boldsymbol{G}^\Gamma\right)
\end{aligned}$$

$$+ \frac{1}{2}\mathrm{tr}\left(\boldsymbol{S}^\Lambda\left(\boldsymbol{U}^\Lambda + \boldsymbol{U}^\Lambda\boldsymbol{G}^\Lambda\boldsymbol{U}^\Lambda + \dots\right)\right). \tag{2.23}$$

Here, it is important to note that we exploited the cyclic invariance of the trace and also defined the so-called single-scale propagator

$$\boldsymbol{S}^\Lambda = \mathrm{diag}\left(S^\Lambda, -S^{\Lambda T}\right) = -\boldsymbol{G}^\Lambda\dot{\boldsymbol{Q}}^\Lambda\boldsymbol{G}^\Lambda$$

with

$$S^\Lambda = -G^\Lambda\dot{Q}^\Lambda G^\Lambda = \frac{d}{d\Lambda}\left.G^\Lambda\right|_{\Sigma^\Lambda\text{ fixed}}.$$

The trace term in (2.23) further reveals the one-loop structure of the formally exact flow equation. Inserting the two series expansions of Γ^Λ in (2.20) and $\boldsymbol{U}$ in (2.21) into (2.23), we obtain a system of differential equations for the coefficients $\mathcal{A}^{(2m)\Lambda}$:

$$\frac{d}{d\Lambda}\mathcal{A}^{(0)\Lambda} = -\mathrm{tr}\left(\dot{Q}^\Lambda G^\Gamma\right)$$

$$\frac{d}{d\Lambda}\mathcal{A}^{(2)\Lambda} = -\frac{1}{2}\mathrm{tr}\left(\boldsymbol{S}^\Lambda\partial^2\mathcal{A}^{(4)\Lambda}\right) - \left(\overline{\zeta}, \dot{Q}^\Lambda\zeta\right)$$

$$\frac{d}{d\Lambda}\mathcal{A}^{(4)\Lambda} = -\frac{1}{2}\mathrm{tr}\left(\boldsymbol{S}^\Lambda\partial^2\mathcal{A}^{(6)\Lambda}\right) + \frac{1}{2}\mathrm{tr}\left(\boldsymbol{S}^\Lambda\partial^2\mathcal{A}^{(4)\Lambda}\boldsymbol{G}^\Lambda\partial^2\mathcal{A}^{(4)\Lambda}\right)$$

$$\frac{d}{d\Lambda}\mathcal{A}^{(6)\Lambda} = -\frac{1}{2}\mathrm{tr}\left(\boldsymbol{S}^\Lambda\partial^2\mathcal{A}^{(8)\Lambda}\right) + \dots \quad .$$

At this, the first equation corresponds to the flow of the grand-canonical potential. It also turns out that the flow equation for a given $\mathcal{A}^{(2m)\Lambda}$ always contains the next order term $\mathcal{A}^{(2m+2)\Lambda}$ in a tadpole-like diagram. In a next step, we compare the field-independent coefficients in each of these equations and obtain an infinite hierarchy of flow equations for the 1PI vertex functions, of which the first two read as

$$\frac{d}{d\Lambda}\Sigma^\Lambda_{k_1',k_1} = \sum_{q;q'} S^\Lambda_{q,q'}\gamma^{(4)\Lambda}_{k_1',q';k_1,q} \tag{2.24}$$

$$\frac{d}{d\Lambda}\gamma^{(4)\Lambda}_{k_1',k_2';k_1,k_2} = -\sum_{q,q'} S^\Lambda_{q,q'}\gamma^{(6)\Lambda}_{k_1',k_2',q';k_1,k_2,q} \tag{2.25}$$

$$+ \sum_{\substack{k,k'\\q,q'}} G^\Lambda_{k,k'}S^\Lambda_{q,q'} \times \left\{\gamma^{(4)\Lambda}_{k_1',k_2';k,q}\gamma^{(4)\Lambda}_{k',q';k_1,k_2}\right.$$

$$- \left[\gamma^{(4)\Lambda}_{k_1',q';k_1,k}\gamma^{(4)\Lambda}_{k',k_2';q,k_2} + (k \leftrightarrow q, k' \leftrightarrow q')\right]$$

$$+ \left.\left[\gamma^{(4)\Lambda}_{k_2',q';k_1,k}\gamma^{(4)\Lambda}_{k',k_1';q,k_2} + (k \leftrightarrow q, k' \leftrightarrow q')\right]\right\}.$$

Note that in (2.24), we further employed $\gamma^{(2)\Lambda} = Q^\Lambda - \Sigma^\Lambda$ in order to derive a flow equation for the self-energy Σ^Λ. In a graphical representation, these flow equations are shown in Fig. 2.2, where slashed and full lines correspond

Figure 2.2: Flow equations for the first two 1PI vertex functions in (2.24) and (2.25). Slashed and full internal lines represent the single-scale S^Λ and full propagators G^Λ.

to single-scale S^Λ and full propagator G^Λ, respectively. For a numerical implementation and an application to realistic material compounds, we further have to justify the truncation of this infinite hierarchy to a manageable system of flow equations. In addition to that, we need to specify the flow parameter dependence in the quadratic part Q^Λ which was left unspecified in the definition of (2.8).

2.2   Flow Parameters

In the preceding section, we derived flow equations for the effective action and for the associated 1PI vertex functions. The starting point here was the quadratic part of the underlying action which was equipped with an additional parameter dependence in order to interpolate between the bare theory and the full effective action. We further required that this parameter dependence also regularizes infrared singularities which may arise from the unbounded propagator at zero frequency and at Fermi surface momenta. The integration contained in the trace of (2.19) then becomes finite, and a potential singularity can be approached in a controlled way.

One possible choice of flow parameter is implemented in the so-called cutoff schemes where the inverse quadratic part reads as

$$\left(Q^\Lambda_{k,k'}\right)^{-1} = \left(G^{0\Lambda}_k\right) = \frac{\theta^\Lambda_\epsilon(k_0, \boldsymbol{k})}{ik_0 - \xi_b(\boldsymbol{k})}. \tag{2.26}$$

Here, $\theta^\Lambda_\epsilon(k_0, \boldsymbol{k})$ indicates a cutoff function either in frequency $\theta^\Lambda_\epsilon(k_0, \boldsymbol{k}) = \Theta_\epsilon(|k_0| - \Lambda)$ or in momentum space $\theta^\Lambda_\epsilon(k_0, \boldsymbol{k}) = \Theta_\epsilon(|\xi_b(\boldsymbol{k})| - \Lambda)$ with Θ_ϵ denoting a step function of finite width ϵ shown in Fig. 2.3a. The full
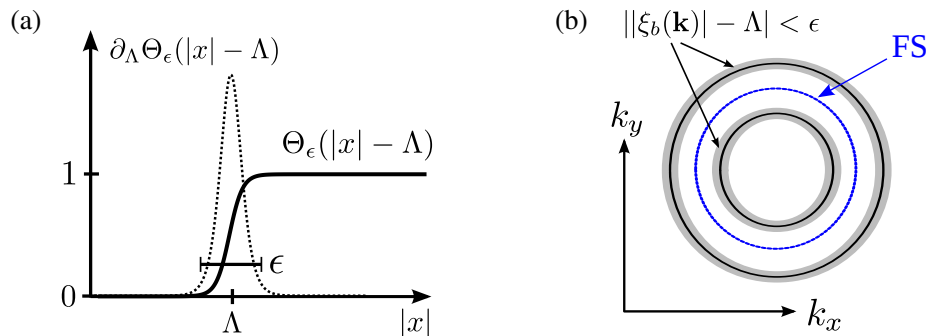
Figure 2.3: (a) Cutoff function Θ_ϵ (full line) and corresponding scale-derivative $\partial_\Lambda \Theta_\epsilon$ (dashed line). (b) Momentum shells (gray) representing the finite support of the single-scale propagator S^Λ at an energy scale Λ away from the Fermi surface (blue).

propagator in (2.17) is then given by

$$G^\Lambda(k_0, \boldsymbol{k}) = \frac{\theta_\epsilon^\Lambda(k_0, \boldsymbol{k})}{ik_0 - \xi_b(\boldsymbol{k}) - \theta_\epsilon^\Lambda(k_0, \boldsymbol{k})\Sigma^\Lambda(k_0, \boldsymbol{k})}, \tag{2.27}$$

and the corresponding single-scale propagator $S^\Lambda = -G^\Lambda \dot{Q}^\Lambda G^\Lambda$ reads as

$$S^\Lambda(k_0, \boldsymbol{k}) = \frac{\partial_\Lambda \theta_\epsilon^\Lambda(k_0, \boldsymbol{k})}{\left[ik_0 - \xi_b(\boldsymbol{k}) - \theta_\epsilon^\Lambda(k_0, \boldsymbol{k})\Sigma^\Lambda(k_0, \boldsymbol{k})\right]^2}, \tag{2.28}$$

with a finite support near the Λ-energy shells as depicted in Fig. 2.3b.

Using the above cutoff scheme, we obtain an implementation similar to Wilson's original idea of integrating out momentum modes shell by shell. For example, if we start with a momentum cutoff Λ greater than the bandwidth, all fluctuations are completely suppressed due to (2.27), and the initial value of the effective action equals the bare action in Eq. (2.1). Following the trajectory of Γ^Λ to lower scales, the calculation of $\partial_\Lambda \Gamma^\Lambda$ comprises a trace over the single-scale propagator S^Λ whose support is restricted to the momentum shells of Fig. 2.3b. For this reason, the calculation of Γ^Λ with a decreasing cutoff-scale Λ then integrates out momentum modes shell by shell and implements Wilson's picture of viewing the physical system at different length scales. Although these cutoff schemes provide a very intuitive understanding of renormalization they also involve serious drawbacks. One is the violation of Ward identities at any finite cutoff value [6, 7], and the other is the non-uniform treatment of particle-hole processes within the momentum-cutoff scheme. In order to explain this latter issue, we first write down the one-loop particle-hole fluctuations arising in simple perturbation theory

$$\chi^{p-h}(\boldsymbol{k}, \boldsymbol{q}) = \frac{n_F(\xi_b(\boldsymbol{k})) - n_F(\xi_b(\boldsymbol{k} + \boldsymbol{q}))}{\xi_b(\boldsymbol{k}) - \xi_b(\boldsymbol{k} + \boldsymbol{q})}. \tag{2.29}$$

During the flow, these contributions are taken into account successively within the trace

$$
\mathrm{tr}\left(\boldsymbol{S}^\Lambda \boldsymbol{U}^\Lambda \boldsymbol{G}^\Lambda \boldsymbol{U}^\Lambda\right) \sim \mathrm{tr}\left(\chi^{p-h}(\boldsymbol{k},\boldsymbol{q}) \cdot \partial_\Lambda(\theta_\epsilon^\Lambda(\boldsymbol{k})\theta_\epsilon^\Lambda(\boldsymbol{k}+\boldsymbol{q})) \cdots \right). \quad (2.30)
$$

Note that we neglected frequency dependences and self-energy insertions in (2.30) for notational clarity. If we now consider particle-hole fluctuations with vanishing momentum transfer, which means $\chi^{p-h}(\boldsymbol{k},\boldsymbol{q} \to 0)$, it turns out that the only nonzero contribution in (2.29) comes from modes $\boldsymbol{k}$ in a small energy region ($\sim T$) around the Fermi surface. However, due to the cutoff function $\theta_\epsilon^\Lambda(\boldsymbol{k})$, these modes are not taken into account until $\Lambda \approx T$. On the other hand, particle-hole fluctuations with large momentum transfer are already taken into account right from the beginning. The cutoff-scheme therefore treats particle-hole fluctuations in a non-uniform way, and it may happen that other channels already indicate a singularity at cutoff values $\Lambda > T$, whereas the small $\boldsymbol{q}$ particle-hole fluctuations have not yet contributed.

In order to avoid this issue, we can exploit the flexibility in the parameter dependence of Γ^Λ and regard the temperature itself as flow parameter. However, we first have to shift the temperature dependences towards the quadratic part of the action (2.1), and we therefore write out all temperature prefactors

$$
S(\overline{\psi},\psi) = -T \int_{k,k'} Q_{k,k'}\overline{\psi}_k\psi_{k'} + T^3 \int_{k_1,k_2,k_1',k_2'} U_{k_1,k_2,k_1',k_2'}\overline{\psi}_{k_1}\overline{\psi}_{k_2}\psi_{k_1'}\psi_{k_2'}
$$

and rescale its field variables according to

$$
\overline{\psi}_k = T^{-3/4}\overline{\phi}_k, \quad \psi_k = T^{-3/4}\phi_k. \quad (2.31)
$$

In the rescaled action, all temperature dependences now occur only within the quadratic part

$$
S(\overline{\phi},\phi) = -T^{-1/2}\int_{k,k'} Q_{k,k'}\overline{\phi}_k\phi_{k'} + \int_{k_1,k_2,k_1',k_2'} U_{k_1,k_2,k_1',k_2'}\overline{\phi}_{k_1}\overline{\phi}_{k_2}\phi_{k_1'}\phi_{k_2'},
$$

and we can then follow the same arguments as in the cutoff case and regard the temperature T itself as flow parameter. Here, it turns out that for temperatures in the order of the bandwidth W, all perturbative corrections to the vertex functions are suppressed with a negative power of T [8], and we obtain the required boundary condition of $\Gamma^{T\sim W} = S$. In addition to that, the temperature also serves as an infrared regulator similar to the momentum or frequency cutoff as it shifts Matsubara frequencies $k_0 = (2n+1)\pi T$ away from zero and hence cuts out the singularities of the bare propagator

$$
\left(\widetilde{Q}_{k,k'}^T\right)^{-1} = \left(\widetilde{G}_k^{0T}\right) = \frac{T^{1/2}}{ik_0 - \xi_b(\boldsymbol{k})}. \quad (2.32)
$$

It is further important to note that all objects in the rescaled fields $\overline{\phi}, \phi$ are highlighted with a tilde, and, to obtain the m-particle Green and vertex functions back in the original fields $\overline{\psi}, \psi$, we have to unscale these functions with a factor of $T^{-3m/2}$ and $T^{3m/2}$, respectively.

The temperature flow scheme can now be implemented in a similar way as the cutoff version. We start again with the bare theory for temperatures in the order of the bandwidth $\Gamma^{T_{init}\sim W} = S$ and then follow the trajectory Γ^T to lower values of T. The difference between both schemes consists in the distinct scale derivatives ∂_Λ and ∂_T, which in the temperature flow case involves the $T-$dependent Green function

$$\widetilde{G}^T(k_0, \boldsymbol{k}) = \frac{T^{1/2}}{ik_0 - \xi_b(\boldsymbol{k}) - T^{1/2}\widetilde{\Sigma}^T(k_0, \boldsymbol{k})}$$

and the single-scale propagator

$$\widetilde{S}^T(k_0, \boldsymbol{k}) = -\frac{1}{2}\frac{T^{-1/2}\left[ik_0 + \xi_b(\boldsymbol{k})\right]}{\left[ik_0 - \xi_b(\boldsymbol{k}) - T^{1/2}\widetilde{\Sigma}^T(k_0, \boldsymbol{k})\right]^2}. \tag{2.33}$$

Using these propagators, the particle-hole contributions contained in the trace (2.23) are given by

$$\text{tr}\left(\boldsymbol{S}^\Lambda \boldsymbol{U}^\Lambda \boldsymbol{G}^\Lambda \boldsymbol{U}^\Lambda\right) \sim \text{tr}\left(\partial_T \chi^{p-h} \cdot \ldots\right) \tag{2.34}$$

and now involve the temperature derivative $\partial_T \chi^{p-h}$ instead of a cutoff function. The broader support of $\partial_T \chi^{p-h}$ then does not distinguish between large and small momentum transfer and, therefore, the temperature flow allows a uniform treatment of all particle-hole fluctuations. In addition to that, Ward identities derived in Sec. 2.4 are also respected in the temperature flow [9], at least in the full hierarchy of differential equations. For these reasons, the temperature flow is more favorable than the cutoff-schemes although the intuitive picture of eliminating short-wavelength fluctuations and obtaining the properties on a coarse-grained scale is lost here. Another cutoff-free scheme is provided by the so-called interaction flow [10] which simply multiplies the quadratic part of the action with a parameter $1/g$. By rescaling the fields, one can show that this corresponds to a substitution of the interacting part $U \rightarrow g^2 U$. The interaction flow therefore interpolates between the noninteracting theory at $g = 0$ and the original one at $g = 1$.

As we have seen in this section, the functional flow equations enable a certain flexibility in the choice of flow parameters, which can be exploited to prove the robustness of the results or to justify certain approximations. The most common implementations involve cutoff-schemes in frequency [11, 12] and momentum-space [13], the addressed temperature scheme [8] and also the interaction flow [10].

2.3   Symmetry Properties of the Functional Flow Equations

A given physical system usually features certain symmetries as for example translational or rotational invariance. According to Noether's theorem, each of these continuous symmetries also entails some kind of conservation law. In the following section, we will hence demonstrate how this symmetry result simplifies the flow equation hierarchy and also provides useful relations between the different n-point vertex functions.

For this purpose, we first introduce a general symmetry transformation as an invertible mapping of fields

$$\psi_k \mapsto \int_{k'} \mathcal{M}_{k,k'} \psi_{k'}, \quad \overline{\psi}_k \mapsto \int_{k'} \overline{\mathcal{M}}_{k,k'} \overline{\psi}_{k'} \tag{2.35}$$

which leaves the action $S(\overline{\psi}, \psi)$ as well as the functional-integral measure $D(\overline{\psi}, \psi)$ invariant:

$$S(\overline{\mathcal{M}} \cdot \overline{\psi}, \mathcal{M} \cdot \psi) = S(\overline{\psi}, \psi) \tag{2.36}$$
$$D(\overline{\mathcal{M}} \cdot \overline{\psi}, \mathcal{M} \cdot \psi) = D(\overline{\psi}, \psi).$$

At this, we used the shortened notation of $\mathcal{M} \cdot \overline{\psi}$ and $\mathcal{M} \cdot \psi$ to denote the mappings of (2.35). Note also that the very general representation of a symmetry transformation in (2.35) comprises space-time as well as internal symmetries and will be specified by various examples during the later discussion. In order to derive the transformation behavior of the 1PI vertex functions and therefore to simplify the flow equations, we first determine the transformation properties of the generating functional $\mathcal{G}[\eta, \overline{\eta}]$ for the connected Green functions. Using the symmetry requirements (2.36), we obtain

$$\mathcal{G}[\eta, \overline{\eta}] = -\ln \int D(\overline{\psi}, \psi) e^{-S(\overline{\psi}, \psi) + (\overline{\eta}, \psi) + (\overline{\psi}, \eta)} \tag{2.37}$$

$$= -\ln \int D(\overline{\mathcal{M}} \cdot \overline{\psi}, \mathcal{M} \cdot \psi) e^{-S(\overline{\mathcal{M}} \cdot \overline{\psi}, \mathcal{M} \cdot \psi) + (\overline{\eta}, \mathcal{M} \cdot \psi) + (\overline{\mathcal{M}} \cdot \overline{\psi}, \eta)}$$

$$= -\ln \int D(\overline{\psi}, \psi) e^{-S(\overline{\psi}, \psi) + (\overline{\eta}, \psi) + (\overline{\mathcal{M}} \cdot \overline{\psi}, \eta)}$$

$$= -\ln \int D(\overline{\psi}, \psi) e^{-S(\overline{\psi}, \psi) + (\mathcal{M}^T \cdot \overline{\eta}, \psi) + (\overline{\psi}, \overline{\mathcal{M}}^T \cdot \eta)}$$

$$= \mathcal{G}[\overline{\mathcal{M}}^T \cdot \eta, \mathcal{M}^T \cdot \overline{\eta}],$$

and the transformation behavior of the source fields $\zeta, \overline{\zeta}$ in the effective action $\Gamma[\zeta, \overline{\zeta}]$ of (2.12) then reads as

$$\zeta(\overline{\mathcal{M}}^T \cdot \eta, \mathcal{M}^T \cdot \overline{\eta}) = -\frac{\partial \mathcal{G}[\overline{\mathcal{M}}^T \cdot \eta, \mathcal{M}^T \cdot \overline{\eta}]}{\partial(\mathcal{M}^T \cdot \overline{\eta})} = -\frac{\partial \mathcal{G}[\eta, \overline{\eta}]}{\partial(\mathcal{M}^T \cdot \overline{\eta})} = (\mathcal{M})^{-1} \cdot \zeta(\eta, \overline{\eta})$$

$$\overline{\zeta}(\mathcal{M}^T \cdot \eta, \mathcal{M}^T \cdot \overline{\eta}) = \frac{\partial \mathcal{G}[\overline{\mathcal{M}}^T \cdot \eta, \mathcal{M}^T \cdot \overline{\eta}]}{\partial \left(\overline{\mathcal{M}}^T \cdot \eta\right)} = \frac{\partial \mathcal{G}[\eta, \overline{\eta}]}{\partial \left(\overline{\mathcal{M}}^T \cdot \eta\right)} = (\overline{\mathcal{M}})^{-1} \cdot \overline{\zeta}(\eta, \overline{\eta}).$$

Applying this result, we can easily infer the effect of (2.35) on the effective action Γ:

$$\begin{aligned}
\Gamma[\zeta, \overline{\zeta}] &\mapsto \Gamma[(\mathcal{M})^{-1}\zeta, (\overline{\mathcal{M}})^{-1}\overline{\zeta}] \qquad\qquad\qquad\qquad (2.38)\\
&= \mathcal{G}[\overline{\mathcal{M}}^T \eta, \mathcal{M}^T \overline{\eta}] + (\mathcal{M}^T \overline{\eta}, (\mathcal{M})^{-1}\zeta) + ((\overline{\mathcal{M}})^{-1}\overline{\zeta}, \overline{\mathcal{M}}^T \eta)\\
&= \Gamma[\zeta, \overline{\zeta}],
\end{aligned}$$

where we made use of the following relation

$$\begin{aligned}
(\mathcal{M}^T \cdot \overline{\eta}, (\mathcal{M})^{-1} \cdot \zeta) &= \int_k \left(\mathcal{M}^T \cdot \overline{\eta}\right)_k \left((\mathcal{M})^{-1} \cdot \zeta\right)_k\\
&= \int_{k,l,m} \left(\mathcal{M}^T\right)_{kl} (\mathcal{M})^{-1}_{km} \overline{\eta}_l \xi_m\\
&= \int_{k,l,m} (\mathcal{M})_{lk} (\mathcal{M})^{-1}_{km} \overline{\eta}_l \xi_m = (\overline{\eta}, \zeta).
\end{aligned}$$

From (2.38) it is then apparent that the effective action Γ remains invariant under all symmetry transformations of the underlying physical system:

$$\Gamma[\mathcal{M} \cdot \zeta, \overline{\mathcal{M}} \cdot \overline{\zeta}] = \Gamma[\zeta, \overline{\zeta}]. \qquad\qquad (2.39)$$

Expanding both sides in powers of the fields, we obtain the following relation for the 1PI vertex functions

$$\gamma^{(2m)}_{k'_1,\ldots,k'_m;k_1,\ldots,k_m} = \int_{\substack{q'_1,\ldots,q'_m\\q_1,\ldots,q_m}} \mathcal{M}_{k'_1 q'_1} \cdots \mathcal{M}_{k'_m q'_m} \mathcal{M}_{k_1 q_1} \cdots \mathcal{M}_{k_m q_m} \cdot \gamma^{(2m)}_{q'_1,\ldots,q'_m;q_1,\ldots,q_m}.$$

$$(2.40)$$

Since we are mainly interested in solid-state compounds with an underlying periodic crystal lattice, we now assume translational symmetry under $x \mapsto x + a$, which then translates into

$$\psi_k \mapsto e^{i\boldsymbol{k}\cdot a}\psi_k, \quad \overline{\psi}_k \mapsto e^{-i\boldsymbol{k}\cdot a}\overline{\psi}_k. \qquad\qquad (2.41)$$

Employing the symmetry relation (2.40), we then end up with

$$\gamma^{(2m)}_{k'_1,\ldots,k'_m;k_1,\ldots,k_m} = e^{i(\boldsymbol{k}_1+\ldots+\boldsymbol{k}_m-\boldsymbol{k}'_1-\boldsymbol{k}'_m)\cdot a} \cdot \gamma^{(2m)}_{k'_1,\ldots,k'_m;k_1,\ldots,k_m}, \qquad (2.42)$$

which in turn implies that all non-vanishing 1PI vertex functions conserve momentum up to a reciprocal lattice vector.

Besides translational symmetry, a periodic crystal lattice also exhibits point group symmetries which, by definition, leave one space point fixed and therefore constitute a subgroup of the orthogonal group $O(n)$ with n

denoting the dimensionality of the lattice. If we now consider a point-group transformation $x \mapsto Rx$ with $R \in O(n)$, its effect in $\boldsymbol{k}$-space is given by $k \mapsto R^T k = (k_0, R^T \boldsymbol{k}, \sigma)$, following from the duality definition of the reciprocal lattice. Accordingly, the fields transform as

$$\psi_k \mapsto \psi_{R^T k}, \quad \overline{\psi}_k \mapsto \overline{\psi}_{R^T k}, \tag{2.43}$$

and, due to (2.40), the 1PI vertex functions remain invariant under all point-group symmetries:

$$\gamma^{(2m)}_{k'_1,\ldots,k'_m;k_1,\ldots,k_m} = \gamma^{(2m)}_{R^T k'_1,\ldots,R^T k'_m;R^T k_1,\ldots,R^T k_m}. \tag{2.44}$$

Another important symmetry describes the invariance under time-reversal $t \to -t$. This operation is known to be peculiar as it must have an antiunitary representation in the space of quantum states. Otherwise, as each symmetry has to be represented either as an unitary or an antiunitary operator according Wigner's fundamental theorem, time-reversal would be a unitary operation which runs into fundamental problems. Time-reversal can therefore be shown to act on a spin one-half state as

$$\Theta = -i\tau^2 K, \tag{2.45}$$

where K denotes complex-conjugation and τ^2 labels the Pauli-matrix σ^y. Under the action of time-reversal (2.45), the fields then transform as

$$\psi_{k\sigma} \mapsto \text{sign}(\sigma)\overline{\psi}_{Tk}, \quad \overline{\psi}_{k\sigma} \mapsto \text{sign}(\sigma)\psi_{Tk}, \tag{2.46}$$

with $Tk = (k_0, -\boldsymbol{k}, -\sigma)$ and $\text{sign}(\uparrow\downarrow) = \pm 1$ according to the matrix $-i\tau^2$. The corresponding effect on the 1PI vertex function now reads as

$$\gamma^{(2m)}_{k'_1,\ldots,k'_m;k_1,\ldots,k_m} = \text{sign}(\sigma'_1)\cdots\text{sign}(\sigma_m)\gamma^{(2m)}_{Rk_m,\ldots,Rk_1;Rk'_m,\ldots,Rk'_1}, \tag{2.47}$$

and the effect of other discrete symmetries like spatial reflection can be derived in a similar fashion.

In addition to these discrete transformations, the underlying system also features certain continuous symmetries as for example the spin-rotational invariance or a global $U(1)$ phase freedom. The corresponding representations of these continuous symmetries can be parametrized, at least locally, by some real parameters $s_1,\ldots,s_n$ such that

$$\mathcal{M}(s_1 = 0,\ldots,s_n = 0) = 1, \tag{2.48}$$

and the associated generators can be defined as

$$T_j = -i \left.\frac{\partial\mathcal{M}(s_1,\ldots,s_n)}{\partial s_j}\right|_{s_1=\ldots=s_n=0}, \quad \overline{T}_j = -i \left.\frac{\partial\overline{\mathcal{M}}(s_1,\ldots,s_n)}{\partial s_j}\right|_{s_1=\ldots=s_n=0}. \tag{2.49}$$

Now, by using the invariance of the effective action in (2.39), we obtain the following relation

$$
0 = \frac{\partial}{\partial s_j} \Gamma[\zeta, \overline{\zeta}] = \left(\frac{\partial \Gamma[\mathcal{M} \cdot \zeta, \overline{\mathcal{M}} \cdot \overline{\zeta}]}{\partial(\mathcal{M} \cdot \zeta)}, \frac{\partial(\mathcal{M} \cdot \zeta)}{\partial s_j} \right)
$$
$$
+ \left(\frac{\partial \Gamma[\mathcal{M} \cdot \zeta, \overline{\mathcal{M}} \cdot \overline{\zeta}]}{\partial(\overline{\mathcal{M}} \cdot \overline{\zeta})}, \frac{\partial(\overline{\mathcal{M}} \cdot \overline{\zeta})}{\partial s_j} \right)
$$
$$
= \left(\frac{\partial \Gamma[\zeta, \overline{\zeta}]}{\partial \zeta}, (iT_j) \cdot \zeta \right) + \left(\frac{\partial \Gamma[\zeta, \overline{\zeta}]}{\partial \overline{\zeta}}, (i\overline{T}_j) \cdot \overline{\zeta} \right). \qquad (2.50)
$$

In the next step, we demonstrate how this symmetry constraint restricts the form of the 1PI vertex functions.

As an example, we therefore consider the case of a global $U(1)$ phase transformation,

$$
\psi_k \mapsto e^{is}\psi_k, \quad \overline{\psi}_k \mapsto e^{-is}\overline{\psi}_k, \qquad (2.51)
$$

which apparently presents a symmetry of the underlying action (2.1). Computing the generators of this symmetry group according to (2.49), one finds that

$$
T = -i \left. \frac{\partial e^{is}}{\partial s} \right|_{s=0} = 1, \quad \overline{T} = -i \left. \frac{\partial e^{-is}}{\partial s} \right|_{s=0} = -1 \qquad (2.52)
$$

and, using (2.50), we end up with

$$
\int_k \left(\zeta_k \frac{\partial}{\partial \zeta_k} - \overline{\zeta}_k \frac{\partial}{\partial \overline{\zeta}_k} \right) \Gamma[\zeta, \overline{\zeta}] = 0. \qquad (2.53)
$$

If we now expand the generating functionals in fields, the only nonzero 1PI vertex functions in (2.53) are those which corresponds to monomials with an equal number of ζ- and $\overline{\zeta}$-fields. Note that we already assumed such a form in the expansion (2.20), which is now justified in hindsight with the global $U(1)$ phase symmetry of the bare action.

As another example, we consider the invariance under spin rotation which, in the spin one-half representation, reads as

$$
\begin{pmatrix} \psi_{\widetilde{k},\uparrow} \\ \psi_{\widetilde{k},\downarrow} \end{pmatrix} \mapsto e^{i\boldsymbol{\tau} \cdot \boldsymbol{s}} \begin{pmatrix} \psi_{\widetilde{k},\uparrow} \\ \psi_{\widetilde{k},\downarrow} \end{pmatrix}, \quad \begin{pmatrix} \overline{\psi}_{\widetilde{k},\uparrow} \\ \overline{\psi}_{\widetilde{k},\downarrow} \end{pmatrix} \mapsto e^{-i\boldsymbol{\tau}^* \cdot \boldsymbol{s}} \begin{pmatrix} \overline{\psi}_{\widetilde{k},\uparrow} \\ \overline{\psi}_{\widetilde{k},\downarrow} \end{pmatrix} \qquad (2.54)
$$

with $\tau^{1,2,3}$ denoting the usual Pauli-matrices. Together with the associated generators

$$
T_i = \tau^i, \quad \overline{T}_i = -\left(\tau^i \right)^* \quad i = 1, 2, 3, \qquad (2.55)
$$

the symmetry restriction (2.50) reads as

$$
\int_{\widetilde{k},\sigma,\sigma'} \left(\tau^i_{\sigma\sigma'} \zeta_{\widetilde{k}\sigma} \frac{\partial}{\partial \zeta_{\widetilde{k}\sigma'}} - \left(\tau^i \right)^*_{\sigma\sigma'} \overline{\zeta}_{\widetilde{k}\sigma} \frac{\partial}{\partial \overline{\zeta}_{\widetilde{k}\sigma'}} \right) \Gamma[\zeta, \overline{\zeta}] = 0. \qquad (2.56)
$$

Here, we explicitly wrote out the spin projection σ and defined the new index $\widetilde{k}$ as containing all remaining degrees of freedom besides σ. Using the $i = 3$ component of (2.56) as well as the $U(1)$ symmetry constraint of (2.53), we then obtain

$$\int_{\widetilde{k}} \left(\zeta_{\widetilde{k}\sigma} \frac{\partial}{\partial \zeta_{\widetilde{k}\sigma}} - \overline{\zeta}_{\widetilde{k}\sigma} \frac{\partial}{\partial \overline{\zeta}_{\widetilde{k}\sigma}} \right) \Gamma[\zeta, \overline{\zeta}] = 0, \qquad (2.57)$$

which restricts an expansion of $\Gamma[\zeta, \overline{\zeta}]$ to consist of monomials with an equal number of $\zeta_{\widetilde{k}\sigma}$- and $\overline{\zeta}_{\widetilde{k}\sigma}$-fields. Therefore, the number of particles with a given spin projection is individually conserved, and we can write the fully spin-dependent 1PI vertex functions as

$$
\begin{aligned}
\gamma^{(2m)\Lambda}_{k_1',\ldots,k_m';k_1,\ldots,k_m} &= \gamma^{(2m)\Lambda}_{\widetilde{k}_1'\sigma_1',\ldots,\widetilde{k}_m'\sigma_m';\widetilde{k}_1\sigma_1,\ldots,\widetilde{k}_m\sigma_m} \\
&= -\sum_{p \in \pi_m} \mathrm{sgn}(p) \cdot \widetilde{V}^{(2m)\Lambda}_{\sigma_1',\ldots,\sigma_m'}(\widetilde{k}_1',\ldots,\widetilde{k}_m';\widetilde{k}_{p(1)},\ldots,\widetilde{k}_{p(m)}) \\
&\quad \times \delta_{\sigma_1'\sigma_{p(1)}} \cdots \delta_{\sigma_m'\sigma_{p(m)}}.
\end{aligned} \qquad (2.58)
$$

Here, the spin-conserving function $\widetilde{V}^{(2m)\Lambda}_{\sigma_1',\ldots,\sigma_m'}$ depends only on the spin projection of the outgoing particles, and it is important to note that the definition of $\widetilde{V}^{(2m)\Lambda}$ is not unique and sometimes occurs with a different sign in the literature. Up to now, we only implemented the $i = 3$ constraint of (2.56) which is equivalent to spin-rotational invariance around the z-axes. Making use of the full $SU(2)$-invariance, one can even show that $\widetilde{V}^{(2m)}$ is independent of $\sigma_1',\ldots,\sigma_m'$ [5], and we define the coupling functions

$$V^{(2m)}_{\widetilde{k}_1',\ldots,\widetilde{k}_m';\widetilde{k}_1,\ldots,\widetilde{k}_m} = \widetilde{V}^{(2m)}_{\sigma_1',\ldots,\sigma_m'}(\widetilde{k}_1',\ldots,\widetilde{k}_m';\widetilde{k}_1,\ldots,\widetilde{k}_m) \qquad (2.59)$$

with $V^{(2m)}$ being independent of any spin projection. The first two vertex functions in (2.58) therefore read as

$$\gamma^{(2)}_{\widetilde{k}_1'\sigma_1';\widetilde{k}_1\sigma_1} = Q_{\widetilde{k}_1',\widetilde{k}_1} - \Sigma_{\widetilde{k}_1',\widetilde{k}_1} = V^{(2)}_{\widetilde{k}_1';\widetilde{k}_1} \qquad (2.60)$$

$$\gamma^{(4)}_{\widetilde{k}_1'\sigma_1',\widetilde{k}_2'\sigma_2';\widetilde{k}_1\sigma_1,\widetilde{k}_2\sigma_2} = -D \cdot V^{(4)}_{\widetilde{k}_1',\widetilde{k}_2';\widetilde{k}_1,\widetilde{k}_2} + E \cdot V^{(4)}_{\widetilde{k}_1',\widetilde{k}_2';\widetilde{k}_2,\widetilde{k}_1}, \qquad (2.61)$$

where we made use of (2.17) in Eq. (2.60) and applied the following notations of $D = \delta_{\sigma_1'\sigma_1}\delta_{\sigma_2'\sigma_2}$, $E = \delta_{\sigma_1'\sigma_2}\delta_{\sigma_2'\sigma_1}$ in (2.61). In order to simplify the flow equations for the 1PI vertex functions, we can now insert (2.60) and (2.61) into (2.24) and (2.25), and, by comparing the coefficient of D, we then obtain the following spin-independent flow equations for the first two terms

$$\frac{d}{d\Lambda} \Sigma^{(2)\Lambda}_{\widetilde{k}_1';\widetilde{k}_1} = \sum_{\widetilde{q},\widetilde{q}'} S^{\Lambda}_{\widetilde{q},\widetilde{q}'} \left\{ V^{(4)\Lambda}_{\widetilde{k}_1',\widetilde{q}';\widetilde{q},\widetilde{k}_1} - 2V^{(4)\Lambda}_{\widetilde{k}_1',\widetilde{q}';\widetilde{k}_1,\widetilde{q}} \right\} \qquad (2.62)$$

$$\frac{d}{d\Lambda} V^{(4)\Lambda}_{\widetilde{k}'_1,\widetilde{k}'_2;\widetilde{k}_1,\widetilde{k}_2} = \sum_{\substack{\widetilde{k},\widetilde{k}' \\ \widetilde{q},\widetilde{q}'}} G^{\Lambda}_{\widetilde{k},\widetilde{k}'} S^{\Lambda}_{\widetilde{q},\widetilde{q}'} \left\{ V^{(4)\Lambda}_{\widetilde{k}'_1,\widetilde{k}'_2;\widetilde{k},\widetilde{q}} V^{(4)\Lambda}_{\widetilde{k}',\widetilde{q}';\widetilde{k}_1,\widetilde{k}_2} \right. \tag{2.63}$$

$$V^{(4)\Lambda}_{\widetilde{k}'_2,\widetilde{q}';\widetilde{k},\widetilde{k}_1} V^{(4)\Lambda}_{\widetilde{k}',\widetilde{k}'_1;\widetilde{k}_2,\widetilde{q}} - 2 V^{(4)\Lambda}_{\widetilde{k}'_1,\widetilde{q}';\widetilde{k}_1,\widetilde{k}} V^{(4)\Lambda}_{\widetilde{k}',\widetilde{k}'_2;\widetilde{q},\widetilde{k}_2} + V^{(4)\Lambda}_{\widetilde{k}'_1,\widetilde{q}';\widetilde{k}_1,\widetilde{k}} V^{(4)\Lambda}_{\widetilde{k}',\widetilde{k}'_2;\widetilde{k}_2,\widetilde{q}}$$

$$\left. + V^{(4)\Lambda}_{\widetilde{k}'_1,\widetilde{q}';\widetilde{k},\widetilde{k}_1} V^{(4)\Lambda}_{\widetilde{k}',\widetilde{k}'_2;\widetilde{q},\widetilde{k}_2} + (\widetilde{k} \leftrightarrow \widetilde{q}, \widetilde{k}' \leftrightarrow \widetilde{q}') \right\}.$$

A diagrammatic expression of the flow equations in (2.62) and (2.63) is further pictured in Fig. 2.4. Due to the spin independence, the complexity of the flow equations reduces by a factor of $2n$ for each of the n-point vertex functions. If the underlying system further shows translational symmetry or an invariance under certain point-group transformations, we can apply (2.42) and (2.44), which further lowers the computational effort. Note that the latter symmetry relations of (2.42) and (2.44) were derived for the full vertex functions $\gamma^{(2m)}$ but do also hold for the spin-independent coupling functions $V^{(2m)}$ defined in (2.58). The influence of the neglected term $V^{(6)}$ in the flow equation for $V^{(4)}$ will be discussed in Sec. 2.5 of this chapter.
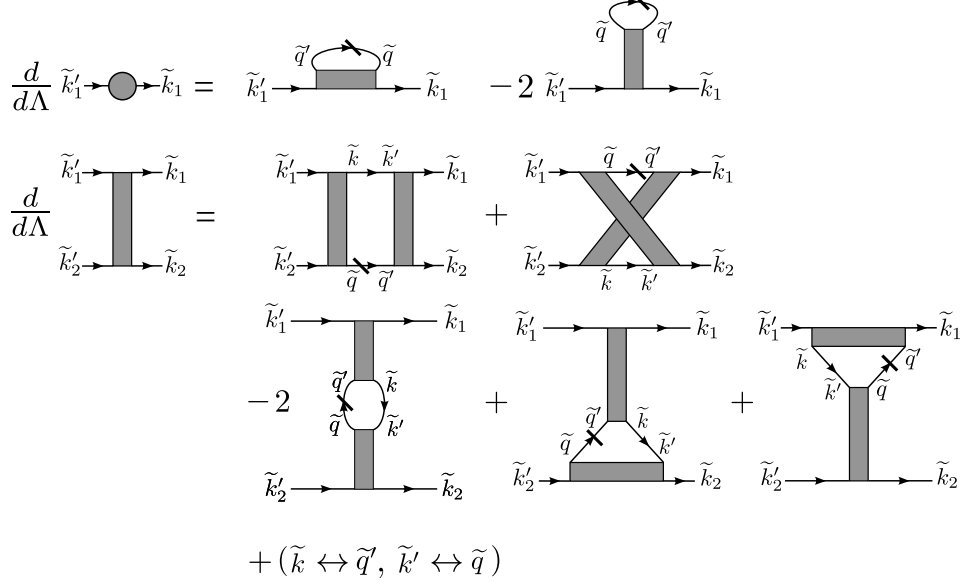

Figure 2.4: First two terms in the infinite hierarchy of flow equations for the coupling functions $V^{(2m)}$. Slashed and full internal lines represent the single-scale S^{Λ} and full propagators G^{Λ}.

2.4   Ward Identities

In the last section, we discussed the effect of symmetry on vertex functions and utilized these insights to reduce the complexity of the corresponding flow equations. Instead of looking at the implications of symmetry on a given vertex function γ^{2m}, we now want to derive exact relations between the different m-point vertex functions, also known as Ward identities. For this purpose, we consider a typical action such as

$$S(\overline{\psi}, \psi) = -(\overline{\psi}, Q\psi) + V_{int}(\overline{\psi}, \psi), \tag{2.64}$$

to which we apply an infinitesimal field transformation

$$\psi' = \psi - T \cdot \psi, \quad \overline{\psi}' = \overline{\psi} - \overline{\psi} \cdot \overline{T} \tag{2.65}$$

characterized by some generators $T, \overline{T}$. The only restriction we require here is that (2.65) does neither change V_{int} nor the functional integration measure $D(\overline{\psi}, \psi)$. Besides these two conditions, the field transformation in (2.65) can be chosen arbitrarily, and the following arguments do not depend on its precise form. Note that, for the sake of clarity, we used the same shortened matrix-vector like notation as in Sec. 2.1. If we then perform (2.65), the action changes only in the quadratic part and hence gives rise to

$$S(\overline{\psi}', \psi') = S(\overline{\psi}, \psi) + \left(\overline{\psi}, \Delta Q \psi\right), \tag{2.66}$$

with an additional quadratic term ΔQ defined by

$$\Delta Q = QT + \overline{T}Q. \tag{2.67}$$

Due to the invariance of the functional integration measure, we further obtain

$$\int D(\overline{\psi}, \psi)e^{-S(\overline{\psi},\psi)+(\overline{\eta},\psi)+(\overline{\psi},\eta)} = \int D(\overline{\psi}', \psi')e^{-S(\overline{\psi}',\psi')+(\overline{\eta},\psi')+(\overline{\psi}',\eta)}$$

$$= \int D(\overline{\psi}, \psi)e^{-S(\overline{\psi},\psi)+(\overline{\eta},\psi)+(\overline{\psi},\eta)} \left[1 - \left(\overline{\psi}, \Delta Q \psi\right) + (\overline{\eta}, T \cdot \psi) + \left(\overline{\psi}, \overline{T} \cdot \eta\right)\right], \tag{2.68}$$

where we relabeled the fields $(\overline{\psi}, \psi) \rightarrow (\overline{\psi}', \psi')$ and applied (2.66). Subtracting the left hand side of (2.68) and employing the definition of the generating functional $W[\eta, \overline{\eta}]$ in (2.5), we derive the following identity

$$0 = \int D(\overline{\psi}, \psi)e^{-S(\overline{\psi},\psi)+(\overline{\eta},\psi)+(\overline{\psi},\eta)} \left[\left(\overline{\psi}, \Delta Q \psi\right) + (\overline{\eta}, T \cdot \psi) - \left(\overline{T} \cdot \eta, \overline{\psi}\right)\right]$$

$$= \left\{(\partial_\eta, \Delta Q \partial_{\overline{\eta}}) + (\overline{\eta}, T \cdot \partial_{\overline{\eta}}) + \left(\overline{T} \cdot \eta, \partial_\eta\right)\right\} W[\eta, \overline{\eta}]. \tag{2.69}$$

Now, starting from this result, we can generate exact relations between the m-point and $(m+2)$-point Green functions, just by taking the appropriate

functional derivatives $\partial/\partial\overline{\eta}, \partial/\partial\eta$ and by setting $\eta = \overline{\eta} = 0$ afterwards. However, as we are mainly dealing with flow equations for the 1PI vertex functions, we now want derive Ward identities between the different m-point 1PI vertex functions. We therefore insert $W = e^{-\mathcal{G}}$ into (2.69), which equals the definition of the generating functional for the connected Green functions $\mathcal{G}$ in (2.7), and multiply with $e^{\mathcal{G}}$ from the right:

$$0 = e^{\mathcal{G}[\eta,\overline{\eta}]} \left(\partial_\eta, \Delta Q \partial_{\overline{\eta}}\right) e^{-\mathcal{G}[\eta,\overline{\eta}]} - \left(\overline{\eta}, T\cdot\partial_{\overline{\eta}}\right)\mathcal{G}[\eta,\overline{\eta}] - \left(\overline{T}\cdot\eta, \partial_\eta\right)\mathcal{G}[\eta,\overline{\eta}].$$
(2.70)

What is striking here is that the first term in (2.70) has exactly the same form as the flow equation (2.10), only with $\dot{Q}^\Lambda$ replaced by ΔQ. Due to this similarity, we can simply apply the calculation steps leading from the flow equation for $\mathcal{G}^\Lambda$ in (2.10) to the one for the effective action Γ^Λ in (2.18). The resulting expression then reads as

$$0 = \left(\overline{\zeta}, \Delta Q \zeta\right) + \operatorname{tr}\left(\Delta Q \left(\left(\boldsymbol{\partial}^2\Gamma[\zeta,\overline{\zeta}]\right)^{-1}\right)_{11}\right)$$
(2.71)
$$- \left(T\cdot\zeta, \partial_\zeta\right)\Gamma[\zeta,\overline{\zeta}] - \left(\overline{\zeta}, \overline{T}\cdot\partial_{\overline{\zeta}}\right)\Gamma[\zeta,\overline{\zeta}]$$

and hence generates all Ward identities for the 1PI vertex functions.

Now, after this general discussion, we want to apply (2.71) and derive the Ward identities associated with a $U(1)$ phase transformation in the one-band Hubbard model

$$S(\overline{\psi},\psi) = -\int_k \overline{\psi}_k Q_{k,k}\psi_k + U\int_{k_1,k_2,k_1',k_2'} \overline{\psi}_{k_1}\overline{\psi}_{k_2}\psi_{k_1'}\psi_{k_2'}.$$
(2.72)

Here, the quadratic part is given by $Q_{k,k} = ik_0 - \xi(\boldsymbol{k})$ with a dispersion relation $\xi(\boldsymbol{k})$ and the condensed notation of $k = (k_0, \boldsymbol{k})$ introduced in (2.1). We now consider the space-time dependent field transformations $\psi_r' = e^{i\alpha(r)}\psi_r'$, $\overline{\psi}_r' = e^{-i\alpha(r)}\overline{\psi}_r$ which, in its infinitesimal form, read as

$$\psi_r' = \psi_r + i\alpha(r)\psi_r, \quad \overline{\psi}_r' = \overline{\psi}_r - i\alpha(r)\overline{\psi}_r.$$
(2.73)

Note that we switched here from frequency- and momentum-dependent fields to its space-time representation with $r = (\tau, \boldsymbol{r})$ including imaginary-time τ and spatial coordinates $\boldsymbol{r}$. The transformation in (2.73) then describes a local $U(1)$ phase transformation and, by switching back to frequency and momentum space, the same transformation is given by the convolution

$$\psi_k' = \psi_k + i\int_q \alpha(-q)\psi_{k+q}, \quad \overline{\psi}_k' = \overline{\psi}_k - i\int_q \alpha(-q)\overline{\psi}_{k-q}.$$
(2.74)

The corresponding generators therefore read as

$$T_{kk'} = i\int_q \alpha(-q)\delta_{k',k+q}, \quad \overline{T}_{kk'} = -i\int_q \alpha(-q)\delta_{k,k'-q}.$$
(2.75)

$$\sum_i \left(\begin{array}{c} \text{[diagram]} \\ k'_1 \quad k_1 \\ \vdots \quad k_i - q \\ k'_n \quad k_n \end{array} \quad - \quad \begin{array}{c} k'_1 \quad k_1 \\ k'_i + q \\ k'_n \quad k_n \end{array} \right)$$

$$= \left(\begin{array}{l} \text{same diagrams as in } \frac{d}{d\Lambda} \gamma^{(2n)}_{k'_1,\ldots,k'_n;k_1,\ldots,k_n} \\ \text{replace } S^\Lambda_{k,k'} \text{ by } S_{k,k'} = G_{k,k}[Q_{k,k} - Q_{k+q,k+q}]G_{k+q,k+q} \cdot \delta_{k',k+q} \end{array} \right)$$

Figure 2.5: $U(1)$-Ward identities for the 1PI vertex functions. The right-hand side equals the flow equation for $\gamma^{(2n)}$ with a replaced single-scale propagator S^Λ, and the left hand side shows the sum of differences of $\gamma^{(2n)}$ functions with q subtracted (added) in the i-th outgoing (ingoing) leg.

Using (2.71) and taking the functional derivative with respect to $\alpha(-q)$, we obtain the following identity

$$\int_k \frac{\partial \Gamma}{\partial \zeta_k} \zeta_{k+q} - \frac{\partial \Gamma}{\partial \overline{\zeta}_{k+q}} \overline{\zeta}_k = \int_k [Q_{k,k} - Q_{k+q,k+q}] \left[\left((\partial^2 \Gamma)^{-1}_{k+q,k} \right)_{11} + \overline{\zeta}_k \zeta_{k+q} \right]. \tag{2.76}$$

Starting from this latter expression, we can now generate all orders of Ward identities just by expanding in powers $\overline{\zeta}, \zeta$ and by comparing coefficients. In the n-th order Ward identity, i.e. in the identity for the coefficients of order $\mathcal{O}((\overline{\zeta}\zeta)^n)$, the right-hand side of (2.76) generates all diagrams of the flow equation in Fig. 2.2 but with a modified single-scale propagator

$$S_{kk'} = G_{k,k} \cdot [Q_{k,k} - Q_{k+q,k+q}] \cdot G_{k+q,k+q} \cdot \delta_{k',k+q}. \tag{2.77}$$

Here, G denotes the full propagator and Q is the quadratic part of the action (2.72). The left-hand side of the n-th order Ward identity then simply consists of a sum over n differences where $\gamma^{(2n)}$ with q added to the i-th ingoing leg is subtracted from $\gamma^{(2n)}$ with $-q$ added to the i-th outgoing leg. The pictorial representation of all expansion orders of (2.76) is shown in Fig. 2.5. For the first order Ward identity, we therefore obtain the following exact relation between the 2-point 1PI vertex function or self-energy Σ and the 4-point 1PI vertex function $\gamma^{(4)}$:

$$\Sigma_{w,w} - \Sigma_{w+q,w+q} = \int_k [Q_{k,k} - Q_{k+q,k+q}] \gamma^{(4)}_{w,k+q;w+q,k} G_{k+q,k+q} G_{k,k}. \tag{2.78}$$

Note that this statement is based on the very general assumption that both the functional integration measure and the non-quadratic part of the action remain invariant under the infinitesimal field-transformation (2.65). Within the functional RG approach, we equipped the quadratic part of the action with some parameter dependence $Q_{k,k} \to Q^\Lambda_{k,k}$ in order to extrapolate from

a solvable model at large values of Λ to the original full model at $\Lambda \to 0$. As this introduced Λ-dependence only changes the quadratic part of the action, the requirements for (2.78) remain valid and equation (2.78) holds on all scales Λ. Yet, if one truncates the infinite hierarchy of flow equations, for example by setting $\gamma^{(2n)} = 0$ for all $n > 2$, the second order Ward identity is no longer fulfilled as this would also include finite contributions from $\gamma^{(6)}$. Even the first order Ward identity (2.78) is then violated by terms in the order of $\mathcal{O}((\gamma^{(4)})^3)$ as shown by Katanin [6]. Here, it was shown that the case of $q = (q_0, \mathbf{0}, \sigma)$ in (2.78) leads to

$$\partial_{w_0} \Sigma^{\Lambda}_{w,w} = -\int_k \gamma^{(4)\Lambda}_{w,k;k,w} \left(G^{\Lambda}_k\right)^2 = \int_{\widetilde{k}} \left\{ V^{(4)\Lambda}_{\widetilde{w},\widetilde{k};\widetilde{k},\widetilde{w}} - 2V^{(4)\Lambda}_{\widetilde{w},\widetilde{k};\widetilde{w},\widetilde{k}} \right\} \left(G^{\Lambda}_{\widetilde{k}}\right)^2, \quad (2.79)$$

where, assuming spin-rotational invariance, the spin sum was already performed with the notation of (2.61) and the Λ dependence was introduced. Now, if (2.79) is fulfilled, the Λ-derivative of the right-side should equal the w_0-derivative of the flow equation $\partial_{\Lambda} \Sigma^{\Lambda}_{w,w}$ due to $\partial_{\Lambda} \partial_{w_0} \Sigma^{\Lambda}_{w,w} = \partial_{w_0} \partial_{\Lambda} \Sigma^{\Lambda}_{w,w}$. This latter equation and therefore the Ward identity (2.79) does not hold if the hierarchy of flow-equations is truncated with $\gamma^{(2n)} = 0$ for all $n > 2$ as shown in [6]. Including certain terms from the neglected $\gamma^{(6)}$ contribution to $\gamma^{(4)}$, Katanin showed that this improves the fulfillment of (2.79) to correction terms in the order of $\mathcal{O}((\gamma^{(4)})^4)$. A simplified version of this scheme, known as Katanin truncation, which replaces the single-scale propagator S^{Λ} by the total derivative $dG^{\Lambda}/d\Lambda$, still leads to an essential improvement [14,15] and, for example, recovers dressed RPA.

2.5   Truncating the Hierarchy of Flow Equations

In order to justify the dropping of the six-point 1PI vertex function $\gamma^{(6)}$ in the truncation of (2.63), we follow the argumentation of Salmhofer *et al.* [16]. Assuming weak to moderate two-particle interactions and $\gamma^{(6)} = 0$ at bare level, one can easily show that for high energy scales, where $\gamma^{(4)}$ is still relatively small, the contributions of $\gamma^{(6)}$ are likewise small as they involve only higher order terms of $\gamma^{(4)}$. At intermediate scales, a phase-space argument for sufficiently smooth and curved Fermi-surfaces then proves that the contribution of $\gamma^{(6)}$ remains small even though the scale dependent $\gamma^{(4)}$ is no longer small. Only at low energy scales, where $\gamma^{(4)}$ starts to diverge, the decreasing phase-space cannot suppress the contribution of $\gamma^{(6)}$, and the flow has to be stopped. The remaining modes must then be treated with different approaches, for example, by using mean-field analysis or more sophisticated methods. For a more detailed discussion we refer to the following two articles [9,16].

2.6 Renormalized Mean-Field Analysis

At sufficiently low energy scales Λ, the four-point function $\gamma^{(4)\Lambda}$ starts to diverge and thus signals a possible onset of spontaneous symmetry breaking. According to the previous discussion, the flow has to be stopped before that critical energy scale Λ_c as the applied truncation of the flow-equation hierarchy is no longer justified. Although it is in principle possible to continue the flow into the symmetry broken phase and to account for order-parameter fluctuations, these techniques have only been worked out for simplified models and are currently too demanding for an investigation of complex multi-orbital systems with competing ordering channels.

In this thesis, we therefore resort to a mean-field treatment of an effective theory obtained at low-energy scales. Similar to the implementation presented by Reiss *et al.* [17], the flow is stopped at an energy scale $\Lambda_{MF} \gtrsim \Lambda_c$, and the renormalized interaction part is decoupled into its leading mean-field channels. For the moment, we assume that the most leading low-energy correlations appear exclusively within the pairing channel, i.e.

$$\gamma^{(4)\Lambda_{MF}}(k_1, k_2; k_3, k_4) \approx V^{pair}_{s_1,\ldots,s_4}(\boldsymbol{k}_1, \boldsymbol{k}_3)\delta_{\boldsymbol{k}_2,-\boldsymbol{k}_1}\delta_{\boldsymbol{k}_4,-\boldsymbol{k}_3}, \qquad (2.80)$$

with $V^{pair}_{s_1,\ldots,s_4}(\boldsymbol{k}_1, \boldsymbol{k}_3) = \gamma^{(4)\Lambda_{MF}}(\boldsymbol{k}_1 s_1, -\boldsymbol{k}_1 s_2; \boldsymbol{k}_3 s_3, -\boldsymbol{k}_3 s_4)$. Note that this latter assumption can of course be easily extended to additional correlation channels, which then merely increase the number of mean-fields during the calculation. The effective low-energy theory taken from the functional RG is then given by the following reduced Hamiltonian

$$H^\Lambda = \sum_{\boldsymbol{k}s} \xi(\boldsymbol{k})c^\dagger_{\boldsymbol{k}s}c_{\boldsymbol{k}s} + \frac{1}{2N}\sum_{s_1,\ldots,s_4}\sum_{\boldsymbol{k},\boldsymbol{q}} V^{pair}_{s_1,\ldots,s_4}(\boldsymbol{k},\boldsymbol{q})c^\dagger_{-\boldsymbol{k}s_1}c^\dagger_{\boldsymbol{k}s_2}c_{\boldsymbol{q}s_3}c_{-\boldsymbol{q}s_4}. \tag{2.81}$$

It is well-known that mean-field theory gives an exact solution of these reduced types of Hamiltonians in the thermodynamic limit [18]. We therefore replace the quartic interaction part by

$$\begin{aligned}
c^\dagger_{-\boldsymbol{k}s_1}c^\dagger_{\boldsymbol{k}s_2}c_{\boldsymbol{q}s_3}c_{-\boldsymbol{q}s_4} &= \langle c^\dagger_{-\boldsymbol{k}s_1}c^\dagger_{\boldsymbol{k}s_2}\rangle c_{\boldsymbol{q}s_3}c_{-\boldsymbol{q}s_4} + c^\dagger_{-\boldsymbol{k}s_1}c^\dagger_{\boldsymbol{k}s_2}\langle c_{\boldsymbol{q}s_3}c_{-\boldsymbol{q}s_4}\rangle \\
&\quad - \langle c^\dagger_{-\boldsymbol{k}s_1}c^\dagger_{\boldsymbol{k}s_2}\rangle\langle c_{\boldsymbol{q}s_3}c_{-\boldsymbol{q}s_4}\rangle \\
&\quad + \left(c^\dagger_{-\boldsymbol{k}s_1}c^\dagger_{\boldsymbol{k}s_2} - \langle c^\dagger_{-\boldsymbol{k}s_1}c^\dagger_{\boldsymbol{k}s_2}\rangle\right)\left(c_{\boldsymbol{q}s_3}c_{-\boldsymbol{q}s_4} - \langle c_{\boldsymbol{q}s_3}c_{-\boldsymbol{q}s_4}\rangle\right)
\end{aligned}$$

$$\tag{2.82}$$

and perform the usual mean-field approximation of neglecting order-parameter fluctuations in the last line of (2.82). Introducing the following two parameters

$$\Delta_{\boldsymbol{k},ss'} = -\frac{1}{N}\sum_{\boldsymbol{k}',\sigma\sigma'} V^{pair}_{s',s,\sigma,\sigma'}(\boldsymbol{k},\boldsymbol{k}')\langle c_{\boldsymbol{k}'\sigma}c_{-\boldsymbol{k}'\sigma'}\rangle$$

$$\Delta^*_{\boldsymbol{k},ss'} = -\frac{1}{N} \sum_{\boldsymbol{k}',\sigma\sigma'} V^{pair}_{\sigma',\sigma,s,s'}(\boldsymbol{k}',\boldsymbol{k}) \langle c^\dagger_{-\boldsymbol{k}'\sigma'} c^\dagger_{\boldsymbol{k}'\sigma} \rangle$$

$$= \frac{1}{N} \sum_{\boldsymbol{k}',\sigma\sigma'} V^{pair}_{\sigma',\sigma,s',s}(\boldsymbol{k}',-\boldsymbol{k}) \langle c^\dagger_{-\boldsymbol{k}'\sigma'} c^\dagger_{\boldsymbol{k}'\sigma} \rangle,$$

the Hamiltonian in (2.81) then reads as

$$H^\Lambda = \sum_{\boldsymbol{k}s} \xi(\boldsymbol{k}) c^\dagger_{\boldsymbol{k}s} c_{\boldsymbol{k}s} + \frac{1}{2} \sum_{\boldsymbol{k},s_1 s_2} \Delta_{\boldsymbol{k},s_1 s_2} c^\dagger_{\boldsymbol{k}s_1} c^\dagger_{-\boldsymbol{k}s_2} - \frac{1}{2} \sum_{\boldsymbol{q},s_3 s_4} \Delta^*_{-\boldsymbol{q},s_4 s_3} c_{-\boldsymbol{q}s_4} c_{\boldsymbol{q}s_3} + \mathcal{K}$$

$$= \frac{1}{2} \sum_{\boldsymbol{k}} C^\dagger_{\boldsymbol{k}} \begin{pmatrix} \xi(\boldsymbol{k})\sigma_0 & \hat{\Delta}_{\boldsymbol{k}} \\ \hat{\Delta}^\dagger_{\boldsymbol{k}} & -\xi(-\boldsymbol{k})\sigma_0 \end{pmatrix} C_{\boldsymbol{k}} + \sum_{\boldsymbol{k}} \xi(\boldsymbol{k}) + \mathcal{K}, \qquad (2.83)$$

with σ_0 denoting the two-dimensional unit matrix and $\hat{\Delta}_{\boldsymbol{k}}$, $C^\dagger_{\boldsymbol{k}}$ given by

$$\hat{\Delta}_{\boldsymbol{k}} = \begin{pmatrix} \Delta_{\boldsymbol{k},\uparrow\uparrow} & \Delta_{\boldsymbol{k},\uparrow\downarrow} \\ \Delta_{\boldsymbol{k},\downarrow\uparrow} & \Delta_{\boldsymbol{k},\downarrow\downarrow} \end{pmatrix}, \quad C^\dagger_{\boldsymbol{k}} = \begin{pmatrix} c^\dagger_{\boldsymbol{k}\uparrow} & c^\dagger_{\boldsymbol{k}\downarrow} & c_{-\boldsymbol{k}\uparrow} & c_{-\boldsymbol{k}\downarrow} \end{pmatrix}. \qquad (2.84)$$

Note that in (2.83), we also made use of $\hat{\Delta}^\dagger_{\boldsymbol{k}} = (\hat{\Delta}^T_{\boldsymbol{k}})^* = -(\hat{\Delta}_{-\boldsymbol{k}})^*$ and introduced the c-number term $\mathcal{K}$ determined by

$$\mathcal{K} = -\frac{1}{2N} \sum_{s_1,\dots,s_4} \sum_{\boldsymbol{k},\boldsymbol{q}} V^{pair}_{s_1,\dots,s_4}(\boldsymbol{k},\boldsymbol{q}) \langle c^\dagger_{-\boldsymbol{k}s_1} c^\dagger_{\boldsymbol{k}s_2} \rangle \langle c_{\boldsymbol{q}s_3} c_{-\boldsymbol{q}s_4} \rangle. \qquad (2.85)$$

Assuming a unitary pairing state, which means that $\hat{\Delta}_{\boldsymbol{k}} \hat{\Delta}^\dagger_{\boldsymbol{k}}$ is proportional to the unit matrix (see Sigrist and Ueda [19] for details), we can diagonalize the quadratic Hamiltonian (2.83):

$$H^{MF} = \frac{1}{2} \sum_{\boldsymbol{k}} C^\dagger_{\boldsymbol{k}} \begin{pmatrix} \xi(\boldsymbol{k})\sigma_0 & \hat{\Delta}_{\boldsymbol{k}} \\ \hat{\Delta}^\dagger_{\boldsymbol{k}} & -\xi(-\boldsymbol{k})\sigma_0 \end{pmatrix} C_{\boldsymbol{k}} + \sum_{\boldsymbol{k}} \xi(\boldsymbol{k}) + \mathcal{K} \qquad (2.86)$$

$$= \frac{1}{2} \sum_{\boldsymbol{k}} C^\dagger_{\boldsymbol{k}} U_{\boldsymbol{k}} \begin{pmatrix} E_{\boldsymbol{k}}\sigma_0 & 0 \\ 0 & -E_{\boldsymbol{k}}\sigma_0 \end{pmatrix} U^\dagger_{\boldsymbol{k}} C_{\boldsymbol{k}} + \sum_{\boldsymbol{k}} \xi(\boldsymbol{k}) + \mathcal{K}$$

$$= \sum_{\boldsymbol{k}s} E_{\boldsymbol{k}} \alpha^\dagger_{\boldsymbol{k}s} \alpha_{\boldsymbol{k}s} - \sum_{\boldsymbol{k}} E_{\boldsymbol{k}} + \sum_{\boldsymbol{k}} \xi(\boldsymbol{k}) + \mathcal{K}. \qquad (2.87)$$

Here, the two twofold degenerate eigenvalues $\lambda_{1,2} = \pm E_{\boldsymbol{k}}$ were obtained by using $\det \begin{pmatrix} A & B \\ C & D \end{pmatrix} = \det(AD - BC)$ for commuting two-dimensional matrices C, D, which then yields the associated energy spectrum

$$E_{\boldsymbol{k}} = \sqrt{\xi^2_{\boldsymbol{k}} + \text{tr}(\hat{\Delta}_{\boldsymbol{k}} \hat{\Delta}^\dagger_{\boldsymbol{k}})/2}. \qquad (2.88)$$

The unitary matrix $U_{\boldsymbol{k}}$ in (2.87) can likewise be identified as

$$U_{\boldsymbol{k}} = \begin{pmatrix} \hat{u}_{\boldsymbol{k}} & \hat{v}_{\boldsymbol{k}} \\ \hat{v}^*_{-\boldsymbol{k}} & \hat{u}^*_{-\boldsymbol{k}} \end{pmatrix} = \frac{1}{\sqrt{2E_{\boldsymbol{k}}(E_{\boldsymbol{k}} + \xi_{\boldsymbol{k}})}} \begin{pmatrix} \sigma_0(E_{\boldsymbol{k}} + \xi_{\boldsymbol{k}}) & -\hat{\Delta}_{\boldsymbol{k}} \\ \hat{\Delta}^\dagger_{\boldsymbol{k}} & \sigma_0(E_{\boldsymbol{k}} + \xi_{\boldsymbol{k}}) \end{pmatrix} \tag{2.89}$$

and determines the quasi-particle excitations $\alpha^\dagger_{\boldsymbol{k}s}, \alpha_{\boldsymbol{k}s}$ mixing particle and hole states:

$$\alpha_{\boldsymbol{k}s} = \sum_{s'} u^*_{\boldsymbol{k},ss'} c_{\boldsymbol{k}s'} + v_{-\boldsymbol{k}ss'} c^\dagger_{-\boldsymbol{k}s'}. \tag{2.90}$$

In matrix-vector notation, (2.90) can also be written as

$$\begin{pmatrix} \alpha^\dagger_{\boldsymbol{k}\uparrow} & \alpha^\dagger_{\boldsymbol{k}\downarrow} & \alpha_{-\boldsymbol{k}\uparrow} & \alpha_{-\boldsymbol{k}\downarrow} \end{pmatrix} = \begin{pmatrix} c^\dagger_{\boldsymbol{k}\uparrow} & c^\dagger_{\boldsymbol{k}\downarrow} & c_{-\boldsymbol{k}\uparrow} & c_{-\boldsymbol{k}\downarrow} \end{pmatrix} U_{\boldsymbol{k}}. \tag{2.91}$$

The grand canonical potential of (2.87) can be easily expressed as

$$\Omega = -T \sum_{\boldsymbol{k}s} \ln\left(1 + e^{-\beta E_{\boldsymbol{k}}}\right) - \sum_{\boldsymbol{k}} E_{\boldsymbol{k}} + \sum_{\boldsymbol{k}} \xi(\boldsymbol{k}) + \mathcal{K}, \tag{2.92}$$

and the calculation of a stationary point in Ω turns out to be equivalent to the self-consistent gap equation:

$$0 = \frac{\partial \Omega}{\partial \langle c^\dagger_{-\boldsymbol{k}s_1} c^\dagger_{\boldsymbol{k}s_2} \rangle} \iff \Delta_{\boldsymbol{k},s_2s_1} = -\frac{1}{N} \sum_{\boldsymbol{q},s's} V^{pair}_{s_1s_2s's}(\boldsymbol{k},\boldsymbol{q}) \frac{\Delta_{\boldsymbol{q},s's}}{2E(\boldsymbol{q})} \tanh\left(\frac{E(\boldsymbol{q})}{2T}\right). \tag{2.93}$$

In order to evaluate Ω in a stationary point and to compare the free energies of different gap solutions, we apply (2.93) and obtain the following expression for the free energy in a stationary solution

$$\Omega^{stat} = -T \sum_{\boldsymbol{k}s} \ln\left(1 + e^{-\beta E(\boldsymbol{k})}\right) + \frac{1}{2} \sum_{\boldsymbol{k},s_1s_2} \frac{\Delta^\dagger_{\boldsymbol{k},s_2s_1} \Delta_{\boldsymbol{k},s_2s_1}}{2E(\boldsymbol{k})} \tanh\left(\frac{E(\boldsymbol{k})}{2T}\right)$$
$$+ \sum_{\boldsymbol{k}} \xi(\boldsymbol{k}) - \sum_{\boldsymbol{k}} E(\boldsymbol{k}). \tag{2.94}$$

During the later analysis, we then take V^{pair} from the functional RG at a scale Λ_{MF} and minimize the grand-canonical potential (2.92). This in turn can be achieved by locating the stationary points of Ω using (2.93) and by comparing the associated free energies via (2.94). Note that this combined functional RG and mean-field approach goes far beyond conventional mean-field studies as the functional RG takes into account all fluctuations down to an energy scale $\Lambda_{MF} \gtrsim \Lambda_c$. For a reasonable estimate, we can also consider the linear gap-equation as a first-order expansion of (2.93) in $\hat{\Delta}_{\boldsymbol{k}}$, which becomes exact in the vicinity of the superconducting transition. The self-consistent gap equation then reads as

$$\Delta_{\boldsymbol{k},s_2s_1} = -\frac{1}{N} \sum_{\boldsymbol{q},s's} V^{pair}_{s_1s_2s's}(\boldsymbol{k},\boldsymbol{q}) \frac{\Delta_{\boldsymbol{q},s's}}{2\xi(\boldsymbol{q})} \tanh\left(\frac{\xi(\boldsymbol{q})}{2T}\right) + \mathcal{O}(\Delta^2)$$

$$= \frac{1}{\lambda} \sum_{s's} \langle V^{pair}_{s_1 s_2 s' s}(\boldsymbol{k}, \boldsymbol{q}) \Delta_{\boldsymbol{q}, s's} \rangle_{\boldsymbol{q} \in FS} + \mathcal{O}(\Delta^2) \tag{2.95}$$

with a constant λ being equivalent to [19]:

$$\frac{1}{\lambda} = -N_0 \int_0^{\Lambda_c} d\xi \frac{\tanh\left(\frac{\xi(\boldsymbol{q})}{2T}\right)}{\xi(\boldsymbol{q})} = -N_0 \ln(1.13\Lambda_c/T). \tag{2.96}$$

In linear order, the gap-equation (2.95) therefore reduces to an eigenvalue problem in the form of

$$\lambda \Delta_{\boldsymbol{k}, s_2 s_1} = \sum_{s's} \langle V^{pair}_{s_1 s_2 s' s}(\boldsymbol{k}, \boldsymbol{q}) \Delta_{\boldsymbol{q}, s's} \rangle_{\boldsymbol{q} \in FS}, \tag{2.97}$$

and the gap Δ of largest negative eigenvalue λ determines the transition temperature T_c through

$$T_c = 1.13\Lambda_c e^{1/(N_0\lambda)} \leq 1.13\Lambda_c. \tag{2.98}$$

During the later discussion, we will usually compare the flow of eigenvalues in order to identify the favored type of order. From (2.98) it is also apparent that the critical energy scale Λ_c already gives an upper bound for T_c. At $T = 0$, we can further apply (2.94) to determine the ground-state energy [20]:

$$\Omega_{T=0} = \frac{1}{2} \sum_{\boldsymbol{k}, s} (\xi(\boldsymbol{k}) - E(\boldsymbol{k})) + \frac{1}{4} \sum_{\boldsymbol{k}} \text{tr}\left(\Delta^\dagger_{\boldsymbol{k}} \Delta_{\boldsymbol{k}}\right) E(\boldsymbol{k})$$

$$\approx -N_0 \text{tr} \langle (\Delta^\dagger_{\boldsymbol{k}} \Delta_{\boldsymbol{k}}) \rangle_{\boldsymbol{k} \in FS}. \tag{2.99}$$

Here, (2.99) implies that gap zeros tend to be unfavorable due to a lower condensation energy.

Chapter 3

Unconventional Superconductivity

According to Landau's theory of phase transitions, different states of matter can be understood from the perspective of spontaneous symmetry breaking. Here, the symmetry of the ground-state is spontaneously reduced below a certain critical temperature, and the system develops some kind of additional order. As a consequence, one can find a field variable which acquires a finite expectation value, known as order parameter.

In this chapter, we study the symmetry classification of the superconducting order on different lattice systems and review some of the current experimental methods to identify the detailed type of pairing order. Based on the superconducting case, we then extend this classification to general particle-particle and particle-hole condensates in arbitrary lattice systems. In addition, we also discuss the influence of spin-orbit coupling on this symmetry classification, which is in turn required for the study of strontium ruthenate in Chapter 6.

3.1 Symmetry Classification of Superconducting Order

In order to classify the superconducting order, we first have a look at the ground-state wave function of the mean-field Hamiltonian (2.87):

$$H^{MF} = \sum_{\boldsymbol{k}s} E_{\boldsymbol{k}} \alpha_{\boldsymbol{k}s}^{\dagger} \alpha_{\boldsymbol{k}s} - \sum_{\boldsymbol{k}} E_{\boldsymbol{k}} + \sum_{\boldsymbol{k}} \xi(\boldsymbol{k}) + \mathcal{K}.$$

Due to the positive-definiteness of $E_{\boldsymbol{k}}$, the ground-state of H^{MF} can be easily derived as a state which is annihilated by all $\alpha_{\boldsymbol{k}s}$, i.e.

$$|BCS\rangle = \prod_{\boldsymbol{k}} \alpha_{\boldsymbol{k}\uparrow} \alpha_{\boldsymbol{k}\downarrow} \alpha_{-\boldsymbol{k}\downarrow} \alpha_{-\boldsymbol{k}\uparrow} |0\rangle,$$

and which obviously constitutes an eigenstate of H^{MF} with a ground-state energy $E_0 = \sum_{\boldsymbol{k}}(\xi(\boldsymbol{k}) - E_{\boldsymbol{k}}) + \mathcal{K}$. If we now insert the definition (2.90) of the Bogoliubov quasi-particles, the ground-state can be written as

$$|BCS\rangle = c \prod_{\boldsymbol{k}} \left(1 + a_{\boldsymbol{k}} c^{\dagger}_{-\boldsymbol{k}\uparrow} c^{\dagger}_{\boldsymbol{k}\downarrow} + b_{\boldsymbol{k}} c^{\dagger}_{-\boldsymbol{k}\downarrow} c^{\dagger}_{\boldsymbol{k}\uparrow} + a'_{\boldsymbol{k}} c^{\dagger}_{-\boldsymbol{k}\uparrow} c^{\dagger}_{\boldsymbol{k}\uparrow} + b'_{\boldsymbol{k}} c^{\dagger}_{-\boldsymbol{k}\downarrow} c^{\dagger}_{\boldsymbol{k}\downarrow} \right. \quad (3.1)$$

$$\left. + c_{\boldsymbol{k}} c^{\dagger}_{-\boldsymbol{k}\uparrow} c^{\dagger}_{-\boldsymbol{k}\downarrow} c^{\dagger}_{\boldsymbol{k}\uparrow} c^{\dagger}_{\boldsymbol{k}\downarrow} \right) |0\rangle$$

with a normalization factor c, and the remaining parameters defined by

$$\begin{pmatrix} a'_{\boldsymbol{k}} & a_{\boldsymbol{k}} \\ b'_{\boldsymbol{k}} & b_{\boldsymbol{k}} \end{pmatrix} = -\hat{v}_{\boldsymbol{k}} \hat{u}_{\boldsymbol{k}}^{-1} = \hat{\Delta}_{\boldsymbol{k}}/(E_{\boldsymbol{k}} + \xi_{\boldsymbol{k}}), \quad c_{\boldsymbol{k}} = a_{\boldsymbol{k}} b'_{\boldsymbol{k}} - a'_{\boldsymbol{k}} b_{\boldsymbol{k}}. \quad (3.2)$$

Using the shortened notation of $\phi_{\alpha\beta}(\boldsymbol{k}) = -(\hat{v}_{\boldsymbol{k}} \hat{u}_{\boldsymbol{k}}^{-1})_{\alpha\beta}$, the ground-state $|BCS\rangle$ now appears as a coherent superposition of Cooper-pairs

$$|BCS\rangle = c \cdot \exp \left(\sum_{\boldsymbol{k}} \phi_{\alpha\beta}(\boldsymbol{k}) c^{\dagger}_{-\boldsymbol{k}\alpha} c^{\dagger}_{\boldsymbol{k}\beta} \right) |0\rangle, \quad (3.3)$$

where each pair is characterized by one and the same wave function $\phi_{\alpha\beta}(\boldsymbol{k})$. This, by the way, illustrates that all pairs condensed into the same state, similar to the superfluid phase of interacting bosons. Note that the pair wave function $\phi_{\alpha\beta}$ in (3.3) can also be expressed as ground-state expectation value with respect to $|BCS\rangle$:

$$\phi_{\alpha\beta}(\boldsymbol{k}) = \langle c^{\dagger}_{-\boldsymbol{k}\alpha} c^{\dagger}_{\boldsymbol{k}\beta} \rangle.$$

It is further apparent that the global $U(1)$-phase transformation

$$c^{\dagger} \to e^{i\gamma/2} c^{\dagger}, \quad c \to e^{i\gamma/2} c \quad (3.4)$$

is broken in $|BCS\rangle$ as this changes the phase of the pair wave function $\phi_{\alpha\beta} \to e^{i\gamma}\phi_{\alpha\beta}$ and leads to different ground-states $|BCS'\rangle$ (see [21] for a detailed discussion). The corresponding one-parametric manifold of different ground-states further suggests the existence of low-energy excitations, the associated Goldstone bosons, which in turn are absorbed by the electromagnetic field and give rise to the characteristic Meissner effect of charged superfluids.

Besides this $U(1)$-phase symmetry, the ground-state can also break additional symmetries of the underlying Hamiltonian, as for example rotational symmetries in spatial- and spin-space, depending on the detailed form of the Cooper-pair wave function $\phi_{\alpha\beta}(\boldsymbol{k})$. The different two-particle bound-states of equal binding energy apparently form an irreducible representation of the underlying symmetry group. According to a fundamental theorem of Schur, the eigenvalues of the Casimir operators in this symmetry group can be used to classify the different irreducible representations. For example, in

the hydrogen atom, the squared angular-momentum operator L^2 presents a Casimir invariant with eigenvalues $\hbar l(l+1)$, and, for a given principal quantum number n, all states with the same angular momentum l also have the same energy and transform in a $(2l+1)$-dimensional irreducible representation. Actually, the energy spectrum in the hydrogen atom only depends on the quantum number n due the peculiarity of a $1/r$-potential and the resulting larger symmetry equivalent to the four-dimensional rotation group [22].

Coming back to the superconducting order and assuming rotational symmetry in spin- and spatial-coordinates, the pair wave function $\phi_{\alpha\beta}(\boldsymbol{k})_{ls}$ for a given angular-momentum and spin quantum-number l and s can be written as a superposition of the $(2l+1)\cdot(2s+1)$ basis functions $c_{sl}Y_{lm_l}\chi_{sm_s}$:

$$\phi_{\alpha\beta}(\boldsymbol{k})_{ls} = \langle c^\dagger_{-\boldsymbol{k}\alpha}c^\dagger_{\boldsymbol{k}\beta}\rangle = \sum_{m_s=-s}^{s}\sum_{m_l=-l}^{l} a_{m_l m_s}c_{sl}(|\boldsymbol{k}|)Y_{lm_l}(\hat{\boldsymbol{k}})\chi_{sm_s}(\alpha,\beta). \quad (3.5)$$

Here, Y_{lm_l} labels spherical harmonics, $c_{sl}(|\boldsymbol{k}|)$ carries the radial dependence, and χ_{sm_s} denotes the total spin-singlet and triplet configurations:

$$\chi_{1m_s}(\alpha,\beta) = \begin{cases} \sigma^+_{\alpha\gamma}\epsilon_{\gamma\beta} & \text{for } m_s = 1 \\ \sigma^3_{\alpha\gamma}\epsilon_{\gamma\beta} & \text{for } m_s = 0 \\ \sigma^-_{\alpha\gamma}\epsilon_{\gamma\beta} & \text{for } m_s = -1 \end{cases}, \quad \chi_{00}(\alpha,\beta) = \epsilon_{\alpha\beta}. \quad (3.6)$$

Note that in (3.6) we used the Pauli-matrices $\sigma^+ = \sigma^1 + i\sigma^2$, $\sigma^- = \sigma^1 - i\sigma^2$ and σ^3 as well as the antisymmetric tensor $\epsilon_{\alpha\beta}$ and an implicit summation over the index γ. For a given radial dependence $c^{sl}(|\boldsymbol{k}|)$ and quantum numbers l,s, all pair-wave functions within the $(2l+1)\cdot(2s+1)$-dimensional representation (3.5) have the same binding energy by symmetry and, consequently, lead to the same transition temperature T_c. The remaining labels m_l and m_s denote the quantum numbers of the projected angular-momentum and spin. Using the vector notation of $\widetilde{\boldsymbol{\sigma}} = (\sigma^+, \sigma^3, \sigma^-)$, we can further rewrite (3.5) in the following compact way for spin-singlet and triplet pairing orders

$$\phi_{\alpha\beta}(\boldsymbol{k})_{l0} = \langle c^\dagger_{-\boldsymbol{k}\alpha}c^\dagger_{\boldsymbol{k}\beta}\rangle = \Phi(\boldsymbol{k})\epsilon_{\alpha\beta}$$

$$\phi_{\alpha\beta}(\boldsymbol{k})_{l1} = \langle c^\dagger_{-\boldsymbol{k}\alpha}c^\dagger_{\boldsymbol{k}\beta}\rangle = \left(\vec{\boldsymbol{\Phi}}(\boldsymbol{k})\cdot\widetilde{\boldsymbol{\sigma}}\right)_{\alpha\gamma}\epsilon_{\gamma\beta} \quad (3.7)$$

with $\Phi(\boldsymbol{k})$ and the components of $\boldsymbol{\Phi}(\boldsymbol{k})$ transforming in an irreducible representation of the underlying space-group. Apparently, for $l \neq 0$ and $s \neq 0$, the pair wave function $\phi_{\alpha\beta}(\boldsymbol{k})_{ls}$ and the associated ground-state of (3.3) break rotational symmetry in spatial- and spin-coordinates. For example, in the superfluid A-phase and A_1-phase of He^3, the pair wave functions read as

$$A\text{-phase:} \quad \phi_{\alpha\beta}(\boldsymbol{k}) = Y_{11}(\boldsymbol{k})\sigma^3_{\alpha\gamma}\epsilon_{\gamma\beta} \Longleftrightarrow (\hat{\boldsymbol{k}}_x + i\hat{\boldsymbol{k}}_y)(|\uparrow\downarrow\rangle + |\downarrow\uparrow\rangle) \quad (3.8)$$

A_1-phase: $\phi_{\alpha\beta}(\boldsymbol{k}) = Y_{11}(\boldsymbol{k})\sigma^+_{\alpha\gamma}\epsilon_{\gamma\beta} \Longleftrightarrow (\hat{\boldsymbol{k}}_x + i\hat{\boldsymbol{k}}_y)|\uparrow\uparrow\rangle,$

and, due to $l = s = 1$ in both states, the rotational symmetries in spatial- and spin-coordinates are broken. In addition, the finite quantum numbers $m_l = 1$, $m_s = 0$ in the A-phase and $m_l = 1$, $m_s = 1$ in the A_1-phase both lead to the breaking of time-reversal symmetry. A two-dimensional lattice representation of the A-phase in (3.8) will further be discussed in the context of ruthenates (see Chap. 6).

Another peculiarity of the pair wave function $\phi_{\alpha\beta}(\boldsymbol{k})_{ls} = \langle c^\dagger_{-\boldsymbol{k}\alpha} c^\dagger_{\boldsymbol{k}\beta}\rangle$ arises from the required antisymmetry under particle exchange. As it is well known, this exchange symmetry restricts Y_{lm} to be odd (even) for spin-triplet (spin-singlet) pairing which is, by the way, not required in the particle-hole condensates discussed below. Yet, before we generalize this symmetry characterization, we first note that the gap-function $\hat{\Delta}_{\boldsymbol{k}}$ in (3.2) transforms in the same way as the pair wave function $\phi_{\alpha\beta}(\boldsymbol{k})$. The associated spin-singlet and triplet contribution of $\hat{\Delta}_{\boldsymbol{k}}$ can therefore be separated into

$$s = 0: \quad \hat{\Delta}_{\boldsymbol{k}} = \delta^0_0(\boldsymbol{k})(|\uparrow\downarrow\rangle - |\downarrow\uparrow\rangle)$$
$$= \begin{pmatrix} 0 & \delta^0_0(\boldsymbol{k}) \\ -\delta^0_0(\boldsymbol{k}) & 0 \end{pmatrix} = i\sigma_y\psi(\boldsymbol{k}) \tag{3.9}$$

$$s = 1: \quad \hat{\Delta}_{\boldsymbol{k}} = \delta^1_{-1}(\boldsymbol{k})|\downarrow\downarrow\rangle + \delta^1_0(\boldsymbol{k})(|\uparrow\downarrow\rangle + |\downarrow\uparrow\rangle) + \delta^1_1(\boldsymbol{k})|\uparrow\uparrow\rangle$$
$$= \begin{pmatrix} \delta^1_1(\boldsymbol{k}) & \delta^1_0(\boldsymbol{k}) \\ \delta^1_0(\boldsymbol{k}) & \delta^1_{-1}(\boldsymbol{k}) \end{pmatrix} = i\,(\boldsymbol{d}(\boldsymbol{k}) \cdot \boldsymbol{\sigma})\,\sigma_y, \tag{3.10}$$

with even $\psi(\boldsymbol{k})$ and odd $\boldsymbol{d}(\boldsymbol{k})$ basis functions similar to (3.5). The matrices $\sigma^{1,2,3}$ in (3.9) and (3.10) as well as its formal vector notation $\boldsymbol{\sigma}$ are again determined by Pauli-matrices, and the so-called $\boldsymbol{d}$-vector is defined by

$$d_1(\boldsymbol{k}) = \frac{1}{2}(\delta^1_{-1}(\boldsymbol{k}) - \delta^1_1(\boldsymbol{k}))$$
$$d_2(\boldsymbol{k}) = \frac{1}{2i}(\delta^1_{-1}(\boldsymbol{k}) + \delta^1_1(\boldsymbol{k}))$$
$$d_3(\boldsymbol{k}) = \delta^1_0(\boldsymbol{k}).$$

The advantage of the $\boldsymbol{d}$-vector notation here lies in its transparent transformation behavior as the spin-one representation of the spin rotation simply transforms $\boldsymbol{d}(\boldsymbol{k})$ as an axial vector. This in turn means that under spin rotation g_s we have

$$g_s\boldsymbol{d}(\boldsymbol{k}) = D^+(g_s)\boldsymbol{d}(\boldsymbol{k})$$

with a three-dimensional rotation matrix $D^+(g_s)$. The $(+)$ here means that, if we fix the $\boldsymbol{k}$-dependence, the vector $\boldsymbol{d}$ remains invariant under space inversion which then accounts for the notion of an axial vector. On the other

hand, the $\boldsymbol{k}$-dependence of $\boldsymbol{d}(\boldsymbol{k})$ must of course be odd under space inversion. This is a very important statement for the later discussion of spin-orbit effects, which then couples the rotation in spin and coordinate space.

transformation	singlet $s = 0$	triplet $s = 1$
space inversion	$I\psi(\boldsymbol{k}) = \psi(-\boldsymbol{k})$	$I\boldsymbol{d}(\boldsymbol{k}) = -\boldsymbol{d}(-\boldsymbol{k})$
time inversion	$K\psi(\boldsymbol{k}) = \psi^*(\boldsymbol{k})$	$K\boldsymbol{d}(\boldsymbol{k}) = \boldsymbol{d}^*(\boldsymbol{k})$
spin rotation	$g_s\psi(\boldsymbol{k}) = \psi(\boldsymbol{k})$	$g_s\boldsymbol{d}(\boldsymbol{k}) = D^+(g_s)\boldsymbol{d}(\boldsymbol{k})$
point group	$g_p\psi(\boldsymbol{k}) = \psi(D^-(g_p)\boldsymbol{k})$	$g_p\boldsymbol{d}(\boldsymbol{k}) = \boldsymbol{d}(D^-(g_p)\boldsymbol{k})$

Table 3.1: Transformation behavior of the singlet $\psi(\boldsymbol{k})$ and triplet $\boldsymbol{d}(\boldsymbol{k})$ gap functions under space inversion I, time inversion K, spin rotation g_s and point-group g_p operations.

In the following table, we summarize the transformation behavior of the superconducting gap function. Here, the sign in the representation matrices $D^\pm(g)$ denotes the transformation behavior under space inversion with $\boldsymbol{k}$ transforming as a vector and $\boldsymbol{d}$ as an axial-vector. Further details on the symmetry classification can be found in the review article of Sigrist $et\ al.$ [19] and in the textbook of Mineev [20]. In the following section, we will shortly address the classification of general particle-particle and particle-hole order-parameter fields.

3.2   Particle-Particle and Particle-Hole Condensates

After we classified the superconducting order in terms of irreducible representations of the underlying symmetry group, we can also extend this analysis to general particle-particle $\phi = \langle c^\dagger c^\dagger \rangle$ and particle-hole $\phi = \langle c^\dagger c \rangle$ like order-parameter fields. Applying Landau's approach of expanding the free energy in polynomials of the order-parameter field ϕ, i.e.

$$F[\phi] \propto (T - T_c)\phi^2 + u\phi^4 + \dots,$$

it is immediately apparent that the fields ϕ of same T_c form an irreducible representation of the normal-state symmetry group. Using the same notation as in (3.7), with $\widetilde{\boldsymbol{\sigma}} = (\sigma^+, \sigma^3, \sigma^-)$ and the antisymmetric tensor $\epsilon_{\alpha\beta}$, the particle-particle like order-parameter fields are characterized by

$$\langle c^\dagger_{-\boldsymbol{k}\alpha} c^\dagger_{\boldsymbol{k}+\boldsymbol{Q}\beta} \rangle = \Phi_{\boldsymbol{Q}}(\boldsymbol{k})\epsilon_{\alpha\beta}$$
$$\langle c^\dagger_{-\boldsymbol{k}\alpha} c^\dagger_{\boldsymbol{k}+\boldsymbol{Q}\beta} \rangle = \left(\vec{\boldsymbol{\Phi}}_{\boldsymbol{Q}}(\boldsymbol{k}) \cdot \widetilde{\boldsymbol{\sigma}} \right)_{\alpha\gamma} \epsilon_{\gamma\beta}. \tag{3.11}$$

Here, we also allowed for a nonzero center-of-mass momentum $\boldsymbol{Q}$ which leads to an additional breaking of translational symmetry and is commonly known as Fulde-Ferrell-Larkin-Ovchinnikov (FFLO) state [23]. Analogous to the spin-singlet and triplet particle-particle fields in (3.11), we likewise decompose the particle-hole fields into irreducible representations of
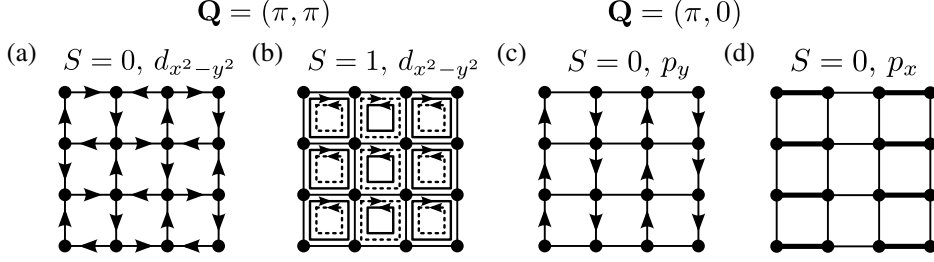
$$\mathbf{Q} = (\pi, \pi)$$ $$\mathbf{Q} = (\pi, 0)$$

(a) $S = 0,\ d_{x^2-y^2}$ (b) $S = 1,\ d_{x^2-y^2}$ (c) $S = 0,\ p_y$ (d) $S = 0,\ p_x$

Figure 3.1: Different examples of particle-hole condensates with finite angular momentum on the square lattice. (a) Singlet *d*-density wave phase with alternating plaquette currents, (b) triplet *d*-density wave phase with alternating currents of spin-up (full-lined arrows) and spin-down (dashed-line arrows). (c) Alternating currents along the vertical bonds and (d) Peierls state with enhanced (thick lines) and reduced (thin lines) hopping amplitudes. (a) and (c) break time-reversal symmetry, (a)-(d) break the C_{4v} point-group symmetry as well as translational symmetry, (b) breaks also spin-rotational symmetry.

the spin-rotation group and obtain the analogous spin-singlet and triplet order-parameter fields

$$\langle c^\dagger_{\mathbf{k}\alpha} c_{\mathbf{k}+\mathbf{Q}\beta} \rangle = \Phi_{\mathbf{Q}}(\mathbf{k})\delta_{\alpha\beta}$$
$$\langle c^\dagger_{\mathbf{k}\alpha} c_{\mathbf{k}+\mathbf{Q}\beta} \rangle = \left(\vec{\mathbf{\Phi}}_{\mathbf{Q}}(\mathbf{k}) \cdot \boldsymbol{\sigma} \right)_{\alpha\beta}. \tag{3.12}$$

Here, $\delta_{\alpha\beta}$ indicates the Kronecker delta and $\boldsymbol{\sigma}$ is given by $\boldsymbol{\sigma} = (\sigma^1, \sigma^2, \sigma^3)$ with the usual Pauli-matrices $\sigma^{1,2,3}$. Note that the singlet and triplet contributions in (3.11) and (3.12) are quite different due to the distinct transformation behavior of particle- and hole-operators under spin rotation. On the other hand, the $\mathbf{k}$-dependent parts $\Phi_{\mathbf{Q}}(\mathbf{k})$ and $\vec{\mathbf{\Phi}}_{\mathbf{Q}}(\mathbf{k})$ transform in both particle-particle and particle-hole cases as irreducible representations of the space group which leaves $\mathbf{Q}$ invariant modulo reciprocal lattice vectors. In Fig. 3.1, we illustrate four examples of unconventional (non *s*-wave) particle-hole condensates on the square lattice. The corresponding order-parameter fields for (a)-(d) read as follows:

$$\mathbf{Q} = (\pi, \pi),\ S = 0,\ L \sim d_{x^2-y^2} : \ \langle c^\dagger_{\mathbf{k}\alpha} c_{\mathbf{k}+(\pi,\pi)\beta} \rangle \propto (\cos(k_x) - \cos(k_y))\delta_{\alpha\beta}$$

$$\mathbf{Q} = (\pi, \pi),\ S = 1,\ L \sim d_{x^2-y^2} : \ \langle c^\dagger_{\mathbf{k}\alpha} c_{\mathbf{k}+(\pi,\pi)\beta} \rangle \propto (\cos(k_x) - \cos(k_y))(\mathbf{n} \cdot \boldsymbol{\sigma})_{\alpha\beta}$$

$$\mathbf{Q} = (\pi, 0),\ S = 0,\ L \sim p_y : \qquad \langle c^\dagger_{\mathbf{k}\alpha} c_{\mathbf{k}+(\pi,0)\beta} \rangle \propto \sin(k_y)\delta_{\alpha\beta}$$

$$\mathbf{Q} = (\pi, 0),\ S = 0,\ L \sim p_x : \qquad \langle c^\dagger_{\mathbf{k}\alpha} c_{\mathbf{k}+(\pi,0)\beta} \rangle \propto \sin(k_x)\delta_{\alpha\beta}.$$

Note that the usual charge- and spin-density waves of ordering vector $\mathbf{Q}$ are similarly described by an *s*-wave particle-hole condensate in the spin-singlet and triplet channel, respectively. For a detailed description of the experimental signatures and the excitation spectrum in unconventional particle-hole condensates we refer to the articles of Nayak *et al.* [24] and Garcia-Aldea [25].

During the next section, we illustrate how to derive the irreducible representations of a given lattice symmetry and how to calculate all associated basis functions $\Phi_Q(k)$ and $\vec{\Phi}_Q(k)$. This in turn provides a complete characterization of two-particle like order-parameter fields on a given lattice, and the classification of more complicated order-parameters containing more than two operators can be accomplished in a similar fashion.

E:	identity operation
C_n:	rotation through $2\pi/n$ with $n = 1, 2, 3, 4, 6$ the axis of highest n is called principle
σ_v:	vertical reflection plane - passing through the origin and the principle axis
σ_d:	special case of σ_v but also bisecting the angle between two two-fold rotational axes perpendicular to the principal axis
σ_h:	horizontal reflection plane - passing through the origin and perpendicular to the principle axis.
S_n:	rotation through $2\pi/n$ followed by a reflection in the plane perpendicular to the axis of rotation

Table 3.2: Symmetry operations of point groups in Schoenflies notation.

3.3 Elements of Representations Theory

In the following section, we want to recap the basic notions of representation theory in order to calculate the above basis functions $\Phi_Q(k)$ and $\vec{\Phi}_Q(k)$ for different lattice systems. However, to begin, we start with the definition of an abstract group consisting of a set of elements $\mathcal{G}$ together with some operation $\circ$ acting on that set.

Definition (Group)

A group $\mathcal{G} = (G, \circ)$ consists of a set G and an operation $\circ$ such that:

1) For all $a, b \in G$, the result $a \circ b$ is also in G

2) The operation $\circ$ is associative, i.e. $a \circ (b \circ c) = (a \circ b) \circ c$ holds for all elements $a, b, c \in G$

3) There exists a unit element such that $a \circ e = e \circ a = a$ for $a \in G$

4) For each $a \in G$, there exists an inverse element $a^{-1} \in G$ such that $a \circ a^{-1} = a^{-1} \circ a = e$.

As an example, we consider the set of transformations which map a given lattice into itself by leaving one point fixed. This point does not necessarily has to be a lattice point, and the corresponding transformations are commonly termed as point groups. The elements in these point groups typically

consist of lattice transformations like the one shown in Tab. 3.2. Note that the last two operations of Tab. 3.2 are contained in the first four in case of a two-dimensional lattice structure. As a useful example, which will be taken up in Chap. 5 and Chap. 6, we depicted the point-groups for the square- and hexagonal-lattice structures in Fig. 3.2. Here $C_{3,4,6}^{-1}$ denote the inverse elements of $C_{3,4,6}$, and all other elements equal their own inverse. Another definition which is essential when discussing representation theory is the notion of conjugate elements and classes given in the following.

$$C_{4v} = \{E, C_2, C_4, C_4^{-1}, \sigma_v^1, \sigma_v^2, \sigma_d^1, \sigma_d^2\}$$

$$C_{6v} = \{E, C_2, C_3, C_3^{-1}, C_6, C_6^{-1}, \sigma_v^1, \sigma_v^2, \sigma_v^3, \sigma_d^1, \sigma_d^2, \sigma_d^3\}$$
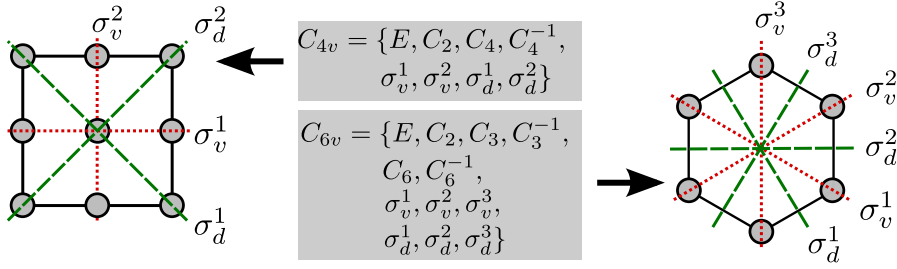
Figure 3.2: Point group elements of the square-lattice C_{4v} (left) and hexagonal-lattice structure C_{6v} (right).

Conjugate Elements and Classes in a Group

1) Two elements a, b of the group $\mathcal{G} = (G, \circ)$ are conjugate, written $a \sim b$, if and only if there is another element $x \in G$ such that $b = x \circ a \circ x^{-1}$.

2) A class is the entirety of conjugate elements.

In order to calculate the classes of a given group, one can simply compute all conjugate elements for each group element. At this, it turns out that the group C_{4v} and C_{6v} consist of 5 and, respectively, 6 different classes written down below

$$C_{4v} : \{E\}, \ \{C_2\}, \ 2C_4 = \{C_4, C_4^{-1}\}, \ 2\sigma_v = \{\sigma_v^1, \sigma_v^2\}, \ 2\sigma_d := \{\sigma_d^1, \sigma_d^2\}$$
$$C_{6v} : \{E\}, \ \{C_2\}, \ 2C_3 = \{C_3, C_3^{-1}\}, \ 2C_6 = \{C_6, C_6^{-1}\},$$
$$3\sigma_v = \{\sigma_v^1, \sigma_v^2, \sigma_v^3\}, \ 3\sigma_d := \{\sigma_d^1, \sigma_d^2, \sigma_d^3\}. \qquad (3.13)$$

Later, it will turn out that the number of classes in a group equals the number of irreducible representations, but, before that, we want to review the basic concepts of representation theory. The idea here is to avoid the calculation with abstract group elements and to represent each element by objects that are more convenient to deal with, for example linear operators in the form of square matrices. Besides that, representation theory often allows to make statements about degeneracies in energy spectra or enables to determine matrix elements without explicit integration. For this reason, we summarize the following notions required for later discussions.

Representation of a Group

A group $\mathcal{R} = (R, \cdot)$ is a representation of another group $\mathcal{G} = (G, \circ)$ if there is a one-to-one mapping $M : G \mapsto R$ such that $M(a \circ b) = M(a) \cdot M(b)$ for all a, b in G. In all cases considered here, R is a set of n-dimensional square matrices, and "$\cdot$" denotes the usual matrix multiplication. In the following, we use the abbreviation Γ to denote a representation of a group $\mathcal{G}$.

1) If the representation Γ consists of $(n \times n)$-matrices, it is termed n-dimensional.

2) Two n-dimensional representations Γ_1, Γ_2 of a group $\mathcal{G}$ are equivalent, if there is a regular $(n \times n)$-matrix U such that $N(a) = U \cdot M(a) \cdot U^{-1}$ for all elements a in $\mathcal{G}$. Here, $N(a)$ and $M(a)$ denote the matrices assigned to a in the representations Γ_1 and Γ_2, respectively.

3) A representation Γ is denoted as reducible if it is equivalent in terms of (2) to a representation where all matrices have a common block structure $M(a) = \begin{pmatrix} M_1(a) & 0 \\ 0 & M_2(a) \end{pmatrix}$. If this is not possible, the representation is denoted as irreducible.

Two immediate consequences follow from this definition. First, the representation matrix of the unit element e is always given by a unit matrix, and, secondly, each group has a trivial representation provided by assigning $M(g) = 1$ to all group elements $g \in \mathcal{G}$. In order to determine all irreducible representations of a given group or to figure out whether a given representation is reducible, we need the following concept of characters.

The Usage of Characters

The character of a group element g in a representation Γ_i is determined by the trace $\chi^i(g) = \mathrm{tr}(D(g))$ of its representing matrix $D(g)$.

1) The dimension n_i of a representation Γ_i is given by the character of the identity map e, i.e. $n_i = \chi_i(e)$.

2) The number of classes n_c in a given group equals the number of (inequivalent) irreducible representations.

3) The characters χ_i of a representation Γ_i are equivalent for all elements in the same class, and, since there are as many classes as (inequivalent) irreducible representations, we can arrange all characters in a $(n_c \times n_c)$-character table:

$\mathcal{G}$	$\mathcal{C}_1$	$\cdots$	$\mathcal{C}_{n_c}$
Γ_1	$\chi_1(\mathcal{C}_1)$	$\cdots$	$\chi_1(\mathcal{C}_{n_c})$
$\vdots$	$\vdots$		$\vdots$
Γ_{n_c}	$\chi_{n_c}(\mathcal{C}_1)$	$\cdots$	$\chi_{n_c}(\mathcal{C}_{n_c})$

4) There are two very elegant orthogonality relations which allow to compute such character tables. The first one states that the scalar product of two columns gives

$$\sum_{i=1}^{n_c} \chi_i(\mathcal{C}_q)\chi_i^*(\mathcal{C}_{q'}) = \delta_{qq'} N/h_q, \tag{3.14}$$

with N denoting the number of elements in the entire group, and h_q labeling the number of elements in class $\mathcal{C}_q$. The second relation provides a similar relation for the weighted scalar product of two rows in the character table:

$$\sum_{q=1}^{n_c} h_q\chi_i(\mathcal{C}_q)\chi_j^*(\mathcal{C}_q) = \delta_{ij} N. \tag{3.15}$$

It is now an easy task to determine the character tables for the two point groups C_{4v} and C_{6v}. Applying (3.14) to the classes $\mathcal{C}_q = \mathcal{C}_q' = \{e\}$ and using $\chi_i(e) = n_i$, we obtain

$$C_{4v}: \quad n_1^2 + n_2^2 + n_3^2 + n_4^2 + n_5^2 = 8$$
$$C_{6v}: \quad n_1^2 + n_2^2 + n_3^2 + n_4^2 + n_5^2 + n_6^2 = 12$$

as the group C_{4v} (C_{6v}) consists of 8 (12) group elements and 5 (6) classes. This in turn implies that C_{4v} has one two-dimensional and four one-dimensional irreducible representations, whereas C_{6v} reveals two two-dimensional and four one-dimensional representations. Therefore, the first columns of the character tables in Fig. 3.3 are already determined, and, as each group has a trivial representation with $M(g) = 1$ for all $g \in \mathcal{G}$, one has in addition one

C_{4v}	E	C_2	$2C_4$	$2\sigma_v$	$2\sigma_d$	C_{6v}	E	C_2	$2C_3$	$2C_6$	$3\sigma_v$	$3\sigma_d$
A_1	1	1	1	1	1	A_1	1	1	1	1	1	1
A_2	1	1	1	-1	-1	A_2	1	1	1	1	-1	-1
B_1	1	1	-1	1	-1	B_1	1	-1	1	-1	1	-1
B_2	1	1	-1	-1	1	B_2	1	-1	1	-1	-1	1
E_1	2	-2	0	0	0	E_1	2	-2	-1	1	0	0
						E_2	2	2	-1	-1	0	0

Figure 3.3: Character tables for the two point groups C_{4v} (left) and C_{6v} (right). The different rows denote the different irreducible representations, the columns label the various classes in each group (see Eq. (3.13)).

trivial row in each character table (see Fig. 3.3). Using the orthogonality of columns and rows according to Eq. (3.14) and (3.15), we can also determine the remaining entries of the character tables illustrated in Fig. 3.3.

In order to decide whether a given representation of a group $\mathcal{G}$ is irreducible, one simply has to compute its characters and see whether these

coincide with a row in the associated character table. If this is not the case, the representation is reducible and there is an equivalent representation where all matrices $M_{red}(g)$ are of the same block structure. Each of these blocks then forms an irreducible representation of the group $\mathcal{G}$, and we can write $M_{red}(g)$ as a direct sum

$$M_{red}(g) = c_1 M_1(g) \oplus c_2 M_2(g) \oplus \cdots c_{n_c} M_{n_c}(g) \qquad (3.16)$$

for all g in $\mathcal{G}$ with

$$c_i = \frac{1}{N} \sum_{q=1}^{n_c} h_q \chi_{red}(g) \chi_q^*(g).$$

The character table therefore allows an efficient way of fully reducing a given representation, and, for example, gives information on crystal field splittings as the irreducible representations of the full rotation group operating on the atomic states is reducible in the lower symmetry subgroup of a crystal structure. This then leads to a splitting of the former degenerate states according to (3.16) with c_i non-degenerate levels which transform with M_i.

Moreover, if we have the character tables for two different groups $\mathcal{G}$ and $\mathcal{K}$, we can easily write down the character table for the direct product $\mathcal{G} \otimes \mathcal{K}$:

$$\chi_{ij}^{\mathcal{G} \otimes \mathcal{K}}(gk) = \chi_i^{\mathcal{G}_1}(g) \chi_j^{\mathcal{G}_2}(k). \qquad (3.17)$$

From this, we can then derive the character tables for $D_{4h} = C_{4v} \otimes C_I$ or $C_{nh} = C_n \otimes C_I$, where C_I is the group consisting only of the identity map and of the space inversion $(x, y, z) \to (-x, -y, -z)$. As an example, we determine the character table of the tetragonal symmetry group D_{4h} in Tab. 3.3.

3.3.1 Basis Functions for Irreducible Representations

As discussed in Sec. 3.2, the particle-particle $\phi = \langle c^\dagger c^\dagger \rangle$ and particle-hole $\phi = \langle c^\dagger c \rangle$ like order-parameter fields can be classified in terms of irreducible
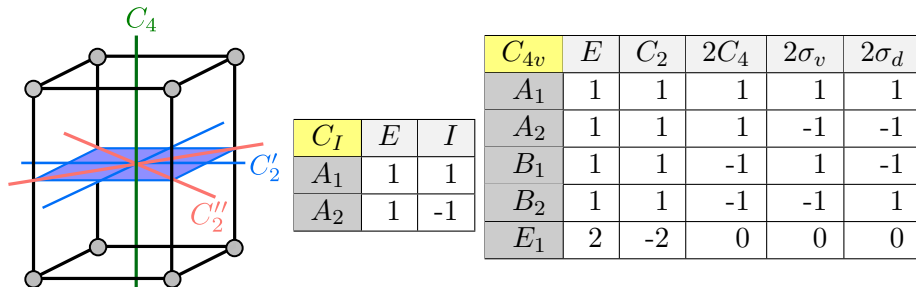

C_I	E	I
A_1	1	1
A_2	1	-1

C_{4v}	E	C_2	$2C_4$	$2\sigma_v$	$2\sigma_d$
A_1	1	1	1	1	1
A_2	1	1	1	-1	-1
B_1	1	1	-1	1	-1
B_2	1	1	-1	-1	1
E_1	2	-2	0	0	0

Figure 3.4: Tetragonal symmetry (left) with one four-fold and four two-fold rotational axes as well as the character tables for the two point groups C_I (middle) and C_{4v} (right).

D_{4h}	E	C_2	$2C_4$	$2\sigma_v$	$2\sigma_d$	I	C_2I	$2C_4I$	$2\sigma_vI$	$2\sigma_dI$
A_{1g}	1	1	1	1	1	1	1	1	1	1
A_{2g}	1	1	1	-1	-1	1	1	1	-1	-1
B_{1g}	1	1	-1	1	-1	1	1	-1	1	-1
B_{2g}	1	1	-1	-1	1	1	1	-1	-1	1
E_g	2	-2	0	0	0	2	-2	0	0	0
A_{1u}	1	1	1	1	1	-1	-1	-1	-1	-1
A_{2u}	1	1	1	-1	-1	-1	-1	-1	1	1
B_{1u}	1	1	-1	1	-1	-1	-1	1	-1	1
B_{2u}	1	1	-1	-1	1	-1	-1	1	1	-1
E_u	2	-2	0	0	0	-2	2	0	0	0

Table 3.3: Character table for the tetragonal symmetry group $D_{4h} = C_{4v} \otimes C_I$ calculated by multiplying the character tables in Fig. 3.4 according to Eq. (3.17). In the literature one often uses the following equivalent notations $\sigma_h = C_2I$, $2S_4 = 2C_4I$, $C_2' = 2\sigma_vI$ and $C_2'' = 2\sigma_dI$. Note that the additional rotational axes C_2' and C_2'' are depicted in Fig. 3.4.

representations of the underlying symmetry group. Separating off the spin part from ϕ, we obtained the following contributions of total spin $S = 1$ and total spin $S = 0$:

$$\langle c^\dagger_{-\boldsymbol{k}\alpha} c^\dagger_{\boldsymbol{k}+\boldsymbol{Q}\beta} \rangle = \Phi_{\boldsymbol{Q}}(\boldsymbol{k})\epsilon_{\alpha\beta}, \qquad \langle c^\dagger_{\boldsymbol{k}\alpha} c_{\boldsymbol{k}+\boldsymbol{Q}\beta} \rangle = \Phi_{\boldsymbol{Q}}(\boldsymbol{k})\delta_{\alpha\beta}$$

$$\langle c^\dagger_{-\boldsymbol{k}\alpha} c^\dagger_{\boldsymbol{k}+\boldsymbol{Q}\beta} \rangle = \left(\vec{\boldsymbol{\Phi}}_{\boldsymbol{Q}}(\boldsymbol{k}) \cdot \widetilde{\boldsymbol{\sigma}} \right)_{\alpha\gamma} \epsilon_{\gamma\beta}, \qquad \langle c^\dagger_{\boldsymbol{k}\alpha} c_{\boldsymbol{k}+\boldsymbol{Q}\beta} \rangle = \left(\vec{\boldsymbol{\Phi}}_{\boldsymbol{Q}}(\boldsymbol{k}) \cdot \boldsymbol{\sigma} \right)_{\alpha\beta}$$

with $\Phi_{\boldsymbol{Q}}$ and the components of $\vec{\boldsymbol{\Phi}}_{\boldsymbol{Q}}$ transforming in the irreducible representation of the space-group that leaves $\boldsymbol{Q}$ invariant (modulo reciprocal lattice vectors). In the following section, we want to demonstrate how to compute all possible basis functions $\Phi_{\boldsymbol{Q}}$ and $\vec{\boldsymbol{\Phi}}_{\boldsymbol{Q}}$ in a systematic way.

First of all, we note that the transformation behavior under lattice translation T is already determined by the center-of-mass momentum $\boldsymbol{Q}$, i.e.

$$T\phi_{\boldsymbol{Q}}(\boldsymbol{k}) = e^{i\boldsymbol{Q}\boldsymbol{r}} \phi_{\boldsymbol{Q}}(\boldsymbol{k}),$$

and it is therefore sufficient to derive the basis functions only for the lattice point-group that leaves $\boldsymbol{Q}$ invariant modulo reciprocal lattice vectors. For this purpose, we consider the real-space representation

$$\phi(r_1, r_2) = \sum_{\boldsymbol{k}} \phi_{\boldsymbol{Q}}(\boldsymbol{k}) \exp(i\boldsymbol{k}(r_1 - r_2)),$$

with $\phi_{\boldsymbol{Q}}(\boldsymbol{k})$ used in place of $\Phi_{\boldsymbol{Q}}$ and in place of the components of $\vec{\boldsymbol{\Phi}}_{\boldsymbol{Q}}$. In order to construct wave functions $\phi(r_1, r_2)$ that transform as an irreducible representation of the point-group, we make use of a fundamental projection theorem stating that the operator

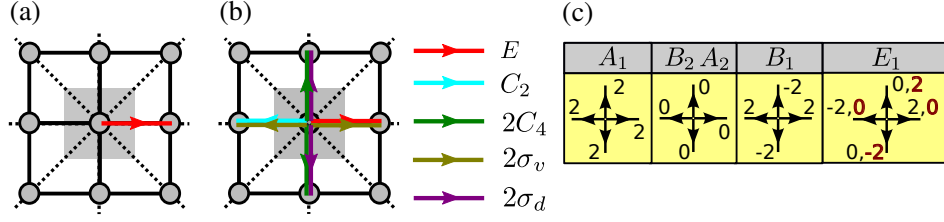$$\mathcal{P}(\Gamma_i) = \sum_g \chi_i^*(g) g \qquad (3.18)$$

Figure 3.5: Projection method for the nearest-neighbor basis functions $\phi(r_i, r_j)$ on the square lattice with C_{4v} symmetry. Starting with a nearest-neighbor bond (a), we obtain the bond structure in (b) with indicated color coding, and, if we assign the complex-conjugated characters according to Table 3.3, we end up with the real-space functions $\phi(r_i, r_j)$ in (c). The black and red numbers in the representation E_1 of (c) correspond to the two required basis functions.

projects out the contribution which transforms in the i-th irreducible representation Γ_i. Here, the sum runs over all point-group operations g with the corresponding complex-conjugate characters $\chi_i^*(g)$. Let us now apply this result to the simplest case of a square lattice with point-group C_{4v} and project out the contributions in Γ_i from the trial wave function given by

$$\phi^{start}(r_i, r_j) = 1\delta_{i,i+x}. \tag{3.19}$$

The trial wave function ϕ^{start} is apparently nonzero only for nearest-neighbor bonds in x-direction as indicated in Fig. 3.5a. Using the characters of Tab. 3.3, we then apply the projection operator (3.18) to ϕ^{start} and obtain the following nearest-neighbor basis function for the trivial representation A_1:

$$\begin{aligned}
\mathcal{P}(A_1)\phi^{start} &= \chi_i^*(E)\delta_{i,i+x} + \chi_i^*(C_2)\delta_{i,i-x} + \chi_i^*(C_4)\delta_{i,i+y} + \chi_i^*(C_4^{-1})\delta_{i,i-y} \\
&+ \chi_i^*(\sigma_v^1)\delta_{i,i+x} + \chi_i^*(\sigma_v^2)\delta_{i,i-x} + \chi_i^*(\sigma_d^2)\delta_{i,i+y} + \chi_i^*(\sigma_d^1)\delta_{i,i-y} \\
&= 2\delta_{i,i+x} + 2\delta_{i,i-x} + 2\delta_{i,i+y} + 2\delta_{i,i-y}. \tag{3.20}
\end{aligned}$$

Repeating this procedure with the characters of the 4 other representations A_2, B_1, B_2 and E_2 (see Tab. 3.3), we obtain the remaining basis functions as depicted in Fig. 3.5c. Here, it turns out that the basis function in B_2 and A_2 vanish for nearest-neighbor bonds. In the case of the two dimensional representation E_1, a single basis function is not sufficient, and we have to apply the projection to another linear independent trial wave functions, for example $\phi^{start}(r_i, r_j) = 1\delta_{i,i+y}$, which then provides the two black and red colored wave functions of Fig. 3.5:

$$\phi_1^{E_1}(r_i, r_j) = \delta_{i,i+x} - \delta_{i,i-x}, \quad \phi_2^{E_1}(r_i, r_j) = \delta_{i,i+y} - \delta_{i,i-y}.$$

Iterating this process for longer-ranged bonds and transforming back to $\boldsymbol{k}$-space, we obtain a complete set of basis functions shown below for up to fourth nearest-neighbors:

$$\phi^{A_1}(\boldsymbol{k}): \; \cos(k_x) + \cos(k_y), \cos(k_x)\cos(k_y), \cos(2k_x) + \cos(2k_y),$$

$$\cos(k_x)\cos(2k_y) + \cos(2k_x)\cos(k_y), \ldots$$

$$\phi^{A_2}(\boldsymbol{k}) : 0, 0, 0, \sin(k_x)\sin(2k_y) - \sin(2k_x)\sin(k_y), \ldots$$

$$\phi^{B_1}(\boldsymbol{k}) : \cos(k_x) - \cos(k_y), 0, \cos(2k_x) - \cos(2k_y),$$

$$\cos(2k_x)\cos(k_y) - \cos(k_x)\cos(2k_y), \ldots$$

$$\phi^{B_2}(\boldsymbol{k}) : 0, \sin(k_x)\sin(k_y), 0, \sin(2k_x)\sin(k_y) + \sin(k_x)\sin(2k_y), \ldots$$

$$\phi^{E_1}_1(\boldsymbol{k}) : \sin(k_x), \sin(k_x + k_y), \sin(2k_x), \sin(2k_x + k_y), \ldots$$

$$\phi^{E_1}_2(\boldsymbol{k}) : \sin(k_y), \sin(-k_x + k_y), \sin(2k_y), \sin(-k_x + 2k_y), \ldots.$$

The above basis functions hold for all particle-particle and particle-hole like order-parameter fields on the square lattice where the center-of-mass momentum $\boldsymbol{Q}$ is also invariant under C_{4v}, as it is the case for $Q = (0,0)$ and $Q = (\pi, \pi)$. On the other hand, for $\boldsymbol{Q} = (0, \pi)$, we have to use the characters of the C_{2v} group since the rotated momentum $\boldsymbol{Q} = (\pi, 0)$ cannot be connected through reciprocal lattice vectors. It is further important to note that in the particle-particle case, the exchange symmetry requires the spin part of the E_1 representation to be of spin-triplet type, whereas all other representations have to be of spin-singlet structure.

The described projection scheme of course works out for all kind of lattice geometries, and for the triangular lattice we then obtain the following nearest-neighbor basis functions (see Fig. 3.6):
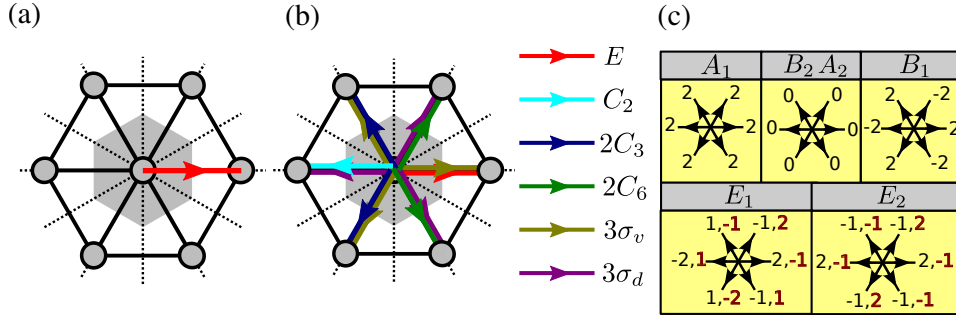
Figure 3.6: Nearest-neighbor basis functions as in Fig. 3.5 for the triangular lattice with C_{6v} symmetry.

$$\phi^{A_1}(\boldsymbol{k}) : \cos((k_x + \sqrt{3}k_y)/2) + \cos((k_x - \sqrt{3}k_y)/2) + \cos(k_x/2), \ldots$$

$$\phi^{A_2}(\boldsymbol{k}) : 0, \ldots$$

$$\phi^{B_1}(\boldsymbol{k}) : \sin(k_x/2)(1 - 2\cos(\sqrt{3}k_y/2)), \ldots$$

$$\phi^{E_1}_1(\boldsymbol{k}) : -2\cos(k_x/2)\cos(\sqrt{3}k_y/2) + 2\sin(k_x), \ldots$$

$$\phi^{E_1}_2(\boldsymbol{k}) : 3\cos(k_x/2)\cos(\sqrt{3}k_y/2) + \sin(k_x/2)\sin(\sqrt{3}k_y/2) - \sin(k_x), \ldots$$

$$\phi^{E_2}_1(\boldsymbol{k}) : 2\cos(k_x) - \cos((k_x + \sqrt{3}k_y)/2) - \cos((k_x - \sqrt{3}k_y)/2), \ldots$$

$$\phi^{E_2}_2(\boldsymbol{k}) : -\cos(k_x) + 2\cos((k_x + \sqrt{3}k_y)/2) - \cos((k_x - \sqrt{3}k_y)/2) \ldots \quad .$$

In multi-orbital or multi-sublattice systems, the above symmetry classification is more intricate since here the orbital or lattice degrees of freedom itself transform under point-group operations. For instance, in the honeycomb lattice with a C_{6v} point-group symmetry, sublattice A is mapped to B under $\pi/3$-rotation, and the characterizing symmetry of the order-parameter field apparently depends on its internal orbital structure. For the intra-orbital case $\langle c^{\dagger}_{-\boldsymbol{k}A\alpha} c^{\dagger}_{\boldsymbol{k}A\beta} \rangle$ and $\langle c^{\dagger}_{-\boldsymbol{k}B\alpha} c^{\dagger}_{\boldsymbol{k}B\beta} \rangle$, we depicted the nearest-neighbor pairing amplitudes in Fig. 3.7c. Here, it is important to note that the A_1, B_1 as well as A_2, B_2 and E_1, E_2 representations only differ by a relative sign between the two different sublattices. In addition, it also turns out that the spin structure in E_1, E_2 is not determined and therefore contains both a spin-singlet and triplet representation as indicated by the upper and lower signs in Fig. 3.7c.
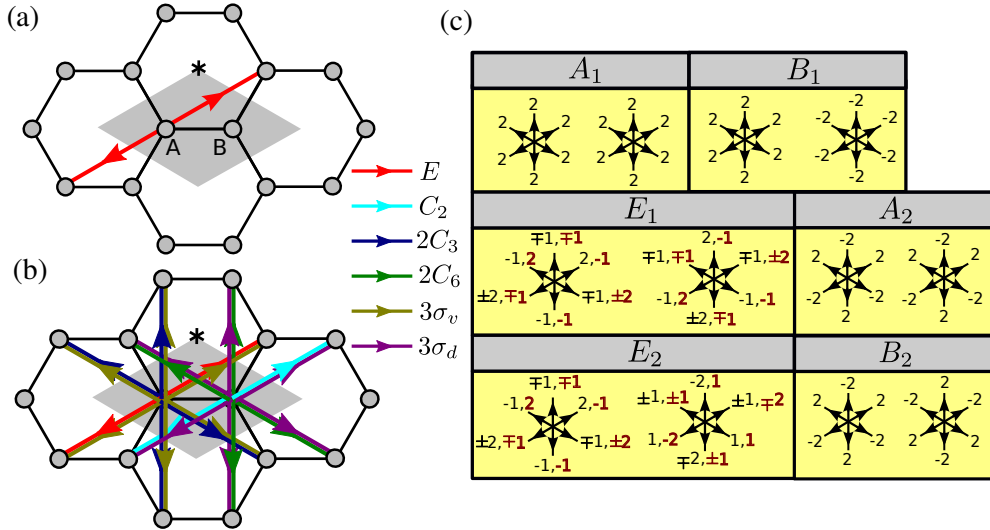
Figure 3.7: Projection method to obtain the nearest-neighbor pairing wave functions $\phi_{AA}(r_i, r_j)$ and $\phi_{BB}(r_i, r_j)$ on the honeycomb lattice. Upper and lower signs in E_1, E_2 denote the corresponding spin-singlet and spin-triplet realizations. The representations A_1, B_1 as well as A_2, B_2 and E_1, E_2 in (c) only differ by a relative sign between the two sublattices A (left) and B (right).

3.4   Spin-Orbit Coupling

In the following section, we study the effect of spin-orbit coupling on the symmetry classification of particle-particle and particle-hole like order-parameter fields. In an intuitive description, the atomic spin-orbit coupling arises from the moving electrons that effectively perceive a magnetic field $\boldsymbol{B}$ within the positively charged ion environment. The coupling between $\boldsymbol{B}$-field in the rest frame of the electrons and their intrinsic spin $\boldsymbol{S}$ then leads

to the coupling term

$$H_{LS} = -\boldsymbol{\mu} \cdot \boldsymbol{B} \sim \boldsymbol{S} \cdot (\boldsymbol{v} \times \boldsymbol{E}) \sim \boldsymbol{S} \cdot (\boldsymbol{v} \times \frac{\boldsymbol{r}}{r}) \sim \boldsymbol{L} \cdot \boldsymbol{S}. \qquad (3.21)$$

If H_{LS} is taken into account, the generators $\boldsymbol{L}$ and $\boldsymbol{S}$ of rotation in spatial- and spin-coordinates do no longer commute with the Hamiltonian, and the corresponding individual symmetries are broken. However, the sum of both $\boldsymbol{J} = \boldsymbol{L} + \boldsymbol{S}$ still commutes with the Hamiltonian and generates a combined rotation in spin and coordinate space. Therefore, each rotation in coordinate space must also rotate the spin in order to present a symmetry of our theory. On the other hand, the spin-orbit coupling (3.21) respects both time- (K) and space-inversion (I) symmetry, and the one-particle spectrum is still fourfold degenerate with eigenstates $|\boldsymbol{k}, a\rangle, |\boldsymbol{k}, b\rangle$ and $|-\boldsymbol{k}, a\rangle, |-\boldsymbol{k}, b\rangle$. Here, the labeling a, b does not corresponds to definite spin-projections but instead describes superpositions of both spin-states:

$$|\boldsymbol{k}, a\rangle = u_{\boldsymbol{k},a}(\boldsymbol{k})|\boldsymbol{k}, \uparrow\rangle + v_{\boldsymbol{k},a}|\boldsymbol{k}, \downarrow\rangle$$
$$|\boldsymbol{k}, b\rangle = u_{\boldsymbol{k},b}(\boldsymbol{k})|\boldsymbol{k}, \uparrow\rangle + v_{\boldsymbol{k},b}|\boldsymbol{k}, \downarrow\rangle.$$

It is further important to note that the labeling a, b was ascribed arbitrarily but can be chosen in way that both states $|\boldsymbol{k}, a\rangle, |\boldsymbol{k}, b\rangle$ have a similar transformation behavior as the original states $|k, \uparrow\rangle, |k, \downarrow\rangle$. Therefore, we start with a minimal subset of $\boldsymbol{k}$-points not related by symmetries and define $(\uparrow \longrightarrow a, \downarrow \longrightarrow b)$ by adiabatically switching on the spin-orbit coupling [26]. Then, we simply define the remaining ones according to

$$|-\boldsymbol{k}, b\rangle = K|\boldsymbol{k}, a\rangle, \quad |-\boldsymbol{k}, a\rangle = I|\boldsymbol{k}, a\rangle \quad |\boldsymbol{k}, b\rangle = KI|\boldsymbol{k}, a\rangle \qquad (3.22)$$

and

$$g_p|\boldsymbol{k}, \gamma\rangle = \sum_{\gamma'} (D_{1/2}^+(g_p))_{\gamma\gamma'} \cdot |D^-(g_p)\boldsymbol{k}, \gamma'\rangle \quad \gamma, \gamma' = a \text{ or } b. \qquad (3.23)$$

Here, $D^-(g_p)$ and $D_{1/2}^+(g_p)$ denote the $\boldsymbol{k}$-space and spin one-half representations of the point-group operation g_p. Up to the linking of rotation in spatial- and spin-coordinates, the transformation properties (3.22) and (3.23) are formally identical to the case of vanishing spin-orbit coupling. Similar to the classification of particle-particle and particle-hole condensates in Sec. 3.2, the order-parameter fields in the new so-called pseudospin basis $|\boldsymbol{k}, a\rangle = c_{\boldsymbol{k}a}^\dagger|0\rangle, |\boldsymbol{k}, b\rangle = c_{\boldsymbol{k}b}^\dagger|0\rangle$ can likewise be decomposed into spin-singlet and spin-triplet parts

$$\langle c_{-\boldsymbol{k}a}^\dagger c_{\boldsymbol{k}+\boldsymbol{Q}b}^\dagger \rangle = \Phi_{\boldsymbol{Q}}(\boldsymbol{k})\epsilon_{ab}, \qquad \langle c_{\boldsymbol{k}a}^\dagger c_{\boldsymbol{k}+\boldsymbol{Q}b}\rangle = \Phi_{\boldsymbol{Q}}(\boldsymbol{k})\delta_{ab}$$

$$\langle c_{-\boldsymbol{k}a}^\dagger c_{\boldsymbol{k}+\boldsymbol{Q}b}^\dagger \rangle = \left(\vec{\boldsymbol{\Phi}}_{\boldsymbol{Q}}(\boldsymbol{k}) \cdot \widetilde{\boldsymbol{\sigma}}\right)_{ac} \epsilon_{cb} \qquad \langle c_{\boldsymbol{k}a}^\dagger c_{\boldsymbol{k}+\boldsymbol{Q}b}\rangle = \left(\vec{\boldsymbol{\Phi}}_{\boldsymbol{Q}}(\boldsymbol{k}) \cdot \boldsymbol{\sigma}\right)_{ab}.$$

The difference here consists in the transformation behavior of the triplet basis function $\vec{\Phi}_Q(\boldsymbol{k})$ which, according to (3.23), transforms in a spin-one representation of the respective point-group element g_p. Therefore, in the case of spin-orbit coupling, the transformation g_p not only affects the individual entries of $\vec{\Phi}_Q$ but also rotates the vector itself.

In the superconducting case, the gap-function $\hat{\Delta}_{\boldsymbol{k}}$ in (3.2) transforms in the same way as $\phi_{ab}(\boldsymbol{k})_{ls} = \langle c^{\dagger}_{-\boldsymbol{k}a} c^{\dagger}_{\boldsymbol{k}b} \rangle$. The associated pseudospin-singlet and triplet contributions of $\hat{\Delta}_{\boldsymbol{k}}$ can therefore be separated into

$$
\text{even parity}: \quad \hat{\Delta}_{\boldsymbol{k}} = \delta_0^0(\boldsymbol{k})(|ab\rangle - |ba\rangle)
$$
$$
= \begin{pmatrix} 0 & \delta_0^0(\boldsymbol{k}) \\ -\delta_0^0(\boldsymbol{k}) & 0 \end{pmatrix} = i\sigma_y \psi(\boldsymbol{k}) \tag{3.24}
$$

$$
\text{odd parity}: \quad \hat{\Delta}_{\boldsymbol{k}} = \delta_{-1}^1(\boldsymbol{k})|bb\rangle + \delta_0^1(\boldsymbol{k})(|ab\rangle + |ba\rangle) + \delta_1^1(\boldsymbol{k})|aa\rangle
$$
$$
= \begin{pmatrix} \delta_1^1(\boldsymbol{k}) & \delta_0^1(\boldsymbol{k}) \\ \delta_0^1(\boldsymbol{k}) & \delta_{-1}^1(\boldsymbol{k}) \end{pmatrix} = i\left(\boldsymbol{d}(\boldsymbol{k}) \cdot \boldsymbol{\sigma}\right)\sigma_y, \tag{3.25}
$$

which is again formally identical to the case of vanishing spin-orbit coupling in (3.9) and (3.10). In addition, the transformation behavior of the gap-functions is also similar to the one of Tab. 3.1, up to the combined transformation of spin- and spatial-coordinates under point-group operations. On

transformation	even parity	odd parity
space inversion	$I\psi(\boldsymbol{k}) = \psi(-\boldsymbol{k})$	$I\boldsymbol{d}(\boldsymbol{k}) = -\boldsymbol{d}(-\boldsymbol{k})$
time inversion	$K\psi(\boldsymbol{k}) = \psi^*(\boldsymbol{k})$	$K\boldsymbol{d}(\boldsymbol{k}) = \boldsymbol{d}^*(\boldsymbol{k})$
point group	$g_p\psi(\boldsymbol{k}) = \psi(D^-(g_p)\boldsymbol{k})$	$g_p\boldsymbol{d}(\boldsymbol{k}) = D^+(g_p)\boldsymbol{d}(D^-(g_p)\boldsymbol{k})$

Table 3.4: Transformation behavior of the pseudospin singlet and triplet gap function.

the other hand, without spin-orbit coupling all entries in the $\boldsymbol{d}$-vector gap function could be chosen independently and, in an m-dimensional representation of a point-group Γ, one then obtains a $3m$-fold degeneracy of possible gap symmetries, all having the same T_c by symmetry. Yet, if spin-rotational symmetry is broken due to spin-orbit coupling, the $\boldsymbol{d}$-vector also rotates under point-group operations and the degeneracy is lifted. As an example, which will be of relevance in Chap. 6, we consider the p-wave pairing on the square lattice (C_{4v}) with a non-negligible spin-orbit coupling. As apparent from the character table in (3.1), the $\boldsymbol{d}$-vector transforms as an axial vector which means $\boldsymbol{d} \sim (E_1 \oplus A_2)$ (see Tab. 3.3), and the entries for p-wave pairing transform itself in the E_1 representation. Altogether, the complete $\boldsymbol{d}$-vector transforms in the following reduced product representation

$$
E_1 \otimes (E_1 \oplus A_2) = A_1 \oplus A_2 \oplus B_1 \oplus B_2 \oplus E_1, \tag{3.26}
$$

and the former six-dimensional degeneracy now splits in four one- and one two-dimensional irreducible representation. Note that the identity (3.26) can be easily determined by applying the results (3.16) in the introductory section on representation theory or by looking up the product tables of C_{4v}. In the nearest-neighbor realization, we then obtain the following table shown in Tab. 3.5, and, by using exactly the same procedure as in section 3.3, we

no spin-orbit	with spin-orbit coupling
	$\boldsymbol{d}^{A_1}(\boldsymbol{k}) = \hat{\boldsymbol{x}}\sin(k_x) + \hat{\boldsymbol{y}}\sin(k_y)$
$\boldsymbol{d}_1(\boldsymbol{k}) = \hat{\boldsymbol{x}}\sin(k_x), \boldsymbol{d}_2(\boldsymbol{k}) = \hat{\boldsymbol{x}}\sin(k_y)$	$\boldsymbol{d}^{A_2}(\boldsymbol{k}) = \hat{\boldsymbol{x}}\sin(k_y) - \hat{\boldsymbol{y}}\sin(k_x)$
$\boldsymbol{d}_3(\boldsymbol{k}) = \hat{\boldsymbol{y}}\sin(k_x), \boldsymbol{d}_4(\boldsymbol{k}) = \hat{\boldsymbol{y}}\sin(k_y)$	$\boldsymbol{d}^{B_1}(\boldsymbol{k}) = \hat{\boldsymbol{x}}\sin(k_x) - \hat{\boldsymbol{y}}\sin(k_y)$
$\boldsymbol{d}_5(\boldsymbol{k}) = \hat{\boldsymbol{z}}\sin(k_x), \boldsymbol{d}_6(\boldsymbol{k}) = \hat{\boldsymbol{z}}\sin(k_y)$	$\boldsymbol{d}^{B_2}(\boldsymbol{k}) = \hat{\boldsymbol{x}}\sin(k_y) + \hat{\boldsymbol{y}}\sin(k_x)$
	$\boldsymbol{d}_1^{E_1}(\boldsymbol{k}) = \hat{\boldsymbol{z}}\sin(k_x), \boldsymbol{d}_2^{E_1}(\boldsymbol{k}) = \hat{\boldsymbol{z}}\sin(k_x)$

Table 3.5: Next-nearest neighbor p-wave gap symmetries on the square lattice with the $\boldsymbol{d}$-vector lying in the linear span of the three unit-vectors $\hat{\boldsymbol{x}}$, $\hat{\boldsymbol{y}}$, $\hat{\boldsymbol{z}}$. By switching on the spin-orbit coupling, the six-dimensional degeneracy is lifted to four one- and one two-dimensional representations.

can also derive the superconducting form factors for all other representations. In the pseudospin-singlet case the form factors or gap functions in a specific representation of the underlying lattice remain the same as in (3.19) and (3.20). However, for triplet-pairing one has to start with an arbitrary vector instead of a scalar and project out the contribution that transforms in the required representation:

$$\boldsymbol{d}^{start}(i,j) = \hat{\boldsymbol{x}} \implies \boldsymbol{d}(i,j) = \sum_{g \in \mathcal{G}} \chi_i^*(g) D^+(g)\hat{\boldsymbol{x}}.$$

Here, the sum runs over all elements in the point-group and $\chi_i^*(g)$ again denotes the complex-conjugate of the corresponding character in the i-th irreducible representation. The initial vector then transforms as an axial vector which is indicated by the matrix $D^+(g)$, i.e. it transforms like a vector but with an additional sign for any type of reflection. Of course, one has to be aware that one does not end up with the trivial form $\boldsymbol{d}(i,j) = \boldsymbol{0}$ which would require a different starting point. Transforming back to $\boldsymbol{k}$-space we then obtain the gap form-factors shown in Tab. 3.5 for the nearest-neighbor case.

3.5   Probing the Pairing Symmetry

In the following section, we discuss various experimental methods to identify the pairing symmetry and to trace back to the underlying pairing mechanism. Of course, there is a huge number of highly sophisticated experiments in this field, and we therefore give only a rough overview in order to compare

our later results with recent experimental findings. In general, one can distinguish between the following types of experiments, of which the mentioned ones are described in more detail below:

- experimental methods that indicate the spin structure of the Cooper pairs (Knight-shift measurements)

- methods that provide informations on the one-particle excitation spectrum (ARPES, specific heat measurements, NMR)

- experimental probes that resolve the phase difference in $\Delta_{\boldsymbol{k}}$ between certain $\boldsymbol{k}$-points (SQUID measurements, quasi-particle interference, neutron scattering).

Specific heat measurements:

The specific heat C indicates the variation of internal energy U as a function of temperature T, i.e. $C = \partial U / \partial T$. Commonly, a solid-state system exhibits various contributions to the specific heat related to the various excitation possibilities as for example by phonons, electrons or collective modes. However, we are mainly interested in the electronic contributions as the electronic one-particle spectrum $E(\boldsymbol{k})$ is most directly affected through the opening of a superconducting gap. If one then calculates the internal-energy contribution of the quasi-particle excitations as a function of temperature, one obtains the following expression for the specific heat at low temperatures $T \ll T_c$ [20]:

$$ C_S = \sum_{\boldsymbol{k},s} E(\boldsymbol{k}) \frac{\partial}{\partial T} (n_F(E(\boldsymbol{k}))) \propto \begin{cases} e^{-\Delta_0/T} & \text{fully gapped} \\ T^2, T^3 & \text{line/point nodes} \\ T & \text{gapless} \end{cases} . $$

Hence, the low-temperature behavior of the specific heat provides valuable informations on the existence of nodes and also its dimensionality. In order to locate the position of the nodes or gap minima, one can further apply an additional magnetic field and study the specific heat as function of field direction. The idea here is the following: if the magnetic-field penetrates through the superconducting sample via vortices, there is a supercurrent of condensate orbiting each vortex in a perpendicular plane. Due to this supercurrent of velocity $\boldsymbol{v}_s$, the quasi-particle spectrum in this region is Doppler-shifted [27]:

$$ E(\boldsymbol{k}) \to E(\boldsymbol{k}) + \boldsymbol{k} \cdot \boldsymbol{v}_s. $$

Therefore, the magnetic field allows to shift the quasi-particle spectrum at certain $\boldsymbol{k}$-points and, thus, enables to draw conclusions on the position of nodes and gap minima. Of course, this is only a simplified semiclassical view to a very intricate phenomena, but it already provides a basic understanding of the idea behind angle-resolved specific heat measurements [28].

Nuclear Magnetic Resonance (NMR):

A second experimental method which provides informations on the quasi-particle spectrum of the superconducting state is the nuclear magnetic resonance (NMR). Here, an external magnetic field splits the nuclear energy levels, and an additional high-frequency field excites these nuclear states to higher energy levels. After switching off this high-frequency field, the electrons in the sample interact with the nuclei and enable its relaxation back to the original state. The corresponding relaxation-time T_1 then measures the efficiency of the energy transfer from the nuclei to the electrons and provides valuable insights into the electronic properties of the sample. Another quantity also accessible in NMR experiments is the so-called Knight shift K describing the variation of the nuclear level-splitting due to an interaction with the electronic environment. From both quantities, the relaxation time T_1 and the Knight-shift K, one can trace back to the nature of the pairing state. At the same time, the NMR method bears several useful advantages as it really measures the bulk properties of the system and does neither rely on the sample size nor requires sample contacts. On the other hand, due to the Meissner effect, it may be problematic to achieve relatively high magnetic fields which penetrate the sample and which do not destroy superconductivity.

In order to derive a formal expression of the relaxation time T_1 and the Knight-Shift K, we now follow the calculation of T. Moriya in [29]. Here, one starts with a hyperfine-coupling term $H_{nf} \sim \boldsymbol{I} \cdot \boldsymbol{S}$ of the nuclear $\boldsymbol{I}$ and electron spin $\boldsymbol{S}$ and determines the transition rate via:

$$W_{n \to n'} \sim \sum_{ee'} p(e) |\langle n'e'|H_{nf}|en \rangle|^2 \delta(E_e + E_n - E_{e'} - E_{n'}).$$

Here, $\langle n'e'|$ denotes the combined many-body state of electrons and nuclei. As the transition rate $W_{n \to n'}$ contains a spin $\boldsymbol{S}$ squared term, the relaxation-time T_1 then has the following form containing the spin susceptibility χ:

$$\frac{1}{T_1} = W_{n \to n'} \sim T \sum_{\boldsymbol{q}} \frac{\text{Im}\chi(\boldsymbol{q},\omega)}{\omega} \sim \int dE \left(\frac{dn_F(E)}{dE} \right) N(E)^2 \qquad (3.27)$$

$$\overset{T \ll T_c}{\propto} \begin{cases} e^{-\Delta_0/T} & \text{fully gapped} \\ T^3, T^5 & \text{line/point nodes} \\ T & \text{gapless} \end{cases} \qquad (3.28)$$

One of the most prominent features in the relaxation-rate measurements is the so-called Hebel-Schlichter peak [30] which describes a cusp in $1/T_1$ directly at the superconducting transition. This behavior can in turn be explained very well by (3.27) and the coherence peak in the density of states of an isotropically gapped superconductor [3].

For the discussion of the Knight shift measurements, we first note that the level-splitting $\Delta\omega$ of an isolated nucleus is proportional to the applied field strength $\Delta\omega = \gamma H$. Within the electronic environment, the splitting $\Delta\omega$ is then modified by the so-called Knight-shift K which is proportional to the paramagnetic susceptibility of the electrons $\chi(\boldsymbol{q} = 0, \omega = 0)$. However, in the superconducting state, there is a crucial difference between spin-triplet and spin-singlet pairs as the latter are totally oblivious to magnetic-fields and do not contribute to the spin-susceptibility. On the other hand, in a spin-triplet superconductor, the Cooper-pairs can be polarized if their spin is not restricted to lie perpendicular to the applied field H, which is in turn equivalent to $\boldsymbol{d} \parallel H$. Therefore, the temperature dependent Knight-shift reads as

$$
K(T) \sim 2\mu_B^2 N_0 \cdot \begin{cases} 1 & \text{for } \boldsymbol{d}(\boldsymbol{k}) \perp H \\ \int dE \frac{\partial n_F(E)}{\partial E} N(E) & \text{for singlet pairing or } \boldsymbol{d}(\boldsymbol{k}) \parallel H \end{cases}
$$

and thus reveals the spin state of the paired electrons.

Angle-resolved photoemission spectroscopy (ARPES):

One of the most direct methods to probe the momentum and energy dependent electronic spectrum is the so-called angle-resolved photoemission spectroscopy (ARPES). Here, one measures the kinetic-energy and angular distribution of photoemitted electrons from a solid-state system, which then provides informations on the electronic dispersion within the sample. In a formal description of the photoemission process, one approximates the transition-probability by Fermi's golden rule:

$$
w_{fi} \propto |\langle \Psi_f^N | \boldsymbol{A} \cdot \boldsymbol{p} | \Psi_i^N \rangle|^2 \delta(E_f^N - E_i^N - h\nu), \tag{3.29}
$$

where we already employed the so-called dipole approach ($\nabla \cdot \boldsymbol{A} = 0$) and neglected the quadratic term $\boldsymbol{A}^2$ contained in the original kinetic term ($H \propto (\boldsymbol{p} + e\boldsymbol{A})^2$). In Eq. (3.29), the initial- and final-states of the N-electron system are denoted by Ψ_i^N and Ψ_f^N with the respective energies E_f^N and E_i^N. The energy of the incident photon is further given by $E_{ph} = h\nu$. Under certain assumptions (see Damascelli *et al.* [31] for details), we can express the initial- and final-states in (3.29) by the following antisymmetrized product

$$
\begin{aligned}
\Psi_i^N &= \phi_i^{\boldsymbol{k}} \Psi_i^{N-1} \\
\Psi_f^N &= \phi_f^{\boldsymbol{k}} \Psi_f^{N-1} = \phi_f^{\boldsymbol{k}} \sum_m \Psi_m^{N-1},
\end{aligned} \tag{3.30}
$$

with $\phi_f^{\boldsymbol{k}}$ describing the photoemitted electron and $\phi_i^{\boldsymbol{k}}$ the one-electron state inside the sample. Note that in (3.30), we expanded the remaining $(N-1)$-particle part in energy eigenstates and, by using the standard definition for
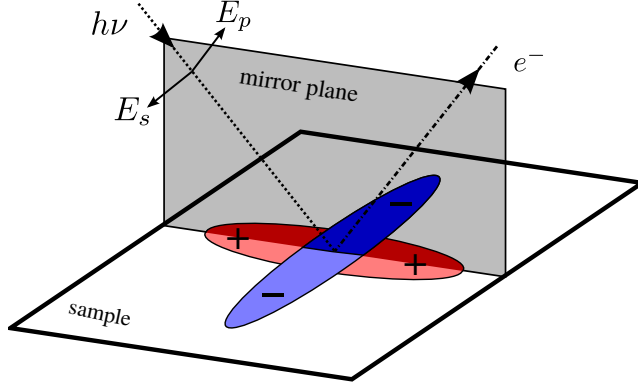
Figure 3.8: Experimental setup to extract the electronic dispersion of one-particle states with even ($\boldsymbol{A}$ in-plane) and odd ($\boldsymbol{A}$ normal to the mirror plane) reflection symmetry with respect to a mirror plane of the sample. In order to extract the parity of the electronic states, both incident photon and emitted electron have to lie within that mirror plane.

the spectral-function $A(\boldsymbol{k}, \omega)$ (see e.g. [32]), the ARPES intensity at $T = 0$ reads as

$$
\begin{aligned}
I(\boldsymbol{k}, \omega) &= \sum_{fi} w_{fi} = \sum_{fi} |\langle \phi_i^{\boldsymbol{k}} | \boldsymbol{A} \cdot \boldsymbol{p} | \phi_f^{\boldsymbol{k}} \rangle|^2 \sum_m |\langle \Psi_i^{N-1} | \Psi_m^{N-1} \rangle|^2 \delta(E_f^N - E_i^N - h\nu) \\
&= \sum_{fi} |\langle \phi_i^{\boldsymbol{k}} | \boldsymbol{A} \cdot \boldsymbol{p} | \phi_f^{\boldsymbol{k}} \rangle|^2 \sum_m |\langle \Psi_m^{N-1} | c_{\boldsymbol{k}} | \Psi_i^N \rangle|^2 \delta(\omega - E_m^{N-1} + E_i^N) \\
&= \sum_{fi} |M_{fi}(\boldsymbol{k})|^2 A(\boldsymbol{k}, \omega) \qquad\qquad\qquad\qquad\qquad\qquad (3.31)
\end{aligned}
$$

with matrix elements $M_{fi}(\boldsymbol{k}) = \langle \phi_i^{\boldsymbol{k}} | \boldsymbol{A} \cdot \boldsymbol{p} | \phi_f^{\boldsymbol{k}} \rangle$. Measuring the kinetic-energy and angular distribution of the emitted electrons $I(\boldsymbol{k}, \omega)$, one can therefore trace back to the $\boldsymbol{k}$- and ω-resolved spectral density $A(\boldsymbol{k}, \omega)$ and with that also to the superconducting gap. Despite the relatively small superconducting gap amplitude of a few meV, this is still possible by using state-of-the-art ARPES techniques with energy resolutions of $\Delta E \approx 2meV$. Moreover, by varying the photon polarization, one can also derive the orbital content of the electronic band structure, which is in turn essential for the correct modeling of multi-orbital systems. For this purpose, the incident photon and the emitted electron have to lie within a mirror plane of the sample (see Fig. 3.8). Then, in order to measure a finite ARPES intensity $I(\boldsymbol{k}, \omega)$, the matrix element $M_{fi}(\boldsymbol{k})$ in (3.31) has to be even with respect to that mirror plane. Moreover, as an odd final state $\phi_f^{\boldsymbol{k}}$ of the photoelectron would be zero on the entire mirror plane, it is also required to be of even symmetry. Therefore, $\phi_i^{\boldsymbol{k}}$ and $\boldsymbol{A} \cdot \boldsymbol{p}$ must have the same parity under mirror plane reflection in order to guarantee the evenness of the entire matrix element $M_{fi}(\boldsymbol{k}) = \langle \phi_i^{\boldsymbol{k}} | \boldsymbol{A} \cdot \boldsymbol{p} | \phi_f^{\boldsymbol{k}} \rangle$. For example, if $\phi_i^{\boldsymbol{k}}$ is even (odd), $\boldsymbol{A}$ has to lie within (normal to) the mirror plane. Thus, by changing the polarization of

the incident photon beam, one can extract the reflection properties of the one-particle state $\phi_i^{\boldsymbol{k}}$, which is in turn characterized by the orbital content of the electronic band structure. For details on that symmetry analysis in the context of iron-based superconductors, we refer to Brouet *et al.* [33].

In order to measure the out-of-plane electronic dispersion, one should also mention that the momentum $\boldsymbol{k}_\perp$ perpendicular to the sample surface is apparently not conserved, and one needs additional informations (see [31]) to deduce the $\boldsymbol{k}_\perp$-dependent electronic band structure.

Phase-sensitive probes (SQUID devices and π-junctions):

The experiments discussed in the previous sections were only sensitive to the magnitude of the superconducting gap or to the mere existence of gap nodes. However, without resolving the gap phase it is not possible to unambiguously determine the complex gap function and to pin down the underlying pairing mechanism. In the following, we want to review some of the experimental techniques which also allow for a direct observation of the gap-phase, the so-called phase-sensitive probes. One of the first implementation was realized by the so-called SQUID devices of Wollman *et al.* [34], which resolved the directional-dependent sign-change in the $d_{x^2-y^2}$-pairing state of the cuprate YBCO. Here, a conventional superconductor is linked to YBCO by means of two Josephson junctions $1, 2$ such that the corresponding loop encircles a magnetic flux Φ as depicted in Fig. 3.9. By varying the flux Φ, the maximal dissipationless current I_c^S (critical current) through the device features a characteristic interference pattern, from which the relative phase difference of the superconducting gap can be inferred. In a quantitative description one assumes that the resulting supercurrent along a closed path C deep inside the superconducting device vanishes [35] and, by integrating along such a curve C, one obtains the following relation between the gap phase ϕ and the magnetic flux Φ:

$$0 = \oint_C \boldsymbol{j} \cdot d\boldsymbol{s} \propto \oint_C \{\boldsymbol{\nabla}\phi - 2e\boldsymbol{A}\} \cdot d\boldsymbol{s} = (\Delta\phi_1 + \delta\phi - \Delta\phi_2 + 2n\pi) - 2\pi\frac{\Phi}{\Phi_0}. \quad (3.32)$$

Here, $\Delta\phi_{i=1,2}$ denotes the jump in the gap phase across the corresponding Josephson junction, $\delta\phi$ is the intrinsic phase difference within the light-gray part of Fig. 3.9, and the additional $2n\pi$ term accounts for the allowed phase-winding in a multiple connected superconductor. Then, the total supercurrent I_c^S running through the SQUID device is given by the sum of tunneling currents across each junction which, according to the DC Josephson effect [36], is determined by the corresponding phase jumps $\Delta\phi_i$:

$$I(\Delta\phi_1, \Delta\phi_2) = I_{c1}\sin(\Delta\phi_1) + I_{c2}\sin(\Delta\phi_2).$$
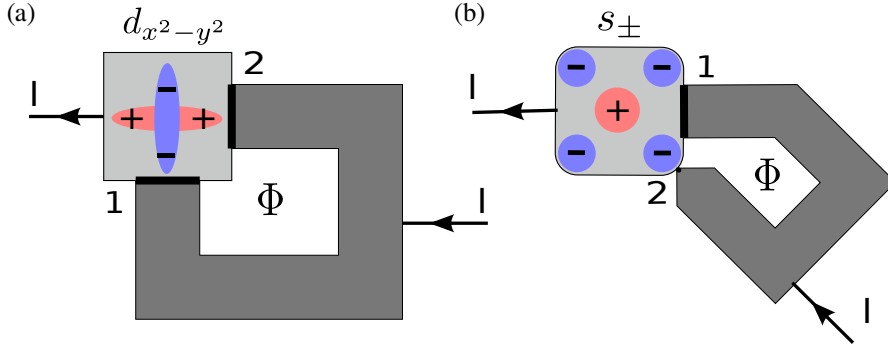
Figure 3.9: SQUID devices for resolving the phase differences in the complex gap function of a $d_{x^2-y^2}$-wave (a) and $s_\pm$-wave (b) superconductor (light-gray). At this, a second, conventional (s-wave) superconductor (dark-gray) is linked via the two Josephson-junctions 1, 2 such that the corresponding loop encircles a magnetic flux Φ. The current running through this device is indicated by the two arrows.

Assuming further a symmetric device with equal critical junction currents $I_{c1} = I_{c2} = I_c$, one ends up with

$$I(\Delta\phi_1, \Delta\phi_2) = 2I_c \sin\left(\frac{\Delta\phi_1 + \Delta\phi_2}{2}\right) \cos\left(\frac{\Delta\phi_1 - \Delta\phi_2}{2}\right)$$

$$= I_0 \cos\left(\pi\frac{\Phi}{\Phi_0} - \frac{\delta\phi}{2} - n\pi\right), \qquad (3.33)$$

and the critical-current $I_c^S = \max I(\Delta\phi_1, \Delta\phi_2)$ therefore shows a $(\delta\phi/2)$-shifted interference pattern as a function of the flux Φ. For example, at zero flux the critical current is $I_c^S = 0$ for a $d_{x^2-y^2}$-wave superconductor ($\delta\phi = \pi$) and $I_c^S = \pm I_0$ for an s-wave ($\delta\phi = 0$) superconducting state. Therefore, by applying a bias current through the SQUID and measuring its maximal value until a finite voltage occurs, one can clearly distinguish between an anisotropic s-wave and a sign-changing $d_{x^2-y^2}$-pairing state. Similar measurements in different geometries were performed by Wollman *et al.* [34, 37] and strongly pointed to a $d_{x^2-y^2}$-wave pairing state in the cuprates.

For the recently discovered pnictide superconductors there exist similar proposals [38] although here the sign-change of the most prominent candidate, the $s_\pm$-wave pairing state, occurs between the hole pockets at $(0, 0)$ and electron pockets at (π, π) (see Fig. 3.9b) and is therefore not accessible by real-space transformations. However, it is possible here to employ different tunnel-barriers, for example a thin (specular) one at which all $\boldsymbol{k}$-directions contribute according to an average of Fermi-velocity and electronic density-of-states (DOS) or a thick barrier which suppresses $\boldsymbol{k}$-directions that do not lie parallel to the barrier normal. Then, as depicted in the experimental setup of Fig. 3.9b, the thick barrier (1) only transfers Cooper-pairs located at the hole pockets (red), and the thin one (2) mainly provides Cooper-pairs
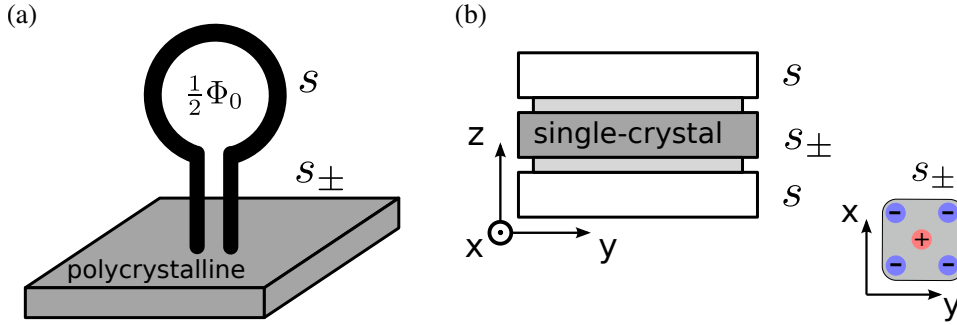
Figure 3.10: Two suggested π-junctions for detecting the sign-change in the proposed $s_\pm$-wave pairing state of iron pnictides. Setup (a) consists of a polycrystalline pnictide (gray) in contact with a conventional s-wave superconductor (black) [45–47], and (b) shows a trilayer device [48] with a single-crystal pnictide superconductor in between.

from the electron pockets (blue) as the mentioned average of Fermi-velocity and DOS is higher there. This in turn would realize the same interference of Cooper-pair wave functions with a π-phase shift as in the cuprate case of Fig. 3.9a. Unfortunately, these type of experiments did not yet provide conclusive indications of the $s_\pm$-pairing symmetry in the pnictides due to difficulties in the junction fabrication. On the other hand, similar experiments were used to ruled out pure d-wave or p-wave pairing orders in certain compounds [39, 40].

Another instructive experiment for resolving the relative gap phase detects the occurrence of half-integer flux quantization in so-called π-junctions. As we noted before, the tunneling current of a single Josephson-junction reads as $I = I_c \sin(\Delta\phi)$ [36], and the phase shift $\Delta\phi$ across the junction adjusts according to the applied current I. So when there is no current passing the junction $I = 0$, the phase shift $\Delta\phi$ is either zero or π, which is then denoted as 0- or π-junction [41, 42], respectively. If a superconducting loop then contains an odd number of π-junctions, the phase flux relation of Eq. (3.32) requires a half-integer flux quantization $\Phi = (n + 1/2)\Phi_0$ as opposed to the usual integer quantization $\Phi = n\Phi_0$. In the ground-state $n = 0$, the π-loop then shows a spontaneous flux of $\Phi = (1/2)\Phi_0$ which was verified by Tsui *et al.* [43, 44] in a tricrystal ring of YBCO and therefore provided an unambiguous evidence for $d_{x^2-y^2}$-wave pairing. In the pnictide superconductors there exist similar proposals for π-junction devices as for example suggested by Chen *et al.* [45, 46]. Here, a polycrystalline pnictide sample as shown in Fig. 3.10a is connected with a conventional superconductor. If the two contact barriers are relatively thick such that the tunneling occurs momentum dependently, there is also a finite probability that the contacted crystallites form a π-loop, of course, provided that the gap function really shows a sign-change and is not just of anisotropic s-wave form. The resulting half-integer flux was subsequently measured by Chen *et al.* [47]

for $NdFeAsO_{0.88}F_{0.12}$ connected with a Nb-loop which strongly supports a sign-changing superconducting gap. On the other hand, SQUID measurements of Hicks *et al.* [49] in the same compound further pointed out that there is no directional sign-change ruling out *d*- and *p*-wave pairing. Other proposed π-junctions like the one in Fig. 3.10b and others [50] could not yet resolve this sign-change partly due to the lack of large single crystals or due to surface degradation.

Coherence factors in quasi-particle interference and neutron scattering:

Another experimental approach for resolving the gap phase exploits the so-called coherence factors of physical response functions within the superconducting regime. In order to illustrate this point, we consider some one-particle operator such as spin or charge which is typically described by

$$\hat{A} = \sum_{\boldsymbol{k}s,\boldsymbol{k}'s'} A_{\boldsymbol{k}s,\boldsymbol{k}'s'} c_{\boldsymbol{k}s}^{\dagger} c_{\boldsymbol{k}'s'} = \frac{1}{2} \sum_{\boldsymbol{k}s,\boldsymbol{k}'s'} A_{\boldsymbol{k}s,\boldsymbol{k}'s'} \left(c_{\boldsymbol{k}s}^{\dagger} c_{\boldsymbol{k}'s'} \pm c_{-\boldsymbol{k}'-s'}^{\dagger} c_{-\boldsymbol{k}-s} \right).$$

(3.34)

The sign $\pm$ in (3.34) refers to the even and odd behavior of $A_{\boldsymbol{k}s,\boldsymbol{k}'s'}$ under time-reversal. If we now enter the superconducting phase, the effect on the corresponding response function is determined by the modified one-particle spectrum ($\xi_{\boldsymbol{k}} \to E_{\boldsymbol{k}} = \sqrt{\xi_{\boldsymbol{k}}^2 + |\Delta_{\boldsymbol{k}}|^2}$) and also by the particle-hole mixing in the new quasi-particle excitations $\alpha^{\dagger}, \alpha$ (see Sec. 2.6). This latter effect is then considered in the so-called coherence factors which, in contrast to the spectrum $E_{\boldsymbol{k}}$, also contain informations on the gap phase. In order to investigate this point, we use the Bogoliubov-transformed operators (2.91)

$$c_{\boldsymbol{k}s}^{\dagger} = u_{\boldsymbol{k}} \alpha_{\boldsymbol{k}s}^{\dagger} - \text{sgn}(s) v_{\boldsymbol{k}} \alpha_{-\boldsymbol{k},-s}$$
$$c_{\boldsymbol{k}'s'} = u_{\boldsymbol{k}'} \alpha_{\boldsymbol{k}',s'} - \text{sgn}(s') v_{\boldsymbol{k}'} \alpha_{-\boldsymbol{k}'-s'}^{\dagger}$$

(3.35)

and rewrite (3.34) in terms of $\alpha^{\dagger}, \alpha$. Note that in (3.35), we used the notation of $\hat{u}_{\boldsymbol{k}} = \sigma_0 u_{\boldsymbol{k}}$ as well as $\hat{v}_{\boldsymbol{k}} = -i\sigma_2 v_{\boldsymbol{k}}$ and also assumed spin-singlet pairing for the sake of clarity. Following the calculation described explicitly in the textbooks of Tinkham [51] and Schrieffer [52], this then leads to

$$\hat{A} = \sum_{\boldsymbol{k}s,\boldsymbol{k}'s'} A_{\boldsymbol{k}s,\boldsymbol{k}'s'} \left\{ (u_{\boldsymbol{k}'} u_{\boldsymbol{k}} \pm v_{\boldsymbol{k}'} v_{\boldsymbol{k}}) \alpha_{\boldsymbol{k}s}^{\dagger} \alpha_{\boldsymbol{k}',s'} + \right.$$
$$\left. \frac{1}{2} \left((u_{\boldsymbol{k}} v_{\boldsymbol{k}'} \pm v_{\boldsymbol{k}} u_{\boldsymbol{k}'}) \text{sgn}(s') \alpha_{\boldsymbol{k}s}^{\dagger} \alpha_{-\boldsymbol{k}'-s}^{\dagger} + \text{h.c} \right) \right\}. \quad (3.36)$$

The external perturbation in an experiment hence consists of quasi-particle/quasi-hole ($\alpha^{\dagger}\alpha$) as well as of quasi-particle/quasi-hole-pair ($\alpha^{\dagger}\alpha^{\dagger}/\alpha\alpha$) excitations weighted with the coherence factors $u_{\boldsymbol{k}}, v_{\boldsymbol{k}}$. These latter terms include the gap function as seen from (2.89), and we now discuss two experiments in which the effect of coherence factors is directly observable.

The first one is the scanning tunneling microscopy (STM). Here, the sample is voltage-biased with respect to a conducting tip and, by measuring the resulting tunneling current along the sample surface, one obtains informations on the local density of states $n(\boldsymbol{r}, \omega)$. In a sample without any impurities or defects, this local density of states (LDOS) would be rather featureless due to translational invariance. However, by introducing a certain amount of disorder, the quasi-particles scatter off these defects and interfere with each other. The resulting LDOS modulation can be transformed to $\boldsymbol{q}$-space and, in a first-order approximation [53–55], reads as

$$n(\boldsymbol{q}, \omega) \propto \sum_{\boldsymbol{k}} n_0(\boldsymbol{k}, \omega) n_0(\boldsymbol{k}+\boldsymbol{q}, \omega) \times \begin{cases} (u_{\boldsymbol{k}} u_{\boldsymbol{k}+\boldsymbol{q}} + v_{\boldsymbol{k}} v_{\boldsymbol{k}+\boldsymbol{q}})(u_{\boldsymbol{k}} v_{\boldsymbol{k}+\boldsymbol{q}} + v_{\boldsymbol{k}} u_{\boldsymbol{k}+\boldsymbol{q}}) \\ (u_{\boldsymbol{k}} u_{\boldsymbol{k}+\boldsymbol{q}} + v_{\boldsymbol{k}} v_{\boldsymbol{k}+\boldsymbol{q}})^2 \\ (u_{\boldsymbol{k}} u_{\boldsymbol{k}+\boldsymbol{q}} - v_{\boldsymbol{k}} v_{\boldsymbol{k}+\boldsymbol{q}})^2, \end{cases}$$

$$(3.37)$$

where the subscript "0" denotes the density of states in the absence of scattering, and the three coherence terms are for vortex, magnetic and potential scattering (from top to bottom). In the cuprate and pnictide superconductors the joint density of states $n_0(\boldsymbol{k}, \omega) n_0(\boldsymbol{k}+\boldsymbol{q}, \omega)$ is dominated by just a few wavevectors, and, as the coherence factor for vortex scattering (top in (3.37)) can be shown to be proportional to $(\Delta_{\boldsymbol{k}} + \Delta_{\boldsymbol{k}+\boldsymbol{q}})$, the peaks for gap-sign preserving (reversing) scatterings are enhanced (suppressed) by an applied magnetic field. In the corresponding experiments, Hanaguri *et al.* [56, 57] and Hoffman *et al.* [58] identified sign-changes in the superconducting gap of cuprates and pnictides that are consistent with the theoretical predicted pairing symmetries of d-wave and $s_{\pm}$-wave, respectively.

A similar coherence effect is also observed in inelastic neutron scattering (INS) experiments. Here, the scattering cross section is proportional to the imaginary part of the spin-spin response function. For low temperatures and relatively large excitation energies one can show that quasi-electron/quasi-hole pair-excitations dominate $\text{Im}\chi(\boldsymbol{q}, \omega)$ [59, 60] which in turn involves the following coherence factor (see Eq. (3.36)):

$$(u_{\boldsymbol{k}} v_{\boldsymbol{k}+\boldsymbol{q}} - v_{\boldsymbol{k}} u_{\boldsymbol{k}+\boldsymbol{q}})^2 = \frac{1}{2} \left(1 - \frac{\Delta_{\boldsymbol{k}} \Delta_{\boldsymbol{k}+\boldsymbol{q}}}{E_{\boldsymbol{k}} E_{\boldsymbol{k}+\boldsymbol{q}}} \right). \qquad (3.38)$$

If the superconducting gap would not feature a sign-change between the two wavevectors $\boldsymbol{k}$ and $\boldsymbol{k} + \boldsymbol{Q}$, i.e. $\Delta_{\boldsymbol{k}+\boldsymbol{Q}} = \Delta_{\boldsymbol{k}}$, the corresponding factor in (3.38) would cancel the magnetic resonance at wavevector $\boldsymbol{Q}$. Again both the cuprates [60, 61] and pnictides [62–64] show resonance peaks in the neutron-scattering cross section below T_c, which in turn provides strong evidence for a sign-changing superconducting gap.

Chapter 4

Superconductivity in Iron-Based Compounds

4.1 Introduction

In 2006, while searching for transparent semiconductors, Kamihara *et al.* [65] found superconductivity in LaFePO with a transition temperature (T_c) of $4K$. Although iron seemed incompatible with superconductivity due to its strong local magnetic moments, its discovery was by no means exceptional as the first iron-containing superconductors were already known since the late fifties [66]. However, only two years later, in 2008, the same group reported another compound (LaFeAsO), characterized by alternating layers of iron-arsenic and lanthanum-oxygen, which revealed superconductivity upon replacing oxygen with fluorine. Soon afterwards, it also turned out that many other materials based on either iron-arsenic or iron-phosphorus layers become superconducting as well. During the last three years, this structural variety then gave rise to many hundreds of new iron-based superconductors (FeSCs) with transition temperatures of up to $56K$ [67]. For the first time, high-T_c superconductivity seemed not to be limited to the cuprates, and the discovery of FeSCs triggered an enormous interest within the condensed-matter community.

In addition to its remarkably high T_c's, the FeSCs also revealed interesting similarities and differences to the cuprates. For example, both material classes feature a close proximity of magnetic and superconducting order, which could in turn point to a common magnetically induced pairing mechanism. On the other hand, the structure of the magnetic ordering is quite different in both materials. In the cuprates, the antiferromagnetism is of Néel-type and evolves from localized charge carriers, whereas the FeSCs show a stripe-like antiferromagnetism resulting from an instability of the moving electrons. Another important distinction between cuprates and FeSCs concerns the effective Coulomb repulsion and correlation effects of

(a)
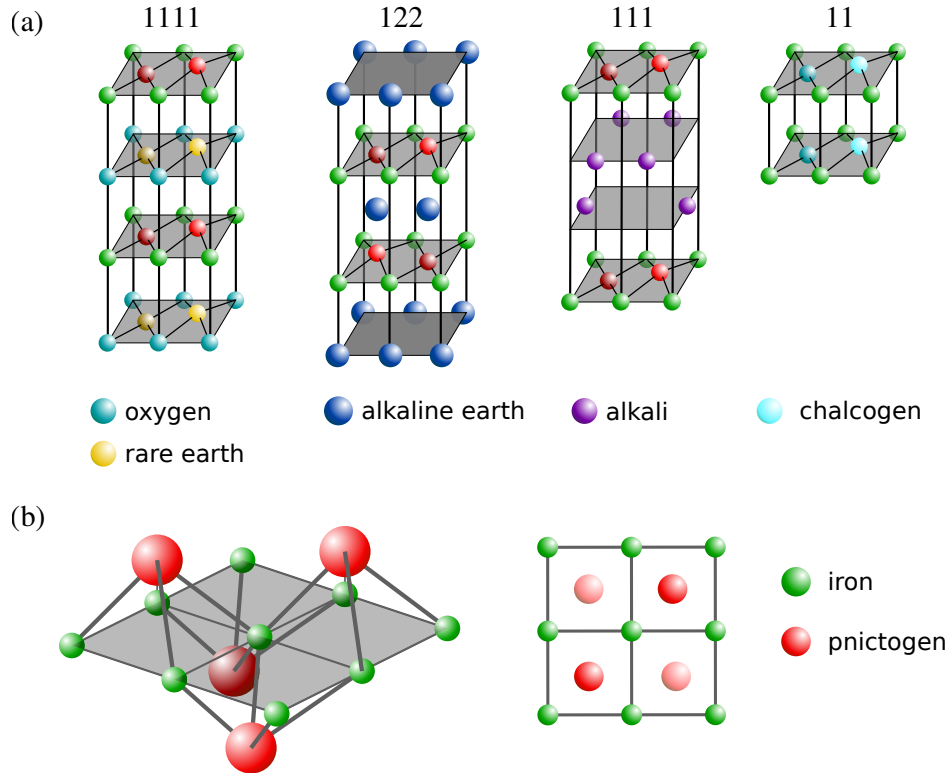
Figure 4.1: (a) The four classes of FeSCs consisting of iron-pnictide (1111, 122, 111) and iron-chalcogen (11) layers. The additional filling layers contain rare-earth oxygen (1111), alkaline-earth (122) and alkali (111) elements. (b) Characteristic trilayer structure consisting of an iron square-lattice with pnictogen (chalcogen) atoms alternately protruding above and below the iron plane.

the low-energy electrons. Here, the correlations in the undoped cuprates appear much stronger and lead to a Mott-insulating behavior, while the FeSCs remain semi-metallic with only weak to moderate correlations. The weaker correlation effects in FeSCs are also consistent with the fact that the low-energy electrons of the cuprates reside in one single d-orbital, whereas the ones of the FeSCs are distributed among all five orbitals.

In the following chapter, we investigate the superconducting state as well as the underlying pairing mechanism of FeSCs. For this purpose, we apply the functional RG which, on the one hand, captures the full multi-orbital complexity of FeSCs and, on the other hand, is also very well suited for studying materials of moderate electronic correlations. Understanding the superconductivity of FeSCs might then point the way to new material variants with even higher T_c's and might also lead to broader insights into superconductivity in general. However, before we start with the functional RG study, we shortly summarize the most essential structural and electronic properties of FeSCs in the following three sections.

4.1.1   Structural and Normal-State Properties

The class of FeSCs by now includes hundreds of different materials. It is therefore common to distinguish between the following major groups, termed after the stoichiometries of their undoped compounds: 1111 (LaFeAsO), 122 (BaFe$_2$As$_2$), 111 (LiFeAs) and 11 (FeSe). As pictured in Fig. 4.1, the structural characteristic of all these compounds consists of an iron square lattice in between two checkerboard lattices of either pnictogen (As,P) or chalcogen (Se,Te,S) atoms. According to these two element groups, the FeSCs are often assigned as iron-pnictides or iron-chalcogenides.

The additional filling-planes between the iron-pnictogen layers contain rare-earth oxygen (1111), alkaline-earth (122) and alkali (111) elements, or are completely absent as in the iron-chalcogenides (11). Nevertheless, superconductivity also occurs in this simplest 11 family with $T_c = 27K$ [68], suggesting that the relevant physics most likely takes places within the iron-chalcogen and iron-pnictogen layers. The same conclusion can also be drawn from the electronic structure of FeSCs. Here, it turns out that the low-energy sector ($< 2eV$) is mainly governed by iron d-states with only small contributions from the energetically higher-lying pnictogen/chalcogen p-states. Yet, as opposed to the cuprates, the low-energy electrons in the FeSCs distribute among all five d-orbitals which in turn results from a closer iron packing in edge-sharing tetrahedrons. In addition, the hopping amplitude between different iron-layers turns out to be small but still leads to non-negligible effects in some of the FeSCs. Taken together, the relevant electrons in the FeSCs are more delocalized than in the cuprates and effectively give rise to smaller electronic correlations effects. In this context, it is also interesting to note that the calculated band structure [69–72] agrees very well with the one determined by ARPES [73, 73–75] and quantum oscillation measurements [76, 77], which can in turn be interpreted as another evidence for the weaker correlation effects in FeSCs.

The band structure of the iron d-electrons in FeSCs then features ten bands according to the five d-orbitals on each of the two non-equivalent iron sites within the unit-cell. In Fig. 4.2a, we depicted the two-iron unit-cell as well as the corresponding Fermi-surface with hole-like pockets (blue) around the Γ-point and electron-like pockets (green) at the M-point. Here, it is important to note that the existence of the dashed pocket depends in a sensitive way on material details like the pnictogen height, whereas the other four pockets appear quite generically in most of the FeSCs. In order to unfold the band structure to the larger Brillouin zone of a one-iron unit cell, one exploits the so-called glide-mirror group (translation plus $z \to -z$) under which all iron sites become equivalent [33, 78]. This unfolding then provides the Fermi-surface pictured in Fig. 4.2b. Note that the difference between these two band-structure representations becomes purely geometrical for vanishing pnictogen or chalcogen potentials. In this case, (b) is obtained
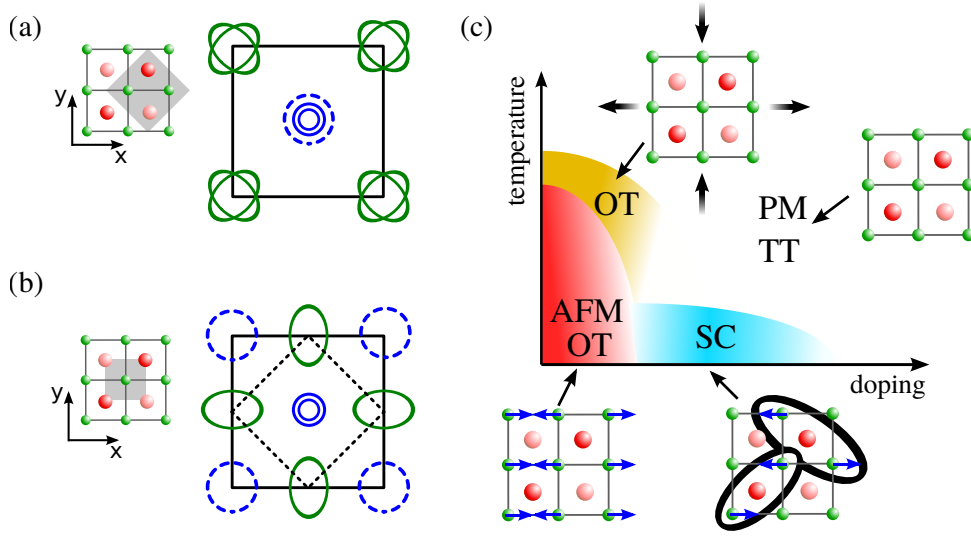
Figure 4.2: (a) Fermi-surface topology of a generic FeSCs represented in the folded Brillouin-zone (BZ), which corresponds to the two Fe-atom unit-cell shown in the inset (light-gray). (b) Fermi-surface topology shown in the unfolded BZ associated with the one Fe-atom containing unit-cell depicted in the inset (light-gray). (c) Schematic phase-diagram for FeSCs including the paramagnetic phase with a tetragonal crystal structure, the structural transition to an orthorhombic crystal structure (yellow), the striped anti-ferromagnetic order (red) as well as the superconducting phase (cyan).

from (c) by shifting all bands into the smaller (dashed) Brillouin zone. If not stated differently, we will only use the one-iron unit cell and its associated unfolded Brillouin zone.

In the undoped FeSCs, the electronic filling of the iron d-orbitals amounts to six electrons per iron site, according to its Fe^{2+} valence state.

4.1.2 Structural Transition and Antiferromagnetic State

Most of the undoped iron-pnictides develop a striped antiferromagnetic order (AFM) at about $150K$. Here, the magnetic moments align parallel to the iron layer and form alternating ferromagnetic stripes along one of the two crystalline axis (see Fig. 4.2c). The two possible magnetic phases are then characterized by ordering vectors $Q_1 = (0, \pi)$ and $Q_2 = (\pi, 0)$, consistent with the Fermi-surface nesting of hole- and electron-like pockets. It seems by now generally accepted that the magnetic ordering results from a spin-density wave (SDW) instability associated with this Fermi-surface nesting. Usually, the SDW formation then leads to a band backfolding into the reduced Brillouin zone and gives rise to a gap opening at the corresponding band crossings. However, in the iron-pnictides, the multi-orbital nature of the electronic states gives rise to symmetry protected Dirac-nodes within the SDW phase [79, 80] and thus implies a semimetallic behavior.

As apparent from the phase diagram in Fig. 4.2c, there is also a structural phase transition from tetragonal (TT) to orthorhombic (OT), which closely follows the magnetic transition line. Within the orthorhombic phase, the degeneracy between the $Q_1 = (0, \pi)$ and $Q_2 = (\pi, 0)$ magnetic ordering is lifted, and the magnetic moments order ferromagnetically along the contracted and antiferromagnetically along the extended axis. Depending on the particular compound, the magnetic phase is either preceded by (1111) or occurs simultaneously (122) to the structural transition. In most cases, the simultaneous transition into the structurally and magnetically ordered phase turns out to be of first order, whereas the separated transition can be either of first or second order. On the other hand, the structural transition is completely absent in the FeSCs that show no magnetic ordering at all (LaFePO [81], LiFeAs [82] and LiFeP [83]).

In order to explain the interplay of structural and magnetic degrees of freedom, Fernandes *et al.* [84] proposed a so-called nematic scenario. Here, the magnetic and structural orders are preceded by an intermediate phase which first breaks the twofold degeneracy of $Q_1 = (0, \pi)$ and $Q_2 = (\pi, 0)$ magnetic fluctuations ($\langle S^2_{Q_1} \rangle \neq \langle S^2_{Q_2} \rangle$) but still respects spin-rotational symmetry ($\langle S_{Q_1} \rangle = \langle S_{Q_2} \rangle = 0$). As a consequence, the breaking of rotational symmetry in this nematic phase then induces the orthorhombic lattice distortion and also selects one of the two magnetic orderings. Several implications of this nematic scenario have been detected experimentally, and, for a detailed discussion of the rich phenomenology, we refer to the following two articles [84, 85] and references therein.

It is also important to note that some of the iron-chalcogenides (11) reveal a different magnetic ordering pattern, although its electronic properties are quite similar to the one in iron-pnictides. The magnetic moments here are rotated by $\pi/4$ and have a doubled real-space period compared to the striped antiferromagnet in Fig. 4.2c. Interestingly, the ordering vector here is determined by $Q_3 = (\pi/2, \pi/2)$ and does not correspond to a Fermi-surface nesting [86, 87]. A possible explanation for this striking behavior is given by Paul *et al.* [88] who calculated the corrections due to magneto-elastic couplings and found strong enhancement of the magnetic fluctuations at Q_3.

4.1.3 Superconducting State

In both iron-pnictides and iron-chalcogenides, the superconductivity can be induced either by chemical doping or by external pressure [89]. Although chemical doping is more convenient, the pressure induced method is also appealing as it allows to study different phases in one and the same sample without comparing different fabricated crystals. In most FeSCs, the superconducting phase then appears in close vicinity to the magnetically ordered state (see Fig. 4.2c), which possibly suggests a common spin-fluctuation
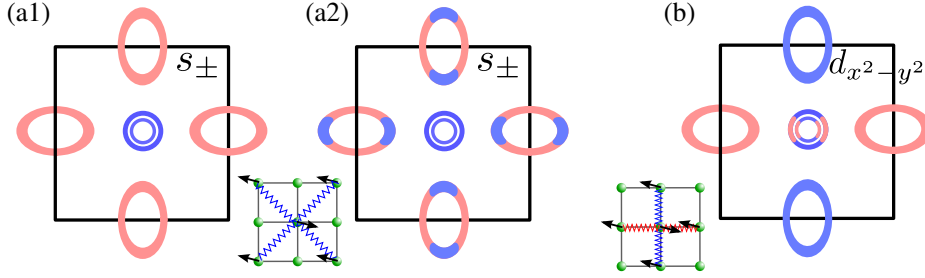
Figure 4.3: Nodeless (a1) and nodal (a2) $s_\pm$-wave gap in the unfolded (one Fe unit-cell) Brillouin zone as well as its lowest-order real-space representation (inset). In (b), the $d_{x^2-y^2}$-wave gap is plotted for comparison. Red and blue springs in the insets denote attractive and repulsive pair interactions.

based pairing mechanism. At this, the rigid magnetic ordering softens and provides a kind of polarizable background, which in turn enables the mediation of pairing. The spin-fluctuation based pairing is therefore most effective in the vicinity away from the magnetically ordered state.

Additionally, the pairing mechanism also affects the symmetry of the superconducting gap (pair wave function) as the spin-fluctuations of ordering momentum Q only induce pairing if the gap changes sign between Q-connected portions of the Fermi-surface. In the FeSCs, this then implies a sign-change of the superconducting gap between hole- and electron-like pockets [90]. The corresponding pairing symmetry is commonly denoted as $s_\pm$-wave since the superconducting gap reveals sign changes but breaks no additional point-group symmetries (see Fig. 4.3a).

Other pairing mechanisms based on the polarizability of the pnictogen or chalcogen ions [91], orbital-fluctuations [92] or on the Hund's rule coupling [93, 94] were also proposed in the beginning, but mostly turned out to be inconsistent with various experiments. In particular, conventional phonon-based pairing was ruled out right from the beginning as the calculated electron-phonon coupling turned out too small [95] to account for the high T_c's in FeSCs. Nevertheless, it was pointed out by Yildrim [96] that phonons could provide an indirect contribution to superconductivity via spin-lattice coupling.

The pairing symmetry and pairing mechanism of FeSCs have also been the focus of numerous experimental works. Even though, the pairing state is not fully understood, several important indications could be obtained during the last three years (see [97] for a detailed review). For example, nuclear magnetic resonance (NMR) measurements reported a vanishing Knight-shift [98, 99] in all crystallographic directions which in turn points to spin-singlet pairing. Other experimental findings like the spin-resonance in neutron-scattering [62–64] or the quasi-particle interference pattern observed in scanning tunneling (STM) experiments [57] suggest a sign-changing pair wave function that is consistent with an $s_\pm$-wave gap. In addition,

Josephson interference experiments make the d-wave pairing (see Fig. 4.3b) unlikely [39, 49] and rather support an $s_\pm$-wave scenario [47]. Usually, the $s_\pm$-wave gap was assumed to be fully gapped and a number of experiments reporting gap nodes seemed to be at odds with such an $s_\pm$-wave pairing state. However, it is by now understood that the existence of nodes in an $s_\pm$-wave gap (see Fig. 4.3a2) depends on details of the multi-orbital band structure and may vary between different FeSC compounds.

From that perspective, it was really striking that angular-resolved photoemission spectroscopy (ARPES) consistently reported a full gap [73–75, 100, 101] and never revealed significant gap-anisotropies or gap nodes which are, one the other hand, clearly seen in the cuprate d-wave gap [31]. A possible explanation for this disagreement between bulk and surface probes was provided by Kemper *et al.* [102], who pointed out the existence of an additional pocket in the surface band structure, which in turn stabilizes a full superconducting gap.

4.2 Electronic Correlations and the Pairing Mechanism of FeSCs

In the following section, we analyze the pairing mechanism and the associated pairing symmetry of FeSCs. In particular, we demonstrate how antiferromagnetic fluctuations drive the pairing instability and also promote a number of other competing ordering tendencies.

4.2.1 Microscopic Model Description

In order to explore the FeSCs on a theoretical basis, it is important to start with an appropriate model description that captures the essential properties in a kind of minimal Hamiltonian. Soon after the first discovery of high-T_c superconductivity in the FeSCs, a number of effective models based on two [103] or three [93] of the five iron d-orbitals were proposed. Yet, each of these models revealed certain shortcomings in describing the low-energy band structure, as for example discussed by Graser *et al.* [104]. For this reason, we consider a five-orbital model suggested by Kuroki *et al.* [71] which provides an almost perfect agreement to the low-energy sector of the band structure. The resulting tight-binding description is then given by

$$H_0 = \sum_{\boldsymbol{k},s} \sum_{a,b=1}^{5} c_{\boldsymbol{k}as}^\dagger K_{ab}(\boldsymbol{k}) c_{\boldsymbol{k}bs}, \qquad (4.1)$$

where $c_{\boldsymbol{k}as}^\dagger$, $c_{\boldsymbol{k}as}$ denote the creation and annihilation operators of an electron with momentum $\boldsymbol{k}$, spin projection s and orbital character a. Note that this model here was constructed for LaFeAsO$_{1-x}$F$_x$ and neglects out-of-plane
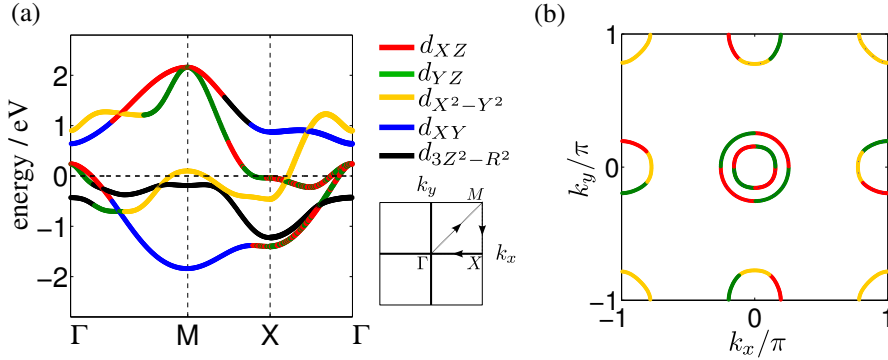
Figure 4.4: Band structure (a) and Fermi-surface topology (b) of LaOFeAs in the unfolded (one iron per unit-cell) Brillouin zone. The colors denote the leading orbital content. (Inset: Brillouin zone and orbital color-coding).

hopping terms along the z-axis. As the class of 1111 compounds generally shows a strongly two-dimensional behavior, this approximation is valid but may be inappropriate for other FeSCs. The corresponding band structure for the undoped case with $n = 6.0$ electrons per Fe-site is then plotted in Fig. 4.4, together with its associated Fermi-surface. Here, it is important to note that the presence of a hole-like pocket at (π, π) strongly depends on the level of doping and on the detailed material composition. The remaining four pockets, on the other hand, appear quite generically in most of the FeSCs. In Fig. 4.4, we also depicted the leading orbital contributions of the corresponding Bloch states.

A minimal interaction part H_{int} considered in the context of FeSCs includes the intra- and inter-orbital repulsion U_1 and U_2, as well as the Hund's rule coupling J_H and the pair-hopping term J_{pair}:

$$H_{int} = \sum_i \left[U_1 \sum_a n_{ia\uparrow} n_{ia\downarrow} + U_2 \sum_{a<b,s,s'} n_{ias} n_{ibs'} \right.$$
$$\left. + J_H \sum_{a<b} \sum_{s,s'} c^\dagger_{ias} c^\dagger_{ibs'} c_{ias'} c_{ibs} + J_{pair} \sum_{a<b} \left(c^\dagger_{ia\uparrow} c^\dagger_{ia\downarrow} c_{ib\downarrow} c_{ib\uparrow} + h.c. \right) \right].$$

The electron density of spin s in orbital a and at site i is, as usual, denoted by $n_{ias} = c^\dagger_{ias} c_{ias}$. It is further important to note that the interaction parameters are actually orbital dependent and can be computed via first-principle methods like constrained RPA [72]. The same first-principle approach then also provides parameter values for longer-ranged interaction terms. Although, both of these more precise informations can be easily included in the functional RG, we first start out with an onsite term only and choose the orbital independent values of $U_1 = 4.0$, $U_2 = 2.0$, $J_H = J_{pair} = 0.7eV$. Note that the often required condition of $U_1 = U_2 + 2J_H$ and $J_{pair} = J_H$, following

from rotational symmetry [105], only holds for the bare values and not for the renormalized ones determined by constrained RPA [72]. Here, the interaction parameters already include for example screening from high-energy bands, which then may violate the above sum-rule.

4.2.2   From Orbital- to Band-Representation

For an efficient solution of the functional flow equations, it is convenient to choose an appropriate one-particle basis which diagonalizes the quadratic part H_0. The corresponding unitary transformation is then given by

$$c_{\boldsymbol{k}as} = \sum_{m=1}^{5} u_{am}(\boldsymbol{k})\gamma_{\boldsymbol{k}ms}, \tag{4.2}$$

and the total Hamiltonian $H_{tot} = H_0 + H_{int}$ in this new band basis reads as

$$
\begin{aligned}
H_{total} = &\sum_{\boldsymbol{k},s} \sum_{m=1}^{5} \gamma_{\boldsymbol{k}ms}^{\dagger} E_m(\boldsymbol{k}) \gamma_{\boldsymbol{k}ms} \\
&+ \sum_{\substack{\boldsymbol{k}_1,\dots\boldsymbol{k}_4 \\ s,s'}} \sum_{m_1,\dots,m_4} V_0(\boldsymbol{k}_1 m_1, \boldsymbol{k}_2 m_2, \boldsymbol{k}_3 m_3, \boldsymbol{k}_4 m_4) \gamma_{\boldsymbol{k}_1 m_1 s}^{\dagger} \gamma_{\boldsymbol{k}_2 m_2 s'}^{\dagger} \gamma_{\boldsymbol{k}_3 m_3 s} \gamma_{\boldsymbol{k}_4 m_4 s'}.
\end{aligned}
\tag{4.3}
$$

Here, the fourth momentum $\boldsymbol{k}_4$ is determined by momentum conservation $\boldsymbol{k_4} = \boldsymbol{k}_3 + \boldsymbol{k}_2 - \boldsymbol{k}_3$, and the eigenvalues $E_m(\boldsymbol{k})$ provide the band structure depicted in Fig. 4.4. It is also important to note that the orbital content of the m-th band at momentum $\boldsymbol{k}$ is characterized by the matrix elements $u_{am}(\boldsymbol{k})$, whose dominant part determines the leading orbital content in Fig. 4.4. In addition, the explicit form of the coupling function now reads as

$$
\begin{aligned}
V_0(\boldsymbol{k}_1 m_1, \boldsymbol{k}_2 m_2, \boldsymbol{k}_3 m_3, \boldsymbol{k}_4 m_4) =& U_1 \sum_{a} u_{am_1}^*(\boldsymbol{k}_1) u_{am_2}^*(\boldsymbol{k}_2) u_{am_3}(\boldsymbol{k}_3) u_{am_4}(\boldsymbol{k}_4) \\
&+ U_2 \sum_{a,b} u_{am_1}^*(\boldsymbol{k}_1) u_{bm_2}^*(\boldsymbol{k}_2) u_{am_3}(\boldsymbol{k}_3) u_{bm_4}(\boldsymbol{k}_4) \\
&+ J_{\mathrm{H}} \sum_{a,b} u_{am_1}^*(\boldsymbol{k}_1) u_{bm_2}^*(\boldsymbol{k}_2) u_{bm_3}(\boldsymbol{k}_3) u_{am_4}(\boldsymbol{k}_4) \\
+ J_{\mathrm{pair}} \sum_{a,b} u_{am_1}^*(\boldsymbol{k}_1) &u_{am_2}^*(\boldsymbol{k}_2) u_{bm_3}(\boldsymbol{k}_3) u_{bm_4}(\boldsymbol{k}_4) \tag{4.4}
\end{aligned}
$$

and again reveals that the matrix elements $u_{am}(\boldsymbol{k})$ cause a pronounced momentum dependence already at bare level (see Fig. 4.6(a1)). As the columns of the unitary matrix $U(\boldsymbol{k}) = (u_{aw}(\boldsymbol{k}))$ correspond to eigenvectors of the matrix $K_{ab}(\boldsymbol{k})$ in (4.1), the elements $u_{aw}(\boldsymbol{k})$ have a local $U(1)$ phase freedom. It is convenient here to require a smooth behavior of the matrix elements $u_{aw}(\boldsymbol{k})$, which would otherwise generate discontinuous sign-changes in the
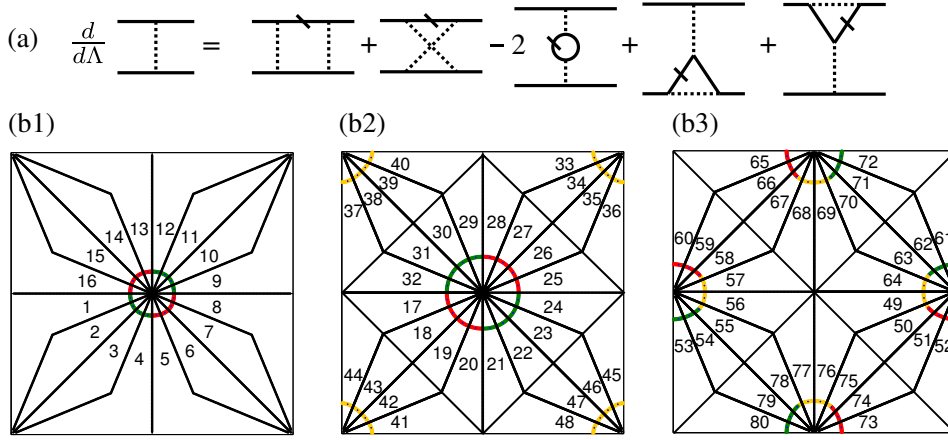
Figure 4.5:   (a) Flow equation of the 4-point function (dashed line) according to Eq. (2.63). Full internal lines denote free propagators, slashed lines indicate single-scale propagators as defined in (2.33) for the cutoff- and in (2.28) for the temperature-scheme. (b1-b3) Patching scheme depicted by the black partitioning of the Brillouin zone for each band that intersects the Fermi-level. The colors again denote the leading orbital content of the Fermi-pockets with an equivalent color coding as in Fig. 4.4b.

resulting gap functions. All smooth choices of the matrix elements then lead to exactly the same results, and the emergent $U(1)$ phase freedom hence represents equivalent descriptions of the same physics.

4.2.3   Functional RG Implementation

In the following section, we describe the numerical implementation of the functional RG as well as its application to the Hamiltonian in (4.3). As discussed in Chap. 2, the starting point consists of the exact hierarchy of flow equations in (2.24) for the one-particle irreducible vertex functions. Restricting to the 4-point function V^Λ, we then obtain the flow equation depicted in Fig. 4.5a, where we applied the widely used approximation of discarding the 6-point function as well as the self-energy feedback to V^Λ. Both types of approximations can be justified for sufficiently small bare interactions [9] since these two terms only generate contributions of third order in V^Λ. For curved and smooth Fermi-surfaces, as it is the case in almost all FeSCs, these approximations are valid up to a scale where the 4-point vertex is very large and the flow has to be stopped (see Sec. 2.5). In order to solve this differential equation numerically, we first divide up the Brillouin zone into patches for each band that intersects the Fermi level (see Fig. 4.5b). Since the leading part of the 4-point function is located at the Fermi surface and at zero frequency [106,107], we neglect all bands that are clearly away from the Fermi-level and compute the 4-point function only at frequency zero and at the Fermi-surface points $\{\boldsymbol{k}_F^s\}$. For momenta $\boldsymbol{k}$ away

from the Fermi-surface we then approximate

$$V^\Lambda(\boldsymbol{k}_1 m_1, \boldsymbol{k}_2 m_2, \boldsymbol{k}_3 m_3, \boldsymbol{k}_4 m_4) \approx$$
$$V^\Lambda(\pi_F(\boldsymbol{k}_1)m_1, \pi_F(\boldsymbol{k}_2)m_2, \pi_F(\boldsymbol{k}_3)m_3, \pi_F(\boldsymbol{k}_4)m_4),$$

where $\pi_F(\boldsymbol{k}_i)$ denotes the projection of $\boldsymbol{k}_i$ within the same patch onto the corresponding Fermi-surface point $\boldsymbol{k}_F^s$. In the following, we will also employ the condensed notation of $k = (\boldsymbol{k}_F^s, m^s)$ since each $\boldsymbol{k}_F^s$ is associated to a fixed band index m^s in the above patching scheme. As the 4-point function V^Λ equals the bare interaction part (4.4) at large energy scales Λ in the order of the bandwidth W, i.e.

$$V^{\Lambda \approx W}(k_1, k_2, k_3, k_4) = V_0(k_1, k_2, k_3, k_4),$$

the flow equation shown in Fig. 4.4a reduces to a well-defined initial value problem. Using standard procedures for the integration of differential equations, we then follow the flow of V^Λ down to low energy scales Λ. An illustration of a characteristic flow is then shown in Fig. 4.6, where we depicted $V^\Lambda(k_1, k_2, k_3, k_4)$ for five different energy scales (decreasing from (a1) to (a5)) as a function of k_1, k_2 with k_3 fixed and k_4 determined by momentum conservation. A detailed discussion will then follow in Sec. 4.2.5.

4.2.4   Channel Decoupling and Order Parameters

In order to infer the favored type of order, we also decompose the 4-point function V^Λ into the following channels

$$H_{int} = \sum_{k_1,\dots,k_4} \sum_{ss'} V^\Lambda(k_1, k_2, k_3, k_4) \gamma^\dagger_{k_1 s} \gamma^\dagger_{k_2 s'} \gamma_{k_3 s} \gamma_{k_4 s'} \tag{4.5}$$

$$= \sum_{k_1,k_2} W^{\Lambda,SDW}(k_1, k_2) \vec{S}^\dagger_{k_1,Q} \vec{S}_{k_2,Q} + \sum_{k_1,k_2} W^{\Lambda,CDW}(k_1, k_2) n^\dagger_{k_1,Q} n_{k_2,Q}$$

$$+ \sum_{k_1,k_2} W^{\Lambda,FI}(k_1, k_2) \vec{S}^\dagger_{k_1,0} \vec{S}_{k_2,0} + \sum_{k_1,k_2} W^{\Lambda,PI}(k_1, k_2) n^\dagger_{k_1,0} n_{k_2,0}$$

$$+ \sum_{k_1,k_2} W^{\Lambda,SCs}(k_1, k_2) p^\dagger_{k_1,s} p_{k_2,s} + \sum_{k_1,k_2} W^{\Lambda,SCt}(k_1, k_2) p^\dagger_{k_1,t} p_{k_2,p} \tag{4.6}$$

$$+ \dots$$

with the composite operators defined by

$$\vec{S}_{k,Q} = \frac{1}{2} \sum_{ss'} \gamma^\dagger_{k+Qs} \vec{\sigma}_{ss'} \gamma_{ks'}, \quad \vec{S}_{k,0} = \frac{1}{2} \sum_{ss'} \gamma^\dagger_{ks} \vec{\sigma}_{ss'} \gamma_{ks'}$$

$$n_{k,Q} = \sum_s \gamma^\dagger_{k+Qs} \gamma_{ks}, \quad n_{k,0} = \sum_s \gamma^\dagger_{ks} \gamma_{ks} \tag{4.7}$$

$$p_{k,s} = \frac{1}{\sqrt{2}} \left(\gamma_{k\uparrow} \gamma_{-k\downarrow} - \gamma_{k\downarrow} \gamma_{-k\uparrow} \right), \quad p_{k,t} = \frac{1}{\sqrt{2}} \left(\gamma_{k\uparrow} \gamma_{-k\downarrow} + \gamma_{k\downarrow} \gamma_{-k\uparrow} \right).$$

Comparing the coefficients of (4.5) and (4.6), one then obtains the following relations between the 4-point function V^Λ and the channel couplings $W^{\Lambda,ch}$ for spin-density wave ($ch = SDW$), charge-density wave ($ch = CDW$), ferromagnetic ($ch = FI$), Pomeranchuk ($ch = PI$), spin-singlet (SCs) and spin-triplet pairing (SCt) orders:

$$W^{\Lambda,SDW}(k_1, k_2) = -2V^\Lambda(k_1, k_2 + Q, k_2, k_1 + Q)$$

$$W^{\Lambda,CDW}(k_1, k_2) = -\frac{1}{2}V^\Lambda(k_1, k_2 + Q, k_2, k_1 + Q) + V^\Lambda(k_1 + Q, k_2, k_1, k_2 + Q)$$

$$W^{\Lambda,FI}(k_1, k_2) = -2V^\Lambda(k_1, k_2, k_2, k_1) \tag{4.8}$$

$$W^{\Lambda,PI}(k_1, k_2) = -2V^\Lambda(k_1, k_2, k_2, k_1) + V^\Lambda(k_1, k_2, k_1, k_2)$$

$$W^{\Lambda,SCs}(k_1, k_2) = V^\Lambda(k_1, -k_1, k_2, -k_2) + V^\Lambda(-k_1, k_1, k_2, -k_2)$$

$$W^{\Lambda,SCt}(k_1, k_2) = V^\Lambda(k_1, -k_1, k_2, -k_2) - V^\Lambda(-k_1, k_1, k_2, -k_2).$$

In case of spin-rotational symmetry, the other two ($S_z = \pm 1$) spin-triplet pairing channels (SCt) are equivalent to the one with $S_z = 0$ presented above. It is important to note here that the channel couplings $W^{\Lambda,ch}(k_1, k_2)$ can be regarded as hermitian operators due to the self-adjointness of H_{int}. For this reason, we can expand the channel-couplings $W^{\Lambda,ch}(k_1, k_2)$ into eigenmodes $f_i^{ch}(k_1)$:

$$W^{\Lambda,ch}(k_1, k_2) = \sum_i w_i^{ch}(\Lambda) f_i^{ch}(k_1)^* f_i^{ch}(k_2), \tag{4.9}$$

where $f_i^{ch}(k_1)$ transforms in an irreducible representation of the symmetry group of $W^{\Lambda,ch}(k_1, k_2)$. For the case of zero momentum transfer ($ch = SCs, SCt, FI, PI$) this symmetry group includes the full point group of the underlying lattice, whereas for nonzero momentum transfer ($ch = SDW$, CDW) it only includes an associated subgroup which leaves the ordering vector Q invariant up to reciprocal lattice vectors. In the case of FeSCs, the two-dimensional iron plane has a C_{4v} lattice symmetry, and the eigenmodes f_i^{ch} with ($ch = SCs, SCt, PI, FI$) transform as an irreducible representation of C_{4v}, whereas f_i^{ch} for ($ch = SDW, CDW$) with ordering momentum $Q = (0, \pi)$ transform as an irreducible representation of C_{2v}. The most diverging eigenvalue $w_i^{ch}(\Lambda)$ as a function of energy scale Λ then signals an ordering tendency characterized by the associated order parameter

$$O_i^{ch} = \sum_k f_i^{ch}(k)\langle \hat{O}_k^{ch} \rangle. \tag{4.10}$$

At this, $\hat{O}_k^{ch}$ denotes the respective composite operators defined in (4.7), and the corresponding eigenmode $f_i^{ch}(k)$ reveals further informations on the real-space ordering pattern as well as on the one-particle spectrum within the symmetry broken phase. This in turn becomes apparent if we only

consider the leading correlation channel $W^{\Lambda,ch}(k_1, k_2)$ within a low-energy description:

$$
\begin{aligned}
H_{eff}^{\Lambda} &= H_0 + \sum_{k_1,k_2} W^{\Lambda,ch}(k_1, k_2) \hat{O}_{k_1}^{ch\dagger} \hat{O}_{k_2}^{ch} \\
&\approx H_0 + \sum_{k_1,k_2} w_1^{ch}(\Lambda) f_1^{ch}(k_1)^* f_1^{ch}(k_2) \hat{O}_{k_1}^{ch\dagger} \hat{O}_{k_2}^{ch} \qquad (4.11) \\
&\overset{mf}{=} H_0 + w_1^{ch}(\Lambda) \sum_k \left\{ O_1^{ch} f_1^{ch}(k)^* \hat{O}_k^{ch\dagger} + O_1^{ch*} f_1^{ch}(k) \hat{O}_k^{ch} \right\}. \qquad (4.12)
\end{aligned}
$$

The k-dependent gap opening (SCs, SCt, CDW, SDW) or shift (PI, FI) in the one-particle spectrum is then directly determined by the eigenmode $f_1^{ch}(k)$. Note that in (4.11), we only considered the leading eigenmode contribution as indicated by the subscript "1", and (4.12) involves a mean-field decoupling which in turn becomes exact in the thermodynamic limit [18]. In the following, we will often use the term form factor for $f_i^{ch}(k)$, which is also common in the literature. In order to determine the real-space pattern of the preferred ordering channel, we transform the order parameter (4.10) from band- and $\boldsymbol{k}$-space back to its real-space and orbital representation

$$
O^{ch} = \sum_k f^{ch}(k) \langle \hat{O}_k^{ch} \rangle = \sum_{ij,ab} \tilde{f}_{ab}^{ch}(r_i - r_j) \langle c_{ias}^{(\dagger)} c_{jbs'}^{(\dagger)} \rangle. \qquad (4.13)
$$

Here, the relation between the two form factors $f^{ch}(k)$ and $\tilde{f}_{ab}^{ch}(r_i - r_j)$ is often not transparent due to the matrix elements $u_{aw}(\boldsymbol{k})$ occurring in the transformation back to orbital representation. Below, we will demonstrate this effect by calculating the real-space and orbital-based Cooper-pair wave function.

4.2.5   Flow to Strong Coupling

Following the flow of the full 4-point function V^{Λ} in Fig. 4.6a, we observe several features which can now be related to the different channel couplings $W^{\Lambda,ch}$ derived in the previous section. Therefore, we first note that Fig. 4.6a displays $V^{\Lambda}(k_1, k_2, k_3, k_4)$ at different energy scales Λ as a function of k_1, k_2 with k_3 fixed to position 71 (see Fig. 4.6b) and k_4 determined by momentum conservation. Now, using the identity (4.6) for the different channel couplings, one can easily verify that the vertical features ($k_2 = k_3 + Q$) correspond to the spin-density wave channel, the diagonals ($k_2 = -k_1$) to the pairing channel and the horizontals ($k_1 = k_3 + Q$) to the charge-density wave channel, though with a different sign as in the spin-density wave case. The positions of the vertical and horizontal features then determine the respective ordering momentum Q, and the ferromagnetic and Pomeranchuk channels are associated with the $Q = (0,0)$ spin- and charge-density waves.
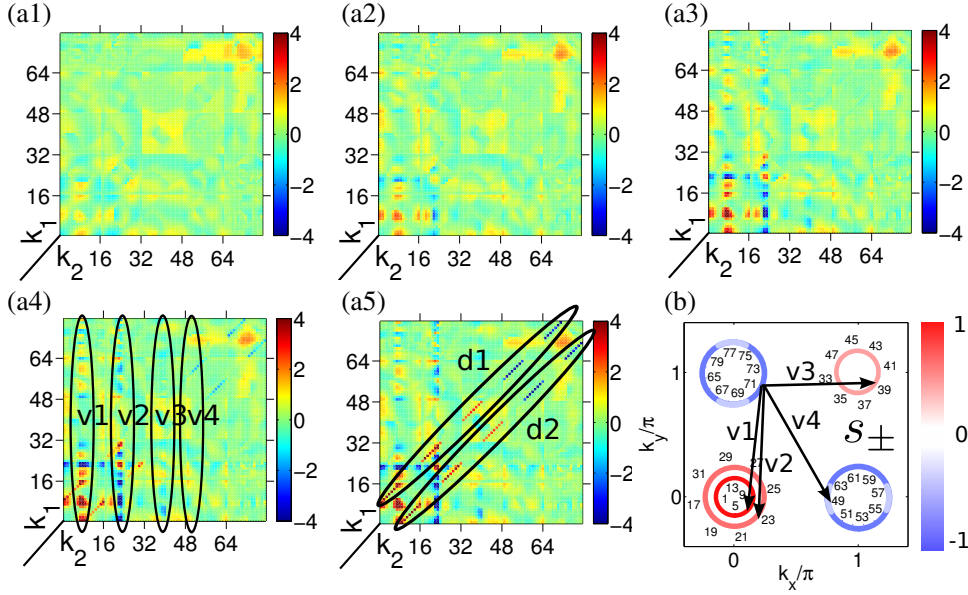
Figure 4.6: (a) $V^\Lambda(k_1, k_2, k_3, k_4)$ as a function of k_1, k_2 with k_3 fixed and k_4 determined by momentum conservation, plotted at five different values of Λ (decreasing from (a1) to (a5)). The numbers 1-80 correspond to positions on the Fermi-surface as indicated in (b). Since k_3 was fixed at position 71 in all (a1)-(a5), the vertical features (v1)-(v4) in the SDW channel correspond to the ordering momenta depicted in (b). The leading antiferromagnetic fluctuations (v1),(v2) drive an $s_\pm$-wave pairing instability (diagonal features (d1),(d2)) with a sign-change between electron- and hole-pockets. The effect of the other two (v3), (v4) will be discussed later. (b) Numbering of the Fermi-surface positions and $s_\pm$-wave gap.

From (4.8) one can further check that the singlet-pairing channel requires the same sign in the upper (d1) and lower (d2) diagonals of Fig. 4.6a, whereas the triplet-pairing channel favors a relative sign change. In addition, the internal sign structure of each channel reflects the leading eigenmode of (4.9) and hence provides informations on the gap symmetry and on the real-space ordering pattern.

4.2.6   Antiferromagnetically Driven Pairing Mechanism

Now, as we identified different physical channels in the 4-point function V^Λ, we can monitor which type of long-range order is preferred and which type of fluctuations serve as a driving force for others. Starting with the initial interaction shown in Fig. 4.6a, we again notice that the bare interaction shows a pronounced k-dependence resulting from the matrix elements $u_{bm}(\boldsymbol{k})$ in (4.4). This initial sign structure can then be rediscovered in the arising SDW fluctuations and will later render the SDW phase gapless. Upon lowering the energy scale Λ from (a1) to (a5) in Fig. 4.6a, these SDW fluctuations become more and more pronounced with the two strongest features (v1)

and (v2) corresponding to an ordering momentum $Q = (\pi, 0)$. Of course, as we do not break lattice symmetries, the same features associated with $Q = (0, \pi)$ are equally strong and appear if the position of the fixed k_3 is rotated by $\pi/2$. The other subdominant SDW fluctuations (v3) and (v4) will have a decisive influence on the anisotropy of the superconducting gap, as will be discussed below.

From the flow pictures (a3) and (a4) it is further apparent that the SDW features (v1,v2) trigger a repulsive inter-pocket pair-scattering $(k, -k) \rightarrow (q, -q)$. During the flow, such pair-scatterings from the electron- to the hole-pockets (inter-pocket) grow stronger (red), whereas the pair-scatterings within the electron-pockets (intra-pocket) weaken and eventually become attractive (blue). At even lower scales, the attractive intra-pocket and the repulsive inter-pocket pair-scatterings are similarly strong in absolute values. Therefore, in order to compensate for the repulsive inter-pocket pair-scattering, the associated gap function changes sign between the hole- and electron-pockets. This reasoning is most clearly seen from the coupling $W^{\Lambda, SCs}$ in the singlet-pairing channel displaying the following structure

$$W^{\Lambda, SCs}(k, q) \sim \begin{pmatrix} -1^{hh} & 1^{he} \\ 1^{eh} & -1^{ee} \end{pmatrix} \begin{matrix} h\text{-pocks} \\ e\text{-pocks} \end{matrix}$$
$$h\text{-pocks} \quad e\text{-pocks}$$

due to the attractive intra-pocket and repulsive inter-pocket pair-scatterings. The eigenmode associated to the leading eigenvalue of $W^{\Lambda, SCs}$ then equals $f_i^{SCs}(k) = (1^h \quad -1^e)^T$ and therefore implies a sign-change between the hole- and electron-like pockets. The corresponding pairing symmetry is commonly termed $s_\pm$-wave as it features sign-changes but, on the other hand, transforms trivially under all point-group actions. In fact, the detailed gap structure is more intricate as the subdominant SDW fluctuations $(v3, v4)$ also favor sign changes in the superconducting gap between the indicated positions of Fig. 4.6b. However, whereas the SDW channel $(v3)$ reinforces the $s_\pm$-wave tendency, $(v4)$ frustrates the sign change between the electron- and hole-like pockets, which in turn leads to pronounced gap anisotropies and even nodes on the electron-pockets (see Fig. 4.6b). For a more precise discussion on this interplay of different competing spin-fluctuations, we refer to Sec. 4.3 and 4.5 or to the article of Hanke et $al.$ [120].

The phenomenology described above is also consistent with a two-patch RG analysis presented by Chubukov et $al.$ [108], where the inter-patch scattering g_3 grows positive and pushes the intra-patch scattering g_4 through zero until both diverge with different sign. However, in our functional RG analysis we take into account the full wavevector dependence around the Fermi surface and we also incorporate the full complexity of a realistic model description. This in turn allows a much more differentiated analysis of the competing phases in FeSCs, which will presented in the following sections.
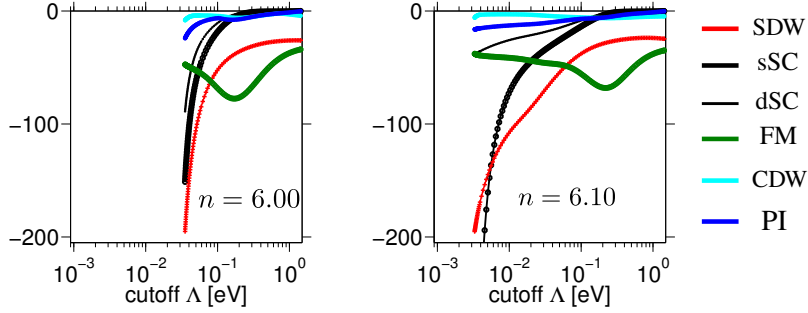
Figure 4.7: Flow of the most leading eigenvalues $w_i^{ch}(\Lambda)$ at $n = 6.00$ and $n = 6.10$ electron filling for the spin-density wave (SDW), singlet pairing (sSC,dSC), ferromagnetic (FI), Pomeranchuk (PI) and charge-density wave (CDW) channels. For the singlet pairing case, we depicted the two leading eigenvalues, of which the first leading one corresponds to $s_\pm$-wave and the second leading one to $d_{x^2-y^2}$-wave order, as will turn out from the associated eigenmodes in Fig. 4.8. The charge- and spin-density wave channels correspond to ordering vectors $(\pi, 0)$ and $(0, \pi)$, which are both degenerate by symmetry.

4.2.7 Channel Flow and Form Factors

In order to develop a broader understanding of the competing phases in FeSCs, we now apply the eigenmode expansion (4.9) and study the flow of the most leading eigenvalues $w_i^{ch}(\Lambda)$. In addition, we also investigate the form factors f_i^{ch} which tell us about the symmetry of the associated order parameter. From the eigenvalue flow in Fig. 4.7, it then turns out that the striped antiferromagnetic phase (SDW) with ordering momentum $Q = (0, \pi)$ or $Q = (\pi, 0)$ is preferred at an electron filling of $n = 6.00$ (undoped). On the other hand, spin-singlet pairing is favored at $n = 6.10$ with a critical energy scale $\Lambda_c \approx T_c$ that is one order of magnitude lower than in the SDW case at $n = 6.00$. A closer look to the corresponding form factors in Fig. 4.8 then reveals that the superconducting phase is of $s_\pm$-wave symmetry (sSC) with a characteristic sign-change between hole- and electron-pockets and with a pronounced anisotropy at X. In the absence of the Fermi-pocket at M, these anisotropies can even lead to nodes (zeros) in the superconducting gap, as will be discussed in Sec. 4.3. The form factor of the SDW phase instead shows a clear nodal behavior which is protected by symmetry [79] due to the transformation behavior of the matrix-elements $u_{am}(\boldsymbol{k})$ in (4.2). However, the real-space order in orbital basis is still of s-wave type with a striped-antiferromagnetic pattern as shown in the (SDW) inset of Fig. 4.8. All these results, including the one of a nodal SDW phase, are in accordance with the overall experimental picture.

In addition, our results also suggest a significant tendency towards $d_{x^2-y^2}$-wave pairing as indicated by the subleading eigenvalue (dSC) in Fig. 4.7. This near degeneracy of $s_\pm$- and $d_{x^2-y^2}$-wave pairing channel can further lead to interesting new phases, as for example a time-reversal symmetry
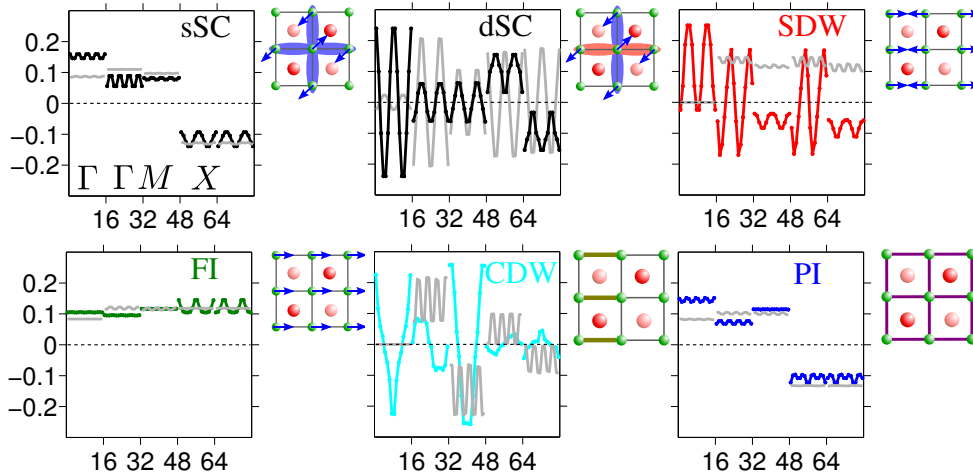
Figure 4.8: Form factors $f^{ch}(k)$ of the leading eigenvalues plotted along the different Fermi-surfaces according to the numbering of Fig. 4.6b. The insets show the nearest-neighbor representation of the corresponding orders. Singlet $s_\pm$-wave (sSC) and $d_{x^2-y^2}$-wave (dSC) pairing orders depicted by its nearest-neighbor wave function, striped antiferromagnetic (SDW) and ferromagnetic (FI) order indicated by blue arrows, Peierls ordering (p-wave CDW) represented by enhanced bond hoppings (olive) and $s_\pm$-wave Pomeranchuk phase leading to a uniform shift of the hopping parameters (purple lines).

broken $(s+id)$-pairing state discussed in Sec. 4.5 or an extended $d_{x^2-y^2}$-wave pairing state presented in Sec. 4.4. Other ordering tendencies like the Pomeranchuk instability (PI), spin-triplet pairing (not shown) and charge-density wave (CDW) channels remain small throughout the entire flow. The ferromagnetic channel (FM), though very pronounced at the beginning, decreases significantly towards low-energy scales.

In order to analyze the influence of the orbital make-up in the electronic states, we also neglect all matrix elements $u_{am}(\boldsymbol{k})$ in the bare interaction (4.4) and simply use $V_0(k_1, k_2, k_3, k_4) = U$ as a starting point of our functional RG implementation. The resulting form factors are then given by the gray lines of Fig. 4.8 and reveal a considerable deviation compared to the ones determined from the correct microscopic interaction. Even though the $s_\pm$-wave pairing symmetry is correctly reproduced, it completely fails to resolve the gap-anisotropies and also predicts a wrong nodeless SDW gap. Therefore, one should carefully interpret the outcomes for such effective interactions which disregard the full complexity of a microscopic multi-orbital interaction.

4.2.8   Real-Space Ordering

In the following section, we uncover the real-space and orbital structure of the different ordering tendencies in FeSCs. For this purpose, we first invert

(a1)   (a2)   (b1)   (b2)
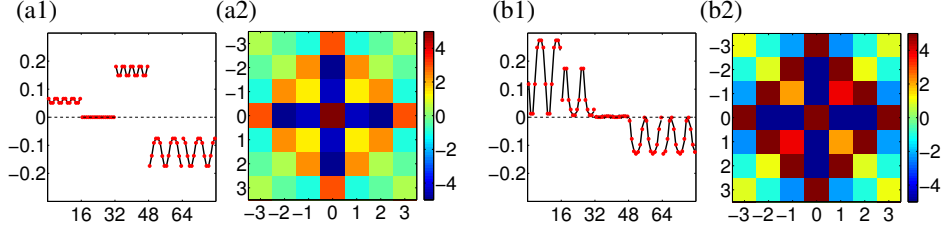
Figure 4.9: Form factors $\tilde{f}_{ab}^{SCs}(k)$ (red points) and harmonic-fit (black lines) for the intra-orbital pairing in the $d_{X^2-Y^2}$-orbital (a1) and d_{XZ}-orbital (b1). (a2,b2) Corresponding pair wave functions $\tilde{f}_{aa}^{SCs}(\boldsymbol{d})$ in dependence of the relative distance $\boldsymbol{d} = \boldsymbol{r}_i - \boldsymbol{r}_j$ plotted in units of the lattice constant. The pair wave function for the electrons in orbital d_{YZ} is obtained by 90 degrees rotation of the one for d_{XZ}. Note that the d_{XZ}-orbital here points to the next-nearest neighbor site.

the transformation from orbital- to band-basis by using

$$\gamma_{\boldsymbol{k}ms} = \sum_{a=1}^{5} u_{am}^*(\boldsymbol{k})c_{\boldsymbol{k}as}, \tag{4.14}$$

and we then rewrite the order parameters (4.10) in terms of $c_{\boldsymbol{k}as}^\dagger$, $c_{\boldsymbol{k}as}$. For the spin-singlet pairing case, this gives rise to

$$O^{SCs} = \sum_{k} f^{SCs}(k)\langle\gamma_{k\uparrow}\gamma_{-k\downarrow} - \gamma_{k\downarrow}\gamma_{-k\uparrow}\rangle$$

$$= \sum_{k,ab} f^{SCs}(k)u_{am}^*(\boldsymbol{k})u_{bm}^*(-\boldsymbol{k})\langle c_{\boldsymbol{k}a\uparrow}c_{-\boldsymbol{k}b\downarrow} - c_{\boldsymbol{k}a\downarrow}c_{-\boldsymbol{k}b\uparrow}\rangle$$

$$= \sum_{ij,ab} \tilde{f}_{ab}^{SCs}(\boldsymbol{r}_i - \boldsymbol{r}_j)\langle c_{ia\uparrow}c_{jb\downarrow} - c_{ia\downarrow}c_{jb\uparrow}\rangle,$$

where we defined the real-space and orbital-based form factor

$$\tilde{f}_{ab}^{SCs}(\boldsymbol{r}_i - \boldsymbol{r}_j) = \sum_{k} e^{i\boldsymbol{k}(\boldsymbol{r}_i-\boldsymbol{r}_j)} f^{SCs}(k)u_{am}^*(\boldsymbol{k})u_{bm}^*(-\boldsymbol{k}).$$

Note here that the k-sum in the last two expressions includes the summation over momenta $\boldsymbol{k}$ and associated band-indices m. According to the discussion in Sec. 3.1, $\tilde{f}_{ab}^{SCs}$ can be interpreted as a wave function of two paired electrons in orbital a and b. In Fig. 4.9, we then pictured $\tilde{f}_{ab}^{SCs}(k) = f^{SCs}(k)u_{am}^*(\boldsymbol{k})u_{bm}^*(-\boldsymbol{k})$ (red points) for the leading intra-orbital pairing $a = b$ between electrons in the $d_{X^2-Y^2}$-orbital (a1) and d_{XZ}-orbital (b1) along the Fermi-surface. The case of d_{YZ} intra-orbital pairing simply follows from the one of d_{XZ} by $\pi/2$-rotation, and the pairing between orbitals other than d_{XZ}, d_{YZ} and $d_{X^2-Y^2}$ is strongly suppressed as these three contribute by far the largest values in $u_{am}(\boldsymbol{k})$. In addition, the pairing between different orbitals is also not favored simply because $\boldsymbol{k}$ and $-\boldsymbol{k}$

share the same orbital weights by symmetry. After that, we further apply a harmonics fit (black lines), which leads to the real-space pair wave functions $f_{ab}^{SCs}(\boldsymbol{r}_i - \boldsymbol{r}_j)$. As the total Cooper-pair momentum is zero, the real-space pairing function features the same translational invariance as the underlying lattice, and we therefore depicted $f_{ab}^{SCs}(\boldsymbol{d})$ in Fig. 4.8(a2,b2) as a function of the relative distance $\boldsymbol{d} = \boldsymbol{r}_i - \boldsymbol{r}_j$. Here, it becomes apparent that the matrix elements $u_{am}(\boldsymbol{k})$ of (4.14) obscure the relation between the form factors in Fig. 4.8 and its corresponding real-space ordering pattern. This is, by the way, also the reason why the $(\pi,0)/(0,\pi)$-SDW gap shows a nodal behavior although its real-space ordering is of conventional structure.

Unlike the spin-density phase, the leading charge-density wave channel shows a p_x/p_y-wave real-space structure for the ordering momenta $(\pi,0)$, $(0,\pi)$ which cannot be ascribed to charge modulations but characterizes a Peierls ordering as shown in the (CDW) inset of Fig. 4.8. Here, certain hopping amplitudes are weakened (thin lines) or enhanced (thick lines), and the corresponding order parameter turns out to be imaginary due to

$$O^{CDW*} = \sum_{i,a,s}(-1)^{i_x}\langle c_{ias}^{\dagger}c_{i+xas} - c_{ias}^{\dagger}c_{i-xas}\rangle^*$$
$$= \sum_{i,a,s}(-1)^{i_x}\langle c_{i+xas}^{\dagger}c_{ias} - c_{i-xas}^{\dagger}c_{ias}\rangle = -O^{CDW}.$$

Note that the real-space patterns displayed in the insets of Fig. 4.8 only represent the nearest-neighbor representation compatible with the symmetry in each channel. Similar to the pair wave function in Fig. 4.9, there are in general also sizeable contributions from higher harmonics.

The real-space form factors of the leading ferromagnetic and Pomeranchuk channels both reveal an s-wave structure in band- and orbital space and its nearest-neighbor representations are shown in the respective insets. Actually, the s-wave Pomeranchuk phase does not break any symmetries and just corresponds to a uniform shift in the hopping-parameters. Other so-called nematic ordering channels with $Q = (0,0)$ and non s-wave form factors, which only break point-group symmetries, are subleading but still close to its s-wave representatives.

4.3 Why Some FeSCs Are Nodal While Others Are Nodeless

In the following section, we address the issue of nodes in the superconducting gap of FeSCs. In particular, we analyse why some FeSCs appear nodal while others are nodeless, despite their similar electronic properties. For example, in the 1111 representative LaFeAsO, a majority of experiments point to the existence of nodeless isotropic gaps [73, 109] on the hole-like Fermi surface (FS) and also nodeless gaps on the electron-like FS, albeit with a larger gap
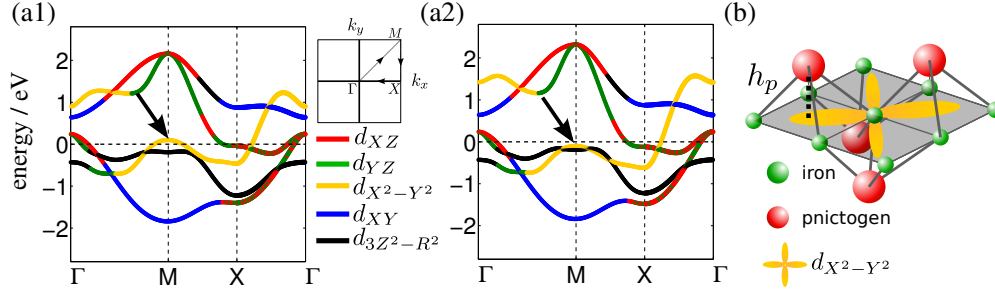
Figure 4.10:   Band structure of LaOFeAs (a1) and LaOFeP (a2) plotted in colors according to its leading orbital content (Inset: Brillouin Zone and orbital color-coding). The dashed horizontal lines denote the Fermi level for the respective undoped compounds. Here, the major difference between (a1) and (a2) is the $d_{X^2-Y^2}$-orbital dominated band, indicated by the arrow, which crosses the Fermi level in (a1), but not in (a2). Being still away from the Fermi level, the $d_{3Z^2-R^2}$-orbital dominated band is shifted up in (a1) compared to (a2). (b) Pnictogen height h_p and position of the iron $d_{X^2-Y^2}$-orbital.

anisotropy [99, 110–113]. On the other hand, in LaFePO, a clear majority of experiments support a nodal gap behavior [114, 115]. This difference is even more puzzling, since both materials display similar FS pockets at the X- and Γ-point of the Brillouin zone, as pointed out in an ARPES study of Lu *et al.* [116].

In what follows, we offer an explanation for the difference between the superconducting gaps in As- and P-based compounds. As it was noted by Kuroki *et al.* [117], the key difference between these two materials consists in a modified pnictogen hight, i.e. the distance measured from the pnictogen to the iron plane (see Fig. 4.10b), which then mainly affects the spread of the iron $d_{X^2-Y^2}$-orbital. Therefore, the appearance of an additional hole-pocket at the M-point of mainly $d_{X^2-Y^2}$-orbital weight is very sensitive to the pnictogen height and, as we will illustrate now, causes a nodal or nodeless pairing gap. The following results are published in:
R. Thomale, C. Platt, W. Hanke, B. Andrei Bernevig, *Mechanism for Explaining Differences in the Order Parameters of FeAs-Based and FeP-based Pnictide Superconductors*, Phys. Rev. Lett. **106**, 187003 (2011).

As a starting point, we use a two-dimensional tight-binding model developed by Kuroki *et al.* [71] to describe the band structure of the 1111-type iron-based superconductors:

$$H_0 = \sum_{\boldsymbol{k},s} \sum_{a,b=1}^{5} c^{\dagger}_{\boldsymbol{k}as} K_{ab}(\boldsymbol{k}) c_{\boldsymbol{k}as}.$$

Here, $c^{\dagger}_{\boldsymbol{k}as}, c_{\boldsymbol{k}as}$ denote the electron creation and annihilation operators, a, b represent the five iron d-orbitals and s the spin projection. While the main electronic structure of P-based and As-based compounds is very similar,

there are certain important differences. Figure 4.10 shows the band structure of LaOFeAs and LaOFeP, where the latter is obtained by adjusting the parameters in [71] according to the changed pnictogen height from As to P [117]. In the vicinity of the Fermi surface, the most notable difference is the presence or absence of a broad $d_{X^2-Y^2}$-orbital dominated band at $M = (\pi, \pi)$, in agreement with ARPES data. To account for this difference, we use a 5 *pocket scenario* for the As-based and a 4 *pocket scenario* for the P-based compounds. The interactions in this model are given by

$$H_{int} = \sum_i \left[U_1 \sum_a n_{ia\uparrow} n_{ia\downarrow} + U_2 \sum_{a<b,s,s'} n_{i,as} n_{ibs'} \right.$$
$$\left. + J_H \sum_{a<b} \sum_{s,s'} c^\dagger_{ias} c^\dagger_{ibs'} c_{ias'} c_{ibs} + J_{pair} \sum_{a<b} \left(c^\dagger_{ia\uparrow} c^\dagger_{ia\downarrow} c_{ib\downarrow} c_{ib\uparrow} + h.c. \right) \right],$$

where n_{ias} denotes the density operator in orbital a at site i and with spin projection s. Here, we consider intra- and inter-orbital interactions U_1 and U_2 as well as the Hund's coupling J_H and the pair-hopping term J_{pair}. In what follows, we choose a physical interaction setting dominated by intra-orbital coupling, $U_1 > U_2 > J_H \sim J_{pair}$, and assume $U_1 = 3.5eV, U_2 = 2.0eV, J_H = J_{pair} = 0.7eV$ [118]. It is also important to note that, even though the interaction scales are relatively high, the bare interaction scale, taking into account the different orbital weights in (4.4), does not exceed $2eV$, whereas the kinetic bandwidth amounts to $5eV$. Actually, this is still a rather simplified picture as the interaction parameters would in general also depend on the different orbitals. However, for the two scenarios representative for As- and P-based compounds, we checked that the main features are stable under variation of these parameters. From the band structure point of view, it should also be noted that the $d_{3Z^2-R^2}$-orbital dominated band moves towards the Fermi level for the P-based compound (Fig. 4.10). However, this band only plays a marginal role since no other relevant band shares the $d_{3Z^2-R^2}$-orbital content, and any scattering to other bands is therefore governed by subleading inter-orbital interactions.

Using the method of functional RG, as described in the previous sections and also in Chap. 2, we study how the renormalized interaction described by the 4-point function V^Λ:

$$V^\Lambda(k_1, k_2, k_3, k_4) \gamma^\dagger_{k_1 m_1 s} \gamma^\dagger_{k_2 m_2 s'} \gamma_{k_3 m_3 s} \gamma_{k_4 m_4 s'} \qquad (4.15)$$

evolves under integrating out high-energy fermionic modes. Here, the flow parameter is an infrared cutoff Λ approaching the Fermi surface, and we also checked the validity of our results by implementing the temperature-flow scheme described in Sec. 2.2. We further employed the condensed notation of $k_i = (\boldsymbol{k}_i, m_i)$ including momenta $\boldsymbol{k}_i$ and band indices m_i. The label s, s'

in (4.15) is again used for the spin projection. Note that in (4.15), we also applied the transformation from orbital- to band-basis ($c_{\boldsymbol{k}as} \to \gamma_{\boldsymbol{k}ms}$) as discussed in Sec. 4.2.2. For a given instability characterized by some finite expectation value of a fermion bilinear $\langle \hat{O}_k^{ch} \rangle \neq 0$, the effective interaction vertex $V^\Lambda(k_1, k_2, k_3, k_4)$ in the particular ordering channel can be written in shorthand notation as $\sum_{k,p} W^{\Lambda,ch}(k,p)\hat{O}_k^{ch\dagger}\hat{O}_p^{ch}$. Accordingly, the coupling $W^{\Lambda,SCs}(k,p)$ in the singlet-pairing channel with $\hat{O}_p^{ch} \sim (\gamma_{p\uparrow}\gamma_{-p\downarrow} - \gamma_{p\downarrow}\gamma_{-p\uparrow})$ can be decomposed into different eigenmode contributions (see Sec. 4.2.4)

$$W^{\Lambda,SCs}(k,p) = \sum_i w_i^{SCs}(\Lambda)f_i^{SCs}(k)^* f_i^{SCs}(p), \qquad (4.16)$$

where i is a symmetry index, and the leading instability of this channel corresponds to the eigenvalue $w_i^{SCs}(\Lambda)$ first diverging under the flow of Λ. The associated form factor $f_i^{SCs}(p)$ then tells us about the pairing symmetry and gap structure. In the functional RG, this quantity $f_i^{SCs}(p)$ is computed along the discretized Fermi surface (see Fig. 4.11a and Fig. 4.12a), and the flow of the leading eigenvalues $w_i^{SCs}(\Lambda)$ is plotted in Fig. 4.11e and Fig. 4.12e.

4.3.1　As-Based Compounds

For the As-based setting, we find that the $s_\pm$-wave pairing instability, giving rise to different gap signs on electron- and hole-pockets, is the leading instability of the model at moderate doping. The setup resembles the situation studied in [118], which, as an additional check, we also studied with a more detailed tight-binding structure beyond 5th next-nearest neighbors. We also find a nodeless $s_\pm$-wave pairing instability. In addition, we can identify the hole-pocket at the M-point to play a major role in contributing to the fully gapped $s_\pm$-wave pairing (Fig. 4.11). In particular, we study the orbital content in detail and analyze how the pairing instability distributes over the different orbitals (Fig. 4.11d). For this purpose, we consider the 4-point function in orbital space

$$V_{c,d\to a,b}^{\Lambda,orb}(\boldsymbol{k}_1, \boldsymbol{k}_2, \boldsymbol{k}_3, \boldsymbol{k}_4) =$$
$$\sum_{n_1,...,n_4=1}^{5} V^\Lambda(k_1, k_2, k_3, k_4)u_{an_1}^*(\boldsymbol{k}_1)u_{bn_2}^*(\boldsymbol{k}_2)u_{cn_3}(\boldsymbol{k}_3)u_{dn_4}(\boldsymbol{k}_4), \qquad (4.17)$$

where the u-coefficients relate the band- and orbital-basis, and also characterize the orbital components of the different bands. The matrix shown in Fig. 4.11d then gives the leading eigenvalue contributions of

$$W_{ab}^{\Lambda,SCs}(\boldsymbol{k},\boldsymbol{p}) = V_{a,a\to b,b}^{\Lambda,orb}(\boldsymbol{k},-\boldsymbol{k},\boldsymbol{q},-\boldsymbol{q}) + V_{a,a\to b,b}^{\Lambda,orb}(-\boldsymbol{k},\boldsymbol{k},\boldsymbol{q},-\boldsymbol{q})$$

i.e. in the spin-singlet Cooper channel of (4.17) where we constrain ourselves to the dominant processes of intra-orbital pairing $(a,a) \to (b,b)$. As above,
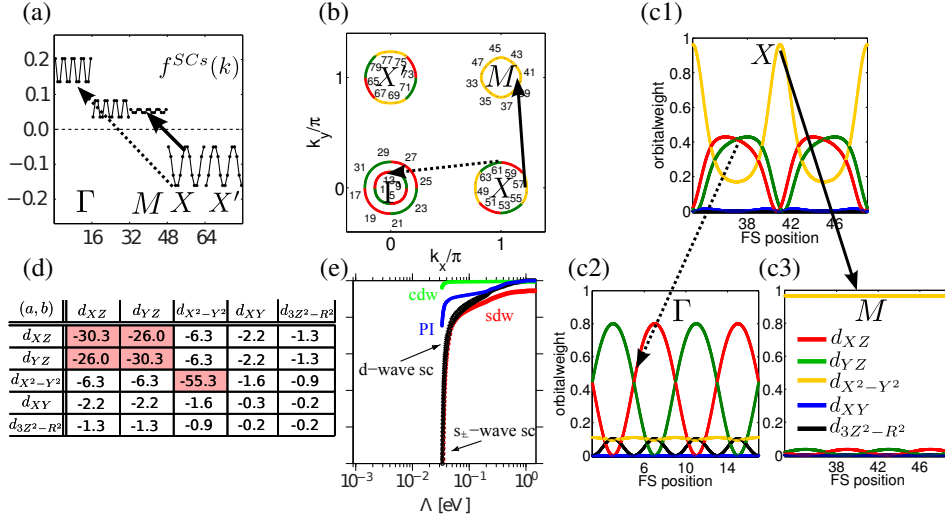
(a,b)	d_{XZ}	d_{YZ}	$d_{X^2-Y^2}$	d_{XY}	$d_{3Z^2-R^2}$
d_{XZ}	-30.3	-26.0	-6.3	-2.2	-1.3
d_{YZ}	-26.0	-30.3	-6.3	-2.2	-1.3
$d_{X^2-Y^2}$	-6.3	-6.3	-55.3	-1.6	-0.9
d_{XY}	-2.2	-2.2	-1.6	-0.3	-0.2
$d_{3Z^2-R^2}$	-1.3	-1.3	-0.9	-0.2	-0.2

Figure 4.11: Five pocket scenario for LaFeAsO. a) Leading pairing form factor $f^{SCs}(k)$ versus patching indices (momenta) shown in b). The gap on the outer hole-pocket at Γ is smaller than of the inner hole-pocket and of the same order as the M pocket gap. The gap on the electron-pockets is very anisotropic but nodeless and of opposite sign from the hole-pocket gap. c1)-c3) Orbital weight distribution on the different pockets (not shown is the outer hole-pocket at Γ, which is similar to c2) rotated by $\pi/2$ assuring orthogonality of the band vectors). Dashed lines indicate most relevant scattering contributions for the dominating U_1 intra-orbital interaction. d) Leading orbital pairing eigenvalues $w^{SCs}_{i,ab}(\Lambda_c)$ from Eq. (4.17): $d_{XZ,YZ}$ and $d_{X^2-Y^2}$ scattering dominates. e) Flow of the leading eigenvalues (charge density wave (CDW), Pomeranchuk instability (PI), spin-density wave SDW, and spin-singlet superconductivity SC). The leading instability appears in the $s_\pm$-wave pairing channel at $\Lambda_c \approx 0.03eV$, d-wave pairing and SDW diverge closely (hardly distinguishable on the log scale).

we decompose $W^{\Lambda,SCs}_{ab}$ into different eigenmodes $\sum_i w^{SCs}_{i,ab}(\Lambda)\tilde{f}^{SCs}_{i,ab}(\boldsymbol{k})^*\tilde{f}^{SCs}_{i,ab}(\boldsymbol{p})$, where the leading eigenvalues at Λ_c for different (a,b) are given in Fig. 4.11d and Fig. 4.12d. Intra-orbital scatterings between the d_{XZ}- or d_{YZ}-orbital dominated parts of the electron- and hole-pockets are most important (see Fig. 4.11). They favor an $s_\pm$-wave pairing instability, as was also found in [118]. However, the leading eigenvalue in the As scenario comes from the diagonal part of the $d_{X^2-Y^2}$-orbital. Pointing in the direction of the $\Gamma \leftrightarrow X$ path, the electron-pocket has a high concentration of the $d_{X^2-Y^2}$-orbital. This part of the electron-pocket then scatters strongly with the hole-pocket at the M-point, which is dominated by the $d_{X^2-Y^2}$-orbital band. The intra-orbital repulsion related to this scattering prefers an $s_\pm$-wave pairing between the hole-pocket at M and the electron-pockets, which reinforces the already present $s_\pm$-wave tendency between the Γ hole-pockets and the X, (X') electron-pockets. Assuming that U_1 is the dominant interaction, the three hole-pockets display a gap of identical sign: two Γ-pockets which are not nested with each other have the same gap sign and are of different orbital content than the hole-pockets at the M-point. However, the electron-

pockets contain contributions from all three relevant d-orbitals. Therefore, the electron-pockets scatter strongly through U_1 with all three hole-pockets, which enhances the $s_\pm$-wave character of the gap.

So, in summary of the As scenario, having the superconducting state orthogonal to the repulsive interaction [119] induced by the presence of the additional M-pocket further increases the $s_\pm$-wave gap between hole- and electron-pockets. The hole-pocket at M is also responsible for the strong SDW signal (4.11) as the nesting wavevector $M \leftrightarrow X$ equals the one between $\Gamma \leftrightarrow X$.

4.3.2   P-Based Compounds

In the P-based compounds, the physical picture changes even qualitatively. As shown in Fig. 4.12, we find a nodal $s_\pm$-wave scenario for the P-based compounds, with lower critical divergence scale $\Lambda_c \sim T_c$ and less SDW-fluctuations. The absence of the M hole-pocket removes the intra-orbital scattering to the electron-pockets. This gives way to previously subleading scattering channels such as, in particular, the pair scattering between the $d_{X^2-Y^2}$-dominated parts of the electron-pockets, but also pair scatterings from the hole-pockets at Γ to the electron-pockets. The former acts between the k-points of the gap function on the electron-pockets given by the peaks and the valleys (Fig. 4.12a) increasing the anisotropy and eventually giving them different signs, thus creating a nodal state. Even if the $d_{3Z^2-R^3}$-orbital dominated band at the M-point (Fig. 4.10a2) were shifted to the Fermi level, the situation remains nearly unchanged as this pocket does not share its orbital content with any other pocket, and hence interactions driven by U_1 are suppressed.

To further substantiate our conclusion, we perform a large sweep in parameter space to resolve the evolution of the superconducting form factor upon varying the interaction parameters. The corresponding results can be found in [120]. From the *ab initio* data stated before, we get $U_1/U_2 \approx 1.5$, $U_1/J_H = U_1/J_{pair} \approx 6.5$. As such, the parameter regime of the As-based and P-based compounds lies in the regime of applicability of our theory and our findings are consistent with experiment: in the P-based compounds, we find (i) a lower divergence scale and, hence, lower T_c compared to As-based compounds, (ii) significantly enhanced low-energy density of states in the (hence nodal) superconducting phase, and (iii) reduced SDW-fluctuations, which, even at pronounced nesting, are insufficient to drive the system to a leading magnetic instability [114–116]. The absence of the hole-pocket at the M-point also manifests itself in the orbital decomposition of the pairing instability (Fig. 4.12d); the diagonal contribution of the $d_{X^2-Y^2}$-orbital, in comparison to the one of the $d_{XZ,YZ}$-orbital, is reduced.

In summary, we find that the broad band at the unfolded M-point plays the major role in explaining the drastic change of superconducting prop-
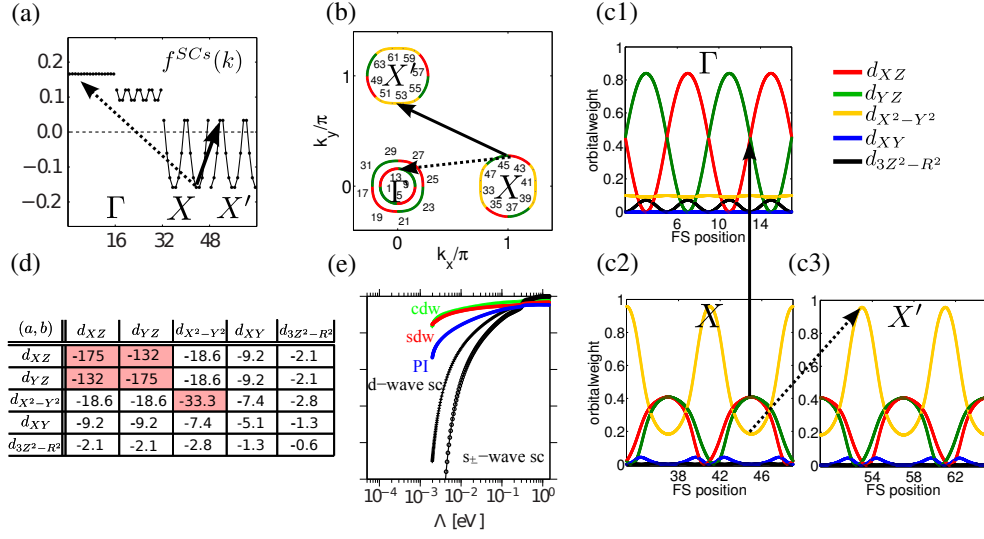
Figure 4.12: Four pocket scenario for LaOFeP. a) Leading $s_\pm$-wave pairing form factor as a function of Fermi-surface positions given in b); the $d_{X^2-Y^2}$-dominated hole-pocket at M is absent, and the hole-pockets at Γ are gapped and isotropic. The electron-pockets show strong anisotropy, being nodal near the $\Gamma \leftrightarrow X(X')$ axes. c) Relevant pair scatterings between different electron-pockets (orbital weights of the pockets are shown in (c1)-(c3)). d) The orbital decomposition of the pairing instability: large $d_{XZ,YZ}$ and less relevant $d_{X^2-Y^2}$ contribution. e) Flow of the leading instability eigenvalues (notation as in Fig. 4.11e); $\Lambda_c \approx 0.002eV$ is smaller than in Fig. 4.11.

erties from the As-based to the P-based 1111 compounds, rendering the former nodeless and the latter nodal. The nodes that appear in the P-based compounds are mainly driven by anisotropy of the electron-pockets. Other compounds such as the 111 representatives LiFeAs and LiFeP display a similar phenomenology of nodal and nodeless pairing (see Sec. 4.6), which has probably the same origin as in the 1111 compounds studied here.

4.4 Exotic d-wave Pairing in Strongly Hole-Doped $K_xBa_{1-x}Fe_2As_2$

In the preceding section, we found that the existence of nodes in the $s_\pm$-wave pairing state of FeSCs is not required by symmetry, but may develop as a compromise between two competing fluctuation channels. Here, the node position was not fixed by symmetry and occurred somewhere near the $\Gamma \leftrightarrow X$ axes on the electron-pockets. It therefore came as a surprise when nodal superconductivity was reported in a strongly hole-doped 122 compound KFe_2As_2 [121–125] where ARPES measurements [126] clearly showed that the two electron-pockets had nearly vanished. In addition, the superconducting transition temperature of $T_c = 3K$ was rather low compared to the moderately doped $K_{0.4}Ba_{0.6}Fe_2As_2$ with $T_c = 38K$ [127],

where all experiments indicate a nodeless superconducting gap [73, 109, 113, 127–130]. For this reason, there must be a nodal to nodeless transition or even a change of the pairing symmetry in between these doping regions.

In the following section, we provide a detailed picture of how the superconducting phase evolves under hole doping in $K_xBa_{1-x}Fe_2As_2$. Here, we find that the nodal pairing phase observed for $x = 1$ is of (extended) d-wave type. Details of this work can be found in:

R. Thomale, C. Platt, W. Hanke, J. Hu, and B. A. Bernevig, *Exotic d-wave Superconducting State of Strongly Hole-Doped $K_xBa_{1-x}Fe_2As_2$*, Phys. Rev. Lett. **107**, 117001 (2011).

We now focus on studying $K_xBa_{1-x}Fe_2As_2$ starting at the optimally doped case around $x = 0.4$ and increasing the hole doping up to $x = 1.0$ in KFe_2As_2. At this, we use an effective 5-band tight-binding model developed by Graser *et al.* [131] to describe the band structure of the 122-type iron-based superconductors (see Fig. 4.13):

$$H_0 = \sum_{\boldsymbol{k},s} \sum_{a,b=1}^{5} c_{\boldsymbol{k}as}^{\dagger} K_{ab}(\boldsymbol{k}) c_{\boldsymbol{k}as}. \qquad (4.18)$$

Here, $c_{\boldsymbol{k}as}^{\dagger}, c_{\boldsymbol{k}as}$ denote the creation and annihilation operators, a, b the five Fe d-orbitals and s the spin index. As seen in Fig. 4.13 and Fig. 4.14, for moderate hole doping, the conventional five pocket scenario with electron-pockets at $X = (\pi, 0, 0)$ and $M = (\pi, \pi, 0)$ emerges. For larger hole doping, the electron-pockets vanish and only small disconnected lobe features are found around X (Fig. 4.14c). The kinetic model then reduces to the effective three-hole-pocket scenario shown in Fig. 4.14c. Other details of the 122 band structure are currently still under debate, with unresolved questions about the Fermi-surface topology at the $Z = (0, 0, \pi)$ point in the three dimensional Brillouin zone and the importance of integrating over the full range along k_z. However, as many of these details mostly affect the electron-pocket anisotropies, they are irrelevant for our proposed pairing mechanism: as we always consider a rather largely hole-doped regime, the electron-pockets can be assumed relatively small – even disappearing in the most interesting case, i.e. that of full hole doping. We, therefore, particularize to the $k_z = 0$ cut of (4.18) in the following, and also omit the lobe features at large hole doping within the RG calculations. To test our assumption of the irrelevance of the k_z dispersion to our results, we have made several other cuts at different k_z and confirmed that our results do not change qualitatively. We cannot ultimately exclude that the lobes may influence the system due to the fact that our Brillouin zone patching scheme is not fully adequate for such small Fermi surface features. Still, within our formalism, we find that the lobes are negligible in the RG flow. A schematic picture of the Fermi-surface topology is given in Fig. 4.13a. Here, the hole-pockets at Γ mainly have d_{xz}- and d_{yz}-
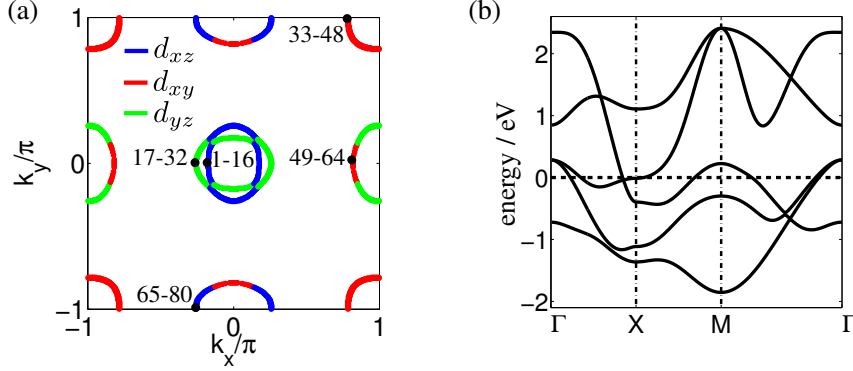
Figure 4.13: (a) Schematic plot of the unfolded Fermi-surface together with the dominant orbital weights. Patches along the pockets are enumerated counterclockwise, starting at each pocket with the patch indicated by a dot. The number of patches with electron-pockets is 80, and without it decreases to 48. (b) The $k_z = 0$ slice of the 122 band structure given in [131].

orbital content, while the hole-pocket at M consists of d_{xy}-orbital weight. When present, the electron-pockets consist of d_{xz}- and d_{yz}-orbital weight. Exceeding a certain size, the front tip along $\Gamma - X$ also has an important d_{xy}-orbital weight on the electron-pockets. We use the conventional onsite orbital model for the interactions, i.e.

$$
H_{int} = \sum_i \left[U_1 \sum_a n_{ia\uparrow} n_{ia\downarrow} + U_2 \sum_{a<b,s,s'} n_{ias} n_{ibs'} \right.
$$

$$
\left. + J_H \sum_{a<b} \sum_{s,s'} c^\dagger_{ias} c^\dagger_{ibs'} c_{ias'} c_{ibs} + J_{pair} \sum_{a<b} \left(c^\dagger_{ia\uparrow} c^\dagger_{ia\downarrow} c_{ib\downarrow} c_{ib\uparrow} + h.c. \right) \right],
$$

where n_{ias} denotes the density operator of orbital a at site i and of spin s. We consider intra- and inter-orbital interactions U_1 and U_2 as well as the Hund's coupling J_H and the pair-hopping term J_{pair}. The corresponding parameter values are chosen close to the ones obtained by constrained RPA calculations [132]: $U_1 > U_2 > J_H \sim J_{pair}$, and set $U_1 = 3.0eV, U_2 = 2.0eV, J_H = J_{pair} = 0.6eV$. While there are variations of these parameters for different classes of pnictides, the values of the parameters are all in the same range, and we have confirmed that variations of 20-30% do not change the picture qualitatively. As a tendency, a comparably large absolute value of U_1 needs to be kept to trigger the pairing instability, where increasing U_2 also helps to increase the critical cutoff scale and, thus, T_c.

Using the multi-band functional RG as described in the previous sections, we study the evolution of the renormalized interaction described by the 4-point function under integrating out high-energy fermionic modes. The diverging channels of this 4-point function under the flow to the Fermi-
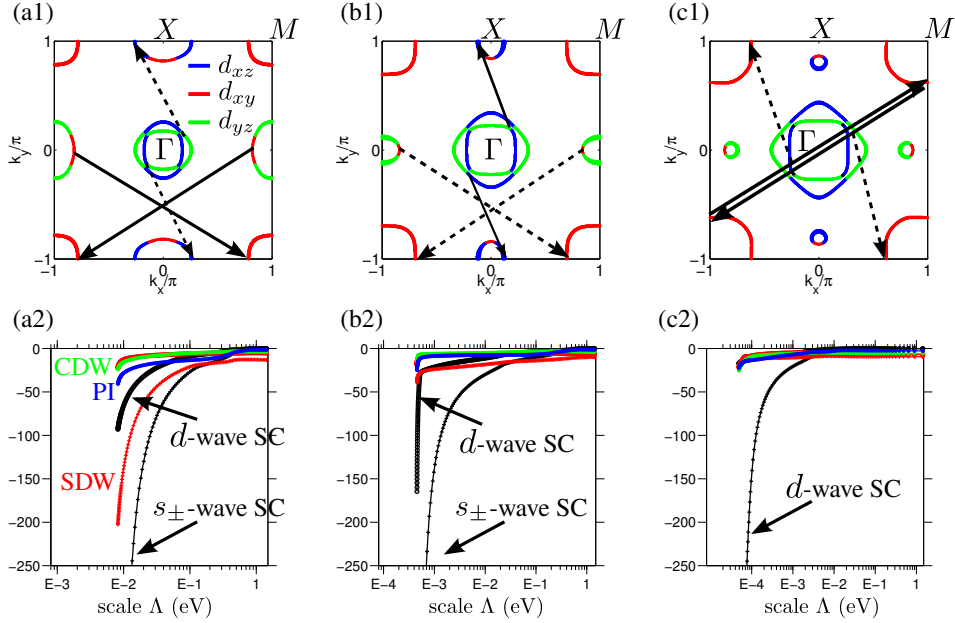
Figure 4.14: Representative scenarios of the Fermi-surface (unfolded BZ) and eigenvalue flows for the electron concentration per iron $n = 5.913$ (a), $n = 5.663$ (b), and $n = 5.346$ in (c). The hole doping of our model calculation in (c), while exceeding the experimental setup $n_{el} = 5.5$, best matches the FS profile from ARPES [126]. The dominant and subdominant scatterings in the Cooper channel are highlighted in (a1)-(c1) by full and dashed arrows. The color contours along the FS label the dominant orbital weights (inset (a1)). The leading eigenvalue flow of the ordering channel for different Fermi instabilities (charge-density wave (CDW), Pomeranchuk (PI), spin-density wave (SDW) and superconductivity (SC)) are plotted in (a2)-(c2) versus the momentum cutoff Λ. For (a) and (b) we find $s_\pm$-wave pairing as the leading Fermi instability. For (c) we observe a leading d-wave pairing instability.

surface then signal the nature of the instability, and the corresponding Λ_c serves as an upper bound for the transition temperature T_c. The Cooper channel of the 4-point function further provides the different pairing form factors - the dominant order parameter having the largest eigenvalue [118, 133–135]. In Fig. 4.14, the leading eigenvalues for different instabilities are plotted against Λ for different fillings between moderately hole-doped from the left to strongly hole-doped to the right. We find that for all scenarios the leading instability is in the Cooper channel.

For the moderately doped case, the electron-pockets are of similar size as the hole-pockets. Figure 4.14 (a1) shows the Fermi-surface structure as well as the dominant (full line) and subdominant scattering (dashed arrow) processes in the Cooper channel. The two major components are given by $\Gamma \leftrightarrow X$ as well as $M \leftrightarrow X$ scatterings. They are particularly important for the front tips of the electron-pockets since these parts can scatter to M via dominant U_1 interaction due to an identical orbital content. The spin-

density wave (SDW) fluctuations are strong, signaling the proximity to the leading magnetic instability scenario of the undoped model (Fig. 4.14 (a2)).

For the intermediate regime, between moderate and strong hole doping, the electron-pockets are already very small (Fig. 4.14 (b1)). The nesting to the hole-pocket is absent, and the SDW fluctuations are strongly reduced. In addition, the SDW fluctuations become less concentrated in the $(\pi, 0)/(0, \pi)$ or (π, π) channel, and spread into various incommensurate sectors [136]. The d_{xy}-orbital weight on the electron-pocket is reduced, and the $M \leftrightarrow X$ scattering becomes subdominant. The main pair scattering is along $\Gamma \leftrightarrow X$. As a consequence, $s_\pm$-wave pairing is still the leading instability, where the form factor and its decomposition into orbital scattering contributions are shown in Fig. 4.15(b1,b2): the largest gap is found for the inner hole-pocket at Γ, followed by the outer hole-pocket and the hole-pocket at M, where the electron-pockets show anisotropic gaps. The orbital decomposition confirms the previous discussion of the dominant scattering contribution, in that the largest weight resides at intra- and inter-orbital scattering of the d_{xz}- and d_{yz}-orbital. However, we already observe that, due to the lack of SDW fluctuations supporting the pairing channel, the critical divergence scale is decreased (Fig. 4.14 (a2)-(c2)). In particular, while still subdominant, we can already see the d-wave pairing evolving as the second-highest eigenvalue in the Cooper channel. When the electron-pockets are still present, the form factor (not shown here) closely resembles the extended d-wave type involving hole- and electron-pockets [133].

At strong hole doping, the electron-pockets are absent, and the hole-pockets are very large. The flow in Fig. 4.14(c2) shows no instability up to small cutoff scales Λ where we find a leading instability in the Cooper channel. Its form factor and orbital scattering decomposition is shown in Fig. 4.15(c1,c2). We observe an extended d-wave instability on the three hole-pockets, with nodes located along the main diagonals in the Brillouin zones (see Fig. 4.15a). A harmonic analysis of the order parameter yields a large contribution of $\cos(2k_x) - \cos(2k_y)$ type and a subdominant $\cos(k_x) - \cos(k_y)$ component, i.e. the form factor is most accurately characterized by $(\cos k_x + \cos k_y)(\cos k_x - \cos k_y)$. The dominant scattering is intra-pocket scattering on the large M hole-pocket, followed by inter-orbital d_{xy} to $d_{xz,yz}$ scattering between $M \leftrightarrow \Gamma$. While the magnetic fluctuations are generally weak in this regime, the dominant contribution is now given by (π, π) SDW fluctuations as opposed to $(\pi, 0)/(\pi, 0)$ for smaller hole doping. For strong hole doping, the hole-pocket at M is large enough to induce higher harmonic d-wave pairing through intra-pocket scattering between the d_{xy}-orbitals as confirmed by the large value of $d_{xy} - d_{xy}$ pairing Fig. 4.15(c2). Via scattering to the other pockets, the superconductivity is likewise induced there, however, with smaller amplitude than for the M-pocket Fig. 4.15(c1). As opposed to conventional first harmonic d-wave pairing, there is no sign change between the extended d-wave form factor on the M-pocket and the
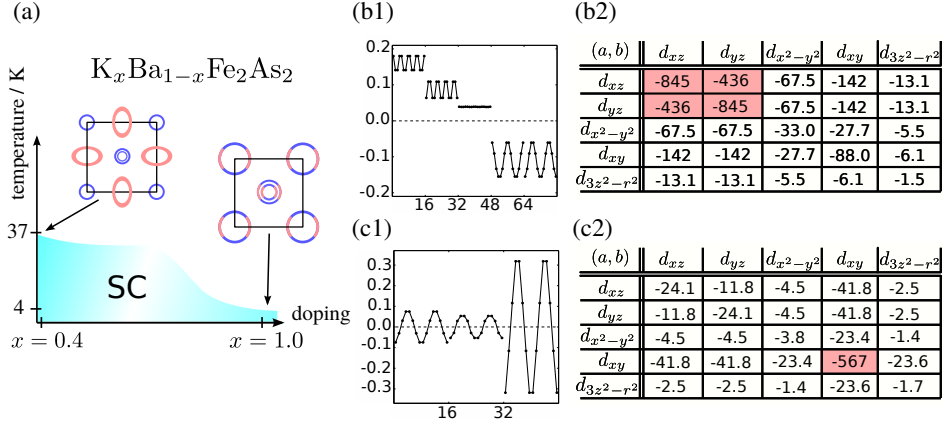
(a) $K_x Ba_{1-x} Fe_2 As_2$

(b1)

(b2)

(a,b)	d_{xz}	d_{yz}	$d_{x^2-y^2}$	d_{xy}	$d_{3z^2-r^2}$
d_{xz}	-845	-436	-67.5	-142	-13.1
d_{yz}	-436	-845	-67.5	-142	-13.1
$d_{x^2-y^2}$	-67.5	-67.5	-33.0	-27.7	-5.5
d_{xy}	-142	-142	-27.7	-88.0	-6.1
$d_{3z^2-r^2}$	-13.1	-13.1	-5.5	-6.1	-1.5

(c1)

(c2)

(a,b)	d_{xz}	d_{yz}	$d_{x^2-y^2}$	d_{xy}	$d_{3z^2-r^2}$
d_{xz}	-24.1	-11.8	-4.5	-41.8	-2.5
d_{yz}	-11.8	-24.1	-4.5	-41.8	-2.5
$d_{x^2-y^2}$	-4.5	-4.5	-3.8	-23.4	-1.4
d_{xy}	-41.8	-41.8	-23.4	-567	-23.6
$d_{3z^2-r^2}$	-2.5	-2.5	-1.4	-23.6	-1.7

Figure 4.15: (a) Qualitative phase-diagram of $K_x Ba_{1-x} Fe_2 As_2$ as a function of doping x with the two determined pairing symmetries depicted in the insets. (b1,c1) Corresponding form factors of the leading pairing instability according to the scenarios in Fig. 4.14(b,c). The numbering in (b1,c1) denotes the position on the Fermi-pockets according to Fig. 4.13a. (b2,c2) Eigenvalues of the orbital decomposition of the superconducting form factor in (b1,c1). Here, the ratio of the values label the relative importance of the orbital scattering channel $V(a, a \to b, b) c_{a\uparrow} c_{a\downarrow} c_{b\downarrow}^\dagger c_{b\uparrow}^\dagger$. In the strongly hole-doped case, we find an extended d-wave form factor with nodal points located along the main diagonal of the Brillouin zone shown in the right inset of (a).

Γ-pocket according to $\cos(2k_x) - \cos(2k_y)$ in Fig. 4.15. This picture of a k-space proximity effect from the M-pocket to the Γ-pockets is substantiated by our checks with calculations involving the M-pocket only, where we see a similar evolution of a pairing instability (the divergence is lower, as the inter-orbital scatterings in the 3-pocket scenario help to renormalize the repulsive Coulomb interactions). This matches the orbital decomposition of the superconducting form factor in Fig. 4.15(c2), showing dominant intra-orbital scattering of the d_{xy}-orbital. As apparent from the ARPES data, the nodal character of the superconducting phase in KFe_2As_2 cannot originate from possible nodes on the electron-pockets (which are gapped out at these doping levels), but must be due to nodes on the hole-pockets. It is then clear that the order parameter cannot be $s_\pm$-wave as it does not tend to allow for an anisotropy that would drive the hole-pockets nodal. The d-wave instability which we find for the strongly hole-doped regime provides an explanation for the general experimental evidence, while the detailed gap structure certainly deserves further investigation [137]. Electron-phonon coupling may change the picture slightly quantitatively, but not qualitatively, as the nodal features, tentatively linked to the d-wave symmetry, are unambiguously observed in experiment. Pnictogen height variations as a function of doping may change the precise value of T_c, and would be important to be studied in general from first principles. Finally, it would be interesting to analyze the transition from $s_\pm$-wave to the d-wave pairing as a function of doping.

4.5   Pairing State with Broken Time-Reversal Symmetry

From the results presented in the previous sections, it became apparent that the multi-pocket Fermi surfaces of FeSCs lead to a complex interplay among pairing interactions, pairing symmetries and Fermi-surface topology. Whereas a repulsive interaction between hole- and electron-pockets gives rise to the $s_\pm$-wave pairing state, the interaction between the two electron-pockets and, as it was the case in the strongly hole-doped $K_xBa_{1-x}Fe_2As_2$, the interaction within the hole-pockets both favor d-wave pairing. As these two pairing symmetries cannot be satisfied simultaneously (see Fig. 4.16a), the system may develop a mixed $(s + id)$-pairing state, which then strikes a compromise between the two competing pairing symmetries. Of course, this compromise is only worthwhile if the frustration between the two pairing tendencies is sufficiently strong. The resulting $(s + id)$-pairing state then obviously breaks time-reversal symmetry (see Sec. 3.1) and shows interesting experimental signatures [138].

Using a combined approach of functional RG and mean-field analysis, we identify the microscopic parameter regime for the $(s + id)$-state, which in turn provides a useful "guiding principle" for an experimental realization of this fascinating pairing state. Details of this work can be found in:
C. Platt, R. Thomale, C. Honerkamp, S. C. Zhang, and Werner Hanke, *Mechanism for a Pairing State with Time-Reversal Symmetry Breaking in Iron-Based Superconductors*, Phys. Rev. B **85**, 180502(R) (2012)

In principle, there are various experimentally tunable parameters to drive the competition between $s_\pm$-wave and d-wave pairing in FeSCs, giving the opportunity to start from both limits.

In $K_xBa_{1-x}Fe_2As_2$, the Fermi surface topology can be chosen as a paradigmatic setup for $s_\pm$-wave, consisting of hole-pockets at $\Gamma = (0, 0)$ and $M = (\pi, \pi)$, as well as two electron-pockets at $X = (\pi, 0)/(0, \pi)$ for optimal doping $x \simeq 0.4$. Upon increasing x, however, the electron-pockets decrease, and have nearly disappeared for $x = 1$ as shown in Fig. 4.16, which has been suggested to host a d-wave pairing symmetry (see Sec. 4.4). In this system, it is hence plausible that an $(s + id)$-pairing state can be realized for intermediate values of x.

In the chalcogenide $K_xFe_{2-y}Se_2$, the electron-pockets at the X-points dominate, and, for a situation seemingly inverse to KFe_2As_2, a d-wave pairing symmetry may likewise be expected [139, 140]. It should be noted that the actual pairing symmetry in the chalcogenides is far from settled, as a strong coupling perspective may likewise suggest $s_\pm$-wave pairing [141]. By tuning doping or other possible parameters affecting the band structure such as pressure, one possibly induces a pocket at the Γ-point, increasing the ten-
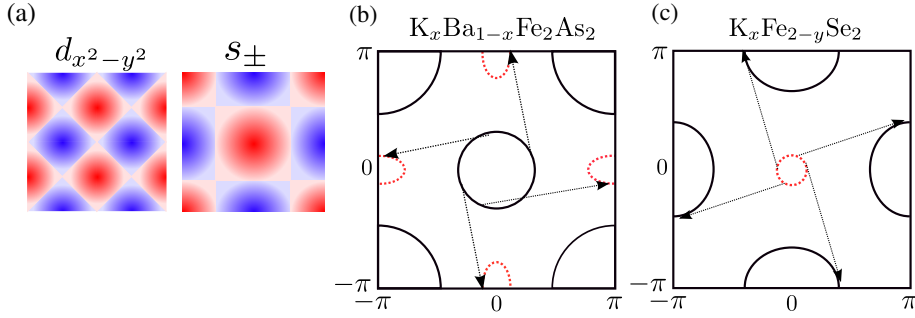
Figure 4.16: (a) The two competing pairing symmetries in FeSCs. Frustrating the d-wave limits of $K_xBa_{1-x}Fe_2As_2$ (b) and $K_xFe_{2-y}Se_2$ (c). Upon doping or differently induced band structure effects, electron-pockets appear (dashed red) in (b) and a hole-pocket appears (dashed red) in (c), which then populate the $q \sim (\pi, 0)/(0, \pi)$ scattering channels and enhance the $s_\pm$-wave pairing symmetry. This leads to frustration and provides the background for $(s + id)$-pairing.

dency towards $s_\pm$-wave pairing (see Fig. 4.16). In this case, one could also expect an $(s + id)$-pairing state. By systematically tuning the Fermi-pocket topologies, one can compare the predicted pairing symmetries with experiments, starting from compound settings with a suspected d-wave symmetry (see Fig. 4.16).

In the following, we rather intend to start from an $s_\pm$-wave pairing state instead, and address how we can enhance the competitiveness of the d-wave symmetry to drive the system into the $(s + id)$ regime. The reason for this is two-fold. First, the $s_\pm$-wave pairing symmetry is much more generic for the different classes of FeSCs. Second, as we will see below, we find the most promising setup to be located on the electron doped side of pnictides, where high-quality samples have already been grown for different families. We hence believe that this regime may be the experimentally most accessible scenario at the present stage, which is why we explicate it in detail. In this paper, we investigate the microscopic mechanism of the $(s + id)$-pairing state by means of a functional RG analysis of a five band model. We systematically vary the doping level and the strength of intra-orbital interaction, which determine the ratio between the electron-hole pocket and the electron-electron pocket mediated pairing interactions. In this microscopic investigation, we find that the $(s + id)$-pairing state can be realized in the intermediate electron-doped regime, given that we also adjust the pnictogen height parameter of the system appropriately.

We start from a representative 5-band model for the pnictides obtained from LDA-type calculations [71]. The same model has also been considered in Sec. 4.3 as a starting point for explaining the difference between the isovalent P-based and As-based 1111 compounds [134]. The LDA "non-

interacting" part is given by

$$H_0 = \sum_{\boldsymbol{k},s} \sum_{a,b=1}^{5} c^{\dagger}_{\boldsymbol{k}as} K_{ab}(\boldsymbol{k}) c_{\boldsymbol{k}bs}. \qquad (4.19)$$

Here, $c^{\dagger}_{\boldsymbol{k}as}, c_{\boldsymbol{k}as}$ denote the electron creation and annihilation operators, a, b the iron d-orbitals and s the spin indices. In addition, the matrix $K_{ab}(\boldsymbol{k})$ is characterized by the orbital (i.e. maximally-localized Wannier function) matrix-elements of the Kohn-Sham Hamiltonian. The corresponding band structure then features electron-pockets at X and hole-pockets at Γ, which is the typical situation in FeSCs (see Fig. 4.17) for sufficient electron doping. The many-body interaction part is given by the intra- and inter-orbital interactions U_1 and U_2, as well as the Hund's coupling J_{H} and the pair hopping J_{pair}:

$$H_{int} = \sum_{i} \left[U_1 \sum_{a} n_{ia\uparrow} n_{ia\downarrow} + U_2 \sum_{a<b,s,s'} n_{ias} n_{ibs'} \qquad (4.20) \right.$$

$$\left. + J_H \sum_{a<b} \sum_{s,s'} c^{\dagger}_{ias} c^{\dagger}_{ibs'} c_{ias'} c_{ibs} + J_{pair} \sum_{a<b} \left(c^{\dagger}_{ia\uparrow} c^{\dagger}_{ia\downarrow} c_{ib\downarrow} c_{ib\uparrow} + h.c. \right) \right],$$

where n_{ias} denote the density operators at site i of spin s and orbital a. Typical interaction settings are dominated by intra-orbital coupling, $U_1 > U_2 > J_{\mathrm{H}} \sim J_{\mathrm{pair}}$. In the multi-band functional RG (see Sec. 4.2), one starts from the bare many-body interaction (4.20) in the Hamiltonian. The pairing is dynamically generated by systematically integrating out the high-energy degrees of freedom including all important fluctuations on equal footing. This differs from the RPA which takes right from the outset a magnetically driven spin-fluctuation type of pairing interaction. For a given instability characterized by some finite expectation value of a fermion bilinear $\langle \hat{O}^{ch}_k \rangle \neq 0$, the effective interaction vertex $V^{\Lambda}(k_1, k_2, k_3, k_4)$ in the particular ordering channel can be written in shorthand notation as $\sum_{k,p} W^{\Lambda,ch}(k,p) \hat{O}^{ch\dagger}_k \hat{O}^{ch}_p$. Accordingly, the effective interaction $W^{\Lambda,SCs}(k,p)$ in the singlet-pairing channel can be decomposed into different eigenmode contributions (see Sec. 4.2.4)

$$W^{\Lambda,SCs}(k,p) = \sum_{i} w^{SCs}_i(\Lambda) f^{SCs}_i(k)^* f^{SCs}_i(p), \qquad (4.21)$$

where i is a symmetry index, and the leading instability of that channel corresponds to the eigenvalue $w^{SCs}_i(\Lambda)$ first diverging under the flow of Λ. The associated form factor $f^{SCs}_i(p)$ then tells us about the pairing symmetry and gap structure. In the functional RG, from the final Cooper
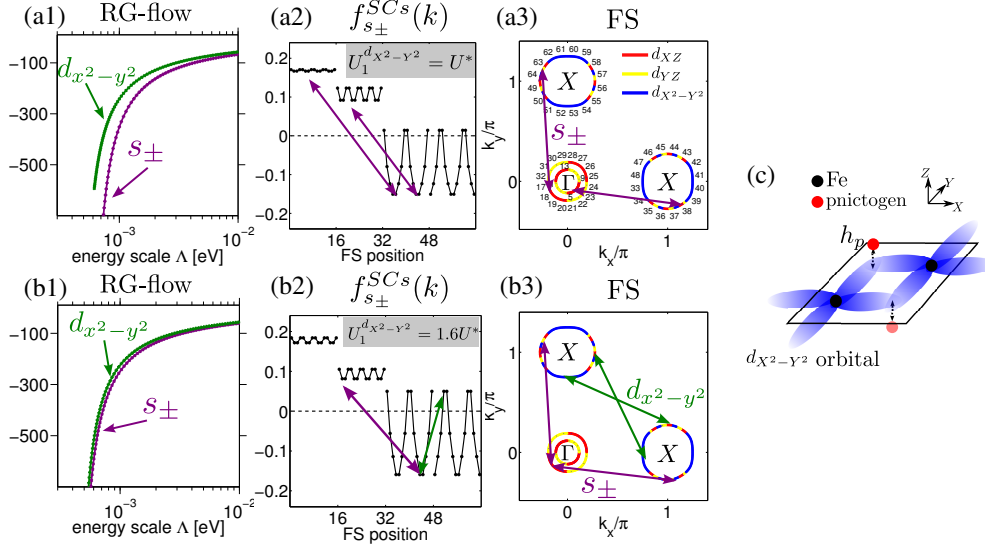
Figure 4.17: Competing pairing orders and $s_\pm$-wave pairing form factors for $U_1(d_{X^2-Y^2}) = U^* = 2.5eV$ (a) and $U_1(d_{X^2-Y^2}) = 1.6U^*$ (b) at the electron doped filling of $n = 6.13$. RG channel flow (a1,b1) and $s_\pm$-wave gap form factor (a2,b2). $s_\pm/d$-wave transition from (a) to (b): increasing $U_1(d_{X^2-Y^2})$ enhances the gap anisotropy of the $s_\pm$-wave form factor on the electron-pockets (**k**-patching: points 33-64 see (a3)) shown in (a2,b2) until the extended $d_{x^2-y^2}$-wave pairing becomes competitive. The d-wave form factor (not shown) does not change from (a) to (b). (a3,b3) Interactions mediated by U_1, inducing $s_\pm$-wave pairing tendency ($\Gamma \leftrightarrow X$) and competing $d_{x^2-y^2}$-wave pairing symmetry due to ($X \leftrightarrow X$). (c) Variation of the pnictogen height h_p mostly affects the spread of the $d_{X^2-Y^2}$-orbital and therefore $U_1(d_{X^2-Y^2})$, as it is oriented to the planar projection of the pnictogen.

channel in the effective interaction vertex, this quantity $f_i^{SCs}(p)$ is computed along the discretized Fermi surfaces as shown in Fig. 4.17(a3), and the flow of the leading eigenvalues $w_i^{SCs}(\Lambda)$ are plotted in Figs. 4.17(a1) and (b1). The interaction parameters are kept fixed at the representative setup $U_1 = 2.5eV, U_2 = 2.2eV, J_{\mathrm{H}} = 1.2eV, J_{\mathrm{pair}} = 0.2eV$. Note that the value of U_1 on the $d_{X^2-Y^2}$-orbital is varied as explicitly stated in Figs. 4.17 and 4.18. The relatively large bare value of J_H is motivated partly by recent findings, in particular, for a sizable Hund's rule coupling [142, 143]. Furthermore, as a parameter trend, larger J_H and smaller J_{pair} tends to prefer the $(s + id)$-phase in the electron-doped regime for rather moderate values of the intra-orbital coupling U_1 (see Fig. 4.18).

The situation in Fig. 4.17 is representative for moderate electron doping and interaction scales of FeSCs, where the $\Gamma \leftrightarrow X$ pair scattering between the hole-pockets at Γ and the electron-pockets at X dominates. Already from the BCS gap equation, a finite momentum transfer can induce pairing only when the wavevector of such an interaction connects regions on one Fermi surface (such as in the cuprate case), or regions on different Fermi

surfaces (such as in the pnictide case), which have opposite signs of the superconducting order-parameter. This corresponds to putting the electron pairs in an anisotropic wave function such as sign-reversing $s_\pm$-wave in Fig. 4.17a, where the wave vector $(\pi, 0)$ in the unfolded Brillouin zone connects hole- and electron-pockets with a sign-changing $s_\pm$-wave gap [90, 108]. However, in the functional RG calculation of Fig. 4.17b with increased U_1 interaction on the $d_{X^2-Y^2}$-orbital, a green arrow for $X \leftrightarrow X$ scattering indicates additional interactions that become similarly important as the $(\pi, 0)$ channel. This increased U_1 can be tuned by the pnictogen height as explained below and frustrates the previous "pure" $s_\pm$-wave limit $(\Gamma \leftrightarrow X)$. The system then strikes a compromise [120] by enhancing the anisotropy of the $s_\pm$-wave form factor (denoted by $f_{s_\pm}^{SCs}(k)$ in Fig. 4.17) on the electron-pockets at X. Throughout this variation of parameters, the sign-changing d-wave form factor (not shown) remains nearly unchanged, providing nodes on the hole-pockets and gaps on the electron-pockets as they do not intersect with the nodal d-wave lines $k_x = \pm k_y$ in the Brillouin zone. This is because the d-wave-driving $X \leftrightarrow X$ scattering is hardly affected by this change of parameters. Instead, the $s_\pm$-wave form factor changes significantly and adjusts the momentum dependence of the gap, i.e. its anisotropy, so as to minimize the effect of the Coulomb repulsion (Fig. 4.17).

We now have all ingredients to tune the pairing symmetry from $s_\pm$-wave to extended $d_{x^2-y^2}$-wave, and, eventually, into the time-reversal symmetry broken $(s+id)$-phase. In most of the FeSCs, the tendency towards $s_\pm$-pairing occurs slightly more pronounced than the competing extended $d_{x^2-y^2}$-wave pairing, and, at first glance, the resulting frustration appears to be too small for causing $(s+id)$-pairing. Therefore, in order to increase frustration, we somehow have to enhance the pair-scattering between the electron-pockets at X which then promotes the subleading $d_{x^2-y^2}$-wave channel. As shown in a-priori determinations of the interaction parameters in (4.20), expressed in terms of orbital matrix elements, the pnictogen height h_p (measured from the iron-plane as pictured in Fig. 4.17c) has a substantial influence on the intra-orbital interaction U_1 between $d_{X^2-Y^2}$-Wannier orbitals [72], which can be either modified by isovalent doping or pressure. By increasing h_p, the Wannier functions in this orbital are further localized, causing an increase of $U_1(d_{X^2-Y^2})$. In Fig. 4.17b, we have already used this fact to demonstrate that, for moderate electron doping (13%), large values of this matrix element drive the pairing instability from $s_\pm$-wave to extended $d_{x^2-y^2}$-wave symmetry. Note that in the situation where we expect $(s+id)$-pairing to occur, both the d-wave and the $s_\pm$-wave exhibit nodal features in the form factor.

For this general scenario, we present our predictions for time-reversal symmetry breaking in the schematic phase diagram of Fig. 4.18. Here, we plotted the leading $s_\pm$-wave, $d_{x^2-y^2}$-wave and finally the $(s+id)$-pairing solutions as a function of $U_1(d_{X^2-Y^2})$, and electron doping. For this purpose,
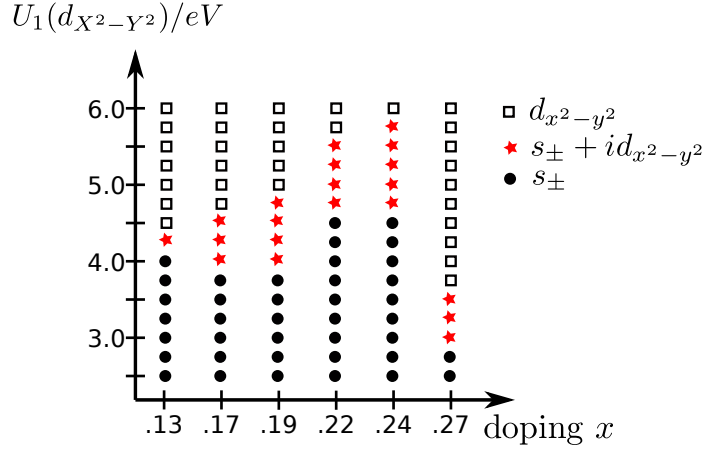
$U_1(d_{X^2-Y^2})/eV$

Figure 4.18: Preferred pairing symmetry as a function of electron doping and intra-orbital Coulomb interaction $U_1(d_{X^2-Y^2})$. The results are obtained by minimizing the mean-field free energy of the effective theory taken from functional RG at $\Lambda \approx 0.001eV$. For 27% electron doping, the $(s+id)$-pairing state occurs at $U_1(d_{X^2-Y^2}) = 3eV$, which is comparable to the intra-orbital repulsion in the remaining orbitals of $U_1 = 2.5eV$.

we used our functional RG result as a starting point for a renormalized mean-field analysis [17]. In this combined approach, the one-loop flow is stopped at a scale Λ which is small compared to the bandwidth, but still safely above the scale Λ_c, where the 2-particle vertex diverges. In this range, the particular choice of the cutoff Λ does not significantly influence the results of Fig. 4.18. The renormalized coupling function $V^\Lambda(k_1, k_2, k_3, k_4)$ is then taken as an input for the mean-field treatment of the remaining modes (see Sec. 2.6). As shown in Fig. 4.17, the regime of $s_\pm/d$-wave pairing competition features a single-channel pairing instability without other competing (e.g. magnetic) instabilities and, therefore, justifies

$$V^\Lambda(k_1, k_2, k_3, k_4) \approx W^{SCs}(k_1, k_3)\delta_{k_2,-k_1}\delta_{k_4,-k_3}, \qquad (4.22)$$

with $W^{SCs}(k_1, k_3) = V^\Lambda(k_1, -k_1, k_3, -k_3)$. The effective theory for quasi-particles near the Fermi surface ($|\xi(k)| < \Lambda$) is modeled by the reduced Hamiltonian

$$H^\Lambda = \sum_{ks} \xi(k)c^\dagger_{ks}c_{ks} + \frac{1}{N}\sum_{k,q} W^{SCs}(k,q)c^\dagger_{k\uparrow}c^\dagger_{-k\downarrow}c_{-q\downarrow}c_{q\uparrow}, \qquad (4.23)$$

where $\xi(k)$ is taken as the bare dispersion due to only weak band renormalization effects. The mean-field solution of this reduced Hamiltonian is obtained as in BCS theory, by solving the self-consistent gap-equation and calculating the corresponding grand potential (see Eq. (2.94)):

$$\Omega^{stat} = -\sum_k \frac{|\Delta_k|^2 + 2\xi(k)^2}{2\sqrt{\xi(k)^2 + |\Delta_k|^2}} + \sum_k \xi(k). \qquad (4.24)$$

Within a reasonable range of parameters for the electron-doped FeSCs, we then find a regime favoring $(s + id)$-pairing due to

$$\Omega_{s+id}^{stat} < \Omega_{s_\pm}^{stat}, \Omega_d^{stat}.$$

The system hence prefers to evolve into a time-reversal symmetry broken pairing state. This is intuitive from the viewpoint of condensation energy in the superconducting phase. While both $s_\pm$-wave and d-wave possess nodal features individually, the combination $(s + id)$ allows to avoid these nodes which then stabilizes the condensate.

Note that the phase regime investigated by us is only a lower bound for the possible existence of $(s + id)$-pairing which may even be larger. This is because the functional RG setup at present only allows us to obtain the leading pairing instability at some finite Λ_c, while the $(s+id)$-phase may well set in below Λ_c. This would manifest itself as a change of the superconducting phase as a function of temperature in experiment.

In summary, we have presented a microscopic analysis, based on a-priori electronic structure determinations and a combination of the functional RG with a mean-field treatment of the remaining low-energy states, to derive a kind of "guiding principle" for a possible $(s+id)$-pairing state in the FeSCs. For the case of increased electron doping and pnictogen height, we have illustrated how this drives the system into an $(s + id)$-pairing state. Aside from this example, other regimes in the FeSCs likewise promise a possible realization of an $(s + id)$-state, such as hole-doped (K,Ba)-122 interpolating between the $s_\pm$-wave limit $(x \sim 0.4)$ and d-wave limit $(x \sim 1)$ as well as possibly the chalcogenides $K_x Fe_{2-y} Se_2$.

4.6   Superconductivity in LiFeAs

Soon after the synthesis of the 1111 and 122 pnictides, LiFeAs as a representative of the 111 family, has been detected with a superconducting phase at $T_c \sim 18K$ [82, 144]. Unlike most of the other FeSCs, LiFeAs becomes superconducting without the need of doping or pressure and shows neither a structural transition nor the usual spin-density wave order. This, together with the report of a nonvanishing Knight-shift in some of the samples [145] and an observed fishtail effect [146] lead to an early proposal of a triplet pairing state in LiFeAs. In addition, ARPES measurements [147] pointed out the proximity to a van-Hove singularity, which was then taken up in an RPA calculation of Brydon *et al.* who started with a three-band ARPES fit and predicted a ferromagnetic fluctuation induced triplet pairing state $\hat{\Delta} \sim \hat{\boldsymbol{z}}(p_x + ip_y)$, similar to the one proposed for strontium ruthenate (see Chap. 6). The possible realization of such a chiral pairing state in LiFeAs with a relatively high T_c of $18K$, opposed to strontium ruthenate with $T_c = 1.5K$, was therefore very appealing. However, after one year, a

growing number of experiments found evidence for antiferromagnetic fluctuations, as for example in NMR measurements [148] and neutron scattering [149], which in addition also reported a magnetic resonance and hence provided strong indications for a usual $s_\pm$-wave pairing. On the other hand, it seems commonly accepted that the superconducting gap is nodeless as confirmed by a large body of experimental results like NMR [150], specific heat [151], ARPES [152] and penetration depth measurements [153, 154], which is however consistent with both $s_\pm$-wave and $(p + ip)$-pairing.

In order to explore these different ordering tendencies, we apply a combined approach of density functional theory (DFT) and functional RG (fRG) which connects a precise ab initio description with the unbiased analysis of functional RG. At this, the DFT description provides a band structure matching ARPES [147] and quantum oscillation measurements, [77] with a nontrivial k_z-dependence. In addition, DFT also enables to compute the orbital dependent interaction parameters. Both of these model informations are essential to explain the interesting properties of LiFeAs. Using the combined DFT+fRG approach, we find that, despite the presence of strong ferromagnetic fluctuations, LiFeAs features a nodeless $s_\pm$-wave pairing state similar to the one in LaFeAsO. Interestingly, its phosphorus based realization LiFeP (111) exhibits nodal superconductivity, which is reminiscent of the nodeless/nodal behavior in LaFeAsO/LaFePO, discussed in Sec. 4.3. Therefore, upon closer inspection, LiFeAs does not appear to be much different from other FeSCs. Details of this work can be found in:
C. Platt, R. Thomale, and W. Hanke, *Superconducting state of the iron pnictide LiFeAs: A combined density-functional and functional-renormalization-group study*, Phys. Rev. B **84**, 235121 (2011)

We again start with the construction of an ab-initio effective Hamiltonian for LiFeAs. As an input to our functional RG calculations, we employ data from a recent work of Miyake *et al.* [72], where details of the ab-initio procedure can be found. The first step is a conventional band-structure calculation in the framework of LDA. From there, "target bands" are chosen around E_F, which define the band complex and the corresponding orbitals, in our case the five d-orbitals of the iron-$3d$ electrons. Simultaneously, the maximally localized Wannier functions (MLWF) are extracted, which, via their matrix elements of the Kohn-Sham Hamiltonian H_{KS}, determine the transfer integrals $t_{mn}(\vec{R})$

$$t_{mn}(\vec{R}) = \langle \phi_{m\vec{0}} | H_{KS} | \phi_{n\vec{R}} \rangle. \tag{4.25}$$

Here, $\phi_{n\vec{R}}(\vec{r})$ denotes the MLWF centered at site $\vec{R}$ for the n-th orbital. The one-body Hamiltonian part is then given by

$$H_0 = \sum_{i,j,\sigma} \sum_{m,n} t_{mn}(\vec{R}_i - \vec{R}_j) a_{in}^{\sigma\,\dagger} a_{in}^{\sigma} \ ,$$

where $a_{in}^{\sigma\,\dagger}$ (a_{in}^{σ}) denote the creation (annihilation) operators of the corresponding MLWF with spin σ. In the second step, effective interaction parameters are extracted in terms of MLWF-matrix elements [72]. A partially screened Coulomb interaction at zero frequency $W(\vec{r}, \vec{r}'; \omega = 0)$ is calculated in the so-called cRPA, i.e. with the constraint that for the "high-energy" non-target bands RPA screening is employed [155]. Note, that the Coulomb interactions $U_{mn}(\vec{R}) = \langle \phi_{m\vec{0}} \phi_{m\vec{0}} | W | \phi_{n\vec{R}} \phi_{n\vec{R}} \rangle$ and exchange interactions $J_{mn}(\vec{R}) = \langle \phi_{m\vec{0}} \phi_{n\vec{0}} | W | \phi_{n\vec{R}} \phi_{m\vec{R}} \rangle$ are orbital dependent, comprising the interaction Hamiltonian:

$$H_I = \frac{1}{2} \sum_{\sigma\delta} \sum_{ij} \sum_{nm} \Big\{ U_{mn}(\vec{R}_i - \vec{R}_j) a_{in}^{\sigma\dagger} a_{jm}^{\rho\dagger} a_{jm}^{\rho} a_{in}^{\sigma}$$

$$+ J_{mn}(\vec{R}_i - \vec{R}_j) \left(a_{in}^{\sigma\dagger} a_{jm}^{\rho\dagger} a_{in}^{\rho} a_{jm}^{\sigma} + a_{in}^{\sigma\dagger} a_{in}^{\rho\dagger} a_{jm}^{\rho} a_{jm}^{\sigma} \right) \Big\}. \qquad (4.26)$$

One challenging problem of the "down-folding" is that, for entangled bands, it is not clear a priori how to "cut out" the d-subspace of the iron-orbitals, and how to unambiguously distinguish the screening channels within the d-space from the total screening. For a practical solution of this problem see again [155] and references therein.

The final data of the ab-initio calculations consisting of band structure, Fermi surfaces, and bare interaction parameters are summarized in Fig. 4.19. The 111 compounds have a relevant dispersion orthogonal to the FeAs layers (Fig. 4.19a) for which we consider both the $k_z = 0$ and $k_z = \pi$ cut. The main features of the z-dispersion are the change of orbital weight along the Fermi surface as well as the absence of the small second hole-pocket at Γ for $k_z = \pi$. As seen from the interaction matrix, e.g. the intra-orbital interactions (with comparably high absolute interaction scales up to 3.85 eV) differ by more than 30% between different orbitals, stressing the need to consider fully orbital-dependent parameters.

It is further important to note that we start from the DFT and not from a full quasi-particle and Green functions description which would employ the type of interactions accounted for in our plaquette diagrams of the 4-point function $V_\Lambda(\boldsymbol{k}_1 n_1, \boldsymbol{k}_2 n_2, \boldsymbol{k}_3 n_3, \boldsymbol{k}_4 n_4)$, but would also include the renormalization of the single-particle Green function (2-point function) due to self-energy effects [13]. While this has not yet been accomplished for the iron pnictides due to conceptual reasons in certain approaches and technical difficulties in others such as our RG, one can provide several arguments supporting the DFT as a reasonable starting point: it is a well-established fact that the DFT-type of calculations employing H_{KS} (Eq. 4.25), e.g. in an LDA-version, produce rather reliable Fermi surfaces in comparison with experiments such as ARPES. Obviously, this is crucial for RG treatments flowing towards the infrared limit at the Fermi surface. In addition, it is also known from existing quasi-particle calculations in various solids [156, 157] that one can get accurate results for electronic single-particle excitations by
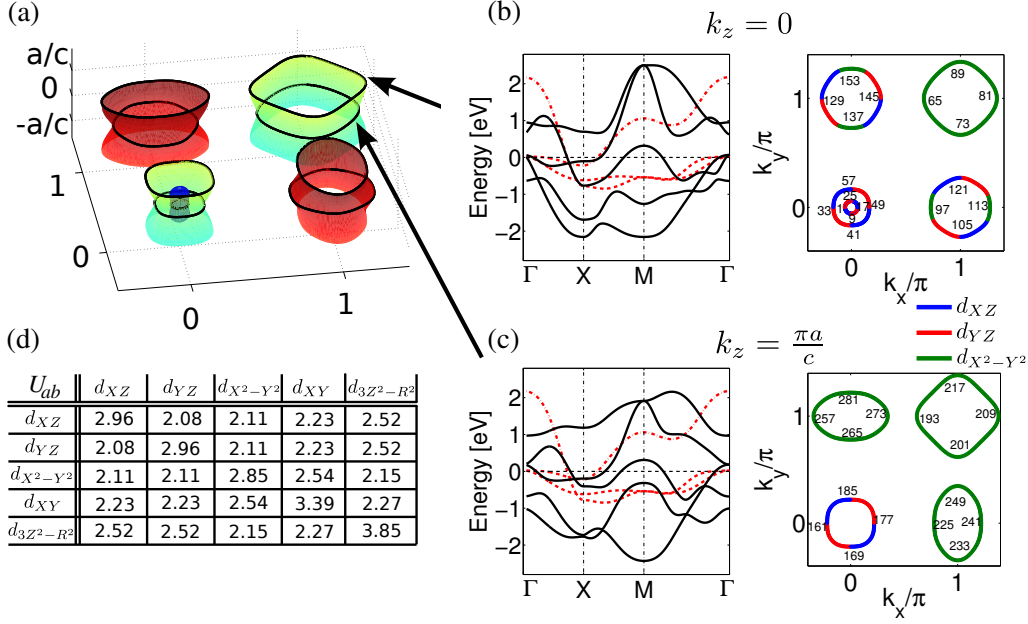
(a)

(b) $k_z = 0$

(c) $k_z = \dfrac{\pi a}{c}$

(d)

U_{ab}	d_{XZ}	d_{YZ}	$d_{X^2-Y^2}$	d_{XY}	$d_{3Z^2-R^2}$
d_{XZ}	2.96	2.08	2.11	2.23	2.52
d_{YZ}	2.08	2.96	2.11	2.23	2.52
$d_{X^2-Y^2}$	2.11	2.11	2.85	2.54	2.15
d_{XY}	2.23	2.23	2.54	3.39	2.27
$d_{3Z^2-R^2}$	2.52	2.52	2.15	2.27	3.85

Figure 4.19: Summary of the ab-initio input on LiFeAs for the DFT-fRG. (a) Three dimensional Fermi surface with visible dispersive features along k_z. 5-orbital band structure and Fermi surfaces for (b) $k_z = 0$ cut of the bands (Brillouin zone patches from 1 to 160) and (c) $k_z = \pi$ cut (Brillouin zone patches from 161 to 288), corresponding to the patching in the insets of Fig. 4.20. The red dashed lines denote the 3-band model used in [158]. Brillouin zone patches and dominant orbital weights are indicated along the Fermi surfaces. (d) Orbital dependent interaction matrix U_{ab} as obtained from cRPA calculations [72].

using the DFT (LDA) Bloch- or Wannier-functions in lowest order. This is because the wave functions are essentially determined from the largest term in the single-particle Hamiltonian being the Hartree potential. Therefore, the interaction part of our Hamiltonian (Eq. 4.26) which is extracted from DFT-Wannier functions should, in principle, also be rather accurate.

Using multi-band functional RG, high-energy electronic excitations ($\varepsilon > \Lambda$) are recursively integrated out, arriving at an effective low-energy interaction or 4-point vertex function $V^\Lambda(k_1, k_2, k_3, k_4)$. Here, $k_i = (\boldsymbol{k}_i, n_i)$ is a condensed notation with $n_1, \ldots n_4$ labeling the different (in our case five) bands of the band complex considered and $\boldsymbol{k}_1$ to $\boldsymbol{k}_4$ denoting the incoming and outgoing momenta. When the infrared cutoff Λ approaches the Fermi surface, a diverging renormalized 4-point function then signals a corresponding instability towards a symmetry-broken phase, with Λ_c serving as an upper bound for the transition temperature T_c. In addition, we also employ a temperature-flow scheme and compare it to the results obtained by the conventional cutoff-flow functional RG [8]. At each renormalization iteration, one sums over the five one-loop diagrams [13, 107, 159], i.e. over the Cooper, spin-density wave (SDW), screening and vertex-correction chan-
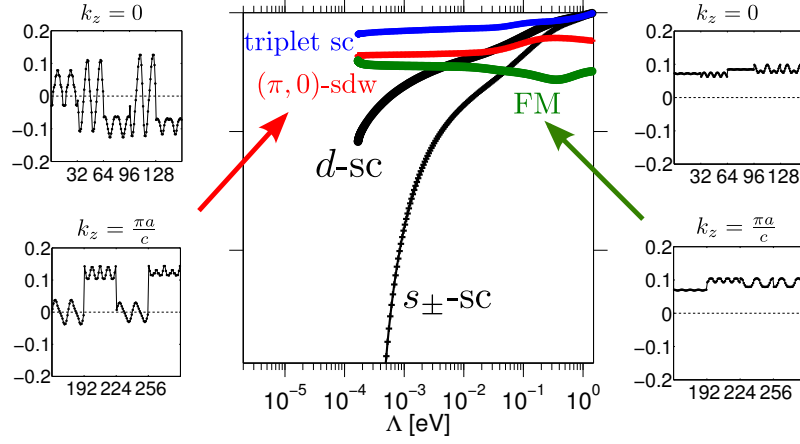
Figure 4.20: Functional RG temperature flow for LiFeAs. The form factors for nodal spin density wave (SDW) (red) and ferromagnetic (FM) fluctuations (green) are shown in the left and right inset. At $\Lambda \sim 0.01eV$, the SDW becomes competitive to FM. The triplet SC (blue) channel is irrelevant and does hardly evolve under the flow. The main instability resides in the singlet SC channel, with $s_\pm$-wave (black crosses) dominating the d-wave solution (filled black circles). The $s_\pm$-wave type form factor is displayed in Fig. 4.21.

nels to arrive at the renormalized vertex function. Technical details of our functional RG procedure can be found in Chap. 2 or in [118, 133, 134]. Due to practical limitations, approximations are made, such as the neglect of the frequency dependence of the 4-point vertex function V^Λ and projecting the external momenta $\boldsymbol{k}_1, \ldots \boldsymbol{k}_3$ onto the Fermi surface (with $\boldsymbol{k}_4$ being determined from momentum conservation). For a given instability characterized by the condensation of a fermion bilinear $\langle \hat{O}_k^{ch} \rangle \neq 0$ (the most important example of which is the singlet-pairing instability $\hat{O}_k^{SCs} = (c_{k\uparrow}c_{-k\downarrow} - c_{k\downarrow}c_{-k\uparrow})$ for LiFeAs), the 4-point function in the particular ordering channel can be written as $\Sigma_{k,p} W^{\Lambda,SCs}(k,p)\hat{O}_k^{SCs\dagger}\hat{O}_p^{SCs}$. It can be decomposed into different eigenmode contributions $W^{\Lambda,SCs}(k,p) = \sum_i w_i^{SCs}(\Lambda)f_i^{SCs}(k)^* f_i^{SCs}(p)$ where i is a symmetry index. The leading instability of a given channel corresponds to the eigenvalue $w_1^{SCs}(\Lambda)$ first diverging under the flow of Λ. The associated eigenmode $f_1^{SCs}(k)$ is the superconducting form factor which tells us about the pairing symmetry and gap structure. For all different ordering channels, the form factors are computed along the discretized Fermi surfaces. (Shown are the ferromagnetic (FM) and spin density wave (SDW) form factor in the insets of Fig. 4.20 as well as the singlet pairing form factor in Fig. 4.21.)

The flow of these leading eigenvalues is summarized in Fig. 4.20. We find that, for high cutoffs (temperatures), the FM fluctuations are dominant in correspondence to previous studies [158]. By removing the small hole-pocket at Γ, we checked that it is, indeed, the main resource for FM
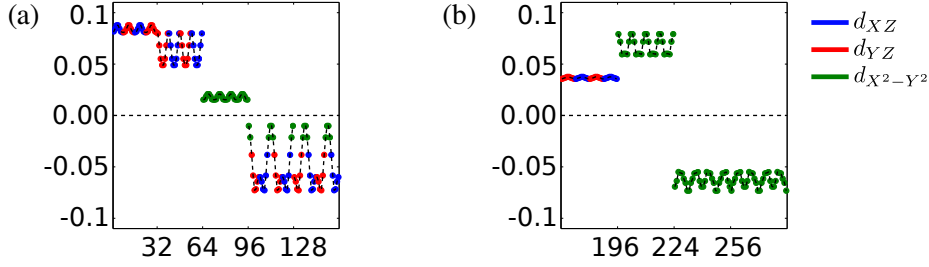
Figure 4.21: Leading superconducting form factor along the cuts for $k_z = 0$ (a) and $k_z = \pi a/c$ (b). The dominant orbital weights for the different patches are indicated by color. The form factor shows multi-gap nodeless anisotropic $s_\pm$-wave pairing order.

fluctuations. At intermediate scales, however, we see in Fig. 4.20 that the collinear SDW fluctuations, driven by hole- to electron-pocket scattering along $(\pi, 0)$ and $(0, \pi)$, become competitive and finally seed an $s_\pm$-wave pairing instability. The same result is identically obtained both for the cut-off and the temperature flow parameter formulation. The latter is more adequate to track FM fluctuations. From there, the vertex flow can be understood along the lines of other pnictide families [118, 134]. These results for the functional RG flow can be physically interpreted by looking at a simplified 2-pocket scenario containing the small hole-pocket at the Γ-point as well as the electron-pocket at X. In the RG treatment of such a 2-pocket scenario [108, 120], one generally finds that the intra-pocket repulsive part of the Coulomb interaction dominates over the repulsive inter-pocket scattering. The reason is that the small q-screening in the intra-pocket term is less effective than the large q-screening in the inter-pocket processes. This holds in the particle-particle as well as the particle-hole channels and is the reason why the small q, i.e. ferromagnetic fluctuations, dominate at and around the initial "high-energy" scale. As discussed in Refs. [120] and [108], however, in the RG the intra-pocket repulsive part of the Coulomb interaction in the pairing channel is renormalized in the flow, eventually even changing its sign to become attractive. Yet, the pairing flow is dominated by the repulsive inter-pocket pair scattering with wavevector $(\pi, 0)$ connecting the electron- and hole-pocket. Thus, in RG, the pairing wave function is optimized in the sense that it gives the largest negative pairing eigenvalue for $s_\pm$-wave pairing.

The form factor of the pairing instability for LiFeAs is plotted in Fig. 4.21 along the $k_z = 0$ and $k_z = \pi$ cuts. The $k_z = 0$ cut in Fig. 4.21a looks typical as for other FeSCs and displays an $s_\pm$-wave form factor changing sign between hole- and electron-like pockets with strong anisotropy features along the electron-pockets. As indicated by the dominant orbital weights along the different patches, we find from Fig. 4.21 that the form factor can be well understood in a scenario where the superconducting form factor seeks

to minimize intra-orbital repulsion, which is the most relevant interaction scale [120]. For $k_z = \pi$, the largest hole-pocket gap is given by the M pocket as it can scatter to the electron-pockets at X through intra-orbital interactions. Since the orbital weight for these pockets is uniformly of $d_{X^2-Y^2}$-type, the form factor anisotropies on the electron-pockets are rather small.

In summary, we have introduced the DFT-fRG formalism to describe Fermi surface instabilities by taking into account a-priori DFT (LDA) band parameters and orbital-dependent interactions, providing a low-energy description in an unbiased fashion. We have applied the DFT-fRG to LiFeAs and find the leading pairing instability to be of $s_\pm$-wave type. Our results of a nodeless superconducting gap are confirmed e.g. by very recent high-precision measurements of the magnetic penetration depth in clean single crystals of LiFeAs [160], which are consistent with previous experimental studies [150–154]. Within functional RG, the FM fluctuations at "high temperatures" are overcome by SDW fluctuations in the effective low-energy sector. These findings are further supported by recent inelastic neutron scattering experiments [149] which reveal a similar pairing mechanism in LiFeAs as in other FeSCs and do not feature any evidence for spin-triplet p-wave superconductivity. Still, LiFeAs provides an interesting and, in particular, experimentally accessible arena to investigate the interplay of ferromagnetic, antiferromagnetic, and superconducting fluctuations.

4.7 Summary and Outlook

Besides its exceptionally high transition-temperatures of up to $56K$, the newly discovered class of FeSCs also attracted great interest due to their variety of different compounds. In order to gain deeper insights into the mechanism of high-T_c superconductivity, it is therefore promising to understand the similarities and distinctions between those different compounds. For this purpose, we applied the functional RG approach and studied the pairing symmetry as well as the underlying mechanism in different material representatives of the FeSCs.

The findings presented here reveal that the pairing in FeSCs is generally driven by antiferromagnetic fluctuations which in turn result from a nested multi-pocket Fermi surface. As the mediated pairing becomes most effective if the superconducting gap changes sign between the nested Fermi-surface portions, the leading spin-fluctuation mode between the hole- and electron-like pockets then gives rise to the $s_\pm$-wave pairing symmetry. However, the multi-pocket Fermi-surface as well as the multi-orbital structure of the low-lying states complicate this picture and also lead to other spin-fluctuation modes which favor competing pairing states with, for example, d-wave symmetry. Depending on this interplay of different spin-fluctuation channels, the $s_\pm$-wave pairing state either appears nodeless or nodal, and

may even change its symmetry to d-wave. At the same time, the transition temperature decreases if there are several competing pairing orders.

In the preceding sections, we used the functional RG to verify this picture in a microscopic model description, and we demonstrated how material specific properties like the pnictogen height or the doping level affect this interplay of different spin-fluctuation channels. For example, we explained why the smaller pnictogen height in LaFePO compared to LaFeAsO causes a transition from nodeless to nodal $s_{\pm}$-wave pairing with considerably smaller T_c. The same phenomenology of a nodeless and nodal $s_{\pm}$-wave pairing also occurs in the 111 compounds, as was shown in the calculation for LiFeAs. We further studied the doping dependence of the pairing symmetry in $\mathrm{Ba}_{1-x}\mathrm{K}_x\mathrm{Fe}_2\mathrm{As}_2$ and found a transition from $s_{\pm}$-wave to d-wave pairing. Finally, we also explored the conditions for a time-reversal symmetry broken $(s + id)$-pairing state by means of a combined approach of functional RG and mean-field analysis.

Chapter 5

Competing Instabilites in Doped Graphene

5.1 Introduction

Since the first fabrication of graphene in 2004 by Novoselov and Geim [161], this fascinating material attracted great interest and generated valuable insights for fundamental science as well as future applications. At the same time, the structure of graphene is fairly simple and consists of carbon atoms arranged in a hexagonal (honeycomb) lattice structure as pictured in Fig. 5.1a. Although its layered analog graphite is known for centuries and is used in any lead pencil, the isolation and detection of a single atomic graphite sheet was for a long time not considered possible. In fact, graphene was the first truly two-dimensional crystalline structure which could be produced and investigated in experiment. In 2010, Novoselov and Geim were therefore honored with the Nobel Prize for their decisive contributions to this development.

Besides its remarkable mechanical features, graphene mainly aroused interest due to its unique electronic properties [162], like the room-temperature quantum Hall effect or the realization of Klein tunneling. Most of these exceptional properties can in turn be ascribed to the close resemblance between the Hamiltonian of graphene and that of massless, relativistic particles. In particular, this similarity is reflected in the respective low-energy spectrum showing linear dispersing bands (see Fig. 5.1b) as well as a vanishing density of states at the Fermi-level. The role of electronic interactions in this semi-metallic environment is on the other hand far from trivial. For example, Meng *et al.* [163] reported that graphene may host an exotic spin-liquid phase at moderate local interactions right before antiferromagnetic order sets in at higher interaction values. In addition, Raghu *et al.* [164] pointed out that longer-ranged interactions in graphene can also generate topological Mott phases displaying quantum Hall and quantum spin Hall like behavior.

(a)

(b)
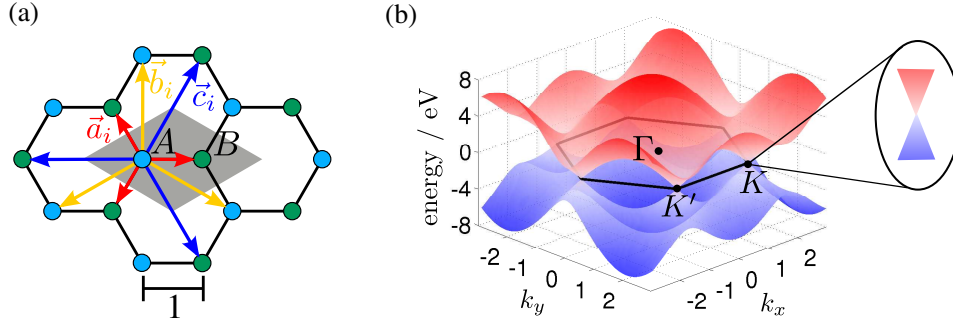
Figure 5.1: (a) Lattice structure of graphene together with the two atomic unit-cell (gray) and the three nearest-neighbor bonds $\vec{a}_i$, $\vec{b}_i$, $\vec{c}_i$. Band structure of graphene for $t_1 = 2.8, t_2 = 0.7, t_3 = 0.02$eV within the hexagonal Brillouin zone (black) as well as the zoomed-in Dirac-cone.

Yet, all these non-trivial phases require a minimum interaction strength as the vanishing density of states at the Fermi-level would otherwise suppress any kind of weak-coupling instability. This behavior of course changes if we vary the carrier density away from the intrinsic half-filled case ($x = 1/2$). Note that x here is defined by $x = n_{el}/2$ with n_{el} denoting the number of electrons per site. According to Fig. 5.2c, the density of states then increases away from half-filling and thus allows for electronic instabilities at arbitrary small interactions. This is, by the way, naturally fulfilled in bilayer graphen which features quadratic rather than linear band-crossings and which therefore displays a number of fascinating weak-coupling instabilities [165, 166].

Doping the single-layer graphene away from half-filling, the Fermi level approaches one of the two van-Hove singularities (VHS) at $x = 3/8$ and $x = 5/8$. Here, the diverging density of states as well as the near-nested Fermi-surface (see Fig. 5.3a) suggest a variety of competing many-body phases with relatively high transition temperatures. Experimentally, this regime has recently become accessible by chemical doping [167] and electrolytic gating [168], which both induce nearly no disorder in the underlying lattice structure. Using ARPES measurements, McChesney *et al.* [167] probed the band structure of such highly doped graphene and indeed found extended saddle points at the Fermi-level as well as a nearly nested Fermi-surface.

Motivated by these experimental findings, we study the competing many-body instabilities in doped graphene and predict a rich phase diagram including topological superconductivity, an exotic spin-order as well as spin-triplet pairing. Although there have been different proposals about superconductivity [169, 170] and magnetic ordering [171] in doped graphene, the competition between these different phases as well as the dependence on the system parameters is poorly understood. For this reason, we apply the method of functional RG which allows an unbiased investigation of the different many-body phases and, at the same time, also enables to include the

full band structure details as well as longer-ranged interactions. Here, the effect of longer-ranged interactions is in turn crucial for a correct model description away from the exact VHS and is also essential for a directed adjustment of certain system parameters through dielectric substrates. The following results are published in:

M. Kiesel, C. Platt, W. Hanke, D. A. Abanin, R. Thomale, *Competing many-body instabilities and unconventional superconductivity in graphene*, Phys. Rev. B **86**, 020507(R) (2012).

5.2   Model and Implementation

As the low energy band structure of graphene is mainly determined by the π-band complex, a convenient starting point consists of a tight-binding model for one single p_z-orbital at each lattice site. The corresponding Hamiltonian including up to third nearest-neighbor hopping is then given by

$$H_0 = \left[t_1 \sum_{\langle i,j \rangle, \sigma} c_{i,\sigma}^\dagger c_{j,\sigma} + t_2 \sum_{\langle\langle i,j \rangle\rangle, \sigma} c_{i,\sigma}^\dagger c_{j,\sigma} + t_3 \sum_{\langle\langle\langle i,j \rangle\rangle\rangle, \sigma} c_{i,\sigma}^\dagger c_{j,\sigma} + \text{h.c.} \right] - \mu n,$$

where $n = \sum_{i,\sigma} n_{i,\sigma} = \sum_{i,\sigma} c_{i,\sigma}^\dagger c_{i,\sigma}$ labels the electron density and $c_{i,\sigma}^\dagger$, $c_{i,\sigma}$ denote the creation and annihilation operator of an electron with spin σ at site i. According to [162], the hopping parameters are determined by $t_1 = 2.8, t_2 = 0.1, t_3 = 0.07 eV$. As the unit-cell of graphene contains two atoms A, B (see Fig. 5.1a), the Hamiltonian H_0 in momentum-space representation can then be written as

$$H_0 = \sum_{\boldsymbol{k}\sigma} \begin{pmatrix} c_{\boldsymbol{k}A,\sigma}^\dagger & c_{\boldsymbol{k}B,\sigma}^\dagger \end{pmatrix} \begin{pmatrix} A(\boldsymbol{k}) - \mu & B(\boldsymbol{k}) + iC(\boldsymbol{k}) \\ B(\boldsymbol{k}) - iC(\boldsymbol{k}) & A(\boldsymbol{k}) - \mu \end{pmatrix} \begin{pmatrix} c_{\boldsymbol{k}A\sigma} \\ c_{\boldsymbol{k}B\sigma} \end{pmatrix}, \quad (5.1)$$

with the following abbreviations

$$A(\boldsymbol{k}) = 2t_2 \sum_{j=1,2,3} \cos(\boldsymbol{k} \cdot \vec{b}_j)$$

$$B(\boldsymbol{k}) = 2t_1 \sum_{j=1,2,3} \cos(\boldsymbol{k} \cdot \vec{a}_j) + 2t_3 \sum_{j=1,2,3} \cos(\boldsymbol{k} \cdot \vec{c}_j)$$

$$C(\boldsymbol{k}) = 2t_1 \sum_{j=1,2,3} \sin(\boldsymbol{k} \cdot \vec{a}_j) + 2t_3 \sum_{j=1,2,3} \sin(\boldsymbol{k} \cdot \vec{c}_j)$$

and bond vectors $\vec{a}_i$, $\vec{b}_i$, $\vec{c}_i$ (see Fig. 5.1a):

$$\vec{a}_1 = (1,0), \qquad\qquad \vec{b}_1 = (0, \sqrt{3}), \qquad\qquad \vec{c}_1 = (-2, 0)$$
$$\vec{a}_2 = (-1/2, \sqrt{3}/2), \qquad \vec{b}_2 = (3/2, -\sqrt{3}/2), \qquad \vec{c}_2 = (-1, \sqrt{3})$$
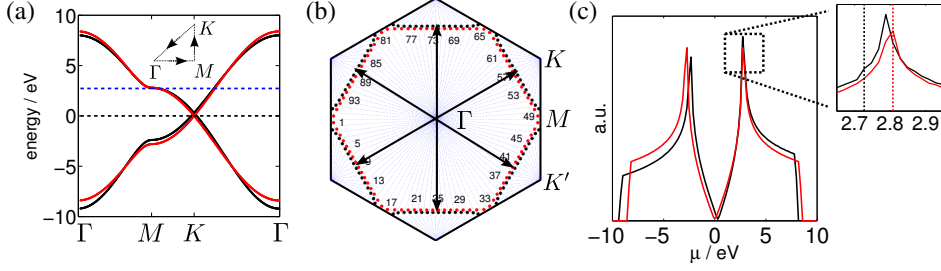
Figure 5.2: (a) Band structure of graphene for $t_1 = 2.8, t_2 = t_3 = 0eV$ (red) and $t_1 = 2.8, t_2 = 0.1, t_3 = 0.07eV$ (black). (b) Brillouin zone displaying the Fermi surface near the van Hove point (dashed blue level in (a)) with 96 patches used in the implementation of the functional RG as well as the (partial) nesting vectors. (c) Density of states for both band structures in (a). The inset shows the position shift of Fermi surface nesting (dashed vertical lines) versus the VHS peak.

$$\vec{a}_3 = (-1/2, -\sqrt{3}/2), \qquad \vec{b}_3 = (-3/2, -\sqrt{3}/2), \qquad \vec{c}_3 = (-1, -\sqrt{3}).$$

The resulting band structure shown in Fig. 5.2a then consists of two bands

$$E_{1,2}(\boldsymbol{k}) = \pm\sqrt{B(\boldsymbol{k})^2 + C(\boldsymbol{k})^2} + A(\boldsymbol{k}) - \mu,$$

which can be easily verified by diagonalizing (5.1). Most of the previous studies on undoped graphene focused on the linear dispersing part near the two inequivalent (not connected through reciprocal-lattice vectors) momenta $\boldsymbol{q} = K, K'$. Here, the band structure is given by

$$E_{1,2}(\boldsymbol{q} + \delta\boldsymbol{q}) = \pm v_F|\delta\boldsymbol{q}| + A - \mu, \tag{5.2}$$

resembling the spectrum of a massless Dirac particle as already mentioned in the introductory part. It is further interesting to note that any diagonal part ($\propto I$) in the Hamiltonian H_0 of (5.1) only shifts the Dirac-like cone in energy and thereby eliminates particle-hole symmetry. In order to open up a gap ($E \sim \pm v_F\sqrt{\delta\boldsymbol{q} + m^2}$), the diagonals of H_0 must involve different signs. This requirement can for example be achieved by a staggered sublattice potential ($m\sigma_z$) with $\sigma_z = \pm 1$ for the different sublattices or by a spatially varying magnetic field with zero net flux ($m\tau_z\sigma_z$), where $\tau_z = \pm 1$ describes the states at K and K'. Here, the former term only breaks inversion symmetry and leads to a trivial insulator, whereas the latter term breaks time-reversal symmetry and gives rise to a quantum Hall insulator as pointed out by Haldane [172]. Another way of opening a gap in (5.2) is to use two copies of the Haldane term with reversed magnetic fields for the two different spins which then fulfills time-reversal symmetry. The resulting term then equals an intrinsic spin-orbit coupling ($ms_z\tau_z\sigma_z$) with $s_z = \pm 1$ for different spins and leads to the quantum spin Hall insulator as worked out by Kane and Mele [173].

Coming back to the doped case, we find that the band structure features two van-Hove singularities (VHS) at $x = 3/8$ and $x = 5/8$ as mentioned in the introductory part (see Fig. 5.2c). Constraining ourselves to the electron-doped case, the $x = 5/8$ electron-like Fermi surface is shown in Fig. 5.2b. As depicted, this is the regime of largely enhanced density of states which we investigate in the following. For $t_2 = t_3 = 0$ (red curve in Fig. 5.2), the VHS coincides with the partial nesting of different sections of the Fermi surface with $Q = (0, 2\pi/\sqrt{3}), (\pi, \pi/\sqrt{3})$, and $(\pi, -\pi/\sqrt{3})$. For a realistic band structure estimate with finite t_2 and t_3 [162] (black curve in Fig. 5.2), this gives a relevant shift of the perfect nesting position versus the VHS and affects the many-body phase found there. We assume Coulomb interactions represented by a long range Hubbard Hamiltonian [174]

$$H_{\text{int}} = U_0 \sum_i n_{i,\uparrow} n_{i,\downarrow} + \frac{1}{2} U_1 \sum_{\langle i,j \rangle, \sigma, \sigma'} n_{i,\sigma} n_{j,\sigma'} + \frac{1}{2} U_2 \sum_{\langle\langle i,j \rangle\rangle, \sigma, \sigma'} n_{i,\sigma} n_{j,\sigma'}, \quad (5.3)$$

where $U_{0,1,2}$ parametrizes the Coulomb repulsion scale from onsite to second nearest-neighbor interactions. At the VHS, we assume perfect screening and consider U_0 only, while away from the VHS, we investigate the phenomenology of taking U_1 and U_2 into consideration. The typical scale of the effective U_0 has been found to be $U_0 = 10eV < W$ [174], where $W \sim 17eV$ is the kinetic bandwidth. Using the above model description, we then employ the functional RG and study how the renormalized interaction evolves under integrating out high-energy fermionic modes. The renormalized interaction at an energy scale Λ then reads as $V^\Lambda(k_1; k_2, k_3, k_4) \gamma^\dagger_{k_1 s} \gamma^\dagger_{k_2 s'} \gamma_{k_3 s} \gamma_{k_4 s'}$, where the flow parameter Λ is given by the temperature and k_1 to k_4 label the incoming and outgoing momenta as well as the associated band indices. It is important to note that we consider the Hamiltonian in band rather than orbital representation similar to the calculations presented in the previous chapter. Within the numerical treatment, the k's are discretized to take on the values representing the different patches of the Brillouin zone as shown in Fig. 5.2b for a 96 patching scheme. We checked for selected representative scenarios that our results are converged against supercomputer simulations with 192 patch resolution. The starting conditions of the RG are then given by the bare interactions at an energy scale in the order of the bandwidth. Following the flow of the 4-point function $V^\Lambda(k_1; k_2, k_3, k_4)$ down to low energies, the diverging channels then signal the nature of the instability. The corresponding Λ_c as a function of some given system parameter such as doping gives the same qualitative behavior as T_c. At an energy scale Λ where the leading instability starts to diverge, we further decompose the different channels such as the superconducting one SC or the spin-density wave channel SDW into different eigenmode contributions and obtain the form factors associated with the different instabilities as discussed in Sec. 4.2.4.
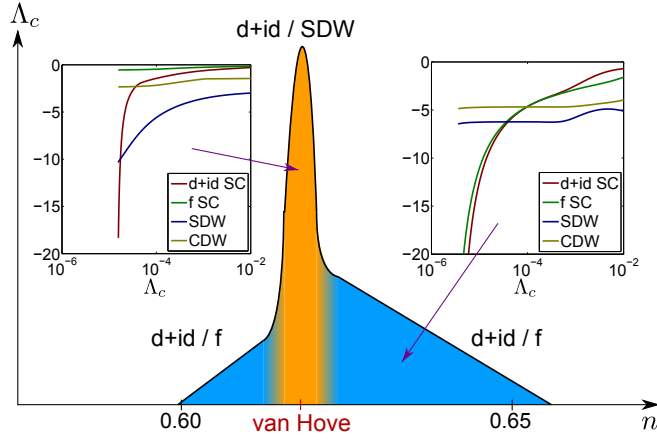
Figure 5.3: Schematic phase diagram displaying the critical instability scale $\Lambda_c \sim T_c$ as a function of doping. At the van Hove singularity (VHS, light shaded (orange) area), $(d + id)$-pairing competes with the spin-density wave (SDW) channel (left flow picture: dominant $(d + id)$-pairing instability for $U_0 = 10eV$ and the band structure in [167]). Away from the VHS (dark shaded (blue) area), Λ_c drops and whether the $(d + id)$ or f-wave pairing instability is preferred depends on the long-rangedness of the interaction (right flow picture: $U_1/U_0 = 0.45$ and $U_2/U_0 = 0.15$).

5.3 Phase Diagram of Doped Graphene

In Fig. 5.3, we now present the phase diagram of doped graphene for realistic microscopic model parameters [167, 174]. Near the van-Hove singularity (orange-shaded area in Fig. 5.3), the density of states is so large that a local Hubbard description is appropriate. Here, we find the $(d+id)$-pairing instability to be dominant for $U_0 \sim 10eV$, whereas a spin-density wave (SDW) phase becomes leading only for very large scales $U_0 > 18eV$. If we, on the other hand, slightly change the band structure parameters such that the shift between Fermi-surface nesting and van-Hove singularity gets reduced (see inset of Fig. 5.2c), the nesting becomes better and the SDW channel enhances. In particular for t_1 only, where the Fermi-surface nesting coincides with the diverging density of state, the SDW phase wins for $U_0 > 8.5eV$. As we move away from the van-Hove singularity (blue-shaded area in Fig. 5.3), details of the band structure become less relevant. In addition, the critical instability scale Λ_c drops stronger towards the Dirac point than away from it which is mainly due to the smaller density of states (see inset of Fig. 5.2b). As the SDW fluctuations are weakened away from van-Hove filling, the pairing channels become more dominant. Again assuming rather local Coulomb interactions ($U_1/U_0 < 0.4$), we find that the system still favors the $(d+id)$-pairing state. However, allowing for longer-ranged Hubbard interactions, the picture changes and charge-density wave (CDW) fluctuations are comparable to the SDW. In this case, the spin-singlet pairing channel, which is biased by the SDW fluctuations, weakens and the spin-triplet f-wave pairing

now becomes competitive. During the next sections, we will further discuss the characteristic properties of each individual phase.

5.3.1 Chiral $(d + id)$-Pairing Phase

We first start out with an analysis of the pairing phase at van-Hove filling. Here, the strongly enhanced density of states justifies a local Hubbard description and we hence restrict ourselves to the onsite repulsion term of H_{int} with $U_0 = 10eV$. Applying the functional RG, we then find the leading instability to occur in the pairing channel with two degenerate eigenvalues. The corresponding gap form factors can be fit to the following lattice harmonics

$$d_{x^2-y^2}(k) = 2\cos(\sqrt{3}k_y) - \cos[(\sqrt{3}k_y - 3k_x)/2] - \cos[(\sqrt{3}k_y + 3k_x)/2]$$
$$d_{xy}(k) = \cos[(\sqrt{3}k_y - 3k_x)/2] - \cos[(\sqrt{3}k_y + 3k_x)/2]$$

and are plotted in Fig. 5.4(a,b) together with their respective real-space representations. As the lattice structure of graphene is characterized by a C_{6v} symmetry, each gap form factor must transform in one of the six irreducible representations of this group. Using the character table of C_{6v}, as derived in Tab. 3.3, it is now easy to verify that $d_{x^2-y^2}$ and d_{xy} transform in the two-dimensional representation E_2. This in turn implies that all superpositions $d_{x^2-y^2} + e^{i\theta}d_{xy}$ must have the same transition temperatures by symmetry but do not necessarily display the same free energies. In order to figure out the superposition of lowest free energy, we therefore optimize the corresponding mean-field free energy. The resulting gap function is then depicted in Fig. 5.4c and corresponds to the fully gapped superposition of $\hat{\Delta}_k = d_{x^2-y^2}(k) + id_{xy}(k)$. This is, by the way, rather generic in a situation of degenerate nodal gap form factors as the complex superposition allows the system to avoid gap nodes. An amazingly simple proof for this statement can also be found in [175]. Apparently, the resulting $(d + id)$-pairing state breaks time-reversal symmetry as well as the reflection symmetry with respect to one spatial coordinate (parity). In the literature, a superconductor with broken time-reversal symmetry and parity is commonly denoted as chiral and it is well known that chiral superconductors with a full bulk gap can be characterized by a topological invariant N [176]. In the following paragraph, we will shortly explain the meaning of this topological characterization before we move on to the discussion of the remaining phases.

In terms of Landau's famous symmetry-breaking theory, different phases of matter can be distinguished according to its symmetries. Although this principle is very successful in describing most of the traditional phases, there are also prominent examples like the quantum Hall state where this description fails. For this reason, a new classification based on topology is required. One possible characterization in bulk-gapped states with broken
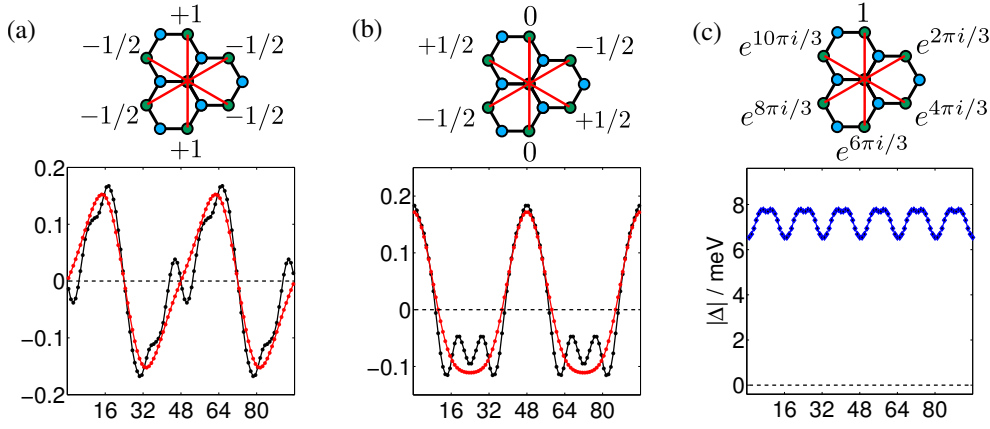
Figure 5.4: The $d_{x^2-y^2}$-wave (a) and d_{xy}-wave (b) form factors (black) for $U_0 = 10eV$ at van-Hove filling, together with an analytical fit (red) given in the text and a corresponding real-space representation (inset). All form factors are plotted along the Fermi surface with patch indices defined in Fig. 5.2b. (c) The gap profile of $(d + id)$ along the Fermi surface (actual connection to experimental energy scale can still vary by a global factor) and its real-space representation (inset) showing a 4π phase winding.

time-reversal symmetry is given by the so-called Chern number N which then provides an alternative classification beyond Landau's approach. Similar to the equivalence of the integer valued Euler characteristic of a manifold and its integrated curvature, this Chern number is also integer valued and equals an integrated Berry curvature. A small continuous variation of the Hamiltonian (manifold) can therefore never change the Chern number (Euler-characteristic) which is in this sense a topological invariant. The only possible way to change this invariant is by closing the bulk gap or, in case of the Euler-characteristic, to vary the number of holes in the manifold. A transparent way of calculating the Chern number in case of a chiral superconductor is to determine the phase winding of the complex gap $\hat{\Delta}_k = |\hat{\Delta}_k|e^{i\phi(k)}$ along the Fermi-surface [175, 177]:

$$N = \frac{1}{2\pi} \oint_{FS} \nabla_k \phi(k) dk. \tag{5.4}$$

From the real-space gap structure pictured in Fig. 5.4c, it is then apparent that the $(d + id)$-pairing state is characterized by Chern number $N = 2$, whereas its time-reversed partner $d - id$ has $N = -2$. Experimentally, this topological invariant manifests itself in quantized values of certain response functions or in the occurrence of chiral Majorana modes at a vortex core and at sample edges. The number of these zero modes is then directly related to the Chern number N [176, 178]. It is also important to note that the case of a single Majorana mode in a vortex core is of special interest as this zero mode obeys non-Abelian statistics [179–182] and its zero energy position is protected by particle-hole symmetry. This is for example the case in a
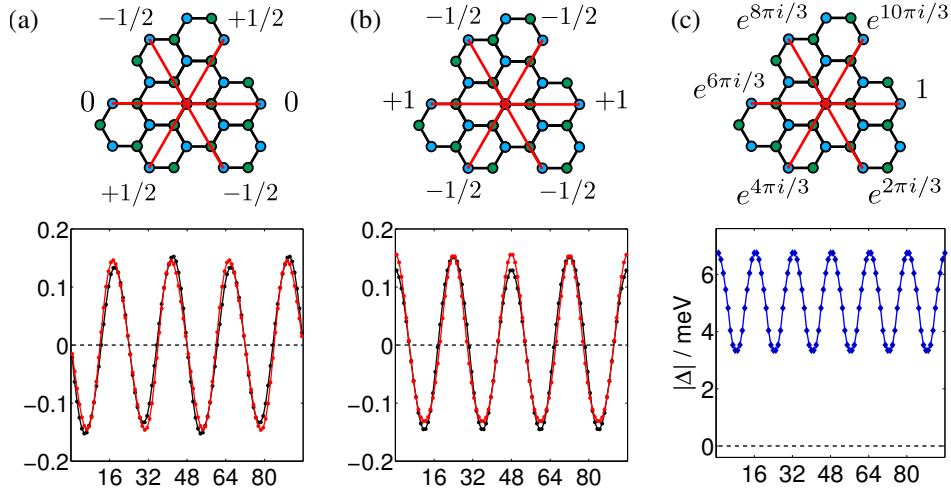
Figure 5.5: The $d_{x^2-y^2}$-wave (a) and d_{xy}-wave (b) form factors (black) plotted as in Fig. 5.4 away from van-Hove filling at $x = 0.65$. Here, we used the longer-ranged interaction parameters $U_0 = 10eV$, $U_1 = 4.5eV$ and $U_2 = 1.5eV$ to account for a reduced screening. As a consequence, the real-space pairing distance increases in order to avoid the longer-ranged Coulomb repulsion.

spinless $(p + ip)$-superconductor with $N = 1$ [183].

After this excursion on topological phases, we will now return to the discussion of doped graphene. Here, the nontrivial topology of the $(d + id)$-pairing state leads, for example, to quantized values of the spin and heat analogous of the Hall conductivity [179, 184, 185]. In addition, Sato *et al.* [186] pointed out that the addition of Rashba spin-orbit coupling and Zeeman field in a $(d + id)$-superconductor effectively realizes the spinless $(p+ip)$-pairing state and therefore leads to the same non-Abelian properties.

Away from van-Hove filling, the screening is expected to decrease away from van-Hove level, and we consider the longer-ranged interactions $U_0 = 10eV$, $U_1 = 4.5eV$ and $U_2 = 1.5eV$. In this case, the $(d + id)$-pairing phase remains energetically preferred but features longer-ranged real-space pairings, as can be seen from the insets of Fig. 5.4 and Fig. 5.5. This behavior can in turn be understood as a way to avoid the longer-ranged Coulomb repulsion by means of an increased Cooper-pair distance. The resulting gap form factors here can be fit by the following higher harmonic d-wave functions

$$d_{x^2-y^2}(k) = 2\cos(3k_x) - \cos[(3\sqrt{3}k_y - 3k_x)/2] - \cos[(3\sqrt{3}k_y + 3k_x)/2]$$
$$d_{xy}(k) = \cos[(3\sqrt{3}k_y - 3k_x)/2] - \cos[(3\sqrt{3}k_y + 3k_x)/2]$$

and are depicted in Fig. 5.5. Interestingly, the additional nodes in the gap form factors also lead to a shift in the phase winding from 4π to 8π indicating a topological transition from Chern number 2 to 4.

The expected experimental evidence for the $(d + id)$-pairing state would hence be a nodeless gap detectable through transport measurements as well as a Knight-shift drop below T_c due to spin-singlet pairing. In addition, the nontrivial topology of $(d + id)$-pairing manifests itself in a quantized spin (σ_{xy}^s) and thermal (κ_{xy}/T) Hall conductivity. A minor caveat is given by the role of impurities which may spoil the symmetry between the two d-wave solutions and which could lead to a nodal gap beyond sufficient impurity concentration [187].

5.3.2 Spin-Triplet Pairing

Besides the $(d + id)$-pairing, it is also interesting to analyze the subleading spin-triplet pairing channel [188] which becomes competitive for longer-ranged Coulomb interaction. We therefore determine the corresponding gap form factors at the representative filling of $x = 0.65$ and consider two different interaction parameter settings. The latter dependence is of particular interest as there are different proposals of tuning these interaction parameters by means of dielectric substrates. For $U_0 = 10eV$, $U_1 = 5eV$, we then obtain the gap form factor shown in Fig. 5.6(a2), which can be fit to the lattice harmonic

$$f_{B_1}(k) = \sin(\sqrt{3}k_y) - 2\sin(\sqrt{3}k_y/2)\cos(3k_x/2),$$

and which transforms in the one-dimensional B_1 representation of C_{6v}. Opposed to the $(d + id)$-pairing phase, this so-called f-wave pairing state has a nodal gap as can be seen from Fig. 5.6(a3). A similar situation occurs for longer-ranged interactions given by $U_0 = 10eV$, $U_1 = 5eV$, $U_2 = 3eV$. Here, the gap form factor is plotted in Fig. 5.6(b2) and can be fit to the B_2 lattice harmonic

$$f_{B_2}(k) = \sin(3k_x) - 2\sin(3k_x/2)\cos(3\sqrt{3}k_y/2).$$

Comparing the corresponding real-space pairing structures of f_{B_1} and f_{B_2} in Fig. 5.6(a1,b1), one again finds that the Cooper-pair distance increases in order to avoid the longer-ranged Coulomb interaction. This then leads to a change of the node position as apparent from Fig. 5.6(b2,b3). The position of the nodes would hence indicate the Cooper-pair distance associated with the long-range properties of the Coulomb interaction. It is important to note that we cannot make any statements on the spin-structure of the spin-triplet Cooper pair simply because we remain in the spin-rotational symmetric state throughout the entire flow. The experimental evidence of the f-wave phase are nevertheless a nodal gap which could be confirmed by transport measurements and an invariant Knight-shift due to spin-triplet pairing. For fillings smaller than van-Hove level, the Fermi surface becomes disconnected, and it may happen that the nodes of the f_{B_2} gap do not coincide with the Fermi surfaces. In this case, the f-wave pairing phase could also appear nodeless.
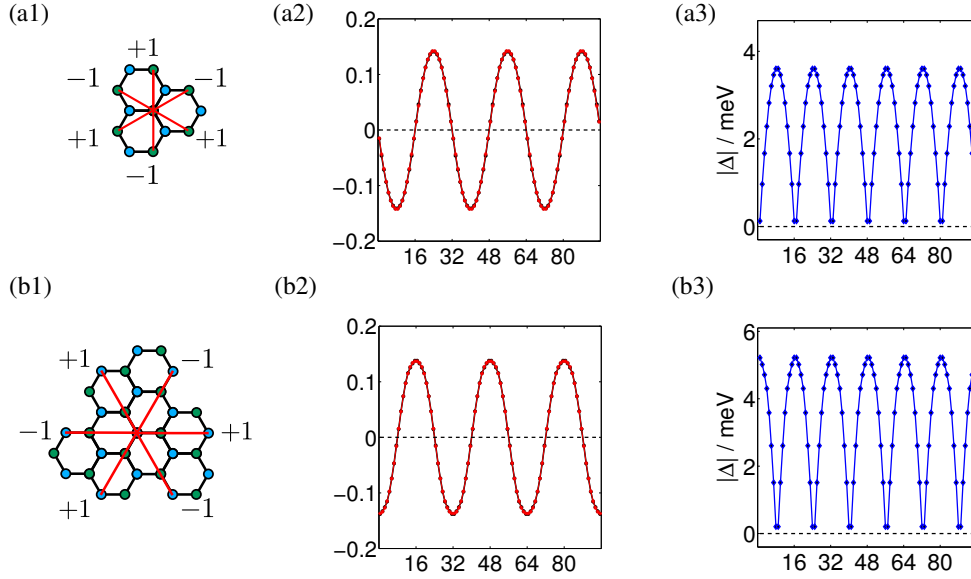
Figure 5.6: Real-space pairing structure, form factor, and gap profile for the f-wave phases. We depicted the results for the representative filling of $x = 0.64$ which is larger than van-Hove filling and chose $U_0 = 10eV$, $U_2 = 6eV$ for (a) and $U_0 = 10eV$, $U_1 = 6eV$, $U_2 = 2eV$ for (b). The gap profiles reveal nodes with positions shifting from (a) to (b).

5.3.3   Spin-Density Wave Phase

Although the $(d + id)$-pairing was the dominant instability at van-Hove filling, a slight variation in the band structure parameters can bias the system towards spin-density wave (SDW) order. Therefore, we also want to study the nature and experimental signatures of the SDW ordered phase during the following section. However, as the Fermi-surface of graphene near van-Hove filling supports three inequivalent nesting vectors Q_1, Q_2, Q_3, there is a variety of possible SDW states. For example, the condensation could occur at one single nesting vector Q_k, i.e. $\langle \vec{S}_i \rangle = \vec{M} e^{iQ_k \cdot r_i}$ with $\vec{M}$ indicating the direction of magnetization, or at all three nesting vectors Q_k

$$\langle \vec{S}_i \rangle = \vec{M}_1 e^{iQ_1 \cdot r_i} + \vec{M}_2 e^{iQ_2 \cdot r_i} + \vec{M}_3 e^{iQ_3 \cdot r_i}. \tag{5.5}$$

Here, the mutual orientation of $\vec{M}_{1,2,3}$ gives rise to further possible SDW phases. From the current functional RG implementation, we cannot specify which of these possibilities is favored as this would require higher-order vertex functions. Alternatively, one can consider the mean-field approximated theory and optimize its free energy with respect to different SDW order parameters. This type of analysis was for example elaborated by Li [171] who found a chiral SDW state (see Fig. 5.7a) similar to the one proposed for the 3/4-filled triangular lattice [189]. Here, the four neighboring spins form a tetrahedron as shown in Fig. 5.7a, which corresponds to an SDW

(a)

(b)
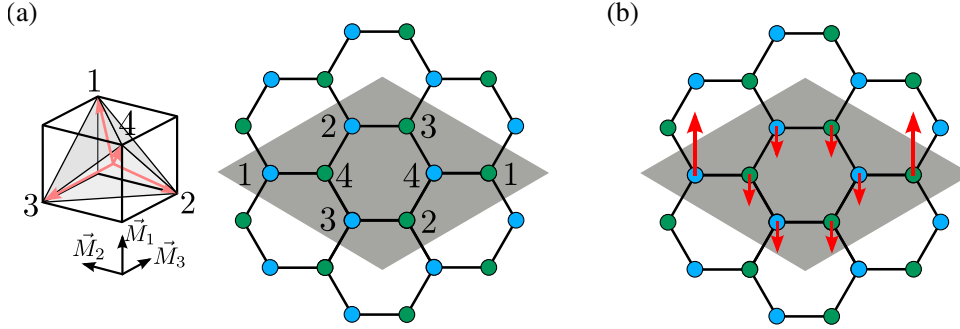
Figure 5.7: (a) Chiral SDW order as proposed in [171, 190] with four neighboring spins forming a tetrahedral ordering pattern (see inset). The spins on positions 1 to 4 are determined by $\vec{M}_1 + \vec{M}_2 + \vec{M}_3$, $-\vec{M}_1 - \vec{M}_2 + \vec{M}_3$, $\vec{M}_1 - \vec{M}_2 - \vec{M}_3$, $-\vec{M}_1 + \vec{M}_2 - \vec{M}_3$ with three mutually orthogonal vectors $\vec{M}_1, \vec{M}_2, \vec{M}_3$. (b) Uniaxial SDW order as suggested in [191]. The shaded area in both subfigures indicates the respective magnetic unit cell.

order described by (5.5) with three mutually orthogonal vectors $\vec{M}_{1,2,3}$. The resulting state is fully gapped and breaks time-reversal symmetry as well as parity due to the nonzero spin chirality, i.e. $\langle \vec{S}_i \cdot (\vec{S}_j \times \vec{S}_k) \rangle \neq 0$ for neighboring sites i, j, k. As a consequence of this nonzero chirality, the moving electrons feel an effective internal magnetic field and feature a spontaneous Hall effect [192] with $\sigma_{xy} = e^2/h$ [171, 189]. The insulating state is therefore a Chern-insulator in the sense of a nonzero quantized Hall conductance, i.e. $\sigma_{xy} = ne^2/h$ with $n \neq 0$. Li argued that this is essentially the same state as proposed for the 3/4-filled triangular lattice.

Recently, Nandkishore *et al.* [191] suggested another SDW state for graphene doped to van-Hove filling. Here, the spins are all aligned along the same axes (uniaxial) as shown in Fig. 5.7b, and the system remains metallic with gapless states having equal spin projection. As all other states with reversed spin projection are gapped out, this uniaxial SDW phase could be quite useful for spin-filtering applications. Further studies beyond mean-field level will have to clarify which of these two exotic SDW orders is energetically favored, and whether the same phase also occurs in the 3/4-filled triangular lattice.

5.4   Summary and Outlook

In summary, we have provided a detailed analysis of the competing many-body phases of graphene at and around van-Hove filling. Using realistic band structure parameters and interactions, we find the chiral $(d + id)$ superconducting phase to be preferred over an extended phase space regime around van-Hove filling. Besides this $(d + id)$-phase, we also find a subleading spin-triplet pairing phase as well as an exotic spin-density wave state. Both of these subleading phases can in turn be realized if the kinetic and interaction parameters are slightly changed, for example through different

substrate materials. We therefore conclude that doped graphene, which has recently become accessible in experiments, shows a variety of interesting many-body phases at relatively high transition temperatures. We think that the realization of only one of these phases would be of great benefit to fundamental science and future applications.

Chapter 6

Superconductivity in Strontium Ruthenate ($\mathrm{Sr_2RuO_4}$)

6.1 Introduction

Soon after Bednorz and Mueller discovered the first cuprate superconductor with a transition temperature (T_c) of $38K$ [1], Meano and coworkers also started the search for high-T_c superconductivity in other transition metal oxides with a similar perovskite structure. In 1994, nearly one decade after the discovery of the cuprates, they found the first non-cooper based perovskite superconductor $\mathrm{Sr_2RuO_4}$ [193] with a transition temperature of only $1.5K$.

Although the crystal structure of $\mathrm{Sr_2RuO_4}$ (SRO) was equivalent to the one of $\mathrm{La_2CuO_4}$, it soon turned out that SRO is quite different from the cuprates. On the one hand, SRO shows no long-range magnetic order and, on the other hand, its superconductivity develops out of a well-formed Fermi-liquid without any doping. In particular, also the superconducting properties of SRO differ in many respects from the one in cuprates. Whereas the pairing state in the cuprates shows spin-singlet pairing with d-wave symmetry, the pairing in SRO is most likely of spin-triplet type and reveals evidence for broken time-reversal symmetry. These latter two properties then strongly point to a $(p + ip)$-wave pairing state and aroused great interest as a natural realization of topological superconductivity. In addition, the multi-component order parameter of this so-called chiral pairing state allows for a rich defect structure including half-quantum vortices with non-Abelian exchange statistics. This is of course fascinating by itself, but also constitutes an essential ingredient for the realization of quantum computing.

However, a growing number of experiments seem to contradict a simple explanation in terms of a $(p+ip)$-wave pairing in SRO. For example, the expected nodeless gap was not confirmed in experiments, and also the assumed
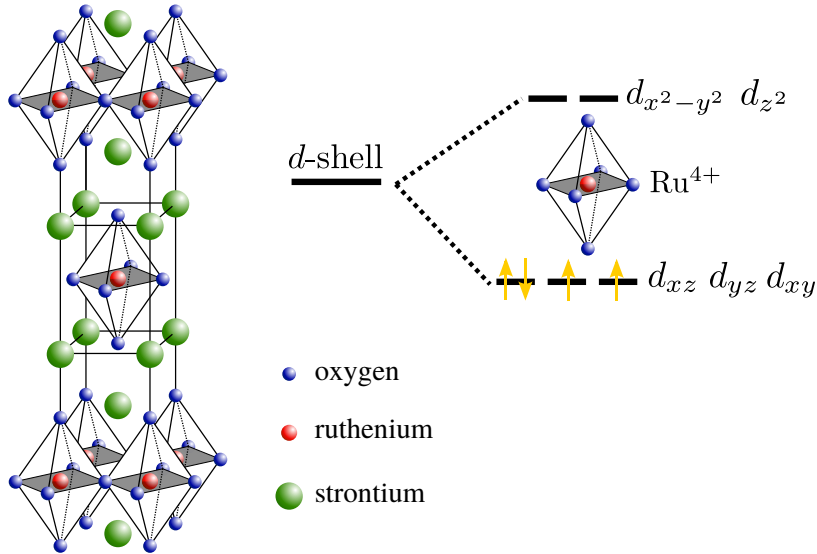
Figure 6.1: Crystal structure of Sr$_2$RuO$_4$ and crystal field splitting of the Ru $4d$ states in an octahedral environment of neighboring oxygen ions. The Ru ion is in a $4d^4$ configuration with four electrons distributed nearly equally among the t_{2g}-orbitals d_{xz}, d_{yz}, d_{xy}.

ferromagnetic-based pairing mechanism was challenged by the existence of pronounced antiferromagnetic fluctuations. Therefore, the correct structure of the superconducting gap as well as the pairing mechanism are still under debate, and we think that an unbiased functional RG analysis could provide valuable insights into these issues.

In the following section, we will review the most relevant properties of the normal and superconducting state of SRO. After that, we will present our functional RG results and discuss how these findings relate to current experimental results. Further informations on the experimental findings can be found in a number of excellent articles [194–196].

6.2   Structural and Electronic Properties

The crystal structure of SRO resembles the one of La$_2$CuO$_4$ and consists of RuO$_2$ layers separated by strontium and oxygen ions. Here, each Ru ion is surrounded by an octahedron of oxygen ions depicted in Fig. 6.1a, and the unit cell is body-centered tetragonal without any structural transition between room temperature and $0.1K$. An important peculiarity of SRO is the availability of high-quality crystals which enabled a direct Fermi-surface mapping by means of quantum oscillation measurements. The corresponding measurements of Bergemann *et al.* [197] then revealed two electron-like Fermi surfaces around the Γ-point and one hole-like at the M-point of the Brillouin zone as illustrated in Fig. 6.2c. Although the first ARPES

measurements suggested a different picture [198, 199], later experiments of Damascelli *et al.* [200] agreed very well with the above quantum oscillation measurements. In addition, band structure calculations such as LDA confirmed this measured Fermi-surface as well [201, 202] but also found clear deviations in the band structure away from the Fermi level. This in turn was suggested to result from correlations effects, which are not as drastic as in the isostructural cuprates, but still show a sizeable effect [203, 204]. One reason for the moderate correlation effects in SRO is the larger extend of the relevant $4d$-shell of ruthenium in comparison to the $3d$-shell of copper. The normal state of SRO then shows a Fermi-liquid like behavior for $T < 50K$ as, for example, apparent from the T^2-like behavior of the electrical resistivity [194].

In order to describe the electronic properties of SRO, we first note that the ruthenium ion Ru^{4+} is left in a $4d^4$ electronic configuration. Due to the crystal field of the surrounding oxygen ions, the degeneracy of the Ru-$4d$ orbitals is lifted as indicated in Fig. 6.1, and the four remaining electrons sit in the lower-lying t_{2g}-orbitals d_{xz}, d_{yz}, d_{xy}. The same t_{2g}-states then also determine the low-energy electronic band structure as confirmed by LDA calculations [201, 202], and the four electrons of Ru^{4+} are distributed nearly equally among the three t_{2g}-orbitals. An appropriate tight-binding description for the t_{2g} states is then given by

$$H_0 = \sum_{\boldsymbol{k},\sigma} \begin{pmatrix} c^\dagger_{\boldsymbol{k},xz,s} & c^\dagger_{\boldsymbol{k},yz,s} & c^\dagger_{\boldsymbol{k},xy,s} \end{pmatrix} \begin{pmatrix} \xi_{xz,xz}(\boldsymbol{k}) & \xi_{xz,yz}(\boldsymbol{k}) & 0 \\ \xi_{yz,xz}(\boldsymbol{k}) & \xi_{yz,yz}(\boldsymbol{k}) & 0 \\ 0 & 0 & \xi_{xy,xy}(\boldsymbol{k}) \end{pmatrix} \begin{pmatrix} c_{\boldsymbol{k},xz,s} \\ c_{\boldsymbol{k},yz,s} \\ c_{\boldsymbol{k},xy,s} \end{pmatrix},$$

$$(6.1)$$

where $c^\dagger_{\boldsymbol{k},o,s}, c_{\boldsymbol{k},o,s}$ denote the creation and annihilation operator of an electron with momentum $\boldsymbol{k}$, spin s and orbital character o. Here, we also used the notations of

$$\xi_{xz,xz}(\boldsymbol{k}) = -2t\cos(\boldsymbol{k}_x) - 2t_2\cos(\boldsymbol{k}_y)$$
$$\xi_{yz,yz}(\boldsymbol{k}) = -2t\cos(\boldsymbol{k}_y) - 2t_2\cos(\boldsymbol{k}_x)$$
$$\xi_{xy,xy}(\boldsymbol{k}) = -2t_3(\cos(\boldsymbol{k}_x) + \cos(\boldsymbol{k}_y)) - 4t_3'\cos(\boldsymbol{k}_x)\cos(\boldsymbol{k}_y) + \xi_3$$
$$\xi_{xz,yz}(\boldsymbol{k}) = \xi_{yz,xz}(\boldsymbol{k}) = -4t'\sin(\boldsymbol{k}_x)\sin(\boldsymbol{k}_y)$$

with parameter values $t = 0.2eV$, $t_2 = 0.1t$, $t_3 = 0.8t$, $t_3' = 0.35t$ and $\xi_3 = -0.25t$. The corresponding band structure and Fermi surface are shown in Fig. 6.2 and agree very well with those from LDA calculations. Due to the large separation of RuO_2 layers, the hybridization between different layers is very small, and we therefore neglect all out-of-plane hopping elements. In addition, as the orbitals $d_{xz,yz}$ and d_{xy} have different parity under $z \to -z$ reflection, a hybridization within the same plane is not allowed, and one of the three bands is hence of pure d_{xy}-orbital weight. The other
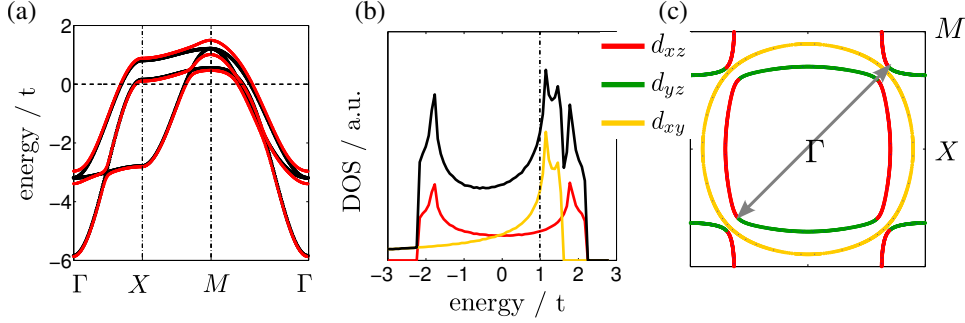
Figure 6.2: Band structure, density of states (DOS) and Fermi surface of H_0 in (6.1) with $t = 0.2eV$. The filling of all three orbitals equals 4/3 as suggested from band-structure calculations. (a) Band structure with (red) and without (black) spin-orbit coupling determined by $H_{LS} = \lambda \sum_i \boldsymbol{L}_i \cdot \boldsymbol{S}_i$ and $\lambda = 0.45t$. (b) Total density of states (black curve) and orbital resolved density of states (colored curves). (c) Fermi-surface and $(4\pi/3, 4\pi/3)$ nesting vector. Note that the depicted nesting vector is equivalent to $\boldsymbol{q} = (2\pi/3, 2\pi/3)$ modulo reciprocal lattice vectors.

two bands reveal quasi-one dimensional behavior as the nearest-neighbor hybridization between the d_{xz}- and d_{yz}-orbitals vanishes also by symmetry, and both orbitals only couple via second-nearest neighbors. The band structure therefore shows two quasi-one dimensional $d_{xz,yz}$-bands and one two-dimensional d_{xy}-band whose Fermi-surface is close to the saddle points at $(0, \pm\pi)$ and $(\pm\pi, 0)$ with a diverging density of states. From Fig. 6.2b, it is further apparent that this two-dimensional d_{xy}-band features the largest density of states near the Fermi-level and hence supports ferromagnetic-like fluctuations with ordering momentum $\boldsymbol{q} \approx (0,0)$. In addition, the Fermi-surface shown in Fig. 6.2c also promotes antiferromagnetic fluctuations of ordering momentum $\boldsymbol{q} \approx (\pm 2\pi/3, \pm 2\pi/3)$, which result from the nested $d_{xz,yz}$-bands [205]. However, whereas the antiferromagnetic fluctuations are well established in neutron scattering experiments [206], the same measurements found no sizeable ferromagnetic peak in SRO. On the other hand, nuclear magnetic resonance (NMR) experiments [207] which, as a local probe only permit momentum integrated insights, revealed a significantly larger susceptibility of the d_{xy}-electrons. Together with the ferromagnetism in the related compounds SrRuO$_3$ [208] and Sr$_4$Ru$_3$O$_{10}$ [209], this suggests that ferromagnetic fluctuations might also be of relevance in SRO and that the role of spin fluctuations is probably much more involved.

In the following, we will now discuss the influence of spin-orbit coupling determined by $H_{LS} = \lambda \sum_i \boldsymbol{L}_i \cdot \boldsymbol{S}_i$. For this purpose, we rewrite H_{LS} as

$$H_{LS} = i\frac{\lambda}{2} \sum_{n,oo'} \epsilon_{oo'n} \sum_{\boldsymbol{k},s,s'} c^\dagger_{\boldsymbol{k},o,s} c_{\boldsymbol{k},o',s'} \sigma^n_{ss'}, \qquad (6.2)$$

where o, o' belong to the ordered set of t_{2g}-orbitals $\{d_{yz}, d_{xz}, d_{xy}\}$, σ^n denotes the n-th Pauli-matrix and $\epsilon_{oo'n}$ is the totally antisymmetric tensor. The red

curve in Fig. 6.2a then indicates the band structure of $H_{tot} = H_0 + H_{LS}$ with a realistic value of $\lambda = 90meV$ [210]. Here, it turns out that the effect of spin-orbit coupling is quite small for the states near the Fermi-level but can become crucial at certain $\boldsymbol{k}$-regions of high-symmetry. In addition, it is also apparent that all three bands show a two-fold degeneracy due to the still present time- and space-inversion symmetry. However, as spin-rotational symmetry is broken by H_{LS}, the single-particle states of H_{tot} cannot be eigenstates of the spin-operator. It is nevertheless possible to construct so-called pseudospin states $|\boldsymbol{k}, \alpha\rangle$, $|\boldsymbol{k}, \beta\rangle$ such that $\alpha \to \uparrow$ and $\beta \to \downarrow$ holds for vanishing spin-orbit coupling and such that all transformation properties remain the same up to the linking of spatial- and pseudospin-rotation. The advantage of this pseudospin-basis lies in its transparent transformation behavior, which enables a simple classification of superconducting order as described in Sec. 3.4. For example, the superconductivity can still be classified in terms of pseudospin singlet- or triplet-pairing and all derived transformation properties of the superconducting gap function remain unchanged up to the linking of spatial- and pseudospin-rotation. Unless stated otherwise, the term spin will therefore refer to the above pseudospin label throughout the following sections.

6.3 Spin-Triplet Pairing and the Effect of Spin-Orbit Coupling

Although the detailed pairing state in SRO is still under debate, its spin-triplet character has been confirmed with reasonable certainty. Using Knight-shift [211] measurements and neutron scattering [212], the local spin susceptibility has been shown to remain unchanged below T_c. This in turn rules out singlet pairing as the corresponding spin-zero pairs could not respond to a magnetic field and the local spin susceptibility would vanish exponentially for $T < T_c$. The unchanged local spin susceptibility below T_c therefore presents a convincing evidence for spin-triplet pairing in SRO. According to Sec. 3.4, the gap function $\hat{\Delta}_{\boldsymbol{k}}$ in a triplet superconductor is conveniently written as

$$\hat{\Delta}_{\boldsymbol{k}} = i(\boldsymbol{d}(\boldsymbol{k}) \cdot \boldsymbol{\sigma})\sigma_y$$

with a three-component vector $\boldsymbol{d}(\boldsymbol{k})$ being odd in $\boldsymbol{k}$ and pointing perpendicular to the total spin of $(\boldsymbol{k}, -\boldsymbol{k})$-paired electrons. The advantage of this $\boldsymbol{d}$-vector notation lies in its transparent transformation behavior under spin rotation. As discussed in Sec. 3.4, the $\boldsymbol{d}$-vector transforms as a classical spin under the rotation in spin-space and, if spin-rotational symmetry is unbroken, all pairing states with a globally rotated $\boldsymbol{d}$-vector must have the same T_c by symmetry. On the other hand, if spin-rotational symmetry is broken due to the spin-orbit coupling in (6.2), any rotation in $\boldsymbol{k}$- and (pseudo)spin-space must be linked in order to describe a symmetry of the underlying theory. As

a consequence, the spin-orbit coupling lifts the six-dimensional degeneracy of spin-triplet pairing states to four one-dimensional and one two-dimensional representations as shown in Tab. 6.1 below. Here, it is important to note

no spin-orbit coupling	with spin-orbit coupling
	$\boldsymbol{d}^{A_1}(\boldsymbol{p}) = \hat{\boldsymbol{x}}p_x + \hat{\boldsymbol{y}}p_y$
$\boldsymbol{d}_1(\boldsymbol{p}) = \hat{\boldsymbol{x}}p_x, \boldsymbol{d}_2(\boldsymbol{p}) = \hat{\boldsymbol{x}}p_y$	$\boldsymbol{d}^{A_2}(\boldsymbol{p}) = \hat{\boldsymbol{x}}p_y - \hat{\boldsymbol{y}}p_x$
$\boldsymbol{d}_3(\boldsymbol{p}) = \hat{\boldsymbol{y}}p_x, \boldsymbol{d}_4(\boldsymbol{p}) = \hat{\boldsymbol{y}}p_y$	$\boldsymbol{d}^{B_1}(\boldsymbol{p}) = \hat{\boldsymbol{x}}p_x - \hat{\boldsymbol{y}}p_y$
$\boldsymbol{d}_5(\boldsymbol{p}) = \hat{\boldsymbol{z}}p_x, \boldsymbol{d}_6(\boldsymbol{p}) = \hat{\boldsymbol{z}}p_y$	$\boldsymbol{d}^{B_2}(\boldsymbol{p}) = \hat{\boldsymbol{x}}p_y + \hat{\boldsymbol{y}}p_x$
	$\boldsymbol{d}_1^{E_1}(\boldsymbol{p}) = \hat{\boldsymbol{z}}p_x, \boldsymbol{d}_2^{E_1}(\boldsymbol{p}) = \hat{\boldsymbol{z}}p_y$

Table 6.1: The different p-wave gap symmetries on the square lattice with and without spin-orbit coupling. The direction of the $\boldsymbol{d}$-vector is characterized by the three unit-vectors $\hat{\boldsymbol{x}}$, $\hat{\boldsymbol{y}}$, $\hat{\boldsymbol{z}}$.

that we used the rotational invariant basis functions p_x, p_y instead of the correct lattice harmonics like $\sin(p_x)$, $\sin(p_y)$ for the nearest-neighbor case. We will keep this widely adopted notation and replace it if necessary.

6.4 Chiral $(p+ip)$-Pairing State

Among the five possible pairing symmetries presented in Tab. 6.1, only the two-dimensional representation E_1 admits a spontaneous breaking of time-reversal symmetry. The associated order parameter is then characterized by

$$\boldsymbol{d}(\boldsymbol{k}) = \hat{\boldsymbol{z}}(p_x \pm ip_y) \tag{6.3}$$

and represents a chiral pairing state as both time-reversal symmetry and the reflection symmetry of one spatial coordinate (parity) are broken. Similar to the $(d+id)$-pairing in the previous chapter, this chirality then leads to topological superconductivity with full bulk gap $|\hat{\Delta}_{\boldsymbol{k}}| = \sqrt{p_x^2 + p_y^2}$ and topologically protected chiral modes at the sample edges. The topological structure of such chiral superconductors in two dimensions is conveniently described by the Chern number N as defined in Eq. (5.4), and for (6.3) N is either $+1$ or -1 depending on which of the two orders $\hat{\boldsymbol{z}}(p_x + ip_y)$ or $\hat{\boldsymbol{z}}(p_x - ip_y)$ is realized. Without closing the bulk gap or breaking additional symmetries, the Chern number N remains invariant and gives rise to gapless modes at all interfaces between states of different topology ($N_1 \neq N_2$) [176]. It can be further shown that the topological invariant N is directly related to the internal angular momentum of the Cooper-pairs [213] which is $\langle L_z \rangle = \pm 1$ in the chiral pairing state (6.3). Of course, the angular momentum is only conserved in the rotational symmetric case and one should instead replace the gap functions p_x, p_y in (6.3) by appropriate lattice harmonics like $\sin(p_x)$ and $\sin(p_y)$. However, the rotational symmetric notation is still a reasonable
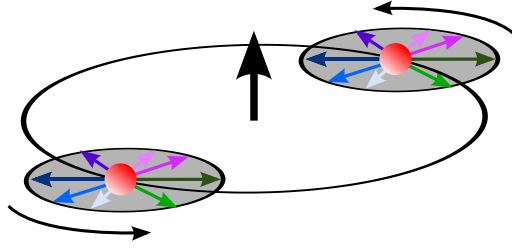
Figure 6.3: Spin S and angular momentum L of a single Cooper pair in the chiral state (6.3). The angular momentum L is depicted by the thick black arrow pointing in $\boldsymbol{z}$-direction, The spin configuration in (6.3) consists of superpositions of equal in-plane spins (equal colored arrows) such that $\langle S \rangle = 0$.

approximation and has been widely adopted in the literature. The magnetic moment associated with the finite angular momentum of the Cooper pairs is usually compensated in the bulk due to Meissner screening but may become visible near defects or sample boundaries with imperfect screening. Although the spontaneous onset of internal magnetic fields near defects occurs also in non-chiral pairing states such as the $(s+id)$-pairing phase with $\langle L \rangle = 0$, it is an unambiguous indication of broken time-reversal symmetry. Therefore, the first experimental evidence for time-reversal symmetry broken pairing in SRO came from muon relaxation rate measurements of Luke *et al.* [214], who reported the onset of a broad distribution of internal magnetic fields near T_c. Further indications of broken time-reversal symmetry were also found in later magneto-optic experiments [215], Josephson measurements [216] and in the magnetic-field distribution of the vortex lattice [217, 218]. Moreover, the spin configuration of the chiral pairing state (6.3) can also be deduced from the uniform $\boldsymbol{d}$-vector direction along the $\boldsymbol{z}$-axis. According to Sec. 3.1, this implies that the Cooper-pairs of total spin $S = 1$ consist of equal in-plane spins with $\langle S \rangle = 0$ as illustrated in Fig. 6.3. The non-vanishing Knight-shift for an applied in-plane magnetic field is therefore fully consistent with the spin structure of (6.3) as the in-plane spins of the Cooper pairs are still polarizable. In contrast to that, the Knight-shift for an applied out-of-plane magnetic field is supposed to vanish in a similar way as in singlet superconductors.

From the symmetry considerations of the previous section, it could by inferred that SRO exhibits five possible triplet pairing symmetries of which only the chiral one in (6.3) breaks time-reversal symmetry. Hence, the non-vanishing Knight shift and the evidence for time-reversal symmetry breaking would be sufficient to uniquely determine the pairing symmetry in SRO. However, the measured power laws in the electronic specific-heat [219], nuclear spin-relaxation [220] and thermal conductivity [221] suggest that SRO cannot have the full bulk gap expected from (6.3) as this would imply an exponential behavior in all these quantities. This of course does not rule out

the chiral pairing symmetry (6.3) but most likely points to multi-orbital effects which are known to cause pronounced gap anisotropies. Another issue of the chiral pairing state (6.3) is the experimental verification of edge currents. Although recent tunneling experiments [222] reported a broad hump of subgap states at the in-plane edges, scanning SQUID measurements [223] found no indications of current induced magnetic fields. As multi-orbital effects are also relevant for explaining this inconsistent behavior [224, 225], a functional RG investigation of the multi-orbital superconductivity in SRO would be quite helpful to understand these issues. In the following section, we will therefore study the pairing mechanism, the detailed structure of the superconducting gap as well as the influence of spin-orbit coupling in a microscopic model description of SRO.

6.5   Implementation and Results

The numerical implementation of the functional RG follows the description of Sec. 4.2.3. Starting point is again the exact hierarchy of flow equations in Eq. (2.24) and, by restricting to the 4-point function V^Λ, we obtain the familiar flow equation depicted in Fig. 6.4a. At this, we further applied the widely used approximation of discarding the 6-point function as well as the self-energy feedback to V^Λ. Both types of approximation can be justified for sufficiently small bare interactions as discussed in Sec. 2.5. Usually, the full 4-point function depends on four band indices m_i as well as on three momenta and frequencies with the respective fourth one determined by conservation laws. However, as we are mainly interested in the most diverging parts of the 4-point function, we compute V^Λ only at zero frequency and at a discrete set of Fermi-surface points $\{k_F^s\}$. For this reason, we divide the Brillouin zone for each band into patches shown in Fig. 6.4(b1-b3), and, as we still need the full momentum dependence of V^Λ to determine its value at the Fermi-surface points $\{k_F^s\}$, we project each k-point in a certain momentum space patch onto its Fermi-surface point k_F^s at the patch center. This then amounts to the following approximation

$$V^\Lambda(k_1 m_1, k_2 m_2, k_3 m_3, k_4 m_4) \approx$$
$$V^\Lambda(\pi_F(k_1)m_1, \pi_F(k_2)m_2, \pi_F(k_3)m_3, \pi_F(k_4)m_4),$$

with $\pi_F(k_i)$ denoting the projection of k_i onto the Fermi-surface point k_F^s of band m_i. For n_p patches and n_b bands we then end up with a closed system of $n_p^3 n_b$ coupled first-order differential equation for V^Λ.

After this short recap on the numerical implementation, we now start applying the functional RG to the three orbital model (6.1) of SRO. Similar to the other multi-orbital models discussed in this thesis, the interaction part H_{int} includes intra- and inter-orbital contributions U_1 and U_2, the Hund's
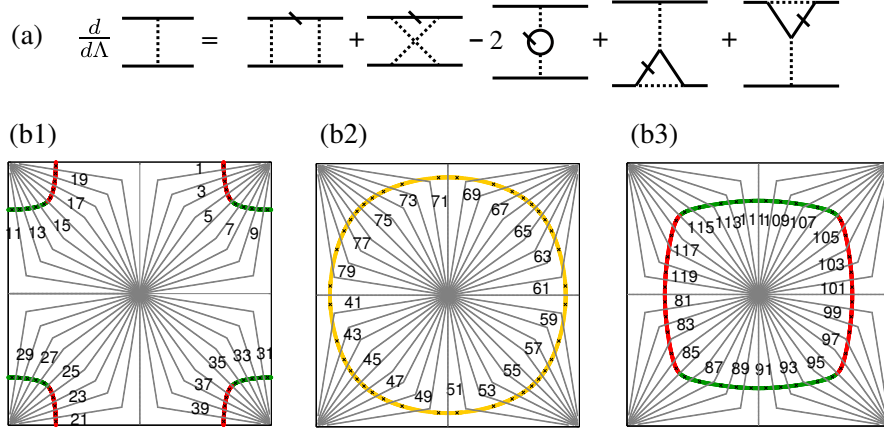
Figure 6.4: (a) Flow equation of the 4-point function (dashed line) according to Eq. (2.63). The full inner lines denote free propagators, slashed inner lines indicate the single-scale propagator as defined in (2.28) for the temperature-flow scheme. (b1-b3) Patching scheme depicted by the black partitioning of the Brillouin zone for the three bands of (6.1). The colors again denote the leading orbital weights with red, green and yellow labeling the d_{xz}-, d_{yz}- and d_{xy}-orbital.

rule coupling J_H as well as a pair-hopping term J_{pair}:

$$H_{int} = \sum_i \left[U_1 \sum_o n_{i,o,\uparrow} n_{i,o,\downarrow} + U_2 \sum_{o<o',s,s'} n_{i,o,s} n_{i,o',s'} \right.$$

$$\left. + J_H \sum_{o<o'} \sum_{s,s'} c^\dagger_{i,o,s} c^\dagger_{i,o',s'} c_{i,o',s'} c_{i,o,s} + J_{pair} \sum_{o<o'} \left(c^\dagger_{i,o,\uparrow} c^\dagger_{i,o,\downarrow} c_{i,o',\downarrow} c_{i,o',\uparrow} + h.c. \right) \right].$$

The operators $c^\dagger_{i,o,s}, c_{i,o,s}$ represent the creation and annihilation operators of an electron with spin s, in orbital o and at site i. The respective electron-density operator is further given by $n_{i,o,s}$. For an efficient computation of the diagrams in Fig. 6.4a, it is also useful to choose an appropriate one-particle basis in which the quadratic term of H_0 becomes diagonal. In case of a multi-orbital model as in (6.1) for SRO, this band basis consists of a superposition of orbital states

$$|\boldsymbol{k}, m, s\rangle = u_{m,xz}(\boldsymbol{k})|\boldsymbol{k}, xz, s\rangle + u_{m,yz}(\boldsymbol{k})|\boldsymbol{k}, yz, s\rangle + u_{m,xy}(\boldsymbol{k})|\boldsymbol{k}, xy, s\rangle, \quad (6.4)$$

whose matrix elements $u_{m,o}(\boldsymbol{k})$ determine the contribution or weight of orbital o in band m. The corresponding operators $\gamma^\dagger_{\boldsymbol{k}ms}, \gamma_{\boldsymbol{k}ms}$ in band basis are then determined by $|\boldsymbol{k}, m, s\rangle = \gamma^\dagger_{\boldsymbol{k}ms}|0\rangle$, and the Hamiltonian in this representation reads as

$$H_{total} = \sum_{\boldsymbol{k},s} \sum_{m=1}^{3} \gamma^\dagger_{\boldsymbol{k}ms} E_m(\boldsymbol{k}) \gamma_{\boldsymbol{k}ms} \qquad (6.5)$$

$$+ \sum_{\substack{k_1,\dots k_4 \\ s,s'}} \sum_{m_1,\dots,m_4} V_0(\boldsymbol{k}_1 m_1, \boldsymbol{k}_2 m_2, \boldsymbol{k}_3 m_3, \boldsymbol{k}_4 m_4) \gamma^\dagger_{\boldsymbol{k}_1 m_1 s} \gamma^\dagger_{\boldsymbol{k}_2 m_2 s'} \gamma_{\boldsymbol{k}_3 m_3 s} \gamma_{\boldsymbol{k}_4 m_4 s'}.$$

Unless stated otherwise, we first neglect the spin-orbit coupling term (6.2) as this would otherwise also mix-up different spin states in an eigenbasis similar to (6.4). The energy bands $E_m(\boldsymbol{k})$ of (6.5) then correspond to the black lines of Fig. 6.2 and the associated Fermi-surface at an electron filling of $n_{xz} = n_{yz} = n_{xy} = 4/3$ is depicted in Fig. 6.4 and Fig. 6.2c. Starting from the bare interaction V_0 of (6.5), which equals the 4-point function V^Λ at high energy scales $\Lambda \approx W$

$$V^{\Lambda \approx W}(k_1, k_2, k_3, k_4) = V_0(k_1, k_2, k_3, k_4), \tag{6.6}$$

we can now easily solve the initial-value problem posed by the flow equation of Fig. 6.4a. Note that in (6.6), we used the condensed notation of $k_i = (\boldsymbol{k}_i, m_i)$ since the above patching scheme assigns each $\boldsymbol{k}_i$-point to a fixed band index m_i. In Figure 6.5a, we then illustrate the initial 4-point function in dependence of the two incoming momenta k_1, k_2 with k_3 fixed to position 59 and k_4 determined by momentum conservation. At this, we assumed a representative set of interaction parameters given by $U_1 = 3t$, $U_2 = 2t$, $J_H = J_{pair} = 0.7t$, and we will later also summarize our results for a broader range of interaction parameters.

6.5.1   Pairing Mechanism and Flow to Strong Coupling

If we now track the flow of the 4-point function down to low energy scales, it is clearly apparent from Fig. 6.5b that the dominant scattering amplitudes are located within the d_{xy}-pocket (40-80). The reason for that is, on the one hand, the nearby van-Hove singularity in the associated d_{xy}-band and, on the other, the dominant intra-orbital repulsion U_1 which acts most effectively on the pocket of pure d_{xy}-orbital weight. Note that the other two pockets are of mixed $d_{xz,yz}$-orbital weight and do not hybridize with the d_{xy}-orbital due to its different reflection properties under $z \to -z$. The broad vertical feature showing up in Fig. 6.5b then indicates ferromagnetic-like fluctuations according to the discussion in Sec. 4.2.4. Although these ferromagnetic fluctuations appear with moderate strength and in a broad momentum-space region near $Q = (0,0)$, these fluctuations are still sufficient to drive spin-triplet pairing as signaled by the relative sign-change of the diagonals in Fig. 6.5b. The antiferromagnetic fluctuations, on the other hand, are also seen when we fix the k_3 momentum away from the d_{xy}-pocket in Fig. 6.5b, but are not sufficiently robust to promote pairing.

6.5.2   Gap Structure of the $(p + ip)$-Pairing State

In order to gain a more quantitative insight, we further decompose the full 4-point function into the most relevant channels and expand each channel
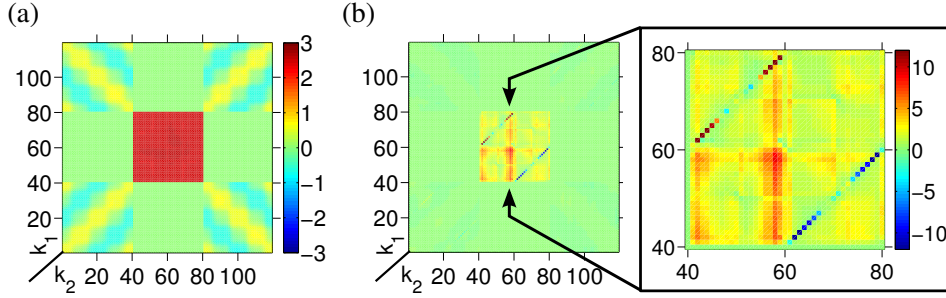
(a)   (b)

Figure 6.5: $V^\Lambda(k_1, k_2, k_3, k_4)$ for initial (a) and final (b) energy scales Λ depicted as a function of k_1, k_2 with k_3 fixed to point 59 and k_4 determined by momentum conservation. The numbering $1 - 120$ corresponds to the Fermi-surface points in Fig. 6.4. As k_3 was fixed to point 59, the broad vertical feature at $k_2 \approx 59$ (see enlarged section) corresponds to ferromagnetic like fluctuations promoting spin-triplet pairing as indicated by the two diagonals with opposite signs.

coupling in terms of eigenmodes. The same channel analysis was, by the way, also performed in the previous chapters and a detailed discussion can be found in Sec. 4.2.4. Applying this decomposition, we then obtain a flow of the leading eigenvalues as well as the associated form factors plotted in Fig. 6.6 along the different Fermi-pockets. At this, it is clearly seen that both ferromagnetic (fm) and antiferromagnetic (afm) fluctuations are sizeable at the beginning, but are overtaken by the p-wave pairing channel at low energy scales. Our results therefore support a ferromagnetically driven p-wave pairing instability with a subleading d-wave tendency induced by antiferromagnetic fluctuations. As the leading p-wave instability mainly originates from the ferromagnetic tendencies at the nearby van-Hove singularity of the d_{xy}-band, the resulting energy gap on the d_{xy}-pocket is one order of magnitude larger than on the other two $d_{xz,yz}$-pockets (see Fig. 6.6(a3)). The $d_{xz,yz}$-electrons, on the other hand, only become superconducting through the J_{pair}-induced proximity effect and therefore reveal a considerably smaller gap. In addition, Fig. 6.6(a3) reveals a fourfold gap oscillation on the d_{xy}-pocket with minima located at the $(k_x, 0)$ and $(0, k_y)$ axes consistent with a $(p_x + ip_y)$-wave pairing symmetry. This fourfold oscillation as well as the position of the gap minima is in perfect agreement with specific heat measurements in rotating magnetic fields [226]. Moreover, the very large gap differences between the d_{xy}-pocket and the remaining $d_{xz,yz}$-pockets can also be ascribed to an observed plateau in the magnetic field dependence of the specific heat [226]. Last but not least, the existence of near gap nodes or low-energy excitations was also very well established by numerous experiments like thermal conductivity [221], specific heat [219] as well as spin-relaxation measurements [220], and was one of the first caveats to the expected fully gapped $(p_x + ip_y)$-pairing state in SRO. It is further interesting to note that the gap oscillations on the other two $d_{xz,yz}$-pockets rather follow a $d_{x^2-y^2}$-

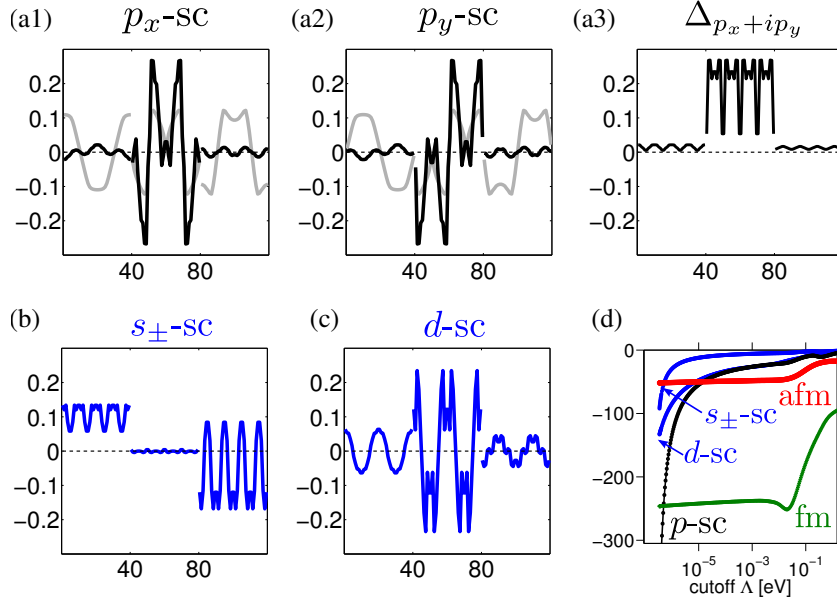**Figure 6.6:** (a1,a2) Form factors for the leading p-wave pairing channel (black) as well as the $\sin(k_x)$ and $\sin(k_y)$ harmonics evaluated at the Fermi-surface points $\boldsymbol{k}_i$ (gray). (a3) Superconducting energy gap ($\propto \sqrt{p_x^2 + p_y^2}$) determined by the form factors of (a1,a2). Subleading $s_\pm$-wave (b) and $d_{x^2-y^2}$-wave (c) pairing form factors. (d) Channel flow of the leading eigenvalues with (afm) denoting the antiferromagnetic fluctuations of ordering momentum $Q = (2\pi/3, 2\pi/3)$, and (fm) labeling the ferromagnetic fluctuations. The spin-singlet pairing channels are indicated d-sc, $s_\pm$-sc.

wave instead of a $(p_x + ip_y)$-wave symmetry. This behavior most likely reflects the antiferromagnetic fluctuations which actually favor a d-wave or $s_\pm$-wave pairing state with form factors depicted in Fig. 6.6(b,c). Based on the discussion in Sec. 4.2.5, this can be easily understood since both symmetries lead to a sign-change in the superconducting gap between Q-shifted Fermi-surface portions shown in Fig. 6.7a.

6.5.3 Phase Diagram away from Stoichiometric Filling

If we also study the phases away from the electron filling of $n = 4$ in SRO, we obtain the phase diagram depicted in Fig. 6.7b as a function of the chemical potential and the interaction parameters $J_H = J_{pair}$. The remaining parameters were chosen as $U_1 = 3t$, $U_2 = 2t$ and do not change the qualitative picture as long as both are in reasonable range with $U_1 > U_2$. From an experimental point of view, the modified filling can be realized by replacing Sr with La, which then causes a rigid band shift in the band structure of (6.1) as was proven by ARPES and quantum-oscillation measurements [227, 228]. The calculated phase diagram of Fig. 6.7 then reveals a ferromagnetic phase in the direct vicinity of van-Hove filling at μ_{vH}. Here,
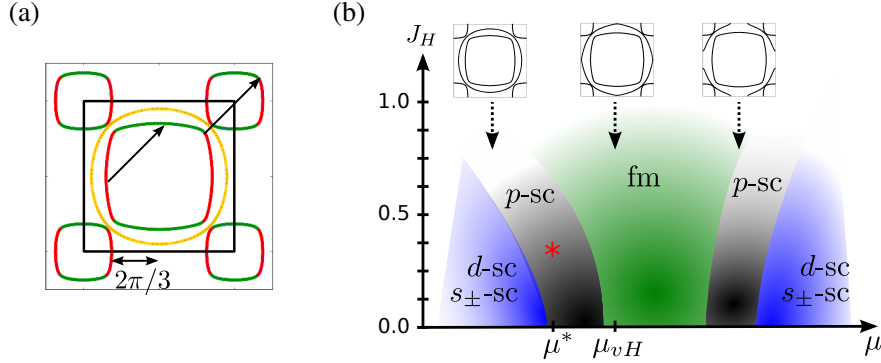
Figure 6.7: (a) Fermi-surface and nesting vector $Q \approx (2\pi/3, 2\pi/3)$ of SRO together with the main orbital weights whose color coding is the same as in Fig. 6.4. (b) Schematic phase diagram of the Hamiltonian in (6.1) as a function of the chemical potential and the interaction parameter J_H in units of U_2. The remaining parameter values were chosen as $U_1 = 3t$, $U_2 = 2t$ and $J_H = J_{pair}$.

the density of states in the d_{xy}-band diverges and induces a ferromagnetic ordering of the d_{xy}-electrons which is then also mediated to the other orbitals by means of J_H. This effect can be easily understood as the Hund's rule coupling J_H prefers parallel spins in different orbitals of the same site, and the ferromagnetic phase therefore extends to a broader filling range if we increase J_H. Close to the ferromagnetic instability we then find the p-wave superconducting phase which includes the pairing state of SRO at μ^*. At this, the role of the interaction parameter J_{pair} is mainly to induce a finite pairing amplitude on the $d_{xz,yz}$-pockets via proximity effects. Further away from van-Hove filling, the competing antiferromagnetic fluctuations of ordering momentum $Q \approx (2\pi/3, 2\pi/3)$ become more dominant and promote the spin-singlet pairing phases of $s_\pm$-wave and d-wave symmetry shown in Fig. 6.7b. Depending on the chosen values of interaction parameters, either the d-wave or $s_\pm$-wave pairing state is preferred since the nesting vector Q connects Fermi-surface portions of similar and reversed orbital weight as apparent from Fig. 6.7a, and a pronounced intra-orbital scattering then, for example, favors the $s_\pm$-wave instead of a d-wave pairing state.

In summary, the effect of the Hund's rule coupling J_H is mainly to extend ferromagnetic fluctuations further away from van Hove filling, whereas the pair-hopping interaction parameter transfers a finite pairing-amplitude either from the d_{xy}-pocket to the $d_{xz,yz}$-pockets or vice versa. On the other hand, the inter-orbital coupling U_2 acts contrary to J_H and weakens the ferromagnetic tendency, while supporting the antiferromagnetic channel. The parameter study presented here is of course far from complete, but provides a first insight into the role of the microscopic interaction parameters.

6.5.4 Including Spin-Orbit Coupling

The p-wave pairing state found in the preceding calculations still reveals a six-fold degeneracy in the sense that every linear combination of p_x and p_y in each of the three spin-triplet states has the same T_c by symmetry. According to the discussion in Sec. 6.3, this degeneracy results from the rotational symmetry in spin- and spatial-coordinates of the underlying model (6.1). However, if we include the spin-orbit coupling H_{LS} of (6.2), these individual rotation symmetries are broken, and the former sixfold degeneracy breaks up into four one-dimensional and one two-dimensional representation summarized in Tab. 6.1. It is also interesting to note here that all these five pairing symmetries lead to the same excitation gap of $|\hat{\Delta}|^2 = \boldsymbol{d} \cdot \boldsymbol{d}^* = p_x^2 + p_y^2$.

Now, in order to figure out which of these five pairing states is realized in the presence of spin-orbit coupling, we first derive an effective low-energy model and then include the spin-orbit coupling term H_{LS} of (6.2). The free part is thus given by

$$H_0 = \sum_{\boldsymbol{k},ss'} \sum_{oo'} \left[\xi_{o,o'}\delta_{ss'} + i\frac{\lambda}{2} \sum_n \epsilon_{oo'n}\sigma_{ss'}^n \right] c_{\boldsymbol{k},o,s}^\dagger c_{\boldsymbol{k},o',s'},$$

where o, o' belong to an ordered set of t_{2g}-orbitals $\{d_{yz}, d_{xz}, d_{xy}\}$, σ^n denotes the n-th Pauli-matrix and $\epsilon_{oo'n}$ is the totally antisymmetric tensor. Extracting the pairing interaction $V_{o_1,\ldots,o_4}^{pair}$ at low energy scales from the RG flow, the interaction part reads as

$$H_{int} = \sum_{\boldsymbol{k},\boldsymbol{q},ss'} \sum_{o_1,\ldots,o_4} V_{o_1,\ldots,o_4}^{pair}(\boldsymbol{k},\boldsymbol{q}) c_{\boldsymbol{k},o_1,s}^\dagger c_{-\boldsymbol{k},o_2,s'}^\dagger c_{-\boldsymbol{q},o_3,s'}^\dagger c_{\boldsymbol{q},o_4,s},$$

where we used $V_{o_1,\ldots,o_4}^{pair}$ in orbital representation, similar as in Sec. 4.2.8. In the next step, we diagonalize H_0 and obtain new quasi-particle states labeled by band m and pseudospin indices s. The new quasi-particles then comprise all different orbital characters and, as spin-rotational symmetry is broken by H_{LS}, also mix-up different spin states. In case of the two-dimensional d_{xy}-band, the corresponding states therefore obtain additional contributions from the d_{xz}- and d_{yz}-orbitals with reversed spin

$$|\boldsymbol{k},m,s\rangle = u_{m,xz}(\boldsymbol{k})|\boldsymbol{k},xz,-s\rangle + u_{m,yz}(\boldsymbol{k})|\boldsymbol{k},yz,-s\rangle + u_{m,xy}(\boldsymbol{k})|\boldsymbol{k},xy,s\rangle$$

such that both $u_{m,xz}$ and $u_{m,yz}$ go to zero with vanishing spin-orbit coupling λ, and the original states of (6.4) are recovered. Note that we used the same label s to denote pseudospin on the left- and physical spin on the right-hand side in order to simplify notation. The respective states for the other two $d_{xz,yz}$-bands then also contain an additional contribution from the d_{xy}-orbital with reversed spin which vanishes for $\lambda \to 0$. If we now represent

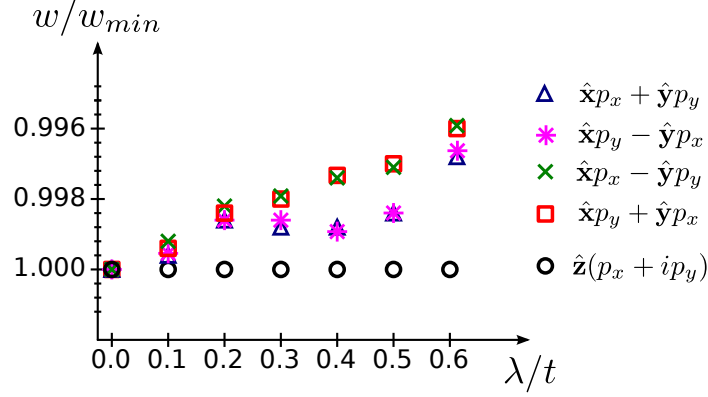**Figure 6.8:** Leading eigenvalues w of the pairing channel $\tilde{V}^{pair}$ in dependence of spin-orbit coupling λ. Here, the values on the vertical axes correspond to the normalized values of w with respect to the most leading one w_{min}. The calculated spin-orbit coupling in SRO amounts to $\lambda = 0.45t$.

the above Hamiltonian $H_0 + H_{int}$ in this new quasi-particle basis, we obtain

$$H_{total} = \sum_{\boldsymbol{k},s} \sum_{m=1}^{3} \gamma^\dagger_{\boldsymbol{k}ms} E_m(\boldsymbol{k}) \gamma_{\boldsymbol{k}ms} \tag{6.7}$$

$$+ \sum_{\substack{\boldsymbol{k},\boldsymbol{q} \\ m,m'}} \sum_{s_1,\dots,s_4} \tilde{V}^{pair}_{s_1,\dots,s_4}(\boldsymbol{k}m,-\boldsymbol{k}m,-\boldsymbol{q}m',\boldsymbol{q}m') \gamma^\dagger_{\boldsymbol{k}ms_1} \gamma^\dagger_{-\boldsymbol{k}ms_2} \gamma_{-\boldsymbol{q}m's_3} \gamma_{\boldsymbol{q}m's_4},$$

where $\gamma^\dagger, \gamma$ denote the creation and annihilation operators with respect to the basis states $|\boldsymbol{k}, m, s\rangle$. A subsequent eigenmode expansion of $\tilde{V}^{pair}$ as a function of spin-orbit coupling then reveals the leading eigenvalues and associated gap symmetries of Fig. 6.8. At this, we find the leading six eigenvalues or transition temperatures to be degenerate for vanishing spin-orbit coupling λ in accordance with our above symmetry consideration. For finite λ, this degeneracy splits and the chiral pairing state $\boldsymbol{d}(\boldsymbol{k}) = \hat{\boldsymbol{z}}(p_x \pm ip_y)$ turns out to be favored due to its lowest eigenvalue or, respectively, its highest transition temperature. This is, by the way, also confirmed by a study of Ng *et al.* [229] who found that the chiral pairing state is stable if the dominant pairing occurs in the d_{xy}-band as it is the case in our calculation. From our functional RG perspective, the chiral p-wave symmetry therefore describes the most preferred pairing state of SRO.

6.6   Summary and Outlook

Although a large number of experiments suggest that superconductivity in SRO is of spin-triplet type and most likely breaks time-reversal symmetry, the microscopic pairing mechanism as well as the detailed gap symmetry

still remain unclear. In order to resolve this issue, we applied the functional RG method which, on the one hand, allows an unbiased analysis and, on the other, also enables the consideration of all relevant material details.

Starting with a three orbital description of SRO, we then find that ferromagnetic fluctuations are still sufficient to drive p-wave superconductivity, whereas the antiferromagnetic ones mainly mediate singlet-pairing of both d-wave and $s_{\pm}$-wave symmetry. As a consequence, the p-wave pairing state is fully gapped on the d_{xy}-pocket and shows a much smaller gap with near-zero minima on the remaining two pockets. The detailed gap behavior observed in our calculation is fully consistent with the majority of experimental data.

Using an effective pairing vertex derived from functional RG, we also included spin-orbit coupling and confirmed that this clearly promotes the chiral pairing state described by $\boldsymbol{d}(\boldsymbol{k}) = \hat{\boldsymbol{z}}(p_x \pm i p_y)$ with broken time-reversal symmetry and in-plane oriented spin pairs. In an upcoming work, we will then consider the spin-orbit coupling right from the beginning of the flow. This is of course more complex due to the broken spin-rotational symmetry, but was already tested successfully in simplified models.

The results presented here in this chapter are of course far from complete and do not yet provide a comprehensive understanding of the pairing state in SRO. However, we think that our work already enables valuable insights into the superconductivity of SRO and also present a promising starting point for future investigations.

Chapter 7

Conclusion

The superconductivity in complex material systems like the recently discovered iron-pnictides or strontium ruthenate often involves multiple orbitals. In order to explore the superconducting properties and the underlying pairing mechanisms in those systems, we developed a multi-orbital extension of the functional RG and studied different characteristic material compounds.

After two introductory chapters on the technical implementation and on unconventional superconductivity in general, we analyzed the pairing mechanism of various material representatives of the iron-pnictide class. Here, we found that superconductivity in all investigated compounds is driven by spin-fluctuations. However, as the multi-orbital nature of these materials and the resulting multi-pocket Fermi-surface promote several competing spin-fluctuation channels, the pairing state may vary from $s_{\pm}$-wave with and without nodes to even d-wave symmetry. In addition to the material dependence, we also studied the influence of doping and pnictogen-height on the pairing state and further predicted the existence of a time-reversal symmetry broken $(s + id)$-pairing near the transition from nodal $s_{\pm}$-wave to d-wave superconductivity.

In Chapter 5, we then discussed the electronic instabilities of another fascinating material system – doped graphene. Using chemical dopants or electrolytic gating, doped graphene has recently become accessible in experiments with nearly no disorder in the underlying lattice structure. Although graphene can be described by one half-filled p_z-orbital per lattice site, there are two non-equivalent sites per unit-cell which can effectively be considered as two distinct orbitals. Near van-Hove filling, we then found a chiral pairing phase with $(d + id)$-symmetry in a wide doping range as well as a subleading triplet pairing channel and an exotic spin-density wave. Both subleading channels can be realized by varying the longer-range hopping and interaction parameters, for example, by using different substrate materials.

Finally, in Chapter 6, we considered the superconductivity of strontium ruthenate, a material that is isostructural to certain high-T_c cuprates and

possibly realizes the chiral pairing state determined by $\hat{\boldsymbol{d}} = \hat{\boldsymbol{z}}(p_x \pm ip_y)$. Applying the functional RG to a three orbital description for the relevant t_{2g}-states of ruthenium, we confirmed the occurence of this chiral pairing phase. In particular, we found that ferromagnetic fluctuations mediate the pairing instead of similarly strong antiferromagnetic fluctuations. The resulting superconducting gap then reveals large anisotropies on the γ-pocket and appears one order of magnitude larger than on the other two α- and β-pockets. The overall gap profile is in very good agreement to recent specific-heat measurements in rotating magnetic fields.

In conclusion, we think that multi-orbital physics plays an essential part in a large number of superconducting materials. A detailed understanding of these multi-orbital effects could therefore open new possibilities to engineer superconducting properties and to fabricate improved material compounds. The ideas and methodical progress developed in this thesis provided first insights into this fascinating field and will hopefully motivate future research.

Bibliography

[1] J. G. Bednorz and K. A. Müller, *Possible High T_c Superconductivity in the Ba-La-Cu-O System*, Z. Phys. B **64**, 189 (1986).

[2] Y. Kamihara, T. Watanabe, M. Hirano and H. Hosono, *Iron-Based Layered Superconductor $LaO_{1-x}F_xFeAs$ ($x = 0.05 - 0.12$) with $T_c = 26$ K*, J. Am. Chem. Soc. **130**, 3296 (2008).

[3] J. Bardeen, L. N. Cooper and J. R. Schrieffer, *Theory of Superconductivity*, Phys. Rev. **108**, 1175 (1957).

[4] T. R. Morris, *The exact renormalization group and approximate solutions*, Int. J. Mod. Phys. **A9**, 2411 (1994).

[5] P. Kopietz, L. Bartosch and F. Schütz, *Introduction to the Functional Renormalization Group*, Springer Berlin, (2010).

[6] A. A. Katanin, *Fulfillment of Ward identities in the functional renormalization group approach*, Phys. Rev. B **70**, 115109 (2004).

[7] T. Enss, *Renormalization, Conservation Laws and Transport in Correlated Electron Systems*, arXiv:0504703 (2005).

[8] C. Honerkamp and M. Salmhofer, *Temperature-flow renormalization group and the competition between superconductivity and ferromagnetism*, Phys. Rev. B **64**, 184516 (2001).

[9] W. Metzner, M. Salmhofer, C. Honerkamp, V. Meden and K. Schönhammer, *Functional renormalization group approach to correlated fermion systems*, Rev. Mod. Phys. **84**, 299 (2012).

[10] C. Honerkamp, D. Rohe, S. Andergassen and T. Enss, *Interaction flow method for many-fermion systems*, Phys. Rev. B **70**, 235115 (2004).

[11] C. Husemann and M. Salmhofer, *Efficient parametrization of the vertex function, Ω scheme, and the t, t' Hubbard model at van Hove filling*, Phys. Rev. B **79**, 195125 (2009).

[12] S. Andergassen, T. Enss, V. Meden, W. Metzner, U. Schollwöck and K. Schönhammer, *Functional renormalization group for Luttinger liquids with impurities*, Phys. Rev. B **70**, 075102 (2004).

[13] C. Honerkamp, M. Salmhofer, N. Furukawa and T. M. Rice, *Breakdown of the Landau-Fermi liquid in two dimensions due to umklapp scattering*, Phys. Rev. B **63**, 035109 (2001).

[14] M. Salmhofer, C. Honerkamp, W. Metzner and Oliver, *Renormalization group flows into phases with broken symmetry*, Prog. Theor. Phys. **112**, 943 (2004).

[15] J. Reuther, *Frustrated Quantum Heisengerg Antiferromagnets: Functional Renormalization-Group Approach in Auxiliary-Fermion Representation*, PhD thesis, Universität Karlsruhe, (2011).

[16] M. Salmhofer and C. Honerkamp, *Fermionic Renormalization Group Flows —Technique and Theory—*, Prog. Theor. Phys. **105**, 1 (2001).

[17] J. Reiss, D. Rohe and W. Metzner, *Renormalized mean-field analysis of antiferromagnetism and d-wave superconductivity in the two-dimensional Hubbard model*, Phys. Rev. B **75**, 075110 (2007).

[18] B. Mühlschlegel, *Asymptotic Expansion of the Bardeen-Cooper-Schrieffer Partition Function by Means of the Functional Method*, J. Math. Phys. **3**, 522 (1962).

[19] M. Sigrist and K. Ueda, *Phenomenological theory of unconventional superconductivity*, Rev. Mod. Phys. **63**, 239 (1991).

[20] V. P. Mineev and K. V. Samokhin, *Introduction to unconventional superconductivity*, Gordon and Breach Science Publishers, (1999).

[21] R. Haag, *The mathematical structure of the Bardeen-Cooper-Schrieffer model*, Nuovo Cimento **25**, 287 (1962).

[22] W. Pauli, *Über das Wasserstoffspektrum vom Standpunkt der neuen Quantenmechanik*, Zeitschrift fur Physik **36**, 336–363 (1926).

[23] P. Fulde and R. A. Ferrell, *Superconductivity in a Strong Spin-Exchange Field*, Physical Review **135**, 550–563 (1964).

[24] Chetan Nayak, *Density-wave states of nonzero angular momentum*, Phys. Rev. B **62**, 4880 (2000).

[25] David Garcia-Aldea and Sudip Chakravarty, *Singlet versus triplet particle-hole condensates in quantum oscillations in cuprates*, Phys. Rev. B **82**, 184526 (2010).

[26] K. Ueda and T. M. Rice, *p-wave superconductivity in cubic metals*, Phys. Rev. B **31**, 7114 (1985).

[27] G. E. Volovik, *Superconductivity with lines of gap nodes: density of states in the vortex*, J. Exp. Theor. Phys. Lett. **58**, 469 (1993).

[28] A. B. Vorontsov and I. Vekhter, *Unconventional superconductors under a rotating magnetic field. I. Density of states and specific heat*, Phys. Rev. B **75**, 224501 (2007).

[29] T. Moriya, *The Effect of Electron-Electron Interaction on the Nuclear Spin Relaxation in Metals*, J. Phys. Soc. Jpn. **18**, 516 (1963).

[30] L. C. Hebel and C. P. Slichter, *Nuclear Spin Relaxation in Normal and Superconducting Aluminum*, Phys. Rev. **113**, 1504 (1959).

[31] A. Damascelli, Z. Hussain and Z. X. Shen, *Angle-resolved photoemission studies of the cuprate superconductors*, Rev. Mod. Phys. **75**, 473 (2003).

[32] A. L. Fetter and J. D. Walecka, *Quantum theory of many-particle systems*, Dover Publications, (2003).

[33] V. Brouet, M. F. Jensen, P.-H. Lin, A. Taleb-Ibrahimi, P. Le Fèvre, F. Bertran, C.-H. Lin, W. Ku, A. Forget and D. Colson, *Impact of the two Fe unit cell on the electronic structure measured by ARPES in iron pnictides*, Phys. Rev. B **86**, 075123 (2012).

[34] D. A. Wollman, D. J. Van Harlingen, W. C. Lee, D. M. Ginsberg and A. J. Leggett, *Experimental determination of the superconducting pairing state in YBCO from the phase coherence of YBCO-Pb dc SQUIDs*, Phys. Rev. Lett. **71**, 2134 (1993).

[35] B. B. Schwartz and L. N. Cooper, *Flux Quantization and Generalized Pairing in Superconducting Cylinders*, Phys. Rev. **137**, A829 (1965).

[36] B. D. Josephson, *The discovery of tunnelling supercurrents*, Rev. Mod. Phys. **46**, 251 (1974).

[37] D. J. Van Harlingen, *Phase-sensitive tests of the symmetry of the pairing state in the high-temperature superconductors - Evidence for $d_{x^2-y^2}$ symmetry*, Rev. Mod. Phys. **67**, 515 (1995).

[38] D. Parker and I. I. Mazin, *Possible Phase-Sensitive Tests of Pairing Symmetry in Pnictide Superconductors*, Phys. Rev. Lett. **102**, 227007 (2009).

[39] X. Zhang, Y. S. Oh, Y. Liu, L. Yan, K. H. Kim, R. L. Greene and I. Takeuchi, *Observation of the Josephson Effect in* $Pb/Ba_{1-x}K_xFe_2As_2$ *Single Crystal Junctions*, Phys. Rev. Lett. **102**, 147002 (2009).

[40] Y. R. Zhou, Y. R. Li, J. W. Zuo, R. Y. Liu, S. K. Su, G. F. Chen, J. L. Lu, N. L. Wang and Y. P. Wang, *Phase-Sensitive measurements on the corner junction of iron-based superconductor* $BaFe_{1.8}Co_{0.2}As_2$, arXiv:0812.3295 (2008).

[41] H. Hilgenkamp, π-*phase shift Josephson structures*, Supercond. Sci. Technol. **21**, 034011 (2008).

[42] A. Gumann, C. Iniotakis and N. Schopohl, *Geometric* π *Josephson junction in d-wave superconducting thin films*, Appl. Phys. Lett. **91**, 192502 (2007).

[43] C. C. Tsuei, J. R. Kirtley, C. C. Chi, L. S. Yu-Jahnes, A. Gupta, T. Shaw, J. Z. Sun and M. B. Ketchen, *Pairing Symmetry and Flux Quantization in a Tricrystal Superconducting Ring of* $YBa_2Cu_3O_{7-\delta}$, Phys. Rev. Lett. **73**, 593 (1994).

[44] C. C. Tsuei and J. R. Kirtley, *Pairing symmetry in cuprate superconductors*, Rev. Mod. Phys. **72**, 969 (2000).

[45] W.-Q. Chen and F. C. Zhang, π-*phase shift at the interface of two pnictide superconductors with antiphase s-wave pairing*, Phys. Rev. B **83**, 212501 (2011).

[46] W.-Q. Chen, F. Ma, Z.-Y. Lu and F.-C. Zhang, π *Junction to Probe Antiphase s-Wave Pairing in Iron Pnictide Superconductors*, Phys. Rev. Lett. **103**, 207001 (2009).

[47] C. T. Chen, C. C. Tsuei, M. B. Ketchen, Z. A. Ren and Z. X. Zhao, *Integer and half-integer flux-quantum transitions in a niobiumiron pnictide loop*, Nature Physics **6**, 260 (2010).

[48] W.-F. Tsai, D.-X. Yao, B. A. Bernevig and J. Hu, *Properties of Josephson junctions involving the* $\cos(k_x) \cdot \cos(k_y)$ *pairing state in iron pnictides*, Phys. Rev. B **80**, 012511 (2009).

[49] C. W. Hicks, T. M. Lippman, M. E. Huber, Z.-A. Ren, J. Yang, Z.-X. Zhao and K. A. Moler, *Limits on the Superconducting Order Parameter in* $NdFeAsO_{1-x}F_y$ *from Scanning SQUID Microscopy*, J. Phys. Soc. Jpn. **78**, 013708 (2009).

[50] P. Seidel, *Josephson effects in iron based superconductors*, Supercond. Sci. Technol. **24**, 043001 (2011).

[51] M. Tinkham, *Introduction to superconductivity*, McGraw-Hill, New York, (1975).

[52] J. R. Schrieffer, *Theory of superconductivity*, Advanced Book Program, Perseus Books, (1999).

[53] R. S. Markiewicz, *Bridging k and q space in the cuprates: Comparing angle-resolved photoemission and STM results*, Phys. Rev. B **69**, 214517 (2004).

[54] Q.-H. Wang and D. H. Lee, *Quasiparticle scattering interference in high-temperature superconductors*, Phys. Rev. B **67**, 020511 (2003).

[55] L. Capriotti, D. J. Scalapino and R. D. Sedgewick, *Wave-vector power spectrum of the local tunneling density of states: Ripples in a d-wave sea*, Phys. Rev. B **68**, 014508 (2003).

[56] T. Hanaguri, Y. Kohsaka, M. Ono, M. Maltseva, P. Coleman, I. Yamada, M. Azuma, M. Takano, K. Ohishi and H. Takagi, *Coherence Factors in a High-T_c Cuprate Probed by Quasi-Particle Scattering Off Vortices*, Science **323**, 923 (2009).

[57] T. Hanaguri, S. Niitaka, K. Kuroki and H. Takagi, *Unconventional s-Wave Superconductivity in Fe(Se,Te)*, Science **328**, 474 (2010).

[58] J. E. Hoffman, K. McElroy, D.-H. Lee, K. M. Lang, H. Eisaki, S. Uchida and J. C. Davis, *Imaging Quasiparticle Interference in $Bi_2Sr_2CaCu_2O_{8+\delta}$*, Science **297**, 1148 (2002).

[59] N. Bulut and D. J. Scalapino, *Weak-coupling analysis of the neutron-scattering spectral weight*, Phys. Rev. B **47**, 3419 (1993).

[60] H. F. Fong, B. Keimer, P. W. Anderson, D. Reznik, F. Dogan and I. A. Aksay, *Phonon and Magnetic Neutron Scattering at 41 meV in $YBa_2Cu_3O_7$*, Phys. Rev. Lett. **75**, 316 (1995).

[61] H. A. Mook, M. Yethiraj, G. Aeppli, T. E. Mason and T. Armstrong, *Polarized neutron determination of the magnetic excitations in $YBa_2Cu_3O_7$*, Phys. Rev. Lett. **70**, 3490 (1993).

[62] M. D. Lumsden and A. D. Christianson, *Magnetism in Fe-based superconductors*, J. Phys.: Condens. Matter **22**, 203203 (2010).

[63] D. S. Inosov, J. T. Park, P. Bourges, D. L. Sun, Y. Sidis, A. Schneidewind, K. Hradil, D. Haug, C. T. Lin, B. Keimer and V. Hinkov, *Normal-state spin dynamics and temperature-dependent spin-resonance energy in optimally doped $BaFe_{1.85}Co_{0.15}As_2$*, Nature Physics **6**, 178 (2010).

[64] A. D. Christianson, E. A. Goremychkin, R. Osborn, S. Rosenkranz, M. D. Lumsden, C. D. Malliakas, I. S. Todorov, H. Claus, D. Y. Chung, M. G. Kanatzidis, R. I. Bewley and T. Guidi, *Unconventional superconductivity in $Ba_{0.6}K_{0.4}Fe_2As_2$ from inelastic neutron scattering*, Nature Physics **456**, 930 (2008).

[65] Y. Kamihara, H. Hiramatsu, M. Hirano, R. Kawamura, H. Yanagi, T. Kamiya and H. Hosono, *Iron-Based Layered Superconductor: LaOFeP*, J. Am. Chem. Soc. **128**, 10012 (2006).

[66] B. S. Chandrasekhar and J. K. Hulm, *The electrical resistivity and super-conductivity of some uranium alloys and compounds*, J. Phys. Chem. Solids **7**, 259 (1958).

[67] C. Wang, L. Li, S. Chi, Z. Zhu, Z. Ren, Y. Li, Y. Wang, X. Lin, Y. Luo, S. Jiang, X. Xu, G. Cao and Z. Xu, *Thorium-doping induced superconductivity up to 56 K in $Gd_{1-x}Th_xFeAsO$*, Europhys. Lett. **83**, 67006 (2008).

[68] Y. Mizuguchi, F. Tomioka, S. Tsuda, T. Yamaguchi and Y. Takano, *Superconductivity at 27 K in tetragonal FeSe under high pressure*, Appl. Phys. Lett. **93**, 152505 (2008).

[69] D. J. Singh and M.-H. Du, *Density Functional Study of $LaFeAsO_{1-x}F_x$: A Low Carrier Density Superconductor Near Itinerant Magnetism*, Phys. Rev. Lett. **100**, 237003 (2008).

[70] M. J. Calderón, B. Valenzuela and E. Bascones, *Tight-binding model for iron pnictides*, Phys. Rev. B **80**, 094531 (2009).

[71] K. Kuroki, S. Onari, R. Arita, H. Usui, Y. Tanaka, H. Kontani and H. Aoki, *Unconventional Pairing Originating form the Disconnected Fermi Surfaces of Superconducting $LaFeAsO_{1-x}F_x$*, Phys. Rev. Lett. **101**, 087004 (2008).

[72] T. Miyake, K. Nakamura, R. Arita and M. Imada, *Comparison of Ab initio Low-Energy Models for LaFePO, LaFeAsO, $BaFe_2As_2$, LiFeAs, FeSe, and FeTe: Electron Correlation and Covalency*, J. Phys. Soc. Jpn. **79**, 044705 (2010).

[73] H. Ding, P. Richard, K. Nakayama, K. Sugawara, T. Arakane, Y. Sekiba, A. Takayama, S. Souma, T. Sato, T. Takahashi, Z. Wang, X. Dai, Z. Fang, G. F. Chen, J. L. Luo and N. L. Wang, *Observation of Fermi-surface-dependent nodeless superconducting gaps in $Ba_{0.6}K_{0.4}Fe_2As_2$*, Eur. Phys. Lett. **83**, 47001 (2008).

[74] M. Yi, D. H. Lu, J. G. Analytis, J.-H. Chu, S.-K. Mo, R.-H. He, R. G. Moore, X. J. Zhou, G. F. Chen, J. L. Luo, N. L. Wang, Z. Hussain, D. J. Singh, I. R. Fisher and Z.-X. Shen, *Electronic structure of the $BaFe_2As_2$ family of iron-pnictide superconductors*, Phys. Rev. B **80**, 024515 (2009).

[75] X.-P. Wang, P. Richard, Y.-B. Huang, H. Miao, L. Cevey, N. Xu, Y.-J. Sun, T. Qian, Y.-M. Xu, M. Shi, J.-P. Hu, X. Dai and H. Ding, *Orbital characters determined from Fermi surface intensity patterns using angle-resolved photoemission spectroscopy*, Phys. Rev. B **85**, 214518 (2012).

[76] A. Carrington, *Quantum oscillation studies of the Fermi surface of iron-pnictide superconductors*, Rep. Prog. Phys. **74**, 124507 (2011).

[77] C. Putzke, A. I. Coldea, I. Guillamón, D. Vignolles, A. McCollam, D. Leboeuf, M. D. Watson, I. I. Mazin, S. Kasahara, T. Terashima, T. Shibauchi, Y. Matsuda and A. Carrington, *de Haas-van Alphen Study of the Fermi Surfaces of Superconducting LiFeP and LiFeAs*, Phys. Rev. Lett. **108**, 047002 (2012).

[78] O.K. Andersen and L. Boeri, *On the multi-orbital band structure and itinerant magnetism of iron-based superconductors*, Ann. Phys. (Berlin) **523**, 8 (2011).

[79] Y. Ran, F. Wang, H. Zhai, A. Vishwanath and D.-H. Lee, *Nodal spin density wave and band topology of the FeAs-based materials*, Phys. Rev. B **79**, 014505 (2009).

[80] P. Richard, K. Nakayama, T. Sato, M. Neupane, Y.-M. Xu, J. H. Bowen, G. F. Chen, J. L. Luo, N. L. Wang, X. Dai, Z. Fang, H. Ding and T. Takahashi, *Observation of Dirac Cone Electronic Dispersion in $BaFe_2As_2$*, Phys. Rev. Lett. **104**, 137001 (2010).

[81] T. M. McQueen, M. Regulacio, A. J. Williams, Q. Huang, J. W. Lynn, Y. S. Hor, D. V. West, M. A. Green and R. J. Cava, *Intrinsic properties of stoichiometric LaFePO*, Phys. Rev. B **78**, 024521 (2008).

[82] X. C. Wang, Q. Q. Liu, Y. X. Lv, W. B. Gao, L. X. Yang, R. C. Yu, F. Y. Li and C. Q. Jin, *The superconductivity at 18 K in LiFeAs system*, Solid State Commun. **148**, 538 (2008).

[83] Z. Deng, X. C. Wang, Q. Q. Liu, S. J. Zhang, Y. X. Lv, J. L. Zhu, R. C. Yu and C. Q. Jin, *A new "111" type iron pnictide superconductor LiFeP*, Europhys. Lett. **87**, 37004 (2009).

[84] R. M. Fernandes, A. V. Chubukov, J. Knolle, I. Eremin and J. Schmalian, *Preemptive nematic order, pseudogap, and orbital order in the iron pnictides*, Phys. Rev. B **85**, 024534 (2012).

[85] R. M. Fernandes and J. Schmalian, *Manifestations of nematic degrees of freedom in the magnetic, elastic, and superconducting properties of the iron pnictides*, Supercond. Sci. Technol. **25**, 084005 (2012).

[86] W. Bao, Y. Qiu, Q. Huang, M. A. Green, P. Zajdel, M. R. Fitzsimmons, M. Zhernenkov, S. Chang, Minghu Fang, B. Qian, E. K. Vehstedt, Jinhu Yang, H. M. Pham, L. Spinu and Z. Q. Mao, *Tunable $(\delta\pi, \delta\pi)$-Type Antiferromagnetic Order in α-Fe(Te,Se) Superconductors*, Phys. Rev. Lett. **102**, 247001 (2009).

[87] S. Li, C. de la Cruz, Q. Huang, Y. Chen, J. W. Lynn, J. Hu, Yi-Lin Huang, F.-C. Hsu, K.-W. Yeh, M.-K. Wu and P. Dai, *First-order magnetic and structural phase transitions in $Fe_{1+y}Se_xTe_{1-x}$*, Phys. Rev. B **79**, 054503 (2009).

[88] I. Paul, *Magnetoelastic Quantum Fluctuations and Phase Transitions in the Iron Superconductors*, Phys. Rev. Lett. **107**, 047004 (2011).

[89] M. S. Torikachvili, S. L. Bud'ko, N. Ni and P. C. Canfield, *Pressure Induced Superconductivity in $CaFe_2As_2$*, Phys. Rev. Lett. **101**, 057006 (2008).

[90] I. I. Mazin, D. J. Singh, M. D. Johannes and M. H. Du, *Unconventional Superconductivity with a Sign Reversal in the Order Parameter of $LaFeAsO_{1-x}F_x$*, Phys. Rev. Lett. **101**, 057003 (2008).

[91] M. Berciu, I. Elfimov and G. A. Sawatzky, *Electronic polarons and bipolarons in iron-based superconductors: The role of anions*, Phys. Rev. B **79**, 214507 (2009).

[92] H. Kontani and S. Onari, *Orbital-fluctuation-mediated superconductivity in iron pnictides: Analysis of the five-orbital hubbard-holstein model*, Phys. Rev. Lett. **104**, 157001 (2010).

[93] P. A. Lee and X.-G. Wen, *Spin-triplet p -wave pairing in a three-orbital model for iron pnictide superconductors*, Phys. Rev. B **78**, 144517 (2008).

[94] X. Dai, Z. Fang, Y. Zhou and F.-C. Zhang, *Even Parity, Orbital Singlet, and Spin Triplet Pairing for Superconducting $LaFeAsO_{1-x}F_x$*, Phys. Rev. Lett. **101**, 057008 (2008).

[95] L. Boeri, O. V. Dolgov and A. A. Golubov, *Is $LaFeAsO_{1-x}F_x$ an Electron-Phonon Superconductor?*, Phys. Rev. Lett. **101**, 026403 (2008).

[96] T. Yildirim, *Strong Coupling of the Fe-Spin State and the As-As Hybridization in Iron-Pnictide Superconductors from First-Principle Calculations*, Phys. Rev. Lett. **102**, 037003 (2009).

[97] P. J. Hirschfeld, M. M. Korshunov and I. I. Mazin, *Gap symmetry and structure of Fe-based superconductors*, Rep. Prog. Phys. **74**, 124508 (2011).

[98] H.-J. Grafe, D. Paar, G. Lang, N. J. Curro, G. Behr, J. Werner, J. Hamann-Borrero, C. Hess, N. Leps, R. Klingeler and B. Büchner, ^{75}As *NMR Studies of Superconducting* $LaFeAsO_{0.9}F_{0.1}$, Phys. Rev. Lett. **101**, 047003 (2008).

[99] K. Matano, Z. A. Ren, X. L. Dong, L. L. Sun, Z. X. Zhao and G. Zheng, *Spin-singlet superconductivity with multiple gaps in* $PrFeAsO_{0.89}F_{0.11}$, Eur. Phys. Lett. **83**, 57001 (2008).

[100] Y. Xia, D. Qian, L. Wray, D. Hsieh, G. F. Chen, J. L. Luo, N. L. Wang and M. Z. Hasan, *Fermi Surface Topology and Low-Lying Quasiparticle Dynamics of Parent* $Fe_{1+x}Te/Se$ *Superconductor*, Phys. Rev. Lett. **103**, 037002 (2009).

[101] T. Kondo, A. F. Santander-Syro, O. Copie, C. Liu, M. E. Tillman, E. D. Mun, J. Schmalian, S. L. Bud'Ko, M. A. Tanatar, P. C. Canfield and A. Kaminski, *Momentum Dependence of the Superconducting Gap in* $NdFeAsO_{0.9}F_{0.1}$ *Single Crystals Measured by Angle Resolved Photoemission Spectroscopy*, Phys. Rev. Lett. **101**, 147003 (2008).

[102] A. F. Kemper, T. A. Maier, S. Graser, H.-P. Cheng, P. J. Hirschfeld and D. J. Scalapino, *Sensitivity of the superconducting state and magnetic susceptibility to key aspects of electronic structure in ferropnictides*, New J. Phys. **12**, 073030 (2010).

[103] S. Raghu, X.-L. Qi, C.-X. Liu, D. J. Scalapino and S.-C. Zhang, *Minimal two-band model of the superconducting iron oxypnictides*, Phys. Rev. B **77**, 220503 (2008).

[104] S. Graser, T. A. Maier, P. J. Hirschfeld and D. J. Scalapino, *Near-degeneracy of several pairing channels in multiorbital models for the Fe-pnictides*, New J. Phys. **11**, 025016 (2009).

[105] C. Castellani, C. R. Natoli and J. Ranninger, *Magnetic structure of* V_2O_3 *in the insulating phase*, Phys. Rev. B **18**, 4945 (1978).

[106] R. Shankar, *Renormalization-group approach to interacting fermions*, Rev. Mod. Phys. **66**, 129 (1994).

[107] D. Zanchi and H. J. Schulz, *Weakly correlated electrons on a square lattice: Renormalization-group theory*, Phys. Rev. B **61**, 13609 (2000).

[108] A. V. Chubukov, D. V. Efremov and I. Eremin, *Magnetism, superconductivity, and pairing symmetry in iron-based superconductors*, Phys. Rev. B **78**, 134512 (2008).

[109] L. Wray, D. Qian, D. Hsieh, Y. Xia, L. Li, J. G. Checkelsky, A. Pasupathy, K. K. Gomes, C. V. Parker, A. V. Fedorov, G. F. Chen, J. L. Luo, A. Yazdani, N. P. Ong, N. L. Wang and M. Z. Hasan, *Momentum dependence of superconducting gap, strong-coupling dispersion kink, and tightly bound Cooper pairs in the high T_c $(Sr, Ba)_{1-x}(K, Na)_x Fe_2 As_2$ superconductors*, Phys. Rev. B **78**, 184508 (2008).

[110] K. Hashimoto, T. Shibauchi, S. Kasahara, K. Ikada, S. Tonegawa, T. Kato, R. Okazaki, C. J. van der Beek, M. Konczykowski, H. Takeya, K. Hirata, T. Terashima and Y. Matsuda, *Microwave Surface-Impedance Measurements of the Magnetic Penetration Depth in Single Crystal $Ba_{1-x}K_x Fe_2 As_2$ Superconductors: Evidence for a Disorder-Dependent Superfluid Density*, Phys. Rev. Lett. **102**, 207001 (2009).

[111] M. M. Parish, J. Hu and B. A. Bernevig, *Experimental Consequences of the s-wave $\cos(k_x) \cdot \cos(k_y)$ Superconductivity in the Iron-Pnictides*, Phys. Rev. B **78**, 144514 (2008).

[112] M. A. Tanatar, J.-P. Reid, H. Shakeripour, X. G. Luo, N. Doiron-Leyraud, N. Ni, S. L. Bud'Ko, P. C. Canfield, R. Prozorov and L. Taillefer, *Doping Dependence of Heat Transport in the Iron-Arsenide Superconductor $Ba(Fe_{1-x}Co_x)_2 As_2$: From Isotropic to a Strongly k-Dependent Gap Structure*, Phys. Rev. Lett. **104**, 067002 (2010).

[113] J. G. Checkelsky, Lu Li, G. F. Chen, J. L. Luo, N. L. Wang and N. P. Ong, *Large quasiparticle thermal Hall conductivity in the superconductor $Ba_{1-x}K_x Fe_2 As_2$*, arXiv:0811.4668 (2011).

[114] M. Yamashita, N. Nakata, Y. Senshu, S. Tonegawa, K. Ikada, K. Hashimoto, H. Sugawara, T. Shibauchi and Y. Matsuda, *Thermal conductivity measurements of the energy-gap anisotropy of superconducting LaFePO at low temperatures*, Phys. Rev. B **80**, 220509 (2009).

[115] C. W. Hicks, T. M. Lippman, M. E. Huber, J. G. Analytis, J.-H. Chu, A. S. Erickson, I. R. Fisher and K. A. Moler, *Evidence for a Nodal Energy Gap in the Iron-Pnictide Superconductor LaFePO from Penetration Depth Measurements by Scanning SQUID Susceptometry*, Phys. Rev. Lett. **103**, 127003 (2009).

[116] D. H. Lu, M. Yi, S.-K. Mo, J. G. Analytis, J.-H. Chu, A. S. Erickson, D. J. Singh, Z. Hussain, T. H. Geballe, I. R. Fisher and Z.-X. Shen, *ARPES studies of the electronic structure of LaOFe(P,As)*, Physica C **469**, 452 (2009).

[117] K. Kuroki, H. Usui, S. Onari, R. Arita and H. Aoki, *Pnictogen height as a possible switch between high-T_c nodeless and low-T_c nodal pairings in the iron-based superconductors*, Phys. Rev. B **79**, 224511 (2009).

[118] F. Wang, H. Zhai, Y. Ran, A. Vishwanath and D.-H. Lee, *Functional Renormalization-Group Study of the Pairing Symmetry and Pairing Mechanism of the FeAs-Based High-Temperature Superconductor*, Phys. Rev. Lett. **102**, 1047005 (2009).

[119] P. W. Anderson, *Is there glue in cuprate superconductors?*, Science **316**, 1705 (2007).

[120] W. Hanke, C. Platt and R. Thomale, *Order-parameter anisotropies in the pnictides: An optimization principle for multi-band superconductivity*, Ann. Phys. (Berlin) **523**, 638 (2011).

[121] J. K. Dong, S. Y. Zhou, T. Y. Guan, H. Zhang, Y. F. Dai, X. Qiu, X. F. Wang, Y. He, X. H. Chen and S. Y. Li, *Quantum Criticality and Nodal Superconductivity in the FeAs-Based Superconductor KFe_2As_2*, Phys. Rev. Lett. **104**, 087005 (2010).

[122] T. Terashima, M. Kimata, N. Kurita, H. Satsukawa, A. Harada, K. Hazama, M. Imai, A. Sato, K. Kihou, C.-H. Lee, H. Kito, H. Eisaki, A. Iyo, T. Saito, H. Fukazawa, Y. Kohori, H. Harima and S. Uji, *Comment on "Quantum Criticality and Nodal Superconductivity in the FeAs-Based Superconductor KFe_2As_2"*, Phys. Rev. Lett. **104**, 259701 (2010).

[123] K. Hashimoto, A. Serafin, S. Tonegawa, R. Katsumata, R. Okazaki, T. Saito, H. Fukazawa, Y. Kohori, K. Kihou, C. H. Lee, A. Iyo, H. Eisaki, H. Ikeda, Y. Matsuda, A. Carrington and T. Shibauchi, *Evidence for superconducting gap nodes in the zone-centered hole bands of KFe_2As_2 from magnetic penetration-depth measurements*, Phys. Rev. B **82**, 014526 (2010).

[124] H. Fukazawa, Y. Yamada, K. Kondo, T. Saito, Y. Kohori, K. Kuga, Y. Matsumoto, S. Nakatsuji, H. Kito, P. M. Shirage, K. Kihou, N. Takeshita, C.-H. Lee, A. Iyo and H. Eisaki, *Possible Multiple Gap Superconductivity with Line Nodes in Heavily Hole-Doped Superconductor KFe_2As_2 Studied by ^{75}As Nuclear Quadrupole Resonance and Specific Heat*, J. Phys. Soc. Jpn. **78**, 083712 (2009).

[125] S. W. Zhang, L. Ma, Y. D. Hou, J. Zhang, T. L. Xia, G. F. Chen, J. P. Hu, G. M. Luke and W. Yu, ^{75}As *NMR study of single crystals of the heavily overdoped pnictide superconductors $Ba_{1-x}K_xFe_2As_2$ (x = 0.7 and 1)*, Phys. Rev. B **81**, 012503 (2010).

[126] T. Sato, K. Nakayama, Y. Sekiba, P. Richard, Y.-M. Xu, S. Souma, T. Takahashi, G. F. Chen, J. L. Luo, N. L. Wang and H. Ding, *Band Structure and Fermi Surface of an Extremely Overdoped Iron-Based Superconductor KFe_2As_2*, Phys. Rev. Lett. **103**, 047002 (2009).

[127] M. Rotter, M. Tegel and D. Johrendt, *Superconductivity at 38 K in the Iron Arsenide $(Ba_{1-x}K_x)Fe_2As_2$*, Phys. Rev. Lett. **101**, 107006 (2008).

[128] C. Martin, R. T. Gordon, M. A. Tanatar, H. Kim, N. Ni, S. L. Bud'ko, P. C. Canfield, H. Luo, H. H. Wen, Z. Wang, A. B. Vorontsov, V. G. Kogan and R. Prozorov, *Nonexponential london penetration depth of external magnetic fields in superconducting $ba_{1-x}k_xfe_2as_2$ single crystals*, Phys. Rev. B **80**, 020501 (2009).

[129] X. G. Luo, M. A. Tanatar, J.-Ph. Reid, H. Shakeripour, N. Doiron-Leyraud, N. Ni, S. L. Bud'ko, P. C. Canfield, Huiqian Luo, Zhaosheng Wang, Hai-Hu Wen, R. Prozorov and Louis Taillefer, *Quasiparticle heat transport in single-crystalline $Ba_{1-x}K_xFe_2As_2$: Evidence for a k-dependent superconducting gap without nodes*, Phys. Rev. B **80**, 140503 (2009).

[130] Y. Zhang, L. X. Yang, F. Chen, B. Zhou, X. F. Wang, X. H. Chen, M. Arita, K. Shimada, H. Namatame, M. Taniguchi, J. P. Hu, B. P. Xie and D. L. Feng, *Out-of-Plane Momentum and Symmetry-Dependent Energy Gap of the Pnictide $Ba_{0.6}K_{0.4}Fe_2As_2$ Superconductor Revealed by Angle-Resolved Photoemission Spectroscopy*, Phys. Rev. Lett. **105**, 117003 (2010).

[131] S. Graser, A. F. Kemper, T. A. Maier, H.-P. Cheng, P. J. Hirschfeld and D. J. Scalapino, *Spin fluctuations and superconductivity in a three-dimensional tight-binding model for $BaFe_2As_2$*, Phys. Rev. B **81**, 214503 (2010).

[132] T. Miyake, K. Nakamura, R. Arita and M. Imada, *Dynamic conductance and the scattering matrix of small conductors*, J. Phys. Soc. Jpn. **79**, 044705 (2010).

[133] R. Thomale, C. Platt, J. Hu, C. Honerkamp and B. A. Bernevig, *Functional renormalization-group study of the doping dependence of pairing symmetry in the iron pnictide superconductors*, Phys. Rev. B **80**, 180505 (2009).

[134] R. Thomale, C. Platt, W. Hanke and B. A. Bernevig, *Mechanism for Explaining Differences in the Order Parameters of FeAs-Based and FeP-Based Pnictide Superconductors*, Phys. Rev. Lett. **106**, 187003 (2011).

[135] C. Platt, C. Honerkamp and W. Hanke, *Pairing in the iron arsenides: a functional RG treatment*, New J. Phys. **11**, 055058 (2009).

[136] C. H. Lee, K. Kihou, H. Kawano-Furukawa, T. Saito, A. Iyo, H. Eisaki, H. Fukazawa, Y. Kohori, K. Suzuki, H. Usui, K. Kuroki and K. Yamada, *Incommensurate Spin Fluctuations in Hole-Overdoped Superconductor KFe_2As_2*, Phys. Rev. Lett. **106**, 067003 (2011).

[137] H. Kawano-Furukawa, C. J. Bowell, J. S. White, R. W. Heslop, A. S. Cameron, E. M. Forgan, K. Kihou, C. H. Lee, A. Iyo, H. Eisaki, T. Saito, H. Fukazawa, Y. Kohori, R. Cubitt, C. D. Dewhurst, J. L. Gavilano and M. Zolliker, *Gap in KFe_2As_2 studied by small-angle neutron scattering observations of the magnetic vortex lattice*, Phys. Rev. B **84**, 024507 (2011).

[138] W.-C. Lee, S.-C. Zhang and C. Wu, *Pairing State with a Time-Reversal Symmetry Breaking in FeAs-Based Superconductors*, Phys. Rev. Lett. **102**, 217002 (2009).

[139] T. A. Maier, S. Graser, P. J. Hirschfeld and D. J. Scalapino, *d-wave pairing from spin fluctuations in the $K_xFe_{2-y}Se_2$ superconductors*, Phys. Rev. B **83**, 100515 (2011).

[140] F. Wang, F. Yang, M. Gao, Z.-Y. Lu, T. Xiang and D.-H. Lee, *The electron pairing of $K_xFe_{2-y}Se_2$*, Europhys. Lett. **93**, 57003 (2011).

[141] C. Fang, Y.-L. Wu, R. Thomale, B. A. Bernevig and J. Hu, *Robustness of s-Wave Pairing in Electron-Overdoped $A_{1-y}Fe_{2-x}Se_2$ (A=K,Cs)*, Phys. Rev. X **1**, 011009 (2011).

[142] J. Zhang, R. Sknepnek, R. M. Fernandes and J. Schmalian, *Orbital coupling and superconductivity in the iron pnictides*, Phys. Rev. B **79**, 220502 (2009).

[143] K Haule and G Kotliar, *Coherence-incoherence crossover in the normal state of iron oxypnictides and importance of Hund's rule coupling*, New J. Phys. **11**, 025021 (2009).

[144] J. H. Tapp, Z. Tang, B. Lv, K. Sasmal, B. Lorenz, P. C. W. Chu and A. M. Guloy, *LiFeAs: An intrinsic FeAs-based superconductor with T_c=18K*, Phys. Rev. B **78**, 060505 (2008).

[145] S.-H. Baek, H.-J. Grafe, F. Hammerath, M. Fuchs, C. Rudisch, L. Harnagea, S. Aswartham, S. Wurmehl, J. van den Brink and B. Büchner, *75As NMR-NQR study in superconducting LiFeAs*, Eur. Phys. J. B **85**, 159.

[146] A. K. Pramanik, L. Harnagea, C. Nacke, A. U. B. Wolter, S. Wurmehl, V. Kataev and B. Büchner, *Fishtail effect and vortex dynamics in LiFeAs single crystals*, Phys. Rev. B **83**, 094502 (2011).

[147] S. V. Borisenko, V. B. Zabolotnyy, D. V. Evtushinsky, T. K. Kim, I. V. Morozov, A. N. Yaresko, A. A. Kordyuk, G. Behr, A. Vasiliev, R. Follath and B. Büchner, *Superconductivity without Nesting in LiFeAs*, Phys. Rev. Lett. **105**, 067002 (2010).

[148] P. Jeglič, A. Potočnik, M. Klanjšek, M. Bobnar, M. Jagodič, K. Koch, H. Rosner, S. Margadonna, B. Lv, A. M. Guloy and D. Arčon, ^{75}As *nuclear magnetic resonance study of antiferromagnetic fluctuations in the normal state of LiFeAs*, Phys. Rev. B **81**, 140511 (2010).

[149] A. E. Taylor, M. J. Pitcher, R. A. Ewings, T. G. Perring, S. J. Clarke and A. T. Boothroyd, *Antiferromagnetic spin fluctuations in LiFeAs observed by neutron scattering*, Phys. Rev. B **83**, 220514 (2011).

[150] D. S. Inosov, J. S. White, D. V. Evtushinsky, I. V. Morozov, A. Cameron, U. Stockert, V. B. Zabolotnyy, T. K. Kim, A. A. Kordyuk, S. V. Borisenko, E. M. Forgan, R. Klingeler, J. T. Park, S. Wurmehl, A. N. Vasiliev, G. Behr, C. D. Dewhurst and V. Hinkov, *Weak Superconducting Pairing and a Single Isotropic Energy Gap in Stoichiometric LiFeAs*, Phys. Rev. Lett. **104**, 187001 (2010).

[151] K. Sasmal, B. Lv, Z. Tang, F. Y. Wei, Y. Y. Xue, A. M. Guloy and C. W. Chu, *Lower critical field, anisotropy, and two-gap features of LiFeAs*, Phys. Rev. B **81**, 144512 (2010).

[152] U. Stockert, M. Abdel-Hafiez, D. V. Evtushinsky, V. B. Zabolotnyy, A. U. B. Wolter, S. Wurmehl, I. Morozov, R. Klingeler, S. V. Borisenko and B. Büchner, *Specific heat and angle-resolved photoemission spectroscopy study of the superconducting gaps in LiFeAs*, Phys. Rev. B **83**, 224512 (2011).

[153] Y. Imai, H. Takahashi, K. Kitagawa, K. Matsubayashi, N. Nakai, Y. Nagai, Y. Uwatoko, M. Machida and A. Maeda, *Microwave Surface Impedance Measurements of LiFeAs Single Crystals*, J. Phys. Soc. Jpn. **80**, 013704 (2011).

[154] Y. J. Song, J. S. Ghim, J. H. Yoon, K. J. Lee, M. H. Jung, H.-S. Ji, J. H. Shim, Y. Bang and Y. S. Kwon, *Small anisotropy of the lower*

critical field and the $s_\pm$-wave two-gap feature in single-crystal LiFeAs, Europhys. Lett. **94**, 57008 (2011).

[155] M. Imada and T. Miyake, *Electronic Structure Calculation by First Principles for Strongly Correlated Electron Systems*, J. Phys. Soc. Jpn. **79**, 112001 (2010).

[156] G. Strinati, H. J. Mattausch and W. Hanke, *Dynamical Correlation Effects on the Quasiparticle Bloch States of a Covalent Crystal*, Phys. Rev. Lett. **45**, 290 (1980).

[157] F. Aryasetiawan and O. Gunnarsson, *The GW method*, Rep. Prog. Phys. **61**, 237 (1998).

[158] P. M. R. Brydon, M. Daghofer, C. Timm and J. van den Brink, *Theory of magnetism and triplet superconductivity in LiFeAs*, Phys. Rev. B **83**, 060501 (2011).

[159] C. J. Halboth and W. Metzner, *Renormalization-group analysis of the two-dimensional hubbard model*, Phys. Rev. B **61**, 7364 (2000).

[160] K. Hashimoto, S. Kasahara, R. Katsumata, Y. Mizukami, M. Yamashita, H. Ikeda, T. Terashima, A. Carrington, Y. Matsuda and T. Shibauchi, *Nodal versus Nodeless Behaviors of the Order Parameters of LiFeP and LiFeAs Superconductors from Magnetic Penetration-Depth Measurements*, Phys. Rev. Lett. **108**, 047003 (2012).

[161] K. S. Novoselov, A. K. Geim, S. V. Morozov, D. Jiang, Y. Zhang, S. V. Dubonos, I. V. Grigorieva and A. A. Firsov, *Electric Field Effect in Atomically Thin Carbon Films*, Science **306**, 666 (2004).

[162] A. H. Castro Neto, F. Guinea, N. M. R. Peres, K. S. Novoselov and A. K. Geim, *The electronic properties of graphene*, Rev. Mod. Phys. **81**, 109 (2009).

[163] Z. Y. Meng, T. C. Lang, S. Wessel, F. F. Assaad and A. Muramatsu, *Quantum spin liquid emerging in two-dimensional correlated Dirac fermions*, Nature **464**, 847 (2010).

[164] S. Raghu, X.-L. Qi, C. Honerkamp and S.-C. Zhang, *Topological Mott Insulators*, Phys. Rev. Lett. **100**, 156401 (2008).

[165] M. M. Scherer, S. Uebelacker and C. Honerkamp, *Instabilities of interacting electrons on the honeycomb bilayer*, Phys. Rev. B **85**, 235408 (2012).

[166] V. N. Kotov, B. Uchoa, V. M. Pereira, F. Guinea and A. H. Castro Neto, *Electron-Electron Interactions in Graphene: Current Status and Perspectives*, Rev. Mod. Phys. **84**, 1067 (2012).

[167] J. L. McChesney, A. Bostwick, T. Ohta, T. Seyller, K. Horn, J. González and E. Rotenberg, *Extended van Hove Singularity and Superconducting Instability in Doped Graphene*, Phys. Rev. Lett. **104**, 136803 (2010).

[168] D. K. Efetov and P. Kim, *Controlling Electron-Phonon Interactions in Graphene at Ultrahigh Carrier Densities*, Phys. Rev. Lett. **105**, 256805 (2010).

[169] J. González, *Kohn-Luttinger superconductivity in graphene*, Phys. Rev. B **78**, 205431 (2008).

[170] R. Nandkishore, L. S. Levitov and A. V. Chubukov, *Chiral superconductivity from repulsive interactions in doped graphene*, Nature Physics **8**, 158 (2012).

[171] T. Li, *Spontaneous quantum Hall effect in quarter-doped Hubbard model on honeycomb lattice and its possible realization in doped graphene system*, Europhys. Lett. **97**, 37001 (2012).

[172] F. D. M. Haldane, *Model for a Quantum Hall Effect without Landau Levels: Condensed-Matter Realization of the "Parity Anomaly"*, Phys. Rev. Lett. **61**, 2015 (1988).

[173] C. L. Kane and E. J. Mele, *Quantum spin hall effect in graphene*, Phys. Rev. Lett. **95**, 226801 (2005).

[174] T. O. Wehling, E. Şaşıoğlu, C. Friedrich, A. I. Lichtenstein, M. I. Katsnelson and S. Blügel, *Strength of Effective Coulomb Interactions in Graphene and Graphite*, Phys. Rev. Lett. **106**, 236805 (2011).

[175] M. Cheng, K. Sun, V. Galitski and S. Das Sarma, *Stable topological superconductivity in a family of two-dimensional fermion models*, Phys. Rev. B **81**, 024504 (2010).

[176] G. E. Volovik, *On edge states in superconductors with time inversion symmetry breaking*, J. Exp. Theor. Phys. Lett. **66**, 522 (1997).

[177] X.-L. Qi, T. L. Hughes and S.-C. Zhang, *Chiral topological superconductor from the quantum Hall state*, Phys. Rev. B **82**, 184516 (2010).

[178] G. E. Volovik, *Fermion zero modes on vortices in chiral superconductors*, J. Exp. Theor. Phys. Lett. **70**, 609 (1999).

[179] N. Read and D. Green, *Paired states of fermions in two dimensions with breaking of parity and time-reversal symmetries and the fractional quantum Hall effect*, Phys. Rev. B **61**, 10267 (2000).

[180] R. Roy, *Topological Majorana and Dirac Zero Modes in Superconducting Vortex Cores*, Phys. Rev. Lett. **105**, 186401 (2010).

[181] C. Nayak, S. H. Simon, A. Stern, M. Freedman and S. Das Sarma, *Non-abelian anyons and topological quantum computation*, Rev. Mod. Phys. **80**, 1083 (2008).

[182] D. A. Ivanov, *Non-Abelian Statistics of Half-Quantum Vortices in p-Wave Superconductors*, Phys. Rev. Lett. **86**, 268 (2001).

[183] J. Alicea, *New directions in the pursuit of Majorana fermions in solid state systems*, Rep. Prog. Phys. **75**, 076501 (2012).

[184] T. Senthil, J. B. Marston and M. P. A. Fisher, *Spin quantum Hall effect in unconventional superconductors*, Phys. Rev. B **60**, 4245 (1999).

[185] B. Horovitz and A. Golub, *Superconductors with broken time-reversal symmetry: Spontaneous magnetization and quantum Hall effects*, Phys. Rev. B **68**, 214503 (2003).

[186] M. Sato, Y. Takahashi and S. Fujimoto, *Non-Abelian topological orders and Majorana fermions in spin-singlet superconductors*, Phys. Rev. B **82**, 134521 (2010).

[187] S. Florens and M. Vojta, *Impact of disorder on unconventional superconductors with competing ground states*, Phys. Rev. B **71**, 094516 (2005).

[188] S. Raghu, S. A. Kivelson and D. J. Scalapino, *Superconductivity in the repulsive hubbard model: An asymptotically exact weak-coupling solution*, Phys. Rev. B **81**, 224505 (2010).

[189] I. Martin and C. D. Batista, *Itinerant Electron-Driven Chiral Magnetic Ordering and Spontaneous Quantum Hall Effect in Triangular Lattice Models*, Phys. Rev. Lett. **101**, 156402 (2008).

[190] W.-S. Wang, Y.-Y. Xiang, Q.-H. Wang, F. Wang, F. Yang and D.-H. Lee, *Functional renormalization group and variational Monte Carlo studies of the electronic instabilities in graphene near 1/4 doping*, Phys. Rev. B **85**, 035414 (2012).

[191] R. Nandkishore, G.-W. Chern and A. V. Chubukov, *Itinerant Half-Metal Spin-Density-Wave State on the Hexagonal Lattice*, Phys. Rev. Lett. **108**, 227204 (2012).

[192] Y. Taguchi, Y. Oohara, H. Yoshizawa, N. Nagaosa and Y. Tokura, *Spin Chirality, Berry Phase, and Anomalous Hall Effect in a Frustrated Ferromagnet*, Science **291**, 2573 (2001).

[193] Y. Maeno, H. Hashimoto, K. Yoshida, S. Nishizaki, T. Fujita, J. G. Bednorz and F. Lichtenberg, *Superconductivity in a layered perovskite without copper*, Nature **372**, 532 (1994).

[194] A. P. Mackenzie and Y. Maeno, *The superconductivity of Sr_2RuO_4 and the physics of spin-triplet pairing*, Rev. Mod. Phys. **75**, 657 (2003).

[195] Y. Maeno, S. Kittaka, T. Nomura, S. Yonezawa and K. Ishida, *Evaluation of Spin-Triplet Superconductivity in Sr_2RuO_4*, J. Phys. Soc. Jpn. **81**, 011009 (2012).

[196] Yoshiteru M., T. M. Rice and M. Sigrist, *The Intriguing Superconductivity of Strontium Ruthenate*, Phys. Today **54**, 42 (2001).

[197] C. Bergemann, S. R. Julian, A. P. Mackenzie, S. NishiZaki and Y. Maeno, *Detailed Topography of the Fermi Surface of Sr_2RuO_4*, Phys. Rev. Lett. **84**, 2662 (2000).

[198] D. H. Lu, M. Schmidt, T. R. Cummins, S. Schuppler, F. Lichtenberg and J. G. Bednorz, *Fermi Surface and Extended van Hove Singularity in the Noncuprate Superconductor Sr_2RuO_4*, Phys. Rev. Lett. **76**, 4845 (1996).

[199] T. Yokoya, A. Chainani, T. Takahashi, H. Ding, J. C. Campuzano, H. Katayama-Yoshida, M. Kasai and Y. Tokura, *Angle-resolved photoemission study of Sr_2RuO_4*, Phys. Rev. B **54**, 13311 (1996).

[200] A. Damascelli, D. H. Lu, K. M. Shen, N. P. Armitage, F. Ronning, D. L. Feng, C. Kim, Z.-X. Shen, T. Kimura, Y. Tokura, Z. Q. Mao and Y. Maeno, *Fermi Surface, Surface States, and Surface Reconstruction in Sr_2RuO_4*, Phys. Rev. Lett. **85**, 5194 (2000).

[201] David J. Singh, *Relationship of Sr_2RuO_4 to the superconducting layered cuprates*, Phys. Rev. B **52**, 1358 (1995).

[202] T. Oguchi, *Electronic band structure of the superconductor Sr_2RuO_4*, Phys. Rev. B **51**, 1385 (1995).

[203] J. Mravlje, M. Aichhorn, T. Miyake, K. Haule, G. Kotliar and A. Georges, *Coherence-Incoherence Crossover and the Mass-Renormalization Puzzles in Sr_2RuO_4*, Phys. Rev. Lett. **106**, 096401 (2011).

[204] Z. V. Pchelkina, I. A. Nekrasov, Th. Pruschke, A. Sekiyama, S. Suga, V. I. Anisimov and D. Vollhardt, *Evidence for strong electronic correlations in the spectra of Sr_2RuO_4*, Phys. Rev. B **75**, 035122 (2007).

[205] I. I. Mazin and D. J. Singh, *Competitions in Layered Ruthenates: Ferromagnetism versus Antiferromagnetism and Triplet versus Singlet Pairing*, Phys. Rev. Lett. **82**, 4324 (1999).

[206] Y. Sidis, M. Braden, P. Bourges, B. Hennion, S. NishiZaki, Y. Maeno and Y. Mori, *Evidence for Incommensurate Spin Fluctuations in Sr_2RuO_4*, Phys. Rev. Lett. **83**, 3320 (1999).

[207] T. Imai, A. W. Hunt, K. R. Thurber and F. C. Chou, *^{17}O NMR Evidence for Orbital Dependent Ferromagnetic Correlations in Sr_2RuO_4*, Phys. Rev. Lett. **81**, 3006 (1998).

[208] S. G. Ovchinnikov, *Exotic superconductivity and magnetism in ruthenates*, Phys.-Usp. **46**, 21 (2003).

[209] G. Cao, S. K. McCall, J. E. Crow and R. P. Guertin, *Ferromagnetism in $Sr_4Ru_3O_{10}$: Relationship to other layered metallic oxides*, Phys. Rev. B **56**, R5740 (1997).

[210] M. W. Haverkort, I. S. Elfimov, L. H. Tjeng, G. A. Sawatzky and A. Damascelli, *Strong Spin-Orbit Coupling Effects on the Fermi Surface of Sr_2RuO_4 and Sr_2RhO_4*, Phys. Rev. Lett. **101**, 026406 (2008).

[211] K. Ishida, H. Mukuda, Y. Kitaoka, K. Asayama, Z. Q. Mao, Y. Mori and Y. Maeno, *Spin-triplet superconductivity in Sr_2RuO_4 identified by ^{17}O Knight shift*, Nature **396**, 658 (1998).

[212] J. A. Duffy, S. M. Hayden, Y. Maeno, Z. Mao, J. Kulda and G. J. McIntyre, *Polarized-Neutron Scattering Study of the Cooper-Pair Moment in Sr_2RuO_4*, Phys. Rev. Lett. **85**, 5412 (2000).

[213] M. Sigrist, *Superconductivity with broken time-reversal symmetry*, Physica B **280**, 154 (2000).

[214] G. M. Luke, Y. Fudamoto, K. M. Kojima, M. I. Larkin, J. Merrin, B. Nachumi, Y. J. Uemura, Y. Maeno, Z. Q. Mao, Y. Mori, H. Nakamura and M. Sigrist, *Time-reversal symmetry-breaking superconductivity in Sr_2RuO_4*, Nature **394**, 558 (1998).

[215] J. Xia, Y. Maeno, P. T. Beyersdorf, M. M. Fejer and A. Kapitulnik, *High Resolution Polar Kerr Effect Measurements of Sr_2RuO_4: Evidence for Broken Time-Reversal Symmetry in the Superconducting State*, Phys. Rev. Lett. **97**, 167002 (2006).

[216] F. Kidwingira, J. D. Strand, D. J. Van Harlingen and Y. Maeno,
Dynamical Superconducting Order Parameter Domains in Sr_2RuO_4,
Science **314**, 1267 (2006).

[217] T. M. Riseman, P. G. Kealey, E. M. Forgan, A. P. MacKenzie,
L. M. Galvin, A. W. Tyler, S. L. Lee, C. Ager, D. M. Paul,
C. M. Aegerter, R. Cubitt, Z. Q. Mao, T. Akima and Y. Maeno,
*Observation of a square flux-line lattice in the unconventional super-
conductor Sr_2RuO_4*, Nature **396**, 242 (1998).

[218] P. G. Kealey, T. M. Riseman, E. M. Forgan, L. M. Galvin,
A. P. Mackenzie, S. L. Lee, D. McK. Paul, R. Cubitt, D. F. Agterberg,
R. Heeb, Z. Q. Mao and Y. Maeno, *Reconstruction from Small-Angle
Neutron Scattering Measurements of the Real Space Magnetic Field
Distribution in the Mixed State of Sr_2RuO_4*, Phys. Rev. Lett. **84**,
6094 (2000).

[219] S. NishiZaki, Y. Maeno and Z. Mao, *Changes in the Superconducting
State of Sr_2RuO_4 under Magnetic Fields Probed by Specific Heat*, J.
Phys. Soc. Jpn. **69**, 572 (2000).

[220] K. Ishida, H. Mukuda, Y. Kitaoka, Z. Q. Mao, Y. Mori and Y. Maeno,
*Anisotropic Superconducting Gap in the Spin-Triplet Superconductor
Sr_2RuO_4: Evidence from a Ru-NQR Study*, Phys. Rev. Lett. **84**, 5387
(2000).

[221] K. Izawa, H. Takahashi, H. Yamaguchi, Yuji Matsuda, M. Suzuki,
T. Sasaki, T. Fukase, Y. Yoshida, R. Settai and Y. Onuki, *Supercon-
ducting Gap Structure of Spin-Triplet Superconductor Sr_2RuO_4 Stud-
ied by Thermal Conductivity*, Phys. Rev. Lett. **86**, 2653 (2001).

[222] S. Kashiwaya, H. Kashiwaya, H. Kambara, T. Furuta, H. Yaguchi,
Y. Tanaka and Y. Maeno, *Edge States of Sr_2RuO_4 Detected by In-
Plane Tunneling Spectroscopy*, Phys. Rev. Lett. **107**, 077003 (2011).

[223] J. R. Kirtley, C. Kallin, C. W. Hicks, E.-A. Kim, Y. Liu, K. A. Moler,
Y. Maeno and K. D. Nelson, *Upper limit on spontaneous supercurrents
in Sr_2RuO_4*, Phys. Rev. B **76**, 014526 (2007).

[224] S. Raghu, A. Kapitulnik and S. A. Kivelson, *Hidden Quasi-One-
Dimensional Superconductivity in Sr_2RuO_4*, Phys. Rev. Lett. **105**,
136401 (2010).

[225] Y. Imai, K. Wakabayashi and M. Sigrist, *Properties of edge states in a
spin-triplet two-band superconductor*, Phys. Rev. B **85**, 174532 (2012).

[226] K. Deguchi, Z. Q. Mao, H. Yaguchi and Y. Maeno, *Gap Structure of the Spin-Triplet Superconductor Sr_2RuO_4 Determined from the Field-Orientation Dependence of the Specific Heat*, Phys. Rev. Lett. **92**, 047002 (2004).

[227] K. M. Shen, N. Kikugawa, C. Bergemann, L. Balicas, F. Baumberger, W. Meevasana, N. J. C. Ingle, Y. Maeno, Z.-X. Shen and A. P. Mackenzie, *Evolution of the Fermi Surface and Quasiparticle Renormalization through a van Hove Singularity in $Sr_{2-y}La_yRuO_4$*, Phys. Rev. Lett. **99**, 187001 (2007).

[228] N. Kikugawa, A. P. Mackenzie, C. Bergemann, R. A. Borzi, S. A. Grigera and Y. Maeno, *Rigid-band shift of the Fermi level in the strongly correlated metal: $Sr_{2-y}La_yRuO_4$*, Phys. Rev. B **70**, 060508 (2004).

[229] K.-K. Ng and M. Sigrist, *The role of spin-orbit coupling for the superconductivity in Sr_2RuO_4*, Phys. B Cond. Mat. **281**, 969 (2000).

List of Publications

[1] M. Kiesel, C. Platt, and R. Thomale, *Unconventional Fermi surface instabilities in the Kagome Hubbard Model*, arXiv:1209.3398 (2012).

[2] L. A. Wray, R. Thomale, C. Platt, D. Hsieh, D. Qian, G. F. Chen, J. L. Luo, N. L. Wang, M. Z. Hasan, *Deviating band symmetries and many-body interactions in a model hole doped iron pnictide superconductor Authors*, Phys. Rev. B **86**, 144515 (2012).

[3] M. Kiesel, C. Platt, W. Hanke, D. Abanin, and R. Thomale *Competing many-body instabilities and unconventional superconductivity in graphene*, Phys. Rev. B **86**, 020507(R) (2012).

[4] C. Platt, R. Thomale, C. Honerkamp, S. C. Zhang, and W. Hanke, *Mechanism for a pairing state with time-reversal symmetry breaking in iron-based superconductors*, Phys. Rev. B **85**, 180502(R) (2012).

[5] C. Platt, R. Thomale, and W. Hanke, *From density functional theory to the functional renormalization group: superconductivity in the iron pnictide LiFeAs*, Phys. Rev. B **84**, 235121 (2011).

[6] W. Hanke, C. Platt, and R. Thomale, *Order-Parameter Anisotropies in the Pnictides - An Optimization Principle for Multi-Band Superconductivity*, Ann. Phys. (Berlin) **523**, 638 (2011).

[7] R. Thomale, C. Platt, W. Hanke, J. Hu, B. A. Bernevig, *Exotic d-wave superconductivity in strongly hole doped $K_x Ba_{1-x} Fe_2 As_2$*, Phys. Rev. Lett. **107**, 117001 (2011).

[8] R. Thomale, C. Platt, W. Hanke, J. Hu, B. A. Bernevig, *Mechanism for Explaining Differences in the Order Parameters of FeAs-Based and FeP-Based Pnictide Superconductors*, Phys. Rev. Lett. **106**, 187003 (2011).

[9] R. Thomale, C. Platt, J. Hu, C. Honerkamp, and B. A. Bernevig *Functional renormalization-group study of the doping dependence of pairing symmetry in the iron pnictide superconductors*, Phys. Rev. B **80**, 180505(R) (2009).

[10] C. Platt, C. Honerkamp, and W. Hanke, *Pairing in the iron arsenides: a functional RG treatment*, New J. Phys. **11**, 055058 (2009).

Curriculum Vitae

Christian Platt
born in Wetzlar, October 1st 1982

Education:

June 2002	Abitur Goetheschule Wetzlar, Germany
2003-2009	Studies of Physics and Mathematics Universität Würzburg, Germany
March 2008	Diploma in Physics *Is the pairing in high-T_c superconductors* *driven by the kinetic energy ?* Advisor: Prof. Werner Hanke
October 2009	Diploma in Mathematics *A new NCP-function applied to nonlinear* *and second-order cone complementarity problems.* Advisor: Prof. Christian Kanzow
since May 2008	Ph.D. Studies Universität Würzburg, Germany Advisor: Prof. Werner Hanke

_____   _____
Ort, Datum   Christian Platt

Danksagung

Versicherung an Eides statt

- Hiermit versichere ich, Christian Platt, geboren am 01.10.1982 in Wetzlar, an Eides statt, dass ich die Dissertation eigenständig, d.h. insbesondere selbstständig und ohne Hilfe einer kommerziellen Promotionsberatung angefertigt und keine anderen als die von mir angegebenen Quellen und Hilfsmittel benutzt habe.
  (gem. §5 Abs. 2 Satz 2 der Promotionsordnung)

- Des Weiteren versichere ich an Eides statt, dass ich die Gelegenheit zum Promotionsvorhaben nicht kommerziell vermittelt bekommen habe und insbesondere nicht eine Person oder Organisation eingeschaltet habe, die gegen Entgelt Betreuer bzw. Betreuerinnen für die Anfertigung von Dissertationen sucht.
  (gem. §5 Abs. 2 Satz 3 der Promotionsordnung)

- Zusätzlich erkläre ich, dass ich die Regeln der Universität Würzburg über gute wissenschaftliche Praxis eingehalten habe.
  (gem. §5 Abs. 2 Satz 4 der Promotionsordnung)

- Außerdem erkläre ich, dass diese Dissertation weder in gleicher noch in anderer Form bereits in einem anderen Prüfungsfach vorliegt.
  (gem. §5 Abs. 2 Satz 6 der Promotionsordnung)

_____   _____

Ort, Datum   Christian Platt